SAIMM
JOURNAL OF THE SOUTHERN AFRICAN INSTITUTE OF MINING AND METALLURGY
FOUNDED 1894
VOLUME 119 NO. 4 APRIL 2019

PASTE 2019

PATERSON & COOKE

Collaborating Organisation

ACG AUSTRALIAN CENTRE FOR GEOMECHANICS

CSIRO | The University of Western Australia | Joint Venture

Founding Body

22nd International Conference on

Paste, Thickened and Filtered Tailings

8-10 May 2019 | The Westin | Cape Town, South Africa

The Australian Centre for Geomechanics is pleased to host the 22nd International Conference on Paste, Thickened and Filtered Tailings in collaboration with Paterson & Cooke.

ASSOCIATED EVENTS:

Paterson & Cooke: Mine Backfill - Design and Operation Course ~ 6 May 2019

ACG: Is the Future Filtered? Paste and Thickened Tailings Short Course ~ 7 May 2019

WWW.PASTE2019.CO.ZA

The Southern African Institute of Mining and Metallurgy

OFFICE BEARERS AND COUNCIL FOR THE 2018/2019 SESSION

Honorary President

Mxolisi Mgojo
President, Minerals Council South Africa

Honorary Vice Presidents

Gwede Mantashe
Minister of Mineral Resources, South Africa

Rob Davies
Minister of Trade and Industry, South Africa

Mmamoloko Kubayi-Ngubane
Minister of Science and Technology, South Africa

President

A.S. Macfarlane

President Elect

M.I. Mthenjane

Senior Vice President

Z. Botha

Junior Vice President

V.G. Duke

Incoming Junior Vice President

I.J. Geldenhuys

Immediate Past President

S. Ndlovu

Co-opted to Office Bearers

R.T. Jones

Honorary Treasurer

V.G. Duke

Ordinary Members on Council

I.J. Geldenhuys
C.C. Holtzhausen
W.C. Joughin
G.R. Lane
E. Matinde
H. Musiyarira
G. Njowa
S.M Rupprecht
N. Singh
A.G. Smith
M.H. Solomon
D. Tudor
A.T. van Zyl
E.J. Walls

Past Presidents Serving on Council

N.A. Barcza
R.D. Beck
J.R. Dixon
M. Dworzanowski
H.E. James
R.T. Jones
G.V.R. Landman
C. Musingwini
J.L. Porter
S.J. Ramokgopa
M.H. Rogers
D.A.J. Ross-Watt
G.L. Smith
W.H. van Niekerk
R.P.H. Willis

G.R. Lane–TPC Mining Chairperson
Z. Botha–TPC Metallurgy Chairperson

K.M. Letsoalo–YPC Chairperson
G. Dabula–YPC Vice Chairperson

Branch Chairpersons

Botswana	Vacant
DRC	S. Maleba
Johannesburg	Vacant
Namibia	N.M. Namate
Northern Cape	F.C. Nieuwenhuys
Pretoria	R.J. Mostert
Western Cape	L.S. Bbosa
Zambia	D. Muma
Zimbabwe	C. Sadomba
Zululand	C.W. Mienie

PAST PRESIDENTS

*Deceased

- * W. Bettel (1894–1895)
- * A.F. Crosse (1895–1896)
- * W.R. Feldtmann (1896–1897)
- * C. Butters (1897–1898)
- * J. Loevy (1898–1899)
- * J.R. Williams (1899–1903)
- * S.H. Pearce (1903–1904)
- * W.A. Caldecott (1904–1905)
- * W. Cullen (1905–1906)
- * E.H. Johnson (1906–1907)
- * J. Yates (1907–1908)
- * R.G. Bevington (1908–1909)
- * A. McA. Johnston (1909–1910)
- * J. Moir (1910–1911)
- * C.B. Saner (1911–1912)
- * W.R. Dowling (1912–1913)
- * A. Richardson (1913–1914)
- * G.H. Stanley (1914–1915)
- * J.E. Thomas (1915–1916)
- * J.A. Wilkinson (1916–1917)
- * G. Hildick-Smith (1917–1918)
- * H.S. Meyer (1918–1919)
- * J. Gray (1919–1920)
- * J. Chilton (1920–1921)
- * F. Wartenweiler (1921–1922)
- * G.A. Watermeyer (1922–1923)
- * F.W. Watson (1923–1924)
- * C.J. Gray (1924–1925)
- * H.A. White (1925–1926)
- * H.R. Adam (1926–1927)
- * Sir Robert Kotze (1927–1928)
- * J.A. Woodburn (1928–1929)
- * H. Pirow (1929–1930)
- * J. Henderson (1930–1931)
- * A. King (1931–1932)
- * V. Nimmo-Dewar (1932–1933)
- * P.N. Lategan (1933–1934)
- * E.C. Ranson (1934–1935)
- * R.A. Flugge-De-Smidt (1935–1936)
- * T.K. Prentice (1936–1937)
- * R.S.G. Stokes (1937–1938)
- * P.E. Hall (1938–1939)
- * E.H.A. Joseph (1939–1940)
- * J.H. Dobson (1940–1941)
- * Theo Meyer (1941–1942)
- * John V. Muller (1942–1943)
- * C. Biccard Jeppe (1943–1944)
- * P.J. Louis Bok (1944–1945)
- * J.T. McIntyre (1945–1946)
- * M. Falcon (1946–1947)
- * A. Clemens (1947–1948)
- * F.G. Hill (1948–1949)
- * O.A.E. Jackson (1949–1950)
- * W.E. Gooday (1950–1951)
- * C.J. Irving (1951–1952)
- * D.D. Stitt (1952–1953)
- * M.C.G. Meyer (1953–1954)
- * L.A. Bushell (1954–1955)
- * H. Britten (1955–1956)
- * Wm. Bleloch (1956–1957)
- * H. Simon (1957–1958)
- * M. Barcza (1958–1959)
- * R.J. Adamson (1959–1960)
- * W.S. Findlay (1960–1961)
- * D.G. Maxwell (1961–1962)
- * J. de V. Lambrechts (1962–1963)
- * J.F. Reid (1963–1964)
- * D.M. Jamieson (1964–1965)
- * H.E. Cross (1965–1966)
- * D. Gordon Jones (1966–1967)
- * P. Lambooy (1967–1968)
- * R.C.J. Goode (1968–1969)
- * J.K.E. Douglas (1969–1970)
- * V.C. Robinson (1970–1971)
- * D.D. Howat (1971–1972)
- * J.P. Hugo (1972–1973)
- * P.W.J. van Rensburg (1973–1974)
- * R.P. Plewman (1974–1975)
- * R.E. Robinson (1975–1976)
- * M.D.G. Salamon (1976–1977)
- * P.A. Von Wielligh (1977–1978)
- * M.G. Atmore (1978–1979)
- * D.A. Viljoen (1979–1980)
- * P.R. Jochens (1980–1981)
  G.Y. Nisbet (1981–1982)
  A.N. Brown (1982–1983)
- * R.P. King (1983–1984)
  J.D. Austin (1984–1985)
  H.E. James (1985–1986)
  H. Wagner (1986–1987)
- * B.C. Alberts (1987–1988)
- * C.E. Fivaz (1988–1989)
- * O.K.H. Steffen (1989–1990)
- * H.G. Mosenthal (1990–1991)
  R.D. Beck (1991–1992)
- * J.P. Hoffman (1992–1993)
- * H. Scott-Russell (1993–1994)
  J.A. Cruise (1994–1995)
  D.A.J. Ross-Watt (1995–1996)
  N.A. Barcza (1996–1997)
- * R.P. Mohring (1997–1998)
  J.R. Dixon (1998–1999)
  M.H. Rogers (1999–2000)
  L.A. Cramer (2000–2001)
- * A.A.B. Douglas (2001–2002)
  S.J. Ramokgopa (2002-2003)
  T.R. Stacey (2003–2004)
  F.M.G. Egerton (2004–2005)
  W.H. van Niekerk (2005–2006)
  R.P.H. Willis (2006–2007)
  R.G.B. Pickering (2007–2008)
  A.M. Garbers-Craig (2008–2009)
  J.C. Ngoma (2009–2010)
  G.V.R. Landman (2010–2011)
  J.N. van der Merwe (2011–2012)
  G.L. Smith (2012–2013)
  M. Dworzanowski (2013–2014)
  J.L. Porter (2014–2015)
  R.T. Jones (2015–2016)
  C. Musingwini (2016–2017)
  S. Ndlovu (2017–2018)

Honorary Legal Advisers
Scop Incorporated

Auditors
Genesis Chartered Accountants

Secretaries
The Southern African Institute of Mining and Metallurgy
Fifth Floor, Minerals Council South Africa
5 Hollard Street, Johannesburg 2001 • P.O. Box 61127, Marshalltown 2107
Telephone (011) 834-1273/7 • Fax (011) 838-5923 or (011) 833-8156
E-mail: journal@saimm.co.za

Typeset and Published by
The Southern African Institute of Mining and Metallurgy
P.O. Box 61127
Marshalltown 2107
Telephone (011) 834-1273/7
Fax (011) 838-5923
E-mail: journal@saimm.co.za

Printed by
Camera Press, Johannesburg

Advertising Representative
Barbara Spence
Avenue Advertising
Telephone (011) 463-7940
E-mail: barbara@avenue.co.za

ISSN 2225-6253 (print)
ISSN 2411-9717 (online)

Directory of Open Access Journals

INDEXED IN DOAJ

FOUNDED 1894

SAIMM

JOURNAL OF THE SOUTHERN AFRICAN INSTITUTE OF MINING AND METALLURGY

VOLUME 119 NO. 4 APRIL 2019

Contents

GEOMETALLURGICAL EDITION

SAIMM
JOURNAL OF THE SOUTHERN AFRICAN INSTITUTE OF MINING AND METALLURGY
VOLUME 119 NO. 4 APRIL 2019

PAPERS OF GENERAL INTEREST

With the increasingly challenging techno-economic climate we now operate in, coupled with the rise in the need to mine more heterogeneous and complex orebodies, geometallurgy represents a collective, multidisciplinary mine-planning approach to both maximizing value and managing the risk emanating from ore variability. The first SAIMM Geometallurgy Conference, held from 7 to 8 August 2018 at the Lagoon Beach Hotel in Cape Town, was attended by close to 90 delegates from 13 different countries spanning several continents and representing industry, consultants, service providers, and academia. This edition of the *Journal* contains some of the excellent papers that were presented at the Geometallurgy Conference. Each of the papers published here has been through a formal peer review process in line with the requirements of the *Journal*.

This first SAIMM Geometallurgy Conference was the culmination of months of planning since the first discussions in 2016 when the Western Cape Branch of the SAIMM proposed holding this conference in Cape Town. The late Professor Dee Bradshaw and Adjunct Professor Mike Solomon were notable champions of the argument for increasing the profile and awareness of geometallurgy within the South African minerals fraternity. Support was thereafter rallied from the SAIMM, the Geological Society of South Africa (GSSA), and the Mineralogical Association of South Africa (MINSA) – with representatives from each of these organizations forming the conference technical committee. This 'coming together' of the different activities in the mining business reflects the nature of geometallurgy as an integrated, multidisciplinary practice.

In organizing the Geometallurgy Conference, we intended to establish a platform to advance the cause of geometallurgy in southern Africa by (i) showcasing some of the exciting geometallurgical work taking place both locally and internationally, (ii) creating a space where those interested in further understanding geometallurgy can come and learn, (iii) establishing a local community of practice and (iv) providing a platform where we can reflect on some of the challenges we are currently facing that are limiting the practice and success of geometallurgy and debate on ideas to overcome them.

Five keynote presentations were delivered at the conference that spoke to the opportunity geometallurgy offers in unlocking complex ores (Professor Alice Clark, SMI, University of Queensland, Australia), the exciting discovery of the Flatreef PGE-Ni-Cu-Au deposit (Sello Kekana, Ivanplats, South Africa), the role of modelling and simulation in geometallurgy (Dr Jussi Lippo and Dr Antti Remes, Outotec, Finland), learnings from the successful practice of geometallurgy at Namakwa Sands (Dr Carlo Philander, Tronox, South Africa) and the missing voice of the mining engineer in geometallurgy (Alistair Macfarlane, Mandela Mining Precinct, SA).

Conference presentations over the two days spanned the role of automated mineralogy, core and belt scanning technologies, geostatistics and modelling, small-scale geometallurgical testing, as well as various case studies describing the implementation and practice of both strategic (project) and tactical (operational) geometallurgy at the Namawka Sands mine, Siguiri gold mine, Orapa diamond mine, and the Kumba iron ore operations amongst others.

The conference closed with an interactive panel discussion allowing delegates to reflect on some critical questions and issues we face with geometallurgy and providing counsel on (i) the need to articulate whether the value-add offered by geometallurgy has been realized and sufficiently paid back the resources used in implementing an on-site geometallurgical programme, (ii) deciding how many samples are needed, which should be informed by a clear understanding of the purpose of the measurements and conversation with your friendly geostatistician, (iii) approaches to making geometallurgy more accessible to the junior and mid-tier mining companies, (iv) the role of academia in providing training and support, and (v) the need to revisit and expand the scope of geometallurgy, in particular to include more routine consideration of deleterious elements and environmental factors.

A very successful pre-conference 'Practical Geometallurgy' workshop was also run by keynote speakers Dr Lippo and Dr Remes from Outotec, that afforded over 30 participants first-hand experience at using the interactive 'OreMet Optimizer' module of the HSC Chemistry software.

A special word of thanks and acknowledgement to the keynote presenters, authors, reviewers, exhibitors, sponsors and the organizing committee – all of whom contributed to the organization of this very successful event. We look forward to the next Geometallurgy Conference – watch this space for more details!

M. Becker
Geometallurgy 2018 Conference Organizer

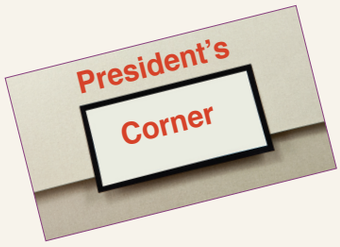

Raising the geometallurgical flag

The papers in this edition of the *Journal* have been written on excellent research work carried out in the field of geometallurgy, presented at the SAIMM's Geometallurgy Conference, held in Cape Town in August 2018.

This conference followed a similar conference held some years earlier, in Johannesburg, and the difference in the quality and content of the papers clearly illustrates how this relatively new discipline has progressed over the last decade.

It is particularly pleasing that the papers include contributions from universities, companies, and presenters from many different countries, including South Africa, Finland, Georgia, Australia, Chile, Botswana, and the United Kingdom. This illustrates a common accord across the globe to collaborate to increase knowledge in this field, in order to improve the efficiency and value of our mining operations.

So, what is geometallurgy, and what is the potential impact? Essentially, it provides a linkage between geology and metallurgy, in that it identifies critical characteristics of an orebody and ore morphology that need to be managed in order to stabilize the metallurgical process and improve metallurgical recoveries.

In terms of orebody morphology, geometallurgy can relate to the size and shape of the orebody and its host rock, and the impact of dilution, mining recovery, and facies boundaries. The characteristics of the dilution material itself can have a profound influence on metallurgical plant efficiency in terms of throughput and recoveries.

Ore morphology has significant impact in terms of mineralogy and mineralogical characteristics, and the effect of different mineralogical units on recovery, grindability, power and reagent consumption, and plant stability. All of these have important ramifications in terms of costs, revenues, and obviously, profitability.

Some of the most significant studies performed in the past have been on base metal deposits. In the Copperbelt deposits of Zambia and the DRC, the first, simple differentiation has to be between oxide and sulphide ores, where the preponderance of one or the other dictates the plant design in terms of either leaching or roasting processes, respectively. This is very simplistic, and simply implies that mine planning and design should keep these ore types separate, and treat them in different plant processes. However, the reality is very much more complex. Many different minerals, being carbonates, oxides, and sulphides, including cuprite, malachite, azurite, chrysocolla, chalcocite, and chalcopyrite may exist, hosted in different units which may be talcose, dolomitic, or wadiferous, all with different hardnesses, densities, and acid-consuming characteristics. Further complicating the situation is the presence of cobalt, in varying grades, depending on the rock unit.

This seemingly complex, multivariate problem could result in fertile ground for endless research, but in reality requires a pragmatic approach that demands an accurate yet practically exploitable geological and geometallurgical model and mine plan, coupled with a stockpiling strategy that allows appropriate blending into the plant within reasonable ranges of variability, to ensure that the metallurgical manager knows what ore is in the pipeline and how to manage and control the plant for optimal performance.

Similar issues and opportunities for improvement exist in most other base metals, but what about other commodities and mineral types?

Papers in this edition illustrate the impacts and opportunities in heavy mineral sands, diamonds, iron ore, and PGMs. This indicates that the field is expanding to all commodities, which is the experience of the writer.

In the coal industry, while it would seem obvious that planning should result in optimal blending of coal to meet market requirements, whether for export or for supply to Eskom, in terms of calorific value in particular, the reality may be quite different. Where seams have narrowed and dilution is included in the mining process, and/or where burnt coal has to be mined, these characteristics will impact severely on

President's Corner (continued)

the washability and saleability of the product. As we have seen, unfortunately, the current Eskom crisis has been exacerbated by the poor quality of coal supply that has resulted from certain illicit and corrupt dealings that have clearly created a situation where the coal supply is far out of specification.

In the diamond business, it is important to understand the diamond grades and characteristics that may be associated with different diamondiferous facies, whether kimberlitic, shale, or breccia. These not only have differing diamond contents, but also significantly different hardnesses, meaning that if the mix of facies is unknown or unstable, milling costs will increase and recoveries will be erratic. The writer experienced an operation where particularly large diamonds, although very few and far between, could be crushed unless means to 'protect' these facies were put in place, coupled with optical sorting.

In the PGM industry, while the separation of UG2 and Merensky ores should be relatively simple, other characteristics, such as variable chrome content, can have a significant impact on recovery in the smelting and refining circuits. While means can be put in place to reduce chrome content, sampling underground could include chrome sampling, to illustrate where subtle changes are occurring, and the data incorporated in a geometallurgical model, such as to optimize recoveries.

The gold industry, especially in the tabular reef environment, has not given a great deal of direct attention to geometallurgical impacts, although they do exist. Obviously, mixing of different reefs is of significance, and if necessary, should be adequately managed. However more subtle factors such as varying channel widths, carbon contents, refractory ore characteristics, grain sizes, and varying amounts of deleterious minerals such as pyrophyllite can occur across the orebody, and can impact on final recoveries. These factors can all be modelled, based on sampling, leading to modifications to the mine plan in order to optimize the plant feed.

The writer was privileged to be a member of the organizing committee for the Cape Town event, and also to be asked to present a paper at the conference. Although the audience was predominantly made up of mineralogists and metallurgists, there were a few miners among the delegates. This indicates a 'missing link' in the geometallurgical discipline. The writer pointed out that while the papers illustrated very deeply researched mineralogical data, and a very precise metallurgical response, the value chain includes a component which is anything but precise – that is, the mining part of the operation. It is therefore vital to develop a value-chain-based approach to geometallurgy that allows for the practical application of the requirements, in terms of issues such as the size of mining equipment (as this affects selectivity), bench heights in open pits, blasting optimization, infrastructural constraints, stockpiling and blending capacity, rock engineering and ventilation constraints, as they impact on scheduling, and sampling frequency and quality.

Geometallurgy is therefore a totally multidisciplinary field, including not only geology and metallurgy, but also mineral resource management, mine planning and design, mining, and engineering. So, perhaps it's just another aspect of 'optimization'?

This year sees the Sixth International Seminar on Geometallurgy, Procemin-Geomet 2019, combined with the 15th International Mineral Processing Conference, to be held in Santiago, Chile, in November. The SAIMM has been invited to participate, and we will be lobbying to become a permanent partner in this international event, in order to bring it to Southern Africa at some stage in the future.

A.S. Macfarlane
President, SAIMM

Geometallurgical characterization of South Georgian complex copper-gold ores

J. Liipo[1], M. Hicks[1], V-P. Takalo[1], A. Remes[1], M. Talikka[1], S. Khizanishvili[2], and M. Natsvlishvili[2]

Affiliation:
[1]Outotec, Finland
[2]JSC RMG Copper, Georgia

Correspondence to:
J. Liipo

Email:
jussi.liipo@outotec.com

Dates:
Received: 7 Jan. 2019
Revised: 14 Mar. 2019
Accepted: 26 Mar. 2019
Published: April 2019

How to cite:
Liipo, J., Hicks, M., Takalo, V-P., Remes, A., Talikka, M., Khizanishvili, S., and Natsvlishvili, M. Geometallurgical characterization of South Georgian complex copper-gold ores. The Southern African Insitute of Mining and Metallurgy

DOI ID:
http://dx.doi.org/10.17159/2411-9717/565/2019

ORCiD ID:
https://orchid.org/0000-0001-9926-4636

This paper was first presented at the *Geometallurgy Conference 2018 'Back to the Future'*, 7–8 August 2018, Lagoon Beach Conference Venue, Cape Town, South Africa.

Synopsis

The complexity of copper-gold ores leads to large variations in recoveries and concentrate grades in the processing plant. Detailed chemical and mineralogical studies revealed considerable variation in the ratios of chalcopyrite, chalcocite, and oxidized copper minerals in the ore types studied. The end-member ore types are chalcopyrite-dominated and chalcocite-dominated, while most of the ore types plot between these end-members. In addition, increasing amounts of copper oxide and sulphate minerals result in a decreased response to flotation. Good recoveries and concentrate grades can be achieved from the chalcopyrite-dominated ore type, while the more altered chalcocite-dominated ore type is more challenging to enrich.

Keywords
classification, element-to-mineral conversion, modal composition, grindability.

Introduction

Rich Metals Group (RMG) Copper in Georgia (Figure 1) produces copper-gold concentrates from two open pit mines, Madneuli and Sakdrisi, both located in the Bolnisi mining district in South Georgia. RMG and Outotec began a cooperative project with the aim of improving the recoveries and metal grades in concentrate by gaining an increased understanding of the ore variability and developing more efficient procedures for ore blending, grinding, and flotation. This type of mineralogy-led approach has already been used for other complex ores such as iron oxide copper-gold ores (Hunt, Berry, and Bradshaw, 2011), for iron ores (Lund, Lamberg, and Lindberg, 2013), and for Kupferschiefer ore deposits (Rahfeld *et al.*, 2018).

The project started with process audits and mineralogical and chemical characterization of process samples, followed by detailed chemical and mineralogical characterization of six different ore types with simultaneous flotation test work on the same samples. Since neither the recoveries nor the concentrate grades correlate with the head grades of the ores, the modal mineralogical composition, together with the ore hardness, proved to be the most promising approach in developing the geometallurgical classification of these ore types.

In order to further optimize the process design and improve the efficiency and value of production, the whole value chain was modelled, based on identified geometallurgical ore types, by the OreMet Optimizer module included in Outotec's HSC Chemistry® 9 software (Talikka *et al.*, 2018).

Geology

The copper-gold mineralized domains at Madneuli and Sakdrisi mines are hosted by an upper Cretaceous sequence of volcanic-sedimentary rocks (RMG, 2016). The Madneuli deposit is characterized by a northeast-trending dome, with the limbs of the dome dipping between 10 and 40 degrees. A number of steeply dipping faults occur throughout the deposit. Strata are mainly composed of rhyodacitic pyroclastic rocks, with the core of the dome comprising coarse-grained and medium-grained tuffs. These rocks are overlain by alternating tuffs and tuffaceous sandstones. Hydrothermal alteration of the pyroclastic host rocks of the Madneuli deposit includes intense silicification, chloritization, sericitization, and sulphidization. Alteration is typically irregular and is strongest in the core of the dome, becoming less intense towards the marginal zones (Figure 2).

The Madneuli deposit displays three mineralization styles: vein-disseminated, breccia, and massive stockwork mineralization. The majority of the copper-gold mineralization is confined to areas of ubiquitous silica-rich alteration.

Figure 1—Geographic map of Georgia (www.nationsonline.org)

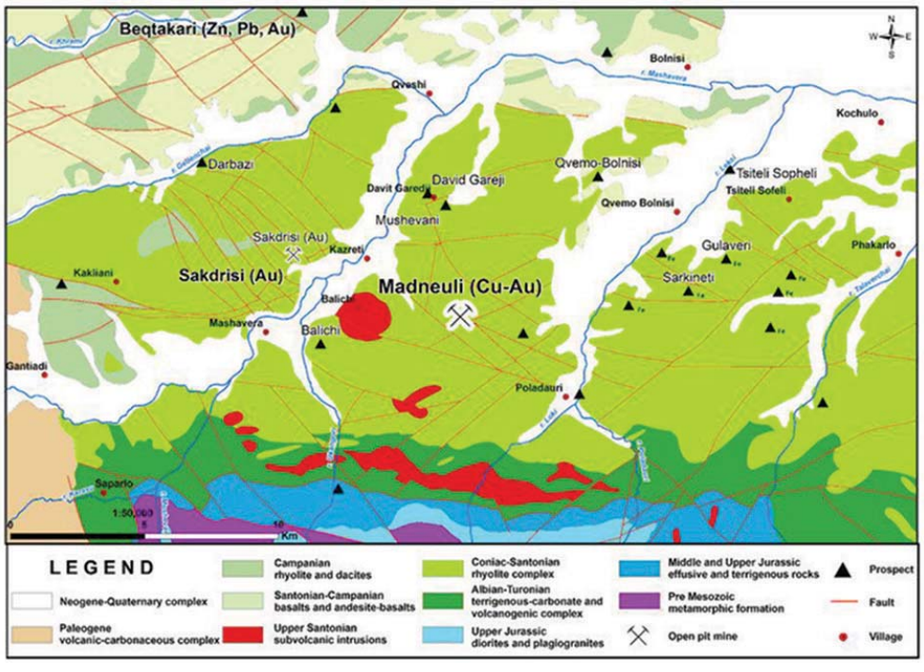

Figure 2—Geological map of Bolnisi ore district showing the locations of Madneuli and Sakdrisi copper-gold deposits

Mineralization within the Sakdrisi deposit is controlled by structure and lithology, comprising predominantly pod-like bodies, sheeted vein sets, and low-grade stockwork. The primary mineralization is overprinted by surface weathering processes, resulting in zones of sporadic supergene enrichment. The mineralization style represents a transitional type between volcanogenic massive sulphide (VMS) and epithermal gold type.

Ore samples and analytical methods

Each of the ore samples collected from the mill feed at Madneuli

and Sakdrisi were divided into subsamples; one subsample was used for chemical analysis and mineralogical studies, and one for flotation test work. The chemical and mineralogical characterization tests were carried out at the Outotec Research Center in Pori, Finland and the locked cycle flotation tests were performed at RMG's Madneuli laboratory in South Georgia.

The locked cycle flotation tests, consisting of five cycles, were carried out at a particle size of 60–62% –74 µm using from 8 to 120 g/t potassium butyl xanthate as collector and 30 to 40g/t Oxal T-92 as frother. A pH range of 12–12.3 was maintained by addition of lime to depress pyrite. The results of the locked cycle tests reflect the variation in plant performance.

The detailed chemical assays by size include complete assays, after total dissolution, by inductively coupled plasma – optical emission spectrometry (Thermo Scientific iCAP 6000), gold and silver by fire assay, and sulphur and carbon by combustion (Eltra CS-2000). In addition, the mineralogy of copper contents was determined according to the four-stage sequential copper phase assay procedure described by Young (1974) and further developed by Outotec. This procedure enables the quantification of different copper sulphates, oxides, secondary copper sulphides, and primary copper sulphides by using the element-to-mineral conversion (EMC) method available in the HSC Chemistry® 9 Geo module (Lamberg *et al.*, 1997; Lund, Lamberg, and Lindberg, 2013).

The main minerals and their modes of occurrence were first studied per size fraction by optical microscopy (Zeiss Axioplan 2) and X-ray diffraction (Bruker D8 Focus). Scanning electron microscopy and liberation measurements were performed using a field emission scanning electron microscope (JEOL JSM-7000F) equipped with an Oxford Instruments energy-dispersive spectrometer (X-Max 80) coupled with INCAMineral liberation measurement software (Liipo *et al.*, 2012). The hardness of each ore type was determined according to the standard Bond grindability test (Bond, 1961).

Chemical and mineral composition of the ore types

The copper and gold contents of the six samples range from 0.28 to 0.77% Cu and 0.19 to 0.75 ppm Au. The main copper minerals are chalcopyrite, and chalcocite-group minerals, which have the general formula $Cu_{2-x}S$ and include chalcocite, digenite, anilite, and geerite, with variable amounts of secondary copper oxides and sulphates (Table I). Gold occurs mainly as the native element, and less often alloyed with silver. In addition, a few grains of sylvanite $(AuAg)_2Te_4$ were found. The main gangue minerals are quartz, muscovite, sericite, chlorite, kaolinite, and pyrite. Minor amounts of sphalerite, barite and siderite were also encountered.

Copper sulphides appear in all ore types in a similar manner. Chalcocite is commonly associated with pyrite, rimming or filling the fractures of pyrite grains. Chalcopyrite appears as complex particles with gangue silicates and pyrite and is replaced by chalcocite along the grain boundaries. Copper sulphides form locked particles, mainly with pyrite, and the bulk liberation of copper sulphides varies from 37% up to 85%, the particle size being 60–62% –74 µm. Gold occurs mainly as fine-grained particles less than 2 µm in diameter, and as inclusions in pyrite and gangue silicates.

The proportion of copper carried by copper sulphides, *i.e.*, chalcopyrite and chalcocite–group minerals, is fairly constant within all the ore types and the sulphides contain anywhere from 69 to 87% of the total copper content. However, the proportion of copper carried by chalcopyrite and chalcocite varies substantially. The proportion of copper carried by chalcopyrite varies from 8% to 62%, and by chalcocite–group minerals from 25% to 67%. The proportion of copper carried by secondary copper oxides and sulphates ranges from 13% to 31% (Table II).

Since the copper oxides and sulphates are not amenable to flotation, the actual amount of copper recoverable by flotation is lower than would be estimated based on total copper assay.

Table I

Mineral composition of different ore sample, wt%

Ore	Madneuli	Madneuli	Madneuli	Madneuli	Sakdrisi	Sakdrisi
Type	1	2	3	4	1	2
Pyrite	5.42	5.58	9.44	9.92	3.04	4.36
Chalcocite	0.29	0.49	0.17	0.19	0.10	0.55
Chalcopyrite	0.35	0.12	0.25	0.11	0.57	0.18
Cu-oxide/sulphates	0.21	0.20	0.11	0.14	0.10	0.37
Quartz	63.00	58.39	68.81	74.16	64.46	67.67
Micas	16.66	17.50	11.73	10.32	16.19	13.44
Chlorite	9.71	14.49	6.90	2.95	3.78	2.99
Others	4.36	3.22	2.58	2.21	11.75	10.44
Sum	100	100	100	100	100	100

Table II

Distribution of copper between copper minerals, %

Ore	Madneuli	Madneuli	Madneuli	Madneuli	Sakdrisi	Sakdrisi
Type	1	2	3	4	1	2
Chalcocite	52.99	67.33	43.06	60.43	25.12	59.31
Chalcopyrite	27.51	8.13	33.97	15.66	61.51	9.46
Cu-oxide/sulphates	19.51	24.54	22.98	23.90	13.37	31.24

The calculated sulphide fraction (SF = pyrite + chalcopyrite + chalcocite) consists mainly of pyrite (74–95%) and the chalcopyrite and chalcocite contents range from 2.3% to 14% and 2.2% to 12%, respectively (Table III). The amount of copper in the sulphide fraction varies from 2.6 to 10.8% Cu_{SF} (Table IV).

Based on their copper mineralogy, the ore types are classified into three groups: chalcopyrite-dominated, chalcocite-dominated, and mixed chalcopyrite-chalcocite (Figure 3). The chalcopyrite-dominated ore type represents less altered primary zones, and with increasing alteration, the amounts of chalcocite and secondary copper oxides increase (Figure 4).

Ore types and geometallurgical classification

The results of mineralogical characterization, ore grindability, Bond Wi, and the locked cycle flotation tests were reprocessed with HSC Chemistry® 9 Data module utilizing linear regression analysis and principal component analysis. The analysed total copper content does not have any correlation with recovery of copper, while the amount of chalcopyrite correlates positively with recovery of copper (Figure 5). The highest concentrate grades and recoveries for both copper and gold were achieved from the chalcopyrite-dominated ore type, and an increasing degree of alteration decreases both grades and recoveries (Figure 5 and Table V), as shown also by principal component analysis.

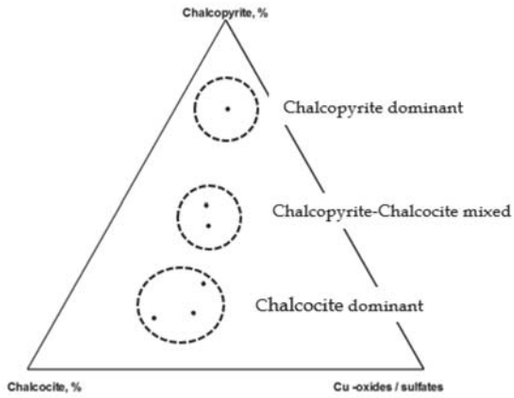

Figure 3—Classification of Madneuli and Sakdrisi ore types based on copper mineralogy

Based on this and previous studies (*e.g.* Hunt, Berry, and Bradshaw, 2011; Lund, Lamberg, and Lindberg, 2013; Rahfeld *et al.*, 2018), the modal mineralogical composition, and in this case especially the modal mineralogy of copper, has been shown to be the main factor in geometallurgical characterization of complex copper-gold ores. However, based on the grindability tests,

Table III

Mineral composition of sulphide fraction, %

Ore	Madneuli	Madneuli	Madneuli	Madneuli	Sakdrisi	Sakdrisi
Type	1	2	3	4	1	2
Pyrite	89.17	86.29	94.90	94.90	74.18	82.39
Chalcorite	4.71	11.08	2.21	2.21	2.32	12.25
Chalcopyrite	5.76	2.26	2.66	2.66	13.94	3.94

Table IV

Chemical composition of sulphide fraction, %

Ore	Madneuli	Madneuli	Madneuli	Madneuli	Sakdrisi	Sakdrisi
Type	1	2	3	4	1	2
Cu, %	5.53	8.62	2.60	2.60	6.34	10.84
Fe, %	44.31	41.88	45.53	45.53	39.75	40.12
Zn, %	0.24	0.23	0.14	0.14	4.87	0.90
S, %	49.86	49.09	51.62	51.62	47.44	47.79

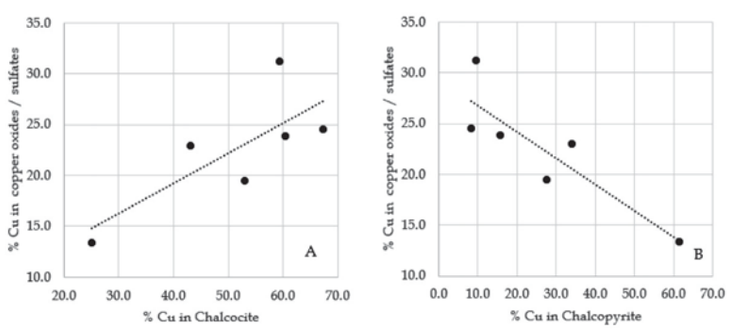

Figure 4—Amount of copper carried in (a) chalcocite and (b) in chalcopyrite *versus* amount of copper carried by copper sulphates and oxides

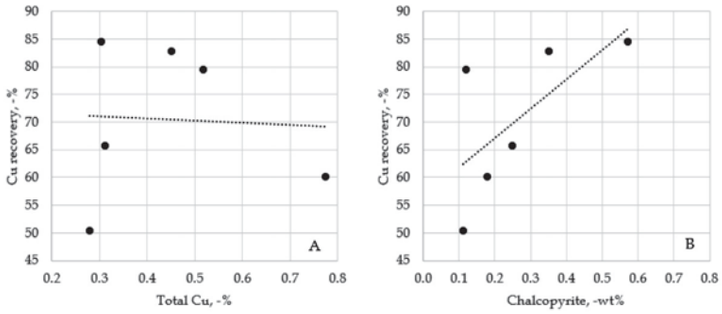

Figure 5—Correlation between (a) total copper and (b) amount of chalcopyrite in the ore and copper recovery

Table V

Geometallurgical ore types and their main characteristics

Type	Copper mineralogy	Cu %	Au g/t	Bond Wi	Cu rec. %	Au rec.%
GMO A	Chalcopyrite	0.30	0.75	15.80	84.49	79.81
GMO B	Chalcopyrite-chalcocite	0.45	0.27	13.61	58.75	50.23
GMO C	Chalcocite	0.48	0.39	10.22	81.18	62.20

copper mineralogy alone is not adequate for geometallurgical classification and the ore hardness needs to be taken into account. Based on the mineralogy and the hardness of these ore types, three geometallurgical ore types (GMO A, GMO B, and GMO C) can be defined (Figure 6). The main characteristics of these three ore types and the test work results are presented in Table V.

Based on the HSC Chemistry® 9 process simulations and estimation of economic revenue by OreMet Optimizer simulation of these geometallurgical ore types (Talikka *et al.*, 2018), the chalcopyrite-dominated ore type GMO A yields by far the highest net smelter return (NSR) and operating profit, despite incurring the highest operating costs. The chalcocite-dominated ore type GMO C yields the second highest NSR and operating profit, and the intermediate chalcopyrite-chalcocite mixed ore type GMO B the lowest NSR and operating profit. The simulation results clearly demonstrate that the variability in the mill feed has significant impact on the processing performance and economics of the operations.

Discussion

This study is the first attempt to develop a geometallurgical classification for the complex copper-gold ores of Madneuli and Sakdrisi. The established geometallurgical ore types, GMO A, B, and C illustrate the variation in copper mineralogy as well as variations in ore hardness and explain the metallurgical response obtained both in locked cycle tests and at the concentration plants.

Element-to-mineral conversion is a practical and inexpensive technique to calculate the modal mineralogical composition, and especially the modal mineralogy of copper of the Madneuli and Sakdrisi ore types. In this study, a large range of chemical assay data was used to establish the modal mineralogical composition of different ore types, but in practice, for geometallurgical classification purposes, only the sequential copper phase assays are required in addition to the plant's routine analyses.

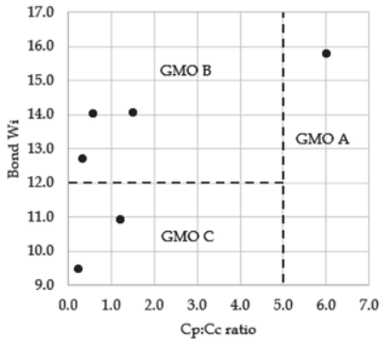

Figure 6—Chalcopyrite to chalcocite ratio (Cp:Cc) *versus* ore hardness, Bond Wi, and geometallurgical classification of the ore types

The ore grindability was determined by Bond grindability tests, which can require up to 10 kg of material and are, in the authors' opinion, not as practical as the methods and quantities used in this investigation. Geometallurgical testing should be viable at a small scale and with only relatively small amounts of sample material. In addition, there should also be the possibility of using the corresponding sample for mineralogical characterization and beneficiation test work such as flotation tests.

Mwanga, Rosenkranz, and Lamberg (2015) give a short review of existing comminution test methods suitable for geometallurgical investigations. One of the methods is the Outotec Mergan mill, developed originally by Niitti (1970), and its usability as a part of a geometallurgical testing procedure was confirmed recently by Heiskari (2017) and Heiskari *et al.* (2018). Mergan grinding tests enable prediction of the Bond work index quickly while using only a small (2–3 kg) sample. Furthermore, the ground sample material is available for analysis of the chemical and mineral composition, and for metallurgical test work.

Conclusions

Identifying the variability within an ore deposit, and understanding the mineralogical composition and the metallurgical performance of the various ore types, are key requirements for efficient mining and minerals processing.

In this study a useful and viable method for mineralogy-led geometallurgical characterization of the Madneuli and Sakdrisi copper-gold ores was developed. Practical geometallurgy requires fast and inexpensive modal mineralogical analyses and a suitable method for determination of the ore hardness.

In this case, the element-to-mineral conversion method can provide the required modal mineral compositions which, combined with a suitable grindability testing method such as the Mergan test, enable the geometallurgical classification of individual ore samples/domains and the prediction of their metallurgical response to be developed.

Acknowledgements

We thank two anonymous referees for their valuable comments and suggestions. We would also like to thank the laboratory technicians at Outotec Research Center, Pori, for their skilful assistance in the experimental and analytical work.

References

Bond, F.C. 1961. Crushing and grinding calculations, part 1. *British Chemical Engineering*, vol. 6, no. 6. pp. 378–385.

Heiskari, H. 2017. Development of comminution test method for small ore samples. MSc thesis, Faculty of Technology, University of Oulu, Finland.

Heiskari, H., Kurki, P., Luukkanen, S., Sinche- Gonzalez, M., Lehto, H., and Liipo, J. 2018. Development of comminution test method for small ore samples. *Minerals Engineering*, vol. 130. pp. 5–11.

Hunt, J., Berry, R., and Bradshaw, D. 2011. Characterising chalcopyrite liberation and flotation potential: Examples from an IOCG deposit. *Minerals Engineering*, vol. 24. pp. 1271–1276.

JSC RMG. 2016. Technical report on the JSC RMG copper mine operations: Madneuli & Sakdrisi in Georgia. Unpublished report.

Lamberg, P., Hautala, P., Sotka, P., and Saavalainen, S. 1997. Mineralogical balances by dissolution methodology. *Proceedings of Short Course on Crystal Growth in Earth Sciences*, Mamede de Infesta, Portugal, 8–10 September. International Mineralogical Association. pp. 1–29.

Liipo, J., Lang, C., Burgess, S., Otterström, H., Person, H., and Lamberg, P. 2012. Automated mineral liberation analysis using INCAMineral. *Proceedings of Process Mineralogy '12*, Cape Town, South Africa, Minerals Engineering International, Falmouth, UK. pp. 1–7.

Lund, C., Lamberg, P., and Lindberg, T. 2013. Practical way to quantify minerals from chemical assays at Malmberget iron ore operations – an important tool for the geometallurgical program. *Minerals Engineering*, vol. 49. pp. 7–16.

Mwanga, A., Rosenkranz, J., and Lamberg, P. 2015. Testing of ore comminution behavior in the geometallurgical context—a review. *Minerals*, vol. 5. pp. 276–297

Rahfeld, A., Kleeberg, R., Möckel, R., and Gutzmer, J. 2018. Quantitative mineralogical analysis of European Kupferschiefer ore. *Minerals Engineering*, vol. 115. pp. 21–32.

Talikka, M., Remes, A., Hicks, M., Liipo, J., Takalo, V-P., Khizanishvili, S., and Natsvlishvili, M. 2018. Copper ore variability – benefits of advanced simulation. *Proceedings of Copper Cobalt Africa Conferenc*e, Livingstone, Zambia, 9–13 July 2018. Southern African Institute of Mining and Metallurgy, Johannesburg.

Young, R.S. 1974. Chemical Phase Analysis. Charles Griffin and Company, London. ◆

Prediction of copper recovery from geometallurgical data using D-vine copulas

E. Addo Jr[1], A.V. Metcalfe[2], E.K. Chanda[1], E. Sepulveda[1,5], W. Assibey-Bonsu[3], and A. Adeli[4]

Affiliation:
[1]School of Civil, Environmental and Mining Engineering, University of Adelaide, Australia
[2]School of Mathematical Sciences, University of Adelaide, Australia
[3]Group Geostatiscian and Evaluator, Gold Fields Limited, South Africa
[4]Department of Mining Engineering, University of Chile, Chile
[5]School of Mining Engineering, University of Talca, Chile

Correspondence to:
E. Addo Jr

Email:
emmanuel.addojunior@adelaide.edu.au

Dates:
Received: 10 Sep. 2018
Revised: 1 Apr. 2019
Accepted: 1 Apr. 2019
Published: April 2019

How to cite:
Addo Jr, E., Metcalfe, A.V., Chanda, E.K., Sepulveda, E., Assibey-Bonsu, W., and Adeli, A. Prediction of copper recovery from geometallurgical data using D-vine copulas.
The Southern African Insitute of Mining and Metallurgy

DOI ID:
http://dx.doi.org/10.17159/2411-9717/319/2019

ORCiD ID:
https://orchid.org/0000-0002-5046-8934

This paper was first presented at the *Geometallurgy Conference 2018 'Back to the Future'*, 7–8 August 2018, Lagoon Beach Conference Venue, Cape Town, South Africa.

Synopsis

The accurate modelling of geometallurgical data can significantly improve decision-making and help optimize mining operations. This case study compares models for predicting copper recovery from three indirect test measurements that are typically available, to avoid the cost of direct measurement of recovery. Geometallurgical data from 930 drill core samples, with an average length of 19 m, from an orebody in South America have been analysed. The data includes copper recovery and the results of three other tests: Bond mill index test; resistance to abrasion and breakage index; and semi-autogenous grinding power index test. A genetic algorithm is used to impute missing data at some locations so as to make use of all 930 samples. The distribution of the variables is modelled with D-vine copula and predictions of copper recovery are compared with those from regressions fitted by ordinary least squares and generalized least squares. The D-vine copula model had the least mean absolute error.

Keywords
copula, geometallurgy, modelling, regression, mining.

Introduction

In this paper we compare the use of D-vine copula, generalized least squares (GLS), and ordinary least squares (OLS) for modelling geometallurgical data from an orebody in South America. The first objective is to construct models for predicting copper recovery (Rec) from the Bond mill index test (BWi); resistance to abrasion and breakage index (A*b); and semi-autogenous grinding (SAG) power index test (Spi). This involves fitting a D-vine copula and regression models fitted by OLS and GLS. The second objective is to investigate the performance of the fitted models for predicting Rec (Willmott and Matsuura 2005).

Traditional resource model approaches either ignore the mineral processing characteristics of extracted tonnages or treat processing as an independent component of a mining operation. The net present value (or any other objective) can be truly optimized only by considering the mining operation as an integrated system in which net value is defined as the end-product that the company sells. This approach requires the resource model to be extended to include all relevant rock properties and processing responses.

Comminution performances and mineral processing recovery factors have a substantial effect on production and the final value of the product. Hence their prediction in the early stages of a mining operation is crucial. The accurate and precise prediction of these variables is important for mine planning and project risk assessment. Commonly used tests for determining comminution performances are BWi, Spi, and A*b. Better understanding of the physical and chemical principles on which these performance indices are based has contributed to the acceptance and use of geometallurgy in resource modelling, referred to in a wider context as grade engineering.

Lishchuk *et al.* (2015) define geometallurgy as a multidisciplinary approach that integrates geology, mineralogy, mineral processing, and metallurgy to create spatially based models for production and operational decisions. The primary geological rock properties (*e.g.*, grade, alteration, texture, and grain size) are proxies for predicting metallurgical responses (*e.g.*, type of processing, throughput, recovery, energy consumption, reagent usage, and grindability) (Coward *et al.* 2009; Dowd, Xu, and Coward, 2016). Incorporating these variables into the resource model in a way that can be used effectively in mine planning poses a challenge to geostatisticians and resource modellers. In most projects, the lack of appropriate geometallurgical data collection and analysis leads to unreliable metallurgical response models.

The relatively large difference between the number of samples recorded in the geological database (logging, assays *etc.*) and the relatively few metallurgical test work samples further hinders the integration of metallurgical responses into the resource model using existing geostatistical methods (Hunt, Kojovic,

and Berry, 2013). Also, there is often the problem of missing values of metallurgical variables, which may not be measured at all locations. Retaining only data where all variables are sampled could result in removing a large amount of data from the geometallurgical programme (Deutsch, 2013), which can lead to poor geostatistical modelling in areas where more data (of some variables) is actually sampled.

In addition, most geological and geometallurgical variables have complex multivariate relationships that are the result of a succession of several chaotic, nonlinear natural processes which are often not well modelled by parametric multivariate probability distribution (Deutsch 2013). Moreover the non-additive and compositional nature of geological/geometallurgical variables makes their modelling more difficult (Walters and Kojovic 2006; Williams and Richardson, 2004). An alternative modelling strategy that can capture all these complex multivariate relationships is crucial for successful modelling of geometallurgical variables. Multivariate D-vine copulas are ideal for modelling complex multivariate relationships, skewed distributions, and tail-dependent distributions. Moreover, the D-vine copula models encompass all multivariate distribution, including the multivariate Gaussian distribution (MVG).

This paper is comprised of three main sections. The 'Method' section describes the theory of copulas, pair copulas, and vine copulas (D-vine) construction models. The 'Application' section describes data imputation, modelling of copper recovery in terms of A*b, BWi, and Spi, and finally the prediction of copper recovery from A*b, BWi and Spi. This is followed by the 'Discussion and Conclusion'.

Method

This section gives an overview and summarizes the principles of copulas, pair copulas (D-vine) construction for four variables. Further details about the concept of copulas can be found in Joe (1996) and Nelsen (2006). In addition, more detailed explanation of the pair copula and vine copula models can be found in Aas *et al.* (2009), Bedford and Cooke (2002), and Kurowicka and Cooke (2006). Spatial applications of pair copulas can be found in Gräler and Pebesma (2011), Gräler (2014), Musafer *et al.* (2013), Musafer and Thompson (2016), and Addo, Chanda, and Metcalfe (2018).

Theory of copulas

A copula is a multivariate uniform distribution. It follows that any multivariate distribution has a copula form because the marginal cumulative distribution functions (cdfs) can be transformed to uniform distributions. Conversely, the uniform margins of any copula can be transformed to any continuous probability distributions, which can differ for different margins. Therefore copulas provide a very flexible approach in modelling multivariate data. Consider a random variable $Z = (z_1,\ldots,z_d)$ and define $u_i = F(z_i)$. We can define a copula by its cdf $C(u_1,u_2,\ldots,u_d)$ and the corresponding probability density function (pdf) is

$$c(u_1, u_2, \ldots, u_d) = \frac{\partial C(u_1, u_2, \ldots, u_d)}{\partial u_1 \, \partial u_2 \ldots \partial u_d} \quad [1]$$

The copula pdf links the marginal pdfs to the multivariate pdf:

$$f(z_1, \ldots, z_d) = c(u_1, \ldots, u_d) f(z_1) \ldots . f(z_d) \quad [2]$$

Generally, we often require multivariate distributions of more than two variables. The elliptical copulas (*i.e.* Gaussian and Student-t copula) can easily be extended to more than two variables, but this is not generally the case for the Archimedean copulas (*i.e.* Clayton, Frank, and Gumbel copula). A more flexible approach to modelling such multivariate distributions is the pair-copula D-vines as described by Aas *et al.* (2009), Bedford and Cooke (2002), and Kurowicka and Cooke (2006).

Pair copula

Any multivariate distribution can be factorized in different ways using its conditional distributions. Specifically, a copula can be factorized as a product of the marginal distributions and the bivariate conditional copulas. We often term such factorization 'pair-copula models'. Joe (1996) presented a construction for a pair-copula model for a multivariate copula based on the distribution functions. After Joe's construction of a copula based on the distribution functions, Bedford and Cooke (2002) also presented a construction in terms of the densities. In their work, they organized the constructions in a graphical way involving a sequence of nested trees, which they refer to as 'regular vines'. They defined two popular classes of pair-copula construction (PCC) models, which they refer to as the D-vines and canonical (C) vines. Their work was further developed by Kurowicka and Cooke (2006). The derivation of a D-vine model, which is used in this application, is outlined below.

D-vines

Generally the pair copula can be seen as a multivariate copula that aims to approximate the target copula, since not all copulas can be expressed as a vine copula (Haff, Aas, and Frigessi, 2010). This decomposition is, however, not unique; for example, a five-dimensional density can have about 240 different constructions. In the D-vines, the decomposition of the joint density consists of the pair-copula densities evaluated at conditional distributions functions and for specified indices and marginal densities (Bedford and Cooke 2002; Czado 2010 and Gräler 2014). Figure 1, which is reproduced from Aas *et al.* (2009), shows the graphical model used to demonstrate the D-vines for four variables. This consists of three trees: T_j j=1,2,3. Tree T_j has n+1-j nodes, where n is the number of variables. Using the decomposition shown in Figure 1 and Equation [3], the joint density function of four random variables can be expressed using the D-vines asw

As shown in Equation [3], the D-vine distribution requires the computation of several conditional distribution functions and conditional bivariate copulas. From Joe (1996) and Aas, Frigessi, and Bakken (2009), the conditional distribution functions $F(z|v)$

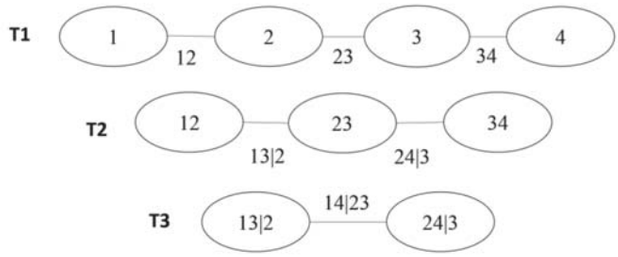

Figure 1 – D-vines for four variables

$$
\begin{aligned}
&f_{1234}(z_1,z_2,z_3,z_4) = \\
&f_1(z_1).f_2(z_2).f_3(z_3).f_4(z_4) \\
&.c_{12}\left(F_1(z_1),F_2(z_2)\right) \\
&.c_{23}\left(F_2(z_2),F_3(z_3)\right) \\
&.c_{34}\left(F_3(z_3),F_4(z_4)\right) \\
&.c_{13|2}\left(F_{1|2}(z_1|z_2),F_{3|2}(z_3|z_2)\right) \\
&.c_{24|3}\left(F_{2|3}(z_2|z_3),F_{4|3}(z_4|z_3)\right) \\
&.c_{14|23}\left(F_{1|23}(z_1|z_2,z_3),F_{4|23}(z_4|z_2,z_3)\right)
\end{aligned}
\qquad [3]
$$

for an m-dimensional vector $v=(v_1,\ldots,v_m)$ can be obtained from the following recursive relationship:

$$
h(z|v) := F(z|v) = \frac{\partial C_{zv_j|v_{-j}}\left(F(z|v_{-j}),F(v_j|v_{-j})\right)}{\partial F(v_j|v_{-j})} \qquad [4]
$$

where v_j (j=1,...,m) is an arbitrary component of v, and $v(-j)$= $(v_1,\ldots,v(j\text{-}1),v(j\text{+}1),\ldots,v_m)$ denotes the vector v excluding element v_j. The bivariate copula function is also specified by $C(zv_j \mid v_j)$. Given u_i (i=1,...,n) to denote $F_i(z_i)$, we can derive the conditional distribution function $F(u_3 \mid u_1,u_2)$ that is needed as an argument for $C_{14|23}$ in a four-dimensional D-vine copula density using Equation [4]. From Figure 1 *Tree* 3 (*T*3) the argument $C_{14|23}$, namely $F_{1|23}(x_1|x_2,x_3)$, can be evaluated using the h function (Kraus and Czado 2016) associated with $C_{13,2}$,C_{12},and C_{23} from the first two trees T_1 and T_2 as

$$
\begin{aligned}
F_{1|23}(z_1|z_2,z_3) &= h_{1|3;2}\left(F_{1|2}(z_1|z_2)F_{3|2}(x_3|x_2)\right) \\
&= h_{1|3;2}\left(h_{1|2}\left(F_1(z_1)|F_2(z_2)\right)\right| \\
&\quad \left.h_{3|2}\left(F_3(z_3)|F_2(z_2)\right)\right)
\end{aligned}
\qquad [5]
$$

D-vine copula-based conditional forecasting model

With the defined conditional distributions function in Equation [5], the inverse forms can also be defined, and can be used in forecasting. Using the bivariate case, the conditional distribution function of two random variables z_1 and z_2 is $h(u_2|u_1)$. The main goal is to be able to obtain u_2 based on the information available at u_1. Given some fixed probabilities τ, we can derive u_2 from $C(u_2|u_1)$using an explicit function $u_2 = u_2 = C^{-1}_{u2|u1}(\tau;u_1) = h^{-1}(\tau|u_1)$, where $C^{-1}_{u2|u1}$ is the inverse of the copula function known as the quantile curve of the copula (Xu and Childs, 2013). The τth copula-based conditional quantile function of variable z_2 is

$$
Q_z(\tau|z_1) = F^{-1}(u_2) = F^{-1}\left(C^{-1}_{u_2|u_1}(\tau;u_1)\right) = F^{-1}\left(h^{-1}(\tau|u_1)\right) \qquad [6]
$$

where F^{-1} is the inverse of u_2. For the four-dimensional case, the τth conditional quantile function of z_4, $Q_{x4}(\tau|z_1,z_2,z_3)$ can be deduced by the recursive computation

$$
\begin{aligned}
Q_{z_4}(\tau|z_1,z_2,z_3) &= F^{-1}(u_4) \\
&= F^{-1}\left(h^{-1}\left\{h^{-1}\left[h^{-1}\left(\tau|h(h(u_3|u_1)|\right.\right.\right. \\
&\quad \left.\left.\left.h(u_2|u_1)\right)\right)|h(u_2|u_1)\right]u_1\right\}\Big)
\end{aligned}
\qquad [7]
$$

Hence we can forecast z_4 based on the variables z_1,z_2, and z_3. Moreover, $Q_{z4}(\tau|z_1,z_2,z_3)$ is monotonically increasing in τ so the crossing of quantile functions corresponding to different quantile levels is not possible. Bernard and Czado (2015) proved that linear regression quantile functions may cross if a non-Gaussian data is modelled.

In general, the multivariate D-vine copula model for the four-dimensional vine model can be implemented by following the steps below. Further details of the method can be found in Kraus and Czado (2016) and Liu *et al.* (2015).

1. Fit an appropriate marginal distribution to each of the variables, z_1,z_2,z_3, and z_4, where z_4 is the predicted variable and all the others are the explanatory variables.
2. Model the joint dependence structure of all the four variables using Equation [5] for the D-vine model.
3. Estimate all the appropriate bivariate copula for each pair copula using the R library VineCopula (Schepsmeier *et al.*, 2015).
4. Estimate the conditional distribution function of variable z_4 conditioned on the given variables z_1,z_2,z_3 using Equation [5].
5. Finally, generate the predicted values of z_4 based on the given variable, z_1,z_2,z_3 using the copula-based quantile function as given in Equation [7].

Performance of models

The mean absolute error (MAE) and root mean square error (RMSE) have been used to assess the prediction performance of the models.

$$
MAE(A_i,\hat{A}_i) = \frac{1}{N}\sum_{i=1}^{n}|A_i - \hat{A}_i| \qquad [8]
$$

$$
RMSE(A_i,\hat{A}_i) = \sqrt{\frac{1}{N}\sum_{i=1}^{n}(A_i - \hat{A}_i)^2} \qquad [9]
$$

where A_i is the observed recovery, and $\hat{A}_i$ is the predicted recovery obtained using a fitted model to all N =930. So, the performance measures are calculated within the entire sample.

Application

Nine hundred and thirty (with some missing values) drill core samples with an average length of 19 m from a mine in South America were sampled for geometallurgical attributes of copper recovery (Rec), Bond mill index test (BWi), resistance to abrasion and breakage index (A*b), and semi-autogenous grinding power index test (Spi). Typical of most geometallurgical data-sets, there are missing values that have not been sampled at some locations. There are 299 non-missing data-sets that are sampled at all locations. To be able to use all 930 georeferenced drill core samples for the analysis, we employed a data imputation algorithm to predict missing values at some locations.

Data imputation

The data-set has 930 georeferenced samples with four attributes of interest: Rec, BWi, Spi, and A*b. Table I shows the summary of descriptive statistics for all four attributes.

Data imputation was formulated as an optimization problem seeking to preserve two main properties: the reproduction of the individual histograms and the bivariate correlation among the variables. Histograms of each of the variables were calculated

Table I

Summary statistics of all four attributes

Variable	Number of non-missing values	Number of missing values	Minimum	Maximum
Rec	560	370	36.20	99.30
BWi	840	90	9.12	15.58
Spi	539	391	10.69	98.60
A*b	300	630	32.38	175.66

using non-missing (informed) values, and correlations were calculated using samples where all variables have non-missing values. Table II indicates the bivariate correlations, and number of missing and non-missing values for the pair attributes. The diagonal shows the number of missing values, the upper triangle shows the Pearson correlation between two attributes, and the lower triangle shows the number of non-missing values for the pair attributes.

The data-sets were decomposed in two sets: non-missing (informed) values and missing values. Hence, the multivariate data-set was defined as: $X = \{X_1,\ldots,X_D\}$, where D is the number of attributes. Each X_i is also defined as follows: $X_i = V_i \cup M_i$, where V_i and M_i represent the informed and missing values respectively, and $V_i \cup M_i$ is used to indicate V_i if available, or M_i otherwise.

The histogram function used for the imputation was denoted by $H(X)$, and used 21 regular bins or class intervals. The correlation is given by

$$CORR(x,y) = \frac{\sum(x-\bar{x})(y-\bar{y})/(n-1)}{S_x S_y} \quad [10]$$

where $\bar{x}$,$\bar{y}$,S_x, and S_y are the mean and standard deviation of x and y, and n is the sample size.

The optimization problem for the data imputation was formulated as follows.

Decision variables

As the main objective is to impute values to all missing values, the decision variables correspond to the set $\{M_1,\ldots,M_D\}$. According to Table I, there are 1481 missing values to impute.

Objective function

Minimization of the mean quadratic error between the histogram of each variable with and without imputed data and the mean quadratic error between the correlations of each pair of variables with and without the imputed data.

$$\boldsymbol{argmin} \sum_{d=1}^{D} \|H(V_d) - H(V_d \cup M_d)\| + \sum_{\substack{u=1,v=1 \\ u>v}}^{D} \|CORR(V_u,V_v) - CORR(V_u \cup M_u, V_v \cup M_v)\|. \quad [11]$$

Constraints

The only imposed constraint is the lower and upper bounds for each attribute, for which the minimum and maximum values are observed from the samples.

$$min(V_d) \le W_i^d \le max(V_d), \forall i \in \{1,\ldots,N^d\}, d \in \{1,\ldots,D\} \quad [12]$$

This formulation is nonlinear and may have no unique solution. Metaheuristics are optimization methods that can deal with these kinds of problems successfully. We therefore solved the optimization formulation by genetic algorithm (GA) metaheuristics due to its flexibility and good performance (Whitley, 1994). The GA is a stochastic method, hence different seeds of random number generator may generate different solutions. In this application, our experiments show that the imputed values change slightly in response to varying the seed, but the histograms and correlations are very stable. We use one representative set of imputed data found by one execution of GA. Table III shows the parameters used in the GA for data imputation.

Table II

Description of all four attributes and simple statistics

	Rec	Bwi	Spi	A*b
Rec	**370**	0.08	0.11	-0.02
BWi	470	**90**	0.31	-0.28
Spi	469	539	**391**	-0.74
A*b	300	300	299	**630**

Table III

Parameters used by GA for data imputation

Parameter	Value	Description
npop	1000	Number of individuals in the population
ngen	500	Number of generations (iterations)
Crossover operator	Uniform crossover	50% probability of getting the gene from parent 1 (and 50% from parent 2)
Mutation operator	Gaussian mutation	10% of genes at random, new value = current value + N(0,1)
Selection operator	Tournament selection	Tournament size of 10 individuals
cxpb	0.9	Probability of applying crossover
mutpb	0.4	Probability of applying mutation

The Pearson's correlation computed for imputed and non-missing samples shows that the correlations were perfectly reproduced. Figure 2 (upper and lower panel) shows the histogram of the imputed data and with non-missing values respectively. Figure 3 also shows all four non-missing variables (*i.e.*, Rec, BWi, Spi, and A*b) in space. We discuss Figure 3 under the 'Discussion and Conclusion' section.

Analysis

The imputed data, consisting of 930 drill core samples for four variables (Rec, BWi, Spi, and A*b), was used for the analysis, the explanatory variables being Spi, BWi, and A*b. The hypothesis of stationarity was tested by fitting a regression of recovery on the mean corrected eastings (x), mean corrected northings (y), mean corrected elevations (z), x^2, y^2, and the cross-product xy in Equation [13]. This model, referred to as *Model*1, is

$$A = \beta_o + \beta_1 x + \beta_2 y + \beta_3 z + \beta_4 x^2 + \beta_5 y^2 + \beta_6 xy + \varepsilon \quad [13]$$

where ε is the random error, which is expected to be spatially correlated, with mean of zero and standard deviation σ_o. *Model*1 was initially fitted by OLS. Then, a spherical variogram was fitted to the residuals and the variogram parameters were used for fitting with a GLS function *gls*( ) in the R library *nlme* (Pinheiro and DebRoy, 2016). The fitted spherical variogram and model parameters are shown in Figure 4. The estimated coefficients for the GLS fit to Model1 are shown in Table IV.

The standard deviation of the residuals is 14.26 on 923 degrees of freedom, which is smaller than the standard deviation of the recovery data (15.02). While this reduction in standard deviation is small, the sample size is relatively large and two of the coefficients in the fitted quadratic surface are highly significant statistically. We then assume the residuals from the GLS regression are a realization of a stationary spatial process.

The residuals from the model res (Rec) were taken as the response variable for recovery (Rec) and were used together with the BWi, Spi, and A*b (referred to as *B*,*C*, and *D* respectively) to fit the D-vine copula. Variables *B*,*C*, and *D* were mean-corrected to avoid the excessively large values of quadratic terms and ill-conditioned matrices that would result if the original data was used. Quadratic terms and interactions between the explanatory variables included were *BD*, *CD*, B^2, C^2, D^2. So a 10-dimensional D-vine based model was constructed, which is made up ofres(Rec), *B*, *C*, *D*, *BC*, *BD*, *CD*, B^2, C^2,and D^2. In the following, the **res**(*Rec*) will be referred to as *A*.

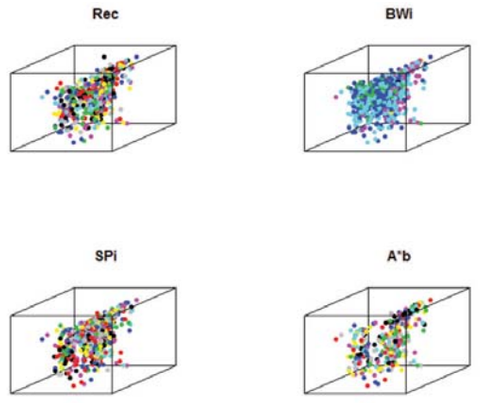

Figure 3—The 3D spatial position of the samples showing non-missing values of Rec (top left), BWi (top right), SPi (bottom left), and A*b (bottom right)

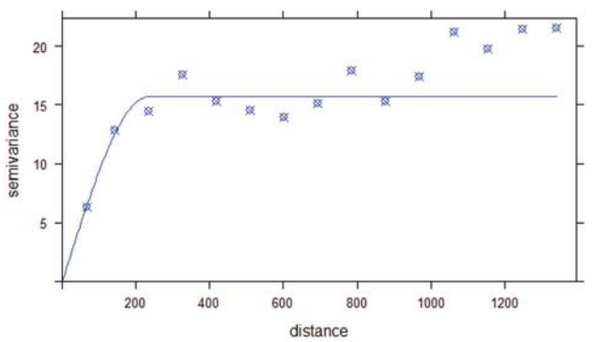

Figure 4—Fitted spherical variogram with range 230, sill 15.7, and nugget 0.3.

Table IV

Estimated coefficients of the fitted GLS model (range, 230 and nugget, 0.5)

Coefficient	Estimate	Estimated standard error	P-value
β_0	133.05554	25.54233	0.00
β_1	0.00247	0.00413	0.55
β_2	-0.00062	0.00158	0.69
β_3	-0.02129	0.00578	0.00
β_4	0.00002	0.9e-5	0.03
β_5	0.3e-5	0.1e-5	0.02
β_6	0.6e-5	0.4e-5	0.19

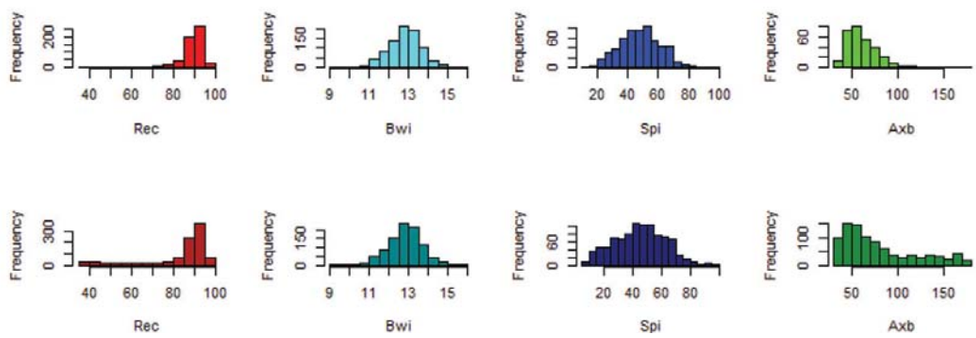

Figure 2—Histogram of four variables with non-missing data (upper panel), histogram of four variables with imputed data (lower panel)

Prediction of copper recovery from geometallurgical data using D-vine copulas

We fitted an appropriate kernel marginal distribution to each of the mean-corrected variables. After obtaining well-fitted marginal distributions, a 10-dimensional D-vine copula was used to join the margins and model the joint dependence structure. To be able to establish the 10-dimensional D-vine copula, we fitted the best fitting bivariate copula for each pair copula using the *R* library *CDVine* developed by Schepsmeier and Brechman (2015). The fitting was done by equating the Kendall's tau to the value of Kendall's tau implied by the dependence parameter (θ_1, θ_2, and ρ), which is referred to as the 'method of moments'. A limitation of the method of moments is that it does not lead easily to a criterion for choosing between the copula forms. Therefore, the method of maximum likelihood was used for choosing between the copula forms, the form with the highest likelihood being chosen. The rotated version of the bivariate copulas (*i.e.*, BB6, BB7, and BB8) with angles 90°, 180°, and 270° was selected by maximum likelihood. In addition, Student-t, normal, and Frank copulas were also selected using maximum likelihood for some trees. Figure 5 illustrates the fitted bivariate copulas and their fitted dependence parameters (θ_1, θ_2, ρ, and *df*) for the 10-dimensional D-vine model. The final forecasting performance of the 10-dimensional D-vine copula model was calculated using a 10D version of Equation [7]. The predicted values were back-transformed to the original unit (recovery per cent, Rec) by adding the predicted values from the 10D model to the predicted values from *Model*1.

We compared the predicted recovery from the 10-dimensional D-vine copula with an OLS regression and a GLS regression model. The residual from model, referred to in this application as *A*, which is the response variable, was regressed on the explanatory variables *B*, *C*, *D*, *BC*, *BD*, *CD*, B^2, C^2,and D^2. Equation [14] shows the OLS regression model fitted, and Table V shows the estimated coefficients for the OLS regression.

$$A^* = \beta_o + \beta_1 B + \beta_2 C + \beta_3 D + \beta_4 BC + \beta_5 BD + \beta_6 CD + \beta_7 B^2 + \beta_8 C^2 + \beta_9 D^2 + \varepsilon \quad [14]$$

The linear regression model was used to predict recovery and the predicted values were back-transformed to the original units (recovery per cent, *Rec*) by adding the predicted values from *Model*1.

The residual from the model referred asA was regressed on the explanatory variables *B*, *C*, *D*, *BC*, *BD*, *CD*, B^2,C^2,and D^2 using the GLS model with spherical variogram parameters of range: 230, nugget: 0.5, and sill: 15.7. The GLS model is given in Equation [14], and the estimated model coefficients are shown in Table VI.

Table V

Estimated coefficients of the fitted OLS regression

Coefficient	Estimate	Estimated standard error	P-value
β_0	1.11996	0.81077	0.17
β_1	-0.22724	0.58045	0.69
β_2	0.22607	0.04255	1.35e-07
β_3	0.10797	0.02407	8.19e-06
β_4	-0.02021	0.04535	0.66
β_5	-0.03634	0.02158	0.09
β_6	0.00116	0.00162	0.47
β_7	0.63571	0.43801	0.15
β_8	-0.00179	0.00233	0.44
β_9	-0.00089	0.00049	0.07

Table VI

Estimated coefficients of the fitted GLS model (range, 230 and nugget, 0.3)

Coefficient	Estimate	Estimated standard error	P-value
β_0	0.78122	0.86786	0.37
β_1	-0.22520	0.58289	0.69
β_2	0.22476	0.00430	0.00
β_3	0.10409	0.02456	0.00
β_4	-0.01938	0.04549	0.67
β_5	-0.03494	0.02161	0.11
β_6	0.00122	0.001673	0.46
β_7	0.65855	0.43858	0.13
β_8	-0.00157	0.00236	0.51
β_9	-0.00078	0.00050	0.12

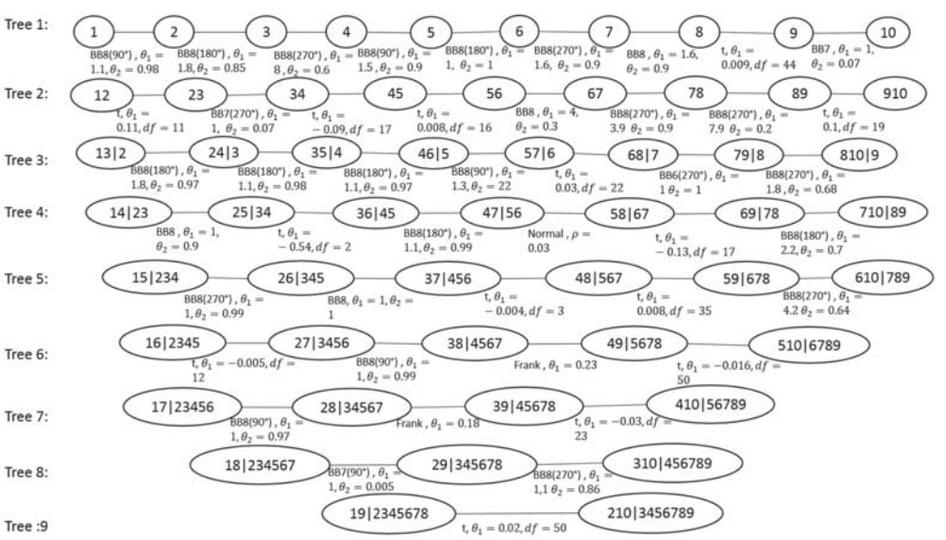

Figure 5—Structure of the 10-dimension D-vine model, where 1, 2, 3, 4, 5, 6, 7, 8, 9, and 10 are A, B, C, D, BC, BD, CD, B^2, C^2, and D^2 respectively

The GLS model was used to make predictions of recovery at each point, and the predicted value was back-transformed to the original unit (recovery per cent *Rec*) by adding the predicted values from *Model*1. A summary of the cross-validation results using all three models is presented in Table VII. There is little difference between the GLS and OLS fits. The D-vine performs better according to the MAE but not according to RMSE. We discuss this in the next section. Figure 6 illustrates a scatter plot of the observed *versus* predicted recoveries from the GLS, D-vine, and OLS models. Further comparisons were made by making out-of-sample predictions. Proportions of 10% and 30% were removed at random locations from the 930 complete geometallurgical data. The models (OLS, GLS and D-vine) were fitted to the remaining 90% and 70% of the data.

Out-of-sample predictions were generated and compared with the known values of the data removed. Figure 7 shows box plots of the removed CuRec (A) and the out-of-sample predictions using OLS (B), GLS (C) and D-vine (D), for 90% and 70% data used for predictions. Summary statistics are given in Table VIII.

The D-vine performs best in terms of MAE, and GLS regression is an improvement on OLS regression, in terms of MAE for both 10% and 30% data removed. However, OLS regression is slightly better than both the D-vine copula and GLS regressions in terms of RMSE.

Discussion and conclusion

Data on four variables (Rec, BWi, Spi, and A*b) from 930 drill core samples at know locations was available. Two hundred and ninety-nine drill cores had a complete record, but there were some missing items from the other 631 cores. In order to use all 930 drill core samples, a genetic algorithm (GA) was used to impute missing items at these locations. The objective function formulated in this case study was designed to reproduce precisely the individual histograms and the linear correlations between pairs of variables. This criterion is, however, subjective and in cases when missing data comes from preferential sampling, the histogram of the imputed data may differ from the actual underlying distribution. For example, it is common to perform metallurgical test work only in ore zones with a high grade profile, hence recovery for low-grade zones will not be well represented in the distribution. The objective function in the data imputation method should be adjusted according to the knowledge of the data-sets. The recovery (Rec), the response in this application, shows a slight, but statistically significant, nonstationarity. The nonstationarity of Rec has been accounted for by fitting a quadratic trend regression surface by the GLS model, with a spherical variogram to approximate the spatial correlation. The residuals from the GLS model were considered as a realization of a stationary process.

Table VII

Summary of the cross-validation

Model	MAE	RMSE
D-vine copula regression	9.12	14.92
GLS regression	10.09	13.91
OLS regression	10.04	13.91

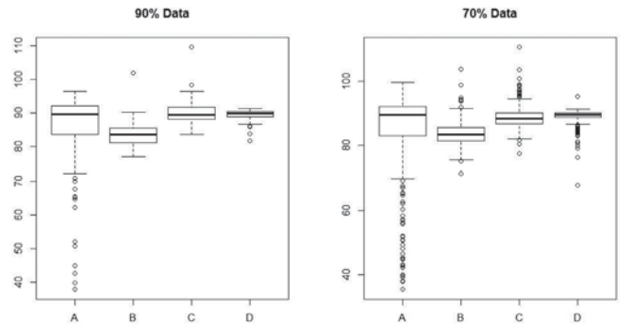

Figure 7—Box plots of removed CuRec (A), out-of-sample predictions of OLS (B), GLS (C), and D-vine (D) models for 90% (left) and 70% (right) of data

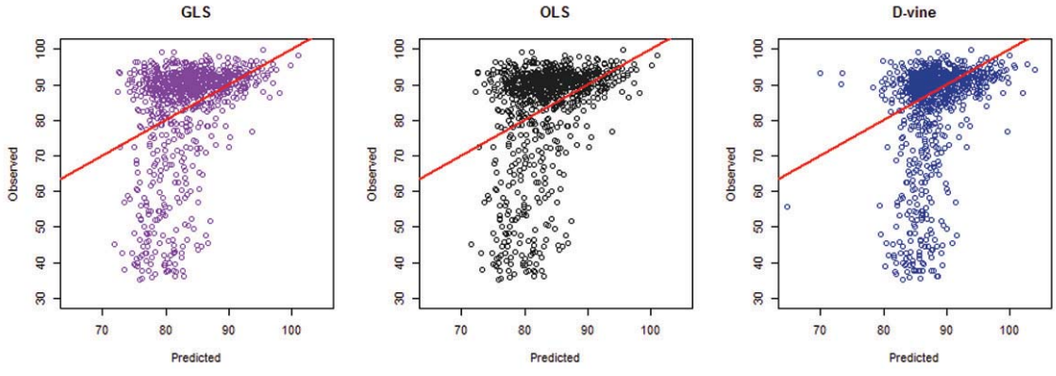

Figure 6—Predicted *vs* observed recoveries for GLS, OLS, and D-vine models

Table VIII

Summary of the out-of- sample predictions

Model	MAE (90%)	RMSE (90%)	MAE (70%)	RMSE (70%)
D-vine copula regression	7.86	13.96	9.33	16.25
GLS regression	8.46	14.29	10.07	16.47
OLS regression	9.49	13.11	11.07	15.20

The residuals from the model and the mean corrected values for BWi, Spi, and A*b, together with two variable interactions and squares for the three variables, were used to fit a 10-dimensional D-vine copula model. The fitted 10-dimensional D-vine copula model was used to predict recovery, and MAE and RMSE were calculated. These predictions were compared with predictions from regressions fitted by OLS and GLS. The D-vine copula model had the smallest MAE. However, the regression models had lower RMSE. A comparison of the scatter plots suggests that the D-vine gives more accurate and precise predictions for high levels of copper recovery. However, the D-vine appears to overestimate the copper recovery at low levels rather more than the regression models. Out-of-sample predictions using the three models were compared as a further check on the D-vine copula regression model. A proportion of the data (*i.e.* 10% and 30%) was removed at random locations from the complete geometallurgical data-sets. The models were fitted to the remaining 90% and 70% of the data, and out-of-sample predictions were estimated and compared with the known values of 10% and 30% data removed. Results from the analysis shows that the D-vine model had the least MAE for both 90% and 70% data, although OLS regression was slightly better on RMSE. An explanation for the finding that the D-vine copula is better on MAE yet slightly worse on RMSE is that the D-vine copula is less affected by outliers. The outliers will make a major contribution to the RMSE, and regression fits the coefficients by minimizing the RMSE. This has the effect that outlying observations are highly influential in the fitting process, drawing the fitted surface towards them and so reducing the RMSE. For this reason the MAE is considered more useful in the mining industry, where outlying values are common and the implicit assumption of a Gaussian distribution, under which GLS would be optimum, is not realistic. The D-vine copula is preferable to capping, which introduces a downward bias. Moreover, the D-vine will generally produce more accurate prediction intervals than a regression model, because it allows for a general form of the distribution of the errors. Generally, geometallurgical tests are expensive and a modelling approach that can provide accurate and precise predictions of some variables from others will save money.

Acknowledgements

This research is supported by an Australian Government Research Training Program Scholarship awarded to Emmanuel Addo Jr. The authors thank the mining company for providing the geometallurgical data-sets used in this case study. We express our gratitude to the reviewers for their comments and suggestions, which have improved the practical application of this manuscript.

References

Aas, K., Czado, C., Frigessi, A., and Bakken, H. 2009. Pair-copula constructions of multiple dependence. *Insurance: Mathematics and Economics*, vol. 44, no. 2. pp. 182–198.

Addo, E., Chanda, E., and Metcalfe,A.V. Spatial pair-copula model of grade for an anisotropic gold deposit. *Mathematical Geosciences*, July. pp. 1–26. doi: 10.1007/s11004-018-9757-7

Bedford, T. and Cooke, R.M. 2002. Vines: A new graphical model for dependent random variables. *Annals of Statistics*, vol. 30, no. 4. pp. 1031–1068.

Bernard, C. and Czado, C. 2015. Conditional quantiles and tail dependence. *Journal of Multivariate Analysis*, vol. 138. pp. 104–126.

Coward, S., Vann, J., Dunham, S., and Stewart, M. 2009. The Primary-Response framework for geometallurgical variables. *Proceedings of the 7th international Mining Geology Conference*, Perth, WA, 17-19 August 2009. Australasian Institute of Mining and Metallurgy, Melbourne. pp. 109–113.

Deutsch, C.V. 2013. Geostatistical modelling of geometallurgical variables - problems and solutions. *Proceedings of the Second AusIMM International Geometallurgy Conference*, Brisbane, QLD, 30 September - 2 October 2013. Australasian Institute of Mining and Metallurgy, Melbourne. pp. 7–16.

Dowd, P., Xu, C., and Coward, S. 2016. Strategic mine planning and design: some challenges and strategies for addressing them. *Mining Technology*, vol. 125, no. 1. pp. 22–34.

Erhardt, T.M., Czado, C., and Schepsmeier, U. 201). R-vine models for spatial time series with an application to daily mean temperature. *Biometrics*, vol. 71, no. 2. pp. 323–332.

Fenske, N., Kneib, T., and Hothorn, T. 2011. Identifying risk factors for severe childhood malnutrition by boosting additive quantile regression. *Journal of the American Statistical Association*, vol. 106, no. 494. pp. 494–510.

Gräler, B. 2014. Developing spatio-temporal copulas. PhD dissertation, Institute for Geoinformatics, University of Münster.

Gräler, B. and Pebesma, E. 2011. The pair-copula construction for spatial data: a new approach to model spatial dependency. *Procedia Environmental Sciences*, vol. 7. pp. 206–211.

Haff, I.H., Aas, K., and Frigessi, A. 2010. On the simplified pair-copula construction—simply useful or too simplistic? *Journal of Multivariate Analysis*, vol. 101, no. 5. pp. 1296–1310.

Hunt, J., Kojovic, T., and Berry, R. 2013. Estimating comminution indices from ore mineralogy, chemistry and drill core logging. *Proceedings of the Second AusIMM International Geometallurgy Conference*, Brisbane, QLD, 30 September - 2 October 2013. Australasian Institute of Mining and Metallurgy, Melbourne. pp. 173–176.

Joe, H. 1996. Families of m-variate distributions with given margins and m (m-1)/2 bivariate dependence parameters. *Lecture Notes - Monograph Series. Institute of Mathematical Statistics*, Hayward, CA. pp. 120–141. https://projecteuclid.org/euclid.lnms/1215452614

Kraus, D. and Czado, C. 2016. D-vine copula based quantile regression. *Computational Statistics and Data Analysis*. https://arxiv.org/abs/1510.04161v4

Kurowicka, D. and Cooke, R.M. 2006. Uncertainty Analysis with High Dimensional Dependence Modelling. Wiley.

Lishchuk, V., Koch, P-H., Lund, C., and Lamberg, P. 2015. The geometallurgical framework. Malmberget and Mikheevskoye case studies. Minerals and Metallurgical Engineering Division, Luleå University of Technology.

Liu, Z., Zhou, P., Chen, X., and Guan, Y. 2015. A multivariate conditional model for streamflow prediction and spatial precipitation refinement. *Journal of Geophysical Research: Atmospheres*, vol. 120, no. 19. https://doi.org/10.1002/2015JD023787

Musafer, G.N. and Thompson, M.H. 2016. Non-linear optimal multivariate spatial design using spatial vine copulas. *Stochastic Environmental Research and Risk Assessment*, vol. 31, no. 2. pp. 551–570.

Musafer, G.N., Thompson, M.H., Kozan, E., and Wolff, R.C. 2013. Copula-based spatial modelling of geometallurgical variables. *Proceedings of the Second AusIMM International Geometallurgy Conference*, Brisbane, QLD, 30 September - 2 October 2013. Australasian Institute of Mining and Metallurgy, Melbourne. pp 239–246.

Nelsen, R. 2006. An introduction to copulas. *Lecture Notes in Statistics*. Springer, New York.

Pinheiro, J., Bates, D., DebRoy, S., Sarkar, D., and R Core Team. 2016. _nlme: Linear and nonlinear mixed effects models_. R package version 3.1-128. http://CRAN.R-project.org/package=nlme

Schepsmeier, U., Stöber, J., Brechmann, E.C., Graeler, B., Nagler, T., and Erhardt, T. 2016. VineCopula: Statistical inference of vine copulas. R package version 2.0.5. https://github.com/tnagler/VineCopula

Walters, S. and Kojovic, T. 2006. Geometallurgical mapping and mine modelling (GEMIII) - the way of the future. *Proceedings of SAG 2006*, Vancouver, Canada, 23-27 September 2006. vol. 4. pp. 411–425.

Whitley, D. 1994. A genetic algorithm tutorial. *Statistics and Computing*, vol. 4, no. 2. pp. 65–85.

Williams, S.R. and Richardson, J. 2004. Geometallurgical mapping: A new approach that reduces technical risk. *Proceedings of the 36th Annual Meeting of the Canadian Mineral Processors*. Canadian Institute of Mining, Metallurgy and Petroleum, Montreal. pp. 241–268.

Willmott, C.J. and Matsuura, K. 2005. Advantages of the mean absolute error (MAE) over the root mean square error (RMSE) in assessing average model performance. *Climate Research*, vol. 30, no. 1. pp. 79–82.

Xu, Q. and Childs, T. 2013. Evaluating forecast performances of the quantile autoregression models in the present global crisis in international equity markets. *Applied Financial Economics*, vol. 23, no. 2. pp. 105–117. ◆

Developing a 3D mineral texture quantification method of drill core for geometallurgy

M.J. Voigt[1,2], J. Miller[3], L. Bbosa[1], R.A. Govender[5], D. Bradshaw[4], A. Mainza[1], and M. Becker[1]

Affiliation:

[1] Centre for Minerals Research, University of Cape Town, Rondebosch, South Africa

[2] Economic Geology Competency, Council for Geoscience, South Africa

[3] Department of Earth Sciences, Stellenbosch University, Matieland, South Africa

[4] Minerals to Metals Initiative, University of Cape Town, Rondebosch, South Africa

[5] Blast Impact and Survivability Research Unit, University of Cape Town, Rondebosch, South Africa

Correspondence to:
M. Voigt

Email:
mvoigt@geoscience.org.za

Dates:
Received: 21 Jan. 2019
Revised: 15 Mar. 2019
Accepted: 26 Mar. 2019
Published: April 2019

How to cite:
Voigt, M.J., Miller, J., Bbosa, L., Govender, R.A., Bradshaw, D., Mainza, A., and Becker, M. Developing a 3D mineral texture quantification method of drill core for geometallurgy.
The Southern African Insitute of Mining and Metallurgy

DOI ID:
http://dx.doi.org/10.17159/2411-9717/590/2019

ORCiD ID:
https://orchid.org/0000-0003-2152-2070

This paper was first presented at the *Geometallurgy Conference 2018 'Back to the Future'*, 7–8 August 2018, Lagoon Beach Conference Venue, Cape Town, South Africa.

Synopsis

Mineral texture is a critical factor which controls ore variability and is an important attribute in geometallurgy. In relation to downstream processes, it affects the fracture pattern during breakage, where rock strength is inherently a function of mineral texture. Because of the subjective nature of mineral texture, it has not been easy to quantify, especially in the context of a measurement suitable for use in geometallurgical programmes. The aim of this paper is to present the first steps in developing a 3D mineral texture quantification method for drill core and to assess its sensitivity to differences in rock strength using a case study. The methodology includes classifying the textural information using the 3D grey level co-occurrence matrices (GLCM) and X-ray computed tomography (XCT) coupled method. Rock strength tests were performed using the split Hopkinson pressure bar (SHPB). The case study investigates a heterogeneous polymetallic sulphide deposit and a homogeneous shale subdivided into three 'mineral textural types'. The variability is largely captured by the GLCM matrices, and preliminary trends can be observed where the shale is finer grained and has a higher yield strength in comparison with the coarser grained polymetallic sulphide ore.

Keywords
drill core, mineral texture, ore variability.

Introduction

Modern mining requires the exploitation of lower grade and more complex, heterogeneous orebodies to address the growing industry demands. Historically, processing plants were designed and built based on average ore characteristics and therefore are relatively inflexible when facing the full spectrum of ore variability in heterogeneous orebodies (Lamberg, 2011; Lotter, 2011; Schouwstra *et al.*, 2013). The practice of geometallurgy represents an opportunity to manage ore variability in the mining industry (Powell 2013; Baum, 2014; Yildirim *et al.*, 2014; Nguyen, 2013). It focuses on quantifying the relationships between ore characteristics and their downstream mining and processing responses, often starting with small-scale laboratory testing. The purpose of geometallurgy is linked to maximizing the net present value (NPV) of an orebody by minimizing technical and operational risk – where 'ore variability' is considered one of the most significant technical risks.

A key parameter that constitutes ore variability is the heterogeneity in mineral texture, which further controls the response of the ore to processing (Schouwstra and Smit, 2011; Schouwstra *et al.*, 2013; Yildirim *et al.*, 2014; Lund; Lamberg, and Lindberg, 2013). Mineral texture summarizes not only the geometrical characteristics of a grain or particle (shape and size), but also includes interrelationships and compositions, *i.e.* mineralogy (Craig and Vaughan, 1994). Numerous examples occur in the literature describing how mineral texture affects downstream processing. For example, in comminution, texture influences rock strength, liberation, product particle size distribution, target grain size, and grindability of the ore (Vizcarra *et al.*, 2010; Lotter *et al.*, 2011; Ghorbani *et al.*, 2011, 2013; Nwaila, 2014; Evans, Wightman, and Yuan, 2015; Little *et al.*, 2016; McGrath, O'Connor, and Eksteen, 2015; Tungpalan *et al.*, 2015; Miller and Lin, 2016). In flotation, texture affects the potential mineral grade-recovery relationship (Gaspar and Pinto, 1991; Gottlieb *et al.*, 2000). In leaching, texture affects the accessibility of the valuable mineral to the lixiviant (Lui, Pawlik, and Laskowski, 2015; Maydagan *et al.*, 2016). Texture has also been used for the characterization and prediction of acid rock drainage (Parbhakar-Fox *et al.*, 2011).

The use of qualitative mineral texture descriptors involves some limitations, because the subjectivity of these descriptors then increases (Vos, 2016). In terms of mineral textural quantification, only aspects of quantified mineral texture (*e.g.* shape or size) are used, and therefore the observed relationships do not always hold because studies have not holistically defined the inherent geometrical and compositional

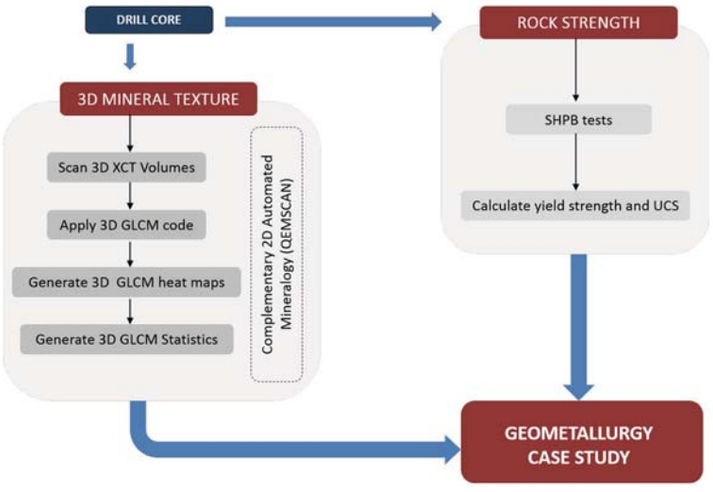

Figure 1—Summarized methodology for this study

variability of different geomaterials. Furthermore, most of these abovementioned studies focused on particulate samples, and therefore the method is not directly applicable to drill cores. More recent studies have therefore focused on developing methods to quantify mineral texture through automated textural pattern recognition on drill cores, as well as testing the potential to predict downstream mineral performance (Becker *et al.*, 2016). Perez-Barnuevo, Lévesquea, and Bazin, (2018) tested the link between texture and mineral behaviour during comminution and heavy liquid separation. They used a method that acquired the textural information through the Mineral Liberation Analyser (MLA), and coupled it with the grey level co-occurrence matrices (GLCM) and grey level run length matrices (GLRLM) for extraction and automated recognition of textural information in 2D. However, mineral texture measurements that are limited to 2D do not necessarily provide complete dimensions for grain characteristics (3D), which also further increases subjectivity. A potential method using X-ray computed tomography (XCT) coupled with 3D GLCM to achieve 3D mineral textural quantification was proposed by Jardine, Becker, and Miller (2018) and its potential as a small-scale geometallurgical test was demonstrated (Becker *et al.*, 2016) using a Ni-Cu sulphide ore. However, because the study used only one ore type, further studies are needed to fully understand the robustness of this method towards a variety of ore types and its suitability regarding downstream processes.

This paper further develops the method using XCT and 3D GLCM to quantify mineral texture in geometallurgy, where rock strength is a function of the inherent mineralogical and textural features of a rock (Olsson, 1974; Howarth and Rowland, 1987). Therefore, in order to demonstrate that the observed differences in mineral textures captured by the abovementioned method are meaningful, rock strength was also measured. The case studies include a heterogeneous polymetallic ore and a homogeneous shale to represent a different suite of mineral textural types as part of the ongoing research (Becker *et al.*, 2016; Jardine, Becker, and Miller, 2018).

Experimental procedure

As a proof of concept, three large pieces of samples (approx. 30 cm^2) were used in this study. The first sample (sample A) is a relatively homogeneous, well characterized Malmesbury shale from a quarry in Cape Town, South Africa (Bbosa, 2007; Hill *et al.*, 2018). The shale was used to develop the initial methodology. The other two rock types were sampled from a local polymetallic (Pb-Zn-Cu) sulphide ore deposit in South Africa (samples B and C). Three cylindrical diamond drill core sets with diameters of 13, 19, and 26 mm were obtained manually from each of the grab samples. The same drill cores were cut into a minimum of 15 pieces (discs) of equal length, which gave an overall 135 pieces for use in the proof of concept.

A subset of the pieces was visually selected and scanned by XCT using the NIKON XTH 225 ST system housed in the Microfocus X-ray Radiography and Tomography facility at the South African Nuclear Energy Corporation (Bam *et al.*, 2016). A constant set of XCT scan parameters was used: 175 kV, 15 µm voxel size, averaging of three frames, 1000 projections, using a 25 mm Cu filter, with approximately 20 minutes per scan. The approach for this study is consistent with the 3D GLCM and XCT method of Jardine, Becker, and Miller (2018). The grey level co-occurrence matrices were extracted from the XCT image stacks using the dedicated MATLAB script by Jardine, Becker, and Miller (2018). After XCT scanning, a subset of the same pieces was prepared into blocks for analysis on an FEI 650F FEG QEMSCAN at the University of Cape Town to determine the basic mineralogical characteristics of each sample. Samples were scanned using the field image analysis routine with instrument operating parameters of 25 kV, 10 nA, 357 fields/frames at a 15 µm pixel spacing. The methodology is summarized in Figure 1.

All rock strength tests were performed on the 135 pieces using the Blast Impact and Survivability Research Unit (BISRU) split Hopkinson bar facility in the Mechanical Engineering department at the University of Cape Town. High strain rate stress-strain responses of geomaterials can be measured through SHPB testing, which can characterize the strength of these materials by using common engineering parameters. SHPB testing was preferred over quasi-static testing, as the high strain rates applied during the SHPB test are more reflective of those encountered in a comminution or milling context. These tests followed the procedure outlined by Bbosa (2007) and Govender *et al.* (2012). After testing different strikers and conditions, the standard conditions for all impacts included using a conical striker (400 mm long, and a mass of 885 g), strain gauge bridge excitation voltage of 2 V, strain gauge amplifier gain of 1000, and

sampling rate of 10 megasamples per second (MSa/s). Three different pressures (using the pressure-controlled gas gun) were tested for every core size. The initial test methodology included testing the samples at the desired pressures of 220 (low), 280 (medium), and 400 kPa (high). A light trap and digital oscilloscope were used to measure the striker velocities for each impact, and hence calculate the kinetic energy for each collision. To facilitate dynamic equilibrium of the specimen as early as possible, pulse smoothing was applied in the form of masking tape between striker and input bar to tune the stress wave rise time. Furthermore, the SHPB data was calibrated by obtaining a constant proportionality constant directly related to the output voltage applied to the stress using one-dimensional theory (see Govender *et al.*, 2012). Calculations for the stress-strain data were done and the results plotted, and the data was used to calculate fracture properties. It should be noted that the data presented in this paper is only for the 13 mm drill core pieces at 220 kPa pressure, for direct comparison between the three mineral texture types.

Results

Initial ore characterization

The different 'mineral texture types' were identified through visual inspection of the different cores, and subsequently divided into shale and the two polymetallic ore samples on the basis of their variability in mineralogical composition as well as their geometrical differences (texture). The variability of these samples is illustrated through the selected hand specimens and QEMSCAN false-colour images in Figures 2 and 3, respectively. Sample A (shale) is a homogeneous (equigranular) fine-grained rock, with quartz, biotite, and feldspar as the dominant minerals. Samples B and C are medium-grained, heterogeneous magnetite rock. Sample B consists predominantly of magnetite and pyroxmangite, and its sulphide minerals are mostly chalcopyrite, and pyrrhotite. Sample C is predominantly quartz, magnetite and pyroxmangite, associated with sphalerite.

Quantification of mineral texture

2D slices extracted from the 3D volumes and the grey level XCT scans are illustrated in Figure 4 A1, B1, and C1 (respectively samples A, B, and C). The XCT images duplicate the basic textures, where sample A is fine-grained, and B and C are

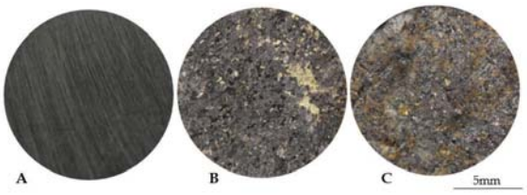

Figure 2—Photographs of the selected samples representing the three mineral texture types: (A) shale, (B) and (C) polymetallic Pb-Cu-Zn ore

medium-grained. The QEMSCAN analysis is further used as a supporting tool to interpret the mineralogy captured by the XCT images, since both the QEMSCAN backscattered electron (BSE) and XCT grey level images represent relative differences in mineral density (Figure 3 D, E, and F against Figure 4 A1, B1, and C1 respectively).

The brighter pixels within a grey level image (*e.g.* Figure 4 A1, B1, and C1) are related to the denser minerals (sulphides), whereas the darker pixels are related to the less dense minerals (quartz, biotite). As an example, the GLCM matrices (Figure 4 A2, B2, and C2) can be calculated based on the grey level information for a selected 2D XCT image extracted from the 3D (XCT) volume. The accompanying GLCM colour heat map distributions are also provided for each GLCM matrix (Figure 4 A3, B3, and C3) to reveal hidden information that is not easily visible to the naked eye. The matrices have two axes related to pixel pairs, where the vertical axis represents the reference pixel value and the horizontal axis represents its neighbouring pixel value (Jardine, Becker, and Miller, 2018).

For the selected XCT slice, the shale (sample A) has a GLCM distribution which is limited to the top left (low-density) quadrant and records no information in the bottom right (high-density) quadrant. The distribution for polymetallic sulphide sample B is also restricted to the top left quadrant (note the absence of sulphides in this particular XCT slice, chosen rather instead to illustrate differences in grain size distribution). The difference between these two distributions is in the width of the matrices. Sample A has a broader distribution than sample B. Sample C has peaks in both quadrants, and has a narrow distribution similar to B. The narrow *versus* broader distributions are indicative of the variation in grain sizes (Jardine, Becker, and Miller, 2018).

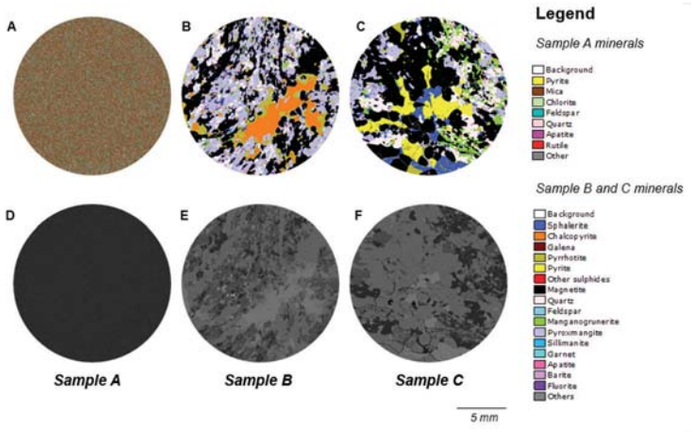

Figure 3—QEMSCAN false-colour images of the three rock samples (A shale, B and C polymetallic ore) accompanied by their corresponding backscattered electron images (D, E, F)

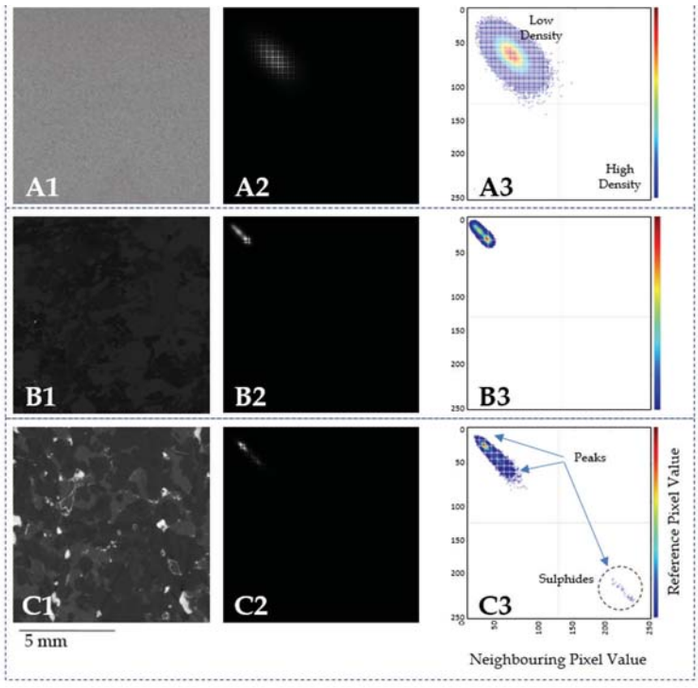

Figure 4—2D XCT images can be extracted from the 3D volumes (A1, B1, C1) and examples are given for the shale (A1) and the polymetallic ore sample B (B1) and sample C (C1). Each XCT image (input) is accompanied by its GLCM matrix (A2, B2, C2 for samples A, B, and C respectively), which summarizes the mineral textural information of the spatial relationship between the grey values within the XCT images (output). The 'colour intensity' heat map further reveals the hidden information which may not be visible to the naked eye (A3, B3, and C3 for each of the samples) and enhances the information on the mineralogical and textural variability for each of the matrices

The broader (sample A) distribution is indicative of a fine-grained material, and the narrower distributions (samples B and C) are indicative of a coarser grained material such as the medium-grained texture for these polymetallic ore samples. The peaks in the quadrants indicate the grey level peaks of either the silicate or BMS/oxide minerals. The sensitivity in the mineralogy can therefore be seen in either the top left quadrant (low-density minerals) or the bottom right quadrant (high-density minerals). For example, sample A is dominated by low-density silicate minerals and has one dominant peak in the top left quadrant, whereas, sample C consists of silicates, oxides, and sulphides, and therefore three peaks can be seen. Two of the peaks are in the low-density quadrant and the third peak is in the bottom right quadrant (representing the sulphide population).

The image information for the entire 3D volumes can be converted to numerical information using statistical descriptors provided by Haralick, Shanmugam, and Dinstein (1973) and the script adaption by Jardine, Becker, and Miller (2018). The four statistical descriptors that link to mineralogy and texture are homogeneity, contrast, correlation, and energy. These descriptors are essentially variability in the grey level information as well as the spatial distribution of these grey levels in relation to each other (Haralick, Shanmugam, and Dinstein, 1973). Homogeneity and contrast refer to the number of grey level transitions and the

Table I

GLCM statistical texture descriptors (*e.g.* contrast) for the three samples for multiple images through a 3D volume

Sample	*N* (2D images)	Minimum	Maximum	Mean
Sample A	100	70 298	70 549	70 385
Sample B	98	68 487	71 375	69 315
Sample C	98	71 004	75 380	74 128

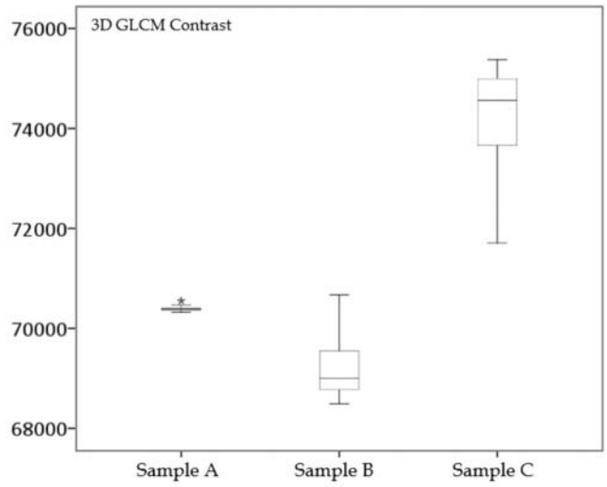

Figure 5—Box-and-whisker plot summarizing the 3D GLCM statistical descriptor (contrast) for all three samples. The intensity of variability can be observed by the range for each sample, where sample A is mineralogicaly the most homogeneous, hence has a short range in comparison with samples B and C, which have a broader range indicative of mineralogical variability

local variability in these transitions respectively. Correlation and energy refer to the probability of the occurrence of any specified pixel pair and the sum of the squared elements in the GLCM, respectively. These four statistical descriptors were calculated for the 3D volumes of each sample. As an example, the descriptive statistics for the contrast descriptor are summarized in Table I and a supporting box-and-whisker plot is illustrated in Figure 5.

The range of these contrast values for a specific sample is indicative of the intensity of the sample's variability, where shorter ranges are indicative of higher homogeneity in comparison with broader ranges, which are indicative of higher mineralogical variability. For example, sample A, has the shortest range (70 298–70 549), and is thus the most homogenous sample. The polymetallic samples, which have broader ranges (68 487–71 375 or 71 004–75 380 respectively), have higher mineralogical variability. However, the polymetallic ores (samples B and C) are distinguishable from each other, as reflected by their variability in mineralogy.

The contrast values can potentially also discriminate between textural features, where the higher positions (*i.e.* visually on the box-and-whisker plot as well as higher values) are indicative of coarser-grained rocks in comparison with finer grained rocks, which would have lower contrast values. However, the XCT analysis does not standardize the grey levels between different samples and hence the grey levels shown in Figure 4 -A1 are actually stretched in relation to Figures 4 -B1 and 3 -B2. While the statistical differences given in Table I are a true reflection of the differences between the images shown, they are not a true reflection of the differences between the samples because of the lack of standardization between the XCT images. These differences are a true reflection of the differences seen in the grey scale images and hence attest to the robustness and viability of the GLCM in differentiating different mineralogies and textures. Future work should address finding appropriate means for XCT calibration so that image information is directly comparable across rocks with different mineralogies.

Quantification of rock strength

Figure 6 shows examples of the true stress-true strain curves for three pieces of the three samples (A, B, and C). The curves follow the conventional trend for compressive loading, whereby stress increases proportionally with strain until a peak value, beyond which it follows an unsteady decrease. The yield strength is the value at which stress begins to asymptote, representing a transition from elastic (reversible) to plastic (irreversible) deformation. The peak value of stress is known as the ultimate compressive strength (UCS), and represents the maximum stress the sample can resist before macroscopic fracture (Napier-Munn *et al.*, 1996). For sample A, the yield strength is distinct from the UCS, such that some plastic damage takes place prior to complete fracture. For samples B and C, fracture occurs immediately following the point of the initial yield.

Sample A has an average yield strength of 180 MPa, with a standard error of 29.1 MPa at the 95% confidence level. Samples B and C have average values of 104 MPa and 80 MPa, with standard errors of 12.4 and 25.9 MPa respectively. This signifies that sample A has a significantly higher yield strength than samples B and C, which have statistically similar strengths.

The Young's modulus is calculated as the gradient of the stress-strain curve over the elastic interval (King, 2001). This value is an indication of a material's susceptibility to deformation under load, where a higher value indicates a higher resistance to elastic behaviour. The average Young's moduli of the three samples were 60.7 ± 3.2 GPa (sample A), 50.6 ± 2.2 GPa (sample B), and 53.9 ± 1.9 GPa (sample C), with all errors calculated at 95% confidence level. The results indicate that of the three samples, the shale (sample A) deforms the least prior to fracture. Values obtained for the yield stress and Young's moduli were consistent with those reported in prior work on compression tests using these ores (Bbosa, 2007; Hill *et al.*, 2018).

Discussion

A key part of geometallurgy includes small-scale testing to capture the ore properties and define their inherent variability, which can potentially be used in geometallurgical proxies and block models. This becomes important in ore breakage characterization studies, especially when the ore feed to the comminution circuit is variable, as this can cause throughput

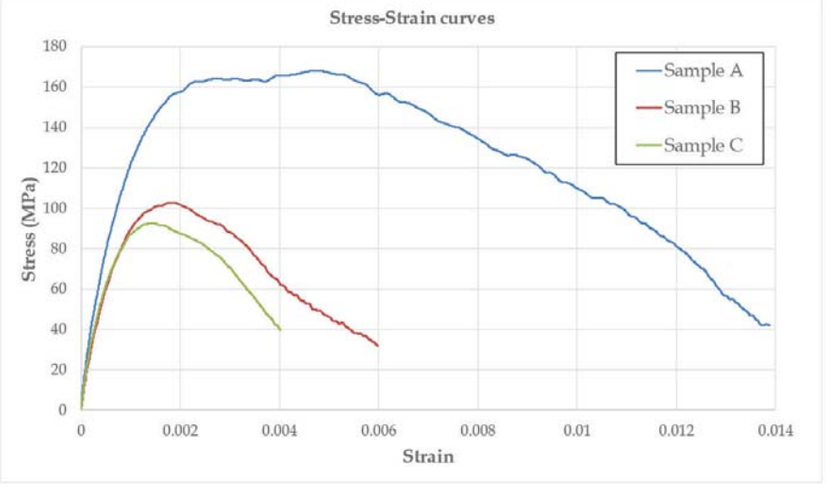

Figure 6—SHPB true stress-true strain curves using one example from each of the mineral texture types, *i.e.* shale (sample A) against the two different polymetallic ore samples (B and C)

fluctuations (Napier-Munn *et al.*, 1996). Through the opportunity that the 3D GLCM and XCT quantification method provides, not only can the textural variation be captured (fine vs. coarse), but also basic mineralogical information. This basic mineral texture capturing has been demonstrated in this study, and the results are as follows.

Sample A is a homogeneous shale consisting predominantly of quartz, feldspar, and micas in a fine-grained matrix. The GLCM heat map distribution confirms the mineralogy and texture through the broad distribution of pixel data in the top left (low-density) quadrant (see Figure 4), which indicates a fine-grained texture dominated by silicates. The GLCM statistics further show a clear trend distinct from the polymetallic ore: sample A has lower values for contrast and correlation, and higher values for energy and homogeneity. Sample A has a yield stress of 180 MPa and has the highest resistance to deformation.

Samples B and C are polymetallic sulphide ores, with a medium-grained matrix dominated by magnetite and quartz. There are subtle differences in their gangue and sulphide mineralogies. Sample B is dominated by pyroxmangite and chalcopyrite, whereas sample C is mostly sphalerite. The GLCM shows narrower distributions for both samples, which also indicates that these samples are more medium-grained in comparison with the finer grained shale. Sample C furthermore show a peak for the sulphides in the bottom right quadrant, indicative of high-density materials (Figure 4 -C3). If sulphides are not present in the grey level image (*e.g.* sample B), the bottom right quadrant will show no information (Figure 4-B3). The GLCM statistics show similar values for these two samples. Both samples B and C have a lower yield strength than the shale.

In this study, the XCT-GLCM method has been applied across two different sample sets to allow the evaluation of the sensitivity of the method to inter-sample variability. The work of Jardine, Becker, and Miller (2018) was limited to samples from a Ni-Cu sulphide ore, and thus did not allow such an evaluation. An important consideration that has emerged through this exercise is that the XCT grey level volumes of samples with very different mineral textures need to be directly comparable with one another, *i.e.* equivalent absolute grey levels will be measured for the same mineral regardless of its mineral matrix. This requires an internal calibration step which is, however, not routine practice in XCT scanning, as evidenced by comparison to the QEMSCAN BSE image (which has a BSE calibration step). Further development should investigate this as a routine step in the application of the method.

A further limitation in this study is the small sample set used. Validation for this work includes QEMSCAN analysis; however, it is not envisaged that the final stages of the 3D mineral texture quantification method will be dependent on QEMSCAN analysis. As demonstrated, the three mineral textural types can be used as building blocks for ongoing research towards the development of a correlation between mineral texture and rock strength using this 3D XCT and GLCM method. Additionally, the GLCM statistical descriptors do show sensitivity to variations in the data-set, and can potentially be used as an indicator of ore variability. Building such basic relationships can improve the management of ore heterogeneity, which is the essence of geometallurgy. Ideally, geometallurgical proxies should be developed and integrated with exploration, where the real need is in core logging systems. Since thousands of metres of core are routinely logged, these proxies can predict processing response months or even years ahead of actual processing. Future work should therefore include incorporating the integral mineral composition and rock strength into potential textural descriptors by continuing testing.

Conclusions and recommendations

Mineral texture is a key parameter in geometallurgy, as is finding appropriate means to quantify it. As part of ongoing research (Becker *et al.*, 2016; Jardine, Becker, and Miller, 2018), this study advances the development of the method for 3D mineral texture quantification by comparing a heterogeneous polymetallic ore with a homogeneous shale. The current method provides a representation of drill core samples and captures the mineral textures through GLCM heat maps and statistical descriptors. The study demonstrated the use of the GLCM statistical descriptors, which potentially capture meaningful information for future quantification, as the complementary 3D GLCM heat map distributions are more graphical outputs. The study also demonstrated that the differences include the capturing of inherent properties, *i.e.* strength. Future work will include not only further testing of the polymetallic ore sample set, but also investigations of the underlying scientific principles of how the 3D quantification method captures the mineral textural variations, and the robustness of the method. The robustness investigation will include testing the quality of the 3D GLCM outputs for different XCT scanning conditions and methods for standardization between different ore types. Additionally, an understanding of the primary factors that contribute to the mineral texture and rock strength relationship is needed.

Acknowledgements

This work is based on research supported in part by the National Research Foundation of South Africa (grant numbers 86054, 99005). Any opinions, findings, and conclusions or recommendations expressed in any publication generated by NRF-supported research are those of the author(s), and the NRF accepts no liability whatsoever in this regard. This work is also supported through the South African Minerals to Metals Research Institute and the Department of Science and Technology. The authors would like to thank Lunga Bam at the Nuclear Energy Corporation South Africa and the rest of the MIXRAD laboratory team for their collaboration in the X-ray computed tomography studies. Gaynor Yorath and the QEMSCAN laboratory team are also acknowledged. Henry Gordon is especially thanked for supplying the appropriate samples.

References

Bam, L.C., Miller, J.A., Becker, M., De Beer, F.C., and Basson, I. 2016. X-ray Computed Tomography: determination of rapid scanning parameters for geometallurgical analysis of iron ore. *Proceedings of the Third AusIMM International Geometallurgy Conference*, Perth, Western Australia, 15–17 June 2016. Australasian Institute of Mining and Metallurgy, Melbourne. pp. 209–220.

Baum, W. 2013. Ore characterization, process mineralogy and lab automation a roadmap for future mining. *Minerals Engineering*, vol. 60. pp. 69–73.

Bbosa, L. 2007. Measurement of impact breakage properties of ore particles using a series of devices. MSc thesis, University of Cape Town.

Becker, M., Jardine, M., Miller, J.A., and Harris, M. 2016. X-ray Computed

Tomography: A geometallurgical tool for 3D textural analysis of drill core? *Proceedings of the Third AusIMM International Geometallurgy Conference*, Perth, Western Australia, 15–17 June 2016 Australasian Institute of Mining and Metallurgy, Melbourne. pp. 15–16.

Craig, J.R. and Vaughan, D.J. 1994. Ore Microscopy and Ore Petrography. 2nd edn. Mineralogical Society of America. http://www.minsocam.org/msa/OpenAccess_publications/Craig_Vaughan/

Evans, C.L., Wightman, E.M., and Yuan, X. 2015. Quantifying mineral grain size distributions for process modelling using X-ray micro-tomography. *Minerals Engineering*, vol. 82. pp. 78–83.

Gaspar, O. and Pinto, A. 1991. The ore textures of the Neves Corvo volcanogenic massive sulphides and their implications for ore beneficiation. *Mineralogical Magazine*, vol. 55. pp. 417–422.

Ghorbani, Y., Becker, M., Petersen, J., Mainza, A.N., and Franzidis, J.P. 2013. Investigation of the effect of mineralogy as rate-limiting factors in large particle leaching. *Minerals Engineering*, vol. 52. pp. 38–51.

Ghorbani, Y., Becker, M., Petersen, J., Morar, S.H., Mainza, A., and Franzidis, J.P. 2011. Use of X-ray computed tomography to investigate crack distribution and mineral dissemination in sphalerite ore particles. *Minerals Engineering*, vol. 24. pp. 1249–1257.

Gottlieb, P., Wilkie, G., Sutherland, D., Ho-Tun, E. Suthers, S., Perera, K., Jenkins, B., Spencer, S., Butcher, A., and Rayner, J. 2000. Using quantitative electron microscopy for process mineralogy applications. *JOM*, vol. 52, no. 4. pp. 24–25.

Govender, R.A., Louca, L.A., Pullen, A., Fallah, A.S., and Nurick, G.N. 2012. Determining the through-thickness properties of thick glass fiber reinforced polymers at high strain rates, *Journal of Composite Materials*, vol. 46. pp. 1219–1228

Haralick, R.M., Shanmugam, K., and Dinstein, I. 1973. Textural features for image classification. *Transactions on Systems and Cybernetics*, vol. 3. pp. 610–621.

Hill, H., Mainza, A., Bbosa, L., and Becker, M. 2018. Comparing the ore breakage characteristics of drill core and crushed ore using the JKRBT. *Proceedings of the XXIX International Mineral Processing Council Conference*, Moscow, 15-21 September.

Howarth, D.F. and Rowland, J.C. 1987. Quantitative assessment of rock texture and correlation with drillability and strength properties. *Rock Mechanics and Rock Engineering*, vol. 20. pp. 61–84.

Jardine, M., Becker, M., and Miller, J. A. 2018. Coupled X-ray computed tomography and grey level co-occurrence matrices as a method for quantification of mineralogy and texture in 3D. *Computers and Geosciences*, vol. 111. pp. 105–117.

King, R.P. 2001. Modeling and Simulation of Mineral Processing Systems. Butterworth-Heinemann.

Little, L., Mainza, A.N., Becker, M., and Wiese, J. 2016. Using mineralogical and particle shape analysis to investigate enhanced mineral liberation through phase boundary fracture. *Powder Technology*, vol. 301. pp. 794–804.

Lotter, N.O. 2011. Modern process mineralogy: An integrated multi-disciplined approach to flowsheeting. *Minerals Engineering*, vol. 24, no. 12. pp. 1229–1237.

Lotter, N.O., Kormos, L.J., Oliveira, J., Fragomeni, D., and Whiteman, E. 2011. Modern process mineralogy: two case studies. *Minerals Engineering*, vol. 24. pp. 638–650.

Lund, C., Lamberg, P., and Lindberg, T. 2013. Practical way to quantify minerals from chemical assays at Malmberget iron ore operations, an important tool for the geometallurgical program. *Minerals Engineering*, vol. 49. pp. 7–16.

Lui, W., Pawlik, M., and Laskowski, J. 2015. The role of colloidal precipitates in the interfacial behaviour of alkyl amines at gas-liquid and gas-liquid-solid interfaces. *Minerals Engineering*, vol. 72. pp. 47–56.

Mariano, R.A. 2016. Measurement and modelling of the liberation and distribution of minerals in comminuted ores. PhD, thesis, University of Queensland.

Maydagan, L., Franchini, M., Impiccini, A., and Lentz, D. 2016. Phyllosilicates geochemistry and distribution in the Altar porphyry Cu-(Au) deposit, Andes Cordillera of San Juan, Argentina: Applications in exploration, geothermometry, and geometallurgy. *Journal of Geochemical Exploration*, vol. 167. pp. 108–109.

McGrath, T.D.H., O'Connor, L., and Eksteen, J.J. 2015. A comparison of 2D and 3D shape characterisations of free gold particles in gravity and flash flotation concentrates. *Minerals Engineering*, vol. 82. pp. 45–53.

Miller, J.D. and Lin, C.L. 2016. Opportunities for plant-site 3D coarse particle characterization with automated high-speed X-ray tomography. *Proceedings of the 2016 SME Annual Conference and Expo: The Future for Mining in a Data-Driven World*, Phoenix, AZ, 21-24 February 2016. pp. 811-814.

Napier-Munn, T.J., Morrell, S., Morrison, R.D., and Kojovic, T. 1996. Mineral Comminution Circuits: their Operation and Optimisation. 6th edn. Julius Kruttschnitt Mineral Research Centre, University of Queensland, Brisbane, Australia.

Nguyen, K. 2013. A new texture analysis technique for geometallurgy. *Proceedings of the Second AusIMM International Geometallurgy Conference*, Brisbane, 30 September - 2 October 2013. Australasian Institute of Mining and Metallurgy, Melbourne. pp. 187–190.

Nwaila, G. 2014. Application of HPGR and X-ray CT to investigate the potential of Witwatersrand gold ore for heap leaching: A process mineralogy approach. MSc thesis, University of Cape Town.

Olsson, W.A. 1974. Grain size dependence of yield stress in marble. *Geophysics*, vol. 79, no. 32. pp. 4859–4861.

Parbhakar-Fox, A.K., Edraki, M., Walters, S., and Bradshaw, D. 2011. Development of a textural index for the prediction of acid rock drainage. *Minerals Engineering*, vol. 24. pp. 1277–1287.

Perez-Barnuevo, L., Lévesquea, S., and Bazin, C. 2018. Automated recognition of drill core textures: A geometallurgical tool for mineral processing prediction. *Minerals Engineering*, vol. 118. pp. 87–96.

Powell, M.S. 2013. Utilising orebody knowledge to improve comminution circuit design and energy utilisation. *Proceedings of the Second AusIMM International Geometallurgy Conference*, Brisbane, 30 September - 2 October 2013. Australasian Institute of Mining and Metallurgy, Melbourne. pp. 27–35.

Schouwstra, R. and Smit, A.J. 2011. Developments of mineralogical techniques. *Minerals Engineering*, vol. 24, no. 12. pp. 1224–1228.

Schouwstra, R., de Vaux, D., Muzondo, T., and Prins, C. 2013. A geometallurgical approach at Anglo American Platinum's Mogalakwena operation. *Proceedings of the Second AusIMM International Geometallurgy Conference*, Brisbane, 30 September - 2 October 2013. Australasian Institute of Mining and Metallurgy, Melbourne. pp. 85–92.

Tavares, L.M. and King, R.P. 1998. Single-particle fracture under impact loading. *Mineral Processing*, vol. 54, no. 1. pp. 1–28.

Tungpalan, K., Manlapig, E., Andrusiewicz, M., Keeney, L., Wightman, E., and Edraki, M. 2015. An integrated approach of predicting metallurgical performance relating to variability in deposit characteristics. *Minerals Engineering*, vol. 71. pp. 49–54.

Vizcarra, T.G., Wightman, E.M., Johnson, N.W., and Manlapig, E.V. 2010. The effect of breakage mechanism on the mineral liberation properties of sulphide ores. *Minerals Engineering*, vol. 23. pp. 374–382.

Vos, F. 2016. The effect of mineral grain textures at particle surfaces on flotation response. PhD thesis, University of Queensland.

Yildirim, B.G., Bradshaw, D., Powell, M., Evans, C., and Clark, A. 2014. Development of an effective and practical Process Alteration Index (PAI) for predicting metallurgical responses of Cu porphyries, *Minerals Engineering*, vol. 69. pp. 91–96. ◆

COUNCIL FOR GEOSCIENCE

April 2019

The Council for Geoscience is the national custodian for the collection and curation of all onshore and offshore geoscience information in South Africa and we aim to use this information to develop geoscience solutions to real-world challenges.

GEOSCIENCE MAPPING
This is our core function and aims to develop geoscience knowledge using an integrated and multidisciplinary approach that merges several onshore and offshore geoscience themes such as Geological, Geotechnical, Geochemical, Geophysical and Seismological Geoscience.

WORLD CLASS FACILITIES
Our work is supported by a lab that performs a wide range of analytical services such as Petrography, Geochemistry, Petrophysics, Coal Science and Hydrochemistry. We also commit to expanding geoscience knowledge and education through a Geoscience Museum and Core Repository.

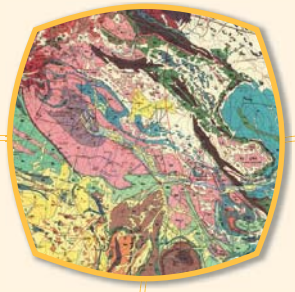

ENGINEERING GEOLOGY AND GEOHAZARDS
We monitor and maintain a Geohazard inventory for South Africa and we aim to use this information toward developing effective and novel Engineering Geology and Geohazard mitigative solutions.

MINERALS AND ENERGY
We aim to generate information and knowledge on mineral and energy resources and their mineralising systems in South Africa, and to use this information to support an increase in sustainable exploration expenditure.

US AT WORK

We are currently undertaking integrated and multidisciplinary geoscience mapping programme across South Africa, some of our recent projects include:

- Regional soil geochemical sampling and detailed follow-up surveys, particularly within the Northern Cape and Mpumalanga provinces.
- Multidisciplinary baseline investigations in the southern Karoo, which uncovered previously undefined and significantly large groundwater aquifers.
- Geothermal and carbon capture and storage research, which aims to expand the current renewable energy mix of South Africa and decrease the carbon footprint.

CONTACT US

Our head office is located at: 280 Pretoria Street, Pretoria, 0184 | @CGS_RSA |
Tel: +27 (0) 841 1911 | Email: info@geoscience.org.za | Web: www.geoscience.org.za

Council for Geoscience

Embracing step-changes in geoscientific information for effective implementation of geometallurgy

R. Lechuti-Tlhalerwa[1], S. Coward[2], and M. Field[3]

Affiliation:
[1]Debswana, Botswana
[2]Interlaced, Australia
[3]Wood Group, United Kingdom

Correspondence to:
S. Coward

Email:
stephen.coward@interlaced consulting.com

Dates:
Received: 15 Jan. 2019
Revised: 12 Mar. 2019
Accepted: 12 Mar. 2019
Published: April 2019

How to cite:
Lechuti-Tlhalerwa, R.[1], Coward, S.[2], and Field, M.[3] Embracing step-changes in geoscientific information for effective implementation of geometallurgy.
The Southern African Insitute of Mining and Metallurgy

DOI ID:
http://dx.doi.org/10.17159/2411-9717/588/2019

ORCiD ID:
https://orchid.org/0000-0002-5187-650

This paper was first presented at the *Geometallurgy Conference 2018 'Back to the Future'*, 7–8 August 2018, Lagoon Beach Conference Venue, Cape Town, South Africa.

Synopsis

Geometallurgy aims to improve mining project value by predicting the impact that ore and waste characteristics will have on mining and metallurgical processes. This requires integration of rich spatial models of orebody characteristics with validated process response models. These models have, until recently, been constrained by the spatial coverage and representativity of relevant data and the ability to validate predictions made.

The revolution in the diversity and volume of data and computational power that is now becoming available for integrated geoscientific modelling of orebodies, and stochastic simulation of mining and mineral processes is accelerating. By embracing emergent integrated data analysis and simulation techniques, geoscientists and engineers can lead a transformation in the way the mining value chain, from orebody to recovery, can be conceived, evaluated, and operated by using the geometallurgical paradigm.

This paper describes a methodology that is applied to an existing diamond operation. Analysis of spatial and process data is used to build an integrated geometallurgical value chain model (IGVCM). This IGVCM is used to generate geometallurgical options and evaluate their potential outcomes. The model facilitates the use of flexible, highly configurable, and potentially automated intelligent approaches to evaluate mining and mineral process configuration, and results in more robust design outcomes. The approach described here, and its successful implementation has potential to deliver step-changes in value.

Keywords
geometallurgy, value chain model, kimberlite processing, ore characteristics, process response.

Introduction

Geometallurgy aims to identify treatability risks – and opportunities – that arise from the interaction of orebody characteristics with mining and treatment. Improved understanding of the rock/process relationships allows project planners and production teams to predict performance, identify potential shortfalls, and thus enable the proactive creation and evaluation of strategies to mitigate these risks. These advanced insights also create opportunities for continually improving operational performance through dynamically adapting and improving the process response to the changing properties of the ore (Figure 1).

The geometallurgical approach to mine optimization aims to improve the operations through a better understanding of the interaction of orebody characteristics with process responses. The value-add from a strategic perspective is the use of this understanding to test and select the most robust mine configuration and improve understanding of the outcomes of high-value irreversible decisions (*e.g.* plant expansion, downsizing, changing mine design, overall design, and operational policy). Strategic use of a geometallurgical framework will increase the probability of making better design and configuration decisions and should result in robust returns, *i.e.* improving stability of financial return in the face of increasingly uncertain futures.

There is also material value-add in the implementation and use of the geometallurgical approach in a tactical framework, for both risk mitigation and operational execution improvement (Wambeke and Benndorf, 2017). This requires the development of several capabilities within the mining organization. These capabilities include the ability to spatially sample and then model the rock characteristics that drive process responses, development of suitable interfaces so that mine planning processes can use these in mine design, and process simulations that respond to the mining inputs to generate predictions of process performance and ore treatability. It is also important to develop a motivated and skilled team that will persistently drive the principles until they become embedded as a way of doing business in the operations. This is a critical success factor.

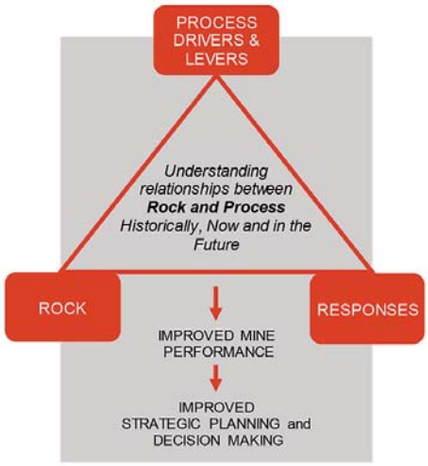

Figure 1—Geometallurgy – finding value by quantifying relationships between rock and process (after Coward *et al*., 2009)

The traditional approach to development of geometallurgical models requires sufficient spatial sampling for ore characteristics that drive process behaviour. These characteristics can be spatially estimated or simulated into a block model. The estimated (or simulated) characteristics of the blocks that are to be mined in each period are used in a dynamic process model (process in the broad sense, including both mining and metallurgical processes) in which the process parameters can be varied in accordance with operational policies and procedures. The virtual models of the process and simulated outcomes can be used to quantify perceived risks, proactively test mitigation strategies, and design plans to benefit from opportunities that are identified or created (*e.g.* choose the best process parameters, reiterate the mine plan, deploy more efficient technology, sample optimization).

Developing the primary response framework for geometallurgy

In an ideal scenario (Ackoff, 1978), the geometallurgical team would be able to readily answer the following questions:

- Which response variables in the mining and treatment processes do we want to model and predict?
- What primary variables drive the response variables, and how must these be measured in the orebody, and at what scale?
- Once we have sampled and measured these variables, how do we estimate their values at unsampled locations?
- Once we have these spatial estimates, how do we build models and simulations that can be used to predict the response variables we want to improve?

Selection of response variables and their geological drivers

The search for the answers to these questions requires an iterative approach to dynamically explore what is desired and what is practically possible. This requires ongoing engagement in a process that requires input from geoscientists and engineers across the structured disciplines that typically characterize the configuration of mining projects and operations. A useful structured approach to the implementation of geometallurgy is provided in Vann *et al.* (2011). This paper addresses what would be considered the transition of geometallurgical capabilities from testing and building models into the use of these models in operational and strategic work flows.

For existing operations, the identification and selection of response variables precedes the design of sampling. This allows the operation to engage in the process and drive the gathering of operating data. Through analysis of performance it is possible to identify which rock characteristics are associated with selected process over- or underperformance. Once the associations have been identified, more experimentation is required to demonstrate causality. This investigation requires analysis of historical data on rock mixes and associated process performance. The characteristics of rock types that shift process performance away from a perceived stable state are tagged and the characteristics of each lithotype are then investigated (*e.g.*, hard or soft ore).

In this process, the analytical geometallurgists will use systems analysis approaches as described by Demming (1986). The availability and use of advanced statistical process control tools in this type of analysis is becoming far more prevalent and hence allows for more meaningful use of historical data.

Design and execution of rock characteristics sampling

Tools and methods used in the descriptive and interpretative process of geological modelling have improved because of the ongoing focus on geometallurgy. The underlying concept of optimizing the sample layout by using a few high-cost samples and then building a calibrated framework to lower cost methods that can increase spatial coverage has been explored by several authors (Esbensen, 1987; Keeney, 2010). The classification, description, and characterization of kimberlite rocks have also improved.

These conceptual frameworks have resulted in improved sample experiment design and increased the number of samples and the metadata that are collected for geometallurgical modelling. The typology is relatively simple and provides a useful framework for interdisciplinary communication. It can be used to develop a programme that aims to achieve a balance between the high cost per sample and low coverage of level 4 data with the lower cost per sample and higher coverage that is associated with collection of level 1 data (Figure 2). This type of trade-off is required for each deposit as the best combinations of number of samples, sample support, and tests carried out. The resulting design will differ between mines, deposits, and lithologies and will require adapting to the level of maturity of the project.

Building spatial models of rock characteristics

To build rich multivariate models of the orebody, optimal use of data generated from a range of samples to predict process responses is required. These models can be used to drive an integrated value-chain model. Linear spatial interpolation estimation techniques, such as linear kriging, can be used to generate minimum error variance, unbiased spatial models of orebody characteristics (Armstrong, 1998). These methods yield estimated values that have less variability than the corresponding actual values. Spatial simulation techniques, such as sequential Gaussian simulation (Dowd and Dare-Bryan, 2007), multivariate co-simulation (Verly, 1993; Boucher and Dimitrakopoulos, 2009; Rondon 2012), and multi-point geostatistics (Ortiz and Deutsch, 2004) can be used to generate spatial models of rock characteristic variables that have a more realistic block-to-block variability.

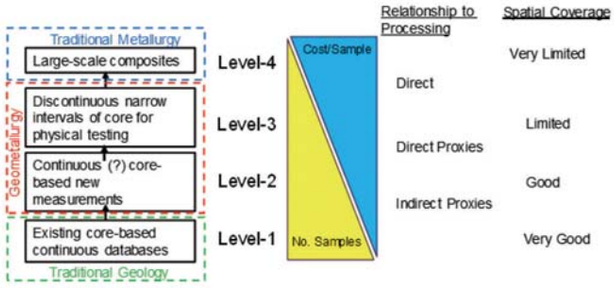

Figure 2—A data typology (after Keeney and Walters, 2008)

The primary response framework suggests that primary variables may in some cases exhibit easy-to-model characteristics, whereas response variables often do not. The response variables are often nonlinear functions of a variety of process inputs and may therefore have non-additive properties. Defining domains for these variables can at times be difficult, though recent research has developed ways to address this concern (Sepulveda *et al.*, 2017).

Developing an integrated value chain model

When an operation has access to an estimated block model of both ore and waste it is possible to overlay a mining plan and generate a rock stream that can be fed to a process simulator to predict process performance. Each of the key processes is modelled using a simplified transfer function to determine the impact that the range of rock characteristics will have on the unit process (Wolf, 2012).

The integrated approach, previously described by Jackson *et al.* (2014), uses block-scale models of the orebody containing both estimated and simulated characteristics. These models are linked to a mining and treatment model. The outputs from the production model are tied to a financial model that facilitates the translation of production outcomes in financial terms.

The benefits of the integrated model are that it can be used to link seemingly different areas of the businesses value chain in a way that reflects the true system constraints and the way in which they interact with variability that originates in the orebody. This approach facilitates an understanding of the system and provides a quantitative evaluation of the impact of variances on the system by explicitly modelling their interaction with real-world constraints (Deming, 1986).

Central to this approach is the integration of complex empirical processing models for *e.g.* crushing (Whitten, 1972), and hydrocyclone separation (Plitt, 1976) with observed process responses. The collection of data over a long period, in the order of five to ten years, enables valid correlations to be identified. These can be evaluated and with additional work, various hypotheses of causation can be tested and rejected or assumed to hold.

Implementation on an operating mine

Setting and methodology

The case review is based on a mine that treats kimberlite sourced from four different pipe-like bodies. The kimberlite comprises several different rock types, as kimberlite is characterized as being a heterogenous rock with a low diamond concentration.

The process plant employs a conventional diamond-winning process that includes crushing, scrubbing, dense media separation, and final recovery using a combination of magnetic and X-ray separation to produce a diamond-rich concentrate.

Although the mine has kept very good records of process performance and mine depletion, there is a complex stockpiling and blending circuit between the mine and the process plant, and the surge capacity both before and inside the processing plant is substantial. This meant that it was not possible to directly relate processed material properties back to *in situ* properties. This required the development of a method to understand the impact of various rock mixes on process performance, and then using this understanding to identify the primary *in situ* properties that were required to be spatially sampled and estimated.

Selection of response variables

The process was usefully divided into seven metallurgical response areas:

1. Mining, blasting, hauling
2. Stockpiling and blending
3. Comminution
4. Dense media separation
5. Undersize, materials handling. and water recovery
6. Magnetic separation
7. X-ray recovery

In consultation with the operation, the objectives of the operational areas were clarified and the rock properties that either hindered or assisted with production were recorded. Detailed monthly data for a period of 10 years was obtained to determine the range and variability of the performance of each of the sections.

Identifying rock characteristics that drive response behaviour

As described above, approximately 60% of treated material is fed to the plant via a stockpile and blending system. It is thus not possible to tie individual process responses back to a single domain or rock type. For each of the seven process response areas, periods where the performance was in the highest or lowest 5th percentile were identified. This was augmented with the use of various statistical process-control techniques (recursive partitioning, cumulative summation charts, v-charts, Manhattan plots *etc.*). The rock mixes that were fed during these periods were identified. The results of 30 rock mixes were then combined and analysed using multidimensional scaling to determine the main groups of rock characteristics that were driving process response. The impact of each of these was then tested by applying the rock mix characteristics in a simple linear model and identifying how well the model predicted actual performance.

Sampling and estimating rock characteristics

As this is a mature operation, several phases of sampling for so-called 'ore dressing studies' (ODS) have been carried out. This sampling has typically been aimed at defining long-term average characteristics, reminiscent of level 4 data. Recently, however, this sampling has been substantially augmented with various proxy measures. This data made it possible to identify approximately 15 rock characteristics that had been measured with sufficient spatial coverage to enable the use of geostatistical estimation. Several of these measured variables had indirect proxies that could be used to expand coverage in the estimate.

An example of this is the estimation of dense media separation yield. Level four sampling typically requires large (approx. 50 kg) samples for a full set of densimetric testing to determine the yield that is expected in the DMS for a given set of operating parameters. It was, however, found that the ore bulk density measures could be used with the full densimetric analysis to expand spatial coverage (Lechuti-Tlhalerwa, 2018).

An important addition to the estimated model was the inclusion of a 'quality indicator index' for each estimated variable. The index was based on several geostatistical estimation quality indicators (*e.g.* kriging variance, distance to nearest sample) and is similar to the processes used for informing the classification of resources and reserves. This index was used in the value chain model to give an indication of the quality of performance forecasts.

The process simulation model

The process model included the mining process, six main stockpiles, and a simplified main treatment plant flow. The distribution of types of material treated during the period under review is depicted in Figure 3.

The data from the mine planning and reconciliation system made it possible to track the material that is delivered to and removed from each stockpile. The properties in each stockpile were averaged every quarter, but the model can be configured in several ways to represent different blending and storage mechanisms (Robinson, 2011). The estimated block-scale rock characteristics delivered to the plant are depicted in Figure 4.

To replicate the flows through the comminution circuit, the material hardness characteristics (UCS, T_{10}, T_a) were used to determine the mass proportion of material that was sent to oversize, grits, and slimes. These characteristics were also used in a simple comminution and screening model (Whiten, 1972) to simulate the operation of the crushing section and predict the mass and size distribution of the feed to the DMS circuit.

The DMS dynamic model was configured to respond to the estimates of proportion of each density class in each size class for the ore block that is treated.

$$Tons\ yield = \sum_{i=1}^{ndc} \sum_{j=1}^{nsc} \sum_{k=1}^{nrc} T_{di}\ x\ T_{sj}\ x\ P_{rk} \quad [1]$$

Equation [1] gives the formula used to calculate the mass of material that is expected to report to the sink fraction, where:

T_{di} = Tons in density class n
T_{sj} = Tons in size class n
P_{rk} = Tons recovery proportion of size/density class k.

In the implementation, the proportion to sinks assumes a constant partition curve that incorporates a fraction of the less dense material that is the same for all periods. It would be possible in further iterations to include a rock type and cyclone configuration dependency in this model (Plitt, 1976). The specific partition curve used in this case is depicted in Figure 5. It would be possible to use historically recorded partition curves informed by regular tracer testing that has been carried out. Historical work has been conducted to develop and test several simulators, and the data and models developed during these prior programmes could be readily used to develop more robust models in this case.

Value chain model results

At this early stage, the correspondence between the outputs of the model and the recorded historical data is encouraging. The proportion of material that reports to the DMS is depicted in Figure 6.

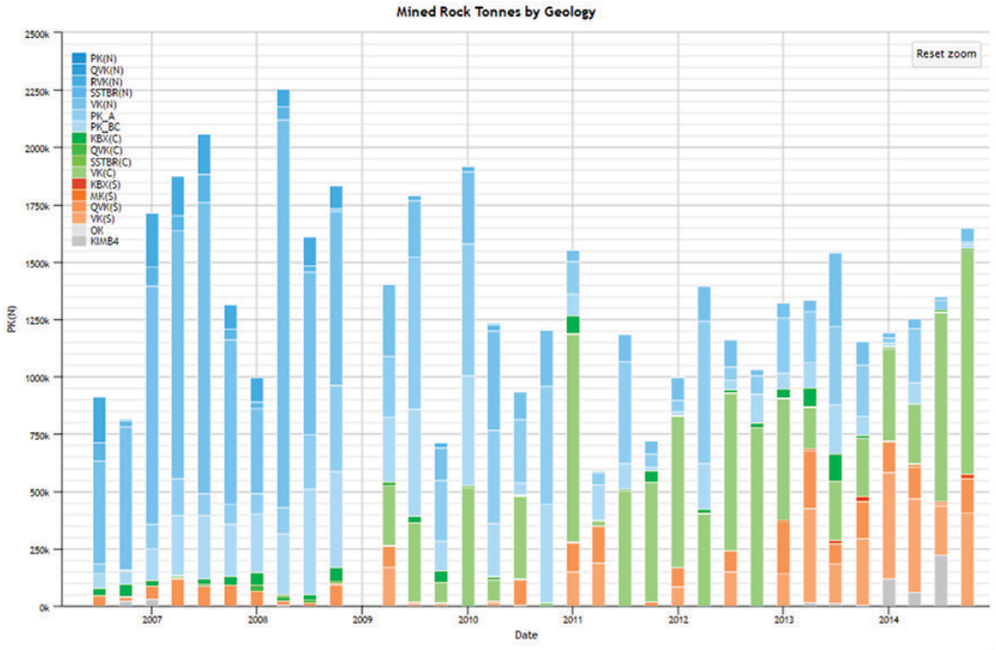

Figure 3—Stacked bar chart depicting rock mix mined. Shades of blue represent pipe 1 material types, shades of green represent pipe 2, and shades of brown represent pipe 3 material

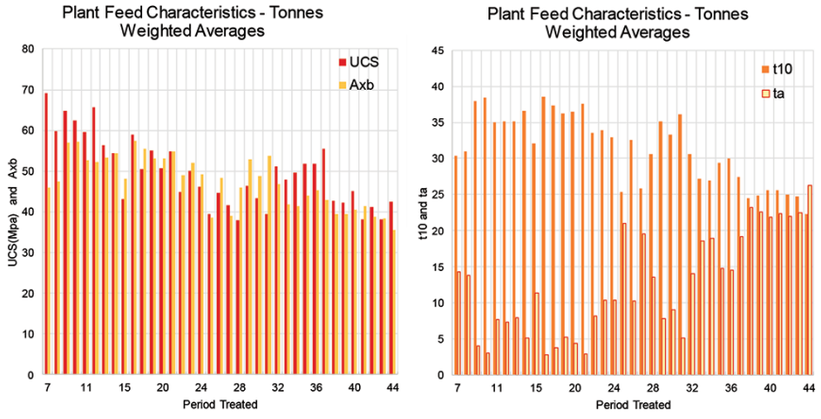

Figure 4—Plot of rock characteristics in the feed to the plant based on the actual mine depletions provided

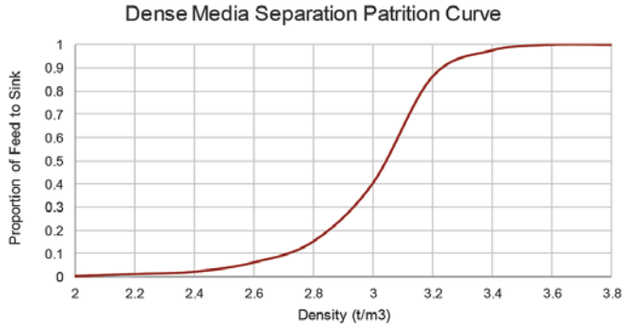

Figure 5—DMS partition curve used to determine sink fraction from blocks treated

The DMS partition model is applied at block scale and the results of the derived DMS concentrate produced are depicted in Figure 7. Although the model underestimates yield in the first few years of the period reviewed, there is good correspondence in the later years.

This process response prediction is based on a relatively smoothed kriged estimate of characteristics based on a few sparse samples. This demonstration model shows that there is indeed sufficient information available to begin building spatial models of geometallurgical characteristics at block scale and that the block-scale estimates can be used in a process simulator to forecast, albeit with some degree of error, the full-scale process plant performance.

It is also evident when calibrating this model that the modes of operation before and after 2009 are markedly different. This suggests that not only should the model be able to reflect the operation of the plant while in a tonnage-constrained mode, but it should also include measures that reflect the changes in efficiency that are achieved (or not) when the plant is run at a lower throughput and hence is responding to different sets of constraints.

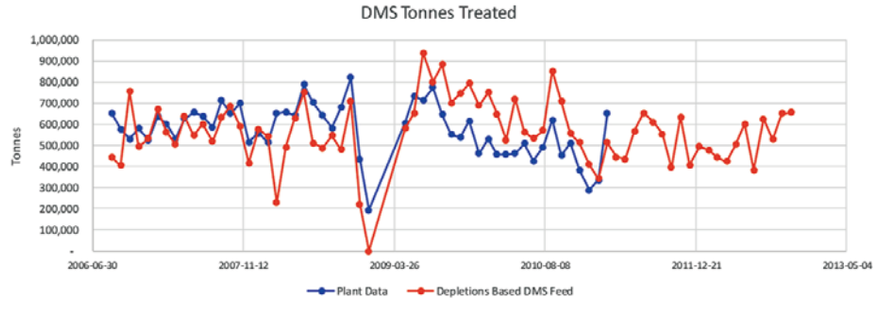

Figure 6—DMS feed comparison between the dynamic value-chain model and historical plant performance data

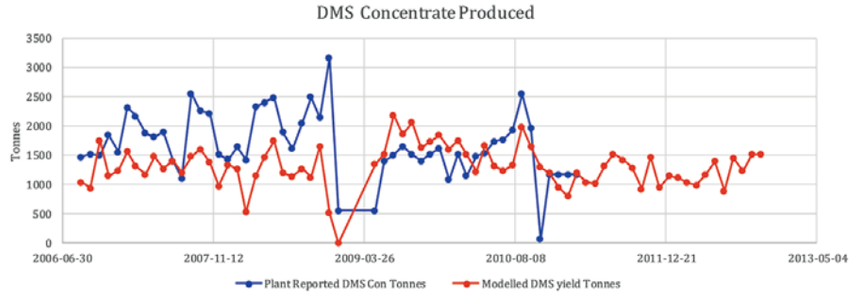

Figure 7—DMS concentrate comparison between the dynamic value-chain model and historic plant performance data

Discussion and interpretation

The geometallurgical modelling process (variable selection, spatial modelling, and process simulation) has shown that it is possible to predict the future performance of the selected unit processes based on models developed from a historical analysis of the relationships between characteristics of the kimberlite that was treated and observed process response.

The next phase of this project aims to use the mine plan for the next 5–10 years with the existing geometallurgical model to predict the average, or estimated, rock characteristics that will be treated by the plant, and its resulting performance. This process will identify which periods will require either changes to the plan or adaption in the process plant to achieve the desired targets.

A second, more challenging but potentially more rewarding, focus is the inclusion of spatial simulations of the orebody characteristics to enable a range analysis to be undertaken. This will provide the mine with a method to understand the impact of extremes in the rock characteristics on overall process performance and quantify the downside and upside of the chosen plan and process configuration.

The feedback loop analysis suggests that as the collection of data of the processed properties improves, so will the models, and hence the ability to move up the 'geomet curve' (Vann *et al.*, 2011) to the next phase, which will see the embedding of the geometallurgical model in mine planning and operational optimization.

Conclusion

The structure and approach to data collection, storage, and interrogation is adapting rapidly (*e.g.*, Internet of Things, Industry Four, Cloud Processing Arbitrage). The three main driving forces are:

1. The development of cheaper, faster, more 'intelligent' sensors with improved granularity that can pre-process data
2. Vast increases in machine and sensor connectivity and networking
3. Ongoing increases in processing speed, and ease of access to transient computing power with a parallel reduction in processing cost.

The implications for geometallurgy are profound. At a strategic level there needs to be focus placed on improving the use of rich, quantitative orebody models, and integration of the approach into the business operating framework. At a tactical level, this urges operations to embrace technically advanced predictive models in both short-term and longer-term capital rationing decision-making (Dowd, 2016).

One way to improve the use of richer geometallurgical models requires an integrated evaluation of the entire value chain design to incorporate explicitly the impact of orebody characteristics across the mining project. Such a platform provides the basis for empirically testing design and operating decisions. This allows project teams to assign financial benefit to increasing geometallurgical insight and to extract additional value from mining projects. The simplest approach is to use spatial models of primary variables that can be converted through transfer functions to process responses, as demonstrated here. Deriving these functions requires simplification of process simulations that emulate the dynamics of inter-block interactions and system interdependencies.

A broad view of geometallurgy suggests that an improved quantitative understanding of the relationships between rock characteristics and the performance of processes used to mine and treat the ore should lead to mining projects that are more successful. The benefits potentially include a more robust return to all stakeholders for a longer period, with mining projects demonstrating resilience in the face of ubiquitous, rapidly changing operating environments.

References

Ackoff, R.L. and Ackoff, K.B. 1978. The Art of Problem Solving Accompanied by Ackoff's Fables. 2nd edn. Wiley, New York.

Armstrong, M. and Myers, D.E. 1998. Basic Linear Geostatistics, Technometrics. doi: 10.2307/1270968

Boucher, A. and Dimitrakopoulos, R. 2009. Block simulation of multiple correlated variables. *Mathematical Geosciences*, vol. 41, no. 2. pp. 215–237. doi: 10.1007/s11004-008-9178-0

Coward, S., Vann, J., Dunham, S., and Stewart, M. 2009. The primary-response framework for geometallurgical variables. *Proceedings of the 7th International Mining Geology Conference*. Dominy, S. (ed.). Australasian Institute of Mining and Metalliurgy, Melbourne. pp. 109–114.

Deming, E. 1986. Out of the Crisis. MIT Press, Cambridge, Massachusetts.

Dowd, P.A. and Dare-Bryan, P.C. 2007. Planning, designing and optimising production using geostatistical simulation. *Orebody Modelling and Strategic Mine Planning*. 2nd edn. Dimitrakopoulos, R. (ed.). *Spectrum Series* 14. Australasian Institute of Mining and Metallurgy, Melbourne. pp. 363–377. https://www.scopus.com/inward/record.uri?eid=2-s2.0-58049141125&partnerID=40&md5=2901d5c3030cf9ca31dfb82051286163

Dowd, P.A., Xu, C., and Coward, S. 2016. Strategic mine planning and design: Some challenges and strategies for addressing them. *Transactions of the Institution of Mining and Metallurgy, Section A: Mining Technology*, vol. 125, no. 1. pp. 22–34.

Esbensen, K., Lindqvist, L., Lundholm, I., Nisca, D., and Wold, S. 1987. Multivariate modelling of geochemical and geophysical exploration data. *Chemometrics and Intelligent Laboratory Systems*, vol. 2, no. 1–3. pp. 161–175. doi: 10.1016/0169-7439(87)80094-1

Jackson, S., Vann, J.E., Coward, S., and Moayer, S. 2014. Scenario-based project evaluation – full mineral value chain stochastic simulation to evaluate development and operational alternatives. *Proceedings of the Ninth International Mining Geology Conference*, Adelaide, South Australia, 18-20 August 2014. Australasian Institute of Mining and Metalliurgy, Melbourne. pp. 18–20.

Keeney, L. 2010. The development of a novel method for integrating geometallurgical mapping and orebody modelling. Julius Kruttschnitt Mineral Research Centre, University of Queensland.

Lechuti-Tlhalerwa, R., Gilika, O., and Field, M. 2018. Modelling geometallurgical variability in Orapa kimberlite ore. *Proceedings of Geometallurgy 2018. Southern African Institute of Mining and Metallurgy*, Johannesburg.

Oakland, J.S. 2008. Statistical Process Control. Elsevier Butterworth-Heinemann.

Ortiz, J.M. and Deutsch, C.V. 2004. Indicator simulation accounting for multiple-point statistics. *Mathematical Geology*, vol. 36, no. 5. pp. 545–565. doi: 10.1023/B:MATG.0000037736.00489.b5

Plitt, L.R. 1976. A mathematical model of the hydro-cyclone classifier. *CIM Bulletin Mineral Processing*, vol. 69 (December). pp. 114–123.

Robinson, G.K. 2011. Managing variation of bulk materials in stockpiles and mineral processing plants. *Design and Selection of Bulk Material Handling Equipment and Systems: Mining, Mineral Processing, Port, Plant and Excavation Engineering*. Bhattacharya, J. (ed.). Wide Publishing, Kolkata, India. pp. 365–413.

Rondon, O. 2012. Teaching aid: minimum/maximum autocorrelation factors for joint simulation of attributes. *Mathematical Geosciences*, vol. 44, no. 4. pp. 469–504.

Sepulveda, E., Dowd, P.A., Xu, C., and Addo, E. 2017. Multivariate modelling of geometallurgical variables by projection pursuit. *Mathematical Geosciences*, vol. 49, no. 1. pp. 121–143. doi: 10.1007/s11004-016-9660-z

Vann, J., Jackson, J., Coward, S.J., and Dunham, S. 2011. The geomet curve – a model for implementation of geometallurgy. *Proceedings of the First AusIMM International Geometallurgy Conference (GeoMet 2011)*, Brisbane. Australasian Institute of Mining and Metalliurgy, Melbourne. pp. 35–43.

Verly, G.W. 1993. Sequential Gaussian co-simulation: a simulation method integrating several types of information. *Proceedings of Geostatistics Tróia '92. Vol 5. Quantitative Geology and Geostatistics*. Soares A. (ed.). Springer, Dordrecht. pp. 543–554. https://doi.org/10.1007/978-94-011-1739-5_42

Wambeke, T. and Benndorf, J. 2017. A simulation-based geostatistical approach to real-time reconciliation of the grade control model. *Mathematical Geosciences*, vol. 49, no. 1. pp. 1–37. doi: 10.1007/s11004-016-9658-6

Whiten, W.J. 1972. The simulation of crushing plants with models developed using multiple spline regression. *Proceedings of the Tenth International Symposium on the Application of Computer Methods in the Minerals Industry*, Johannesburg, 10–14th April 1972. Southern African Institute of Mining and Metallurgy, Johannesburg. pp. 257–264. ◆

Key aspects of bench flotation as a geometallurgical characterization tool

V. Ross[1,2]

Affiliation:
[1]Mintek, Randburg, South Africa
[2]University of the Witwatersrand, Johannesburg, South Africa

Correspondence to:
V. Ross

Email:
VictorR@mintek.co.za

Dates:
Received: 16 Jan. 2019
Revised: N/A
Accepted: 26 Mar. 2019
Published: Alpril

How to cite:
Ross, V.
Key aspects of bench flotation as a geometallurgical characterization tool.
The Southern African Insitute of Mining and Metallurgy

DOI ID:
http://dx.doi.org/10.17159/2411-9717/605/2019

ORCiD ID:
https://orchid.org/0000-0003-4867-6248

This paper was first presented at the *Geometallurgy Conference 2018 'Back to the Future'*, 7–8 August 2018, Lagoon Beach Conference Venue, Cape Town, South Africa.

Synopsis

Bench-scale flotation tests play a major role in the geometallurgical process value chain. Despite their apparent simplicity, these tests pose pitfalls in terms of operation, as well as the interpretation and modelling of results. In this paper we highlight key aspects to consider in generating accurate and reproducible experimental results, and critically review some assumptions relating to the estimation of entrainment and froth recovery. We subsequently focus on first-order equations to model kinetics and propose a method that accounts more realistically for the decay in kinetics over the duration of a float, and the contributions of froth stability and hence mass pull. The method was applied to three case studies on platinum group metal (PGM) ores and matched or outperformed first-order, two-component models. Also, it allows for a deeper analysis of the integrity of the bench-scale flotation results.

Keywords
flotation kinetics, modelling, froth stability, mass pull.

Introduction

Geometallurgy is a structured, multidisciplinary approach that integrates key data from the geological, mining, mineralogical, and metallurgical aspects of the value chain to construct spatial models of an ore deposit such that the overall economic benefit and sustainability of an operation can be optimized. Process geometallurgy is aimed primarily at enhancing metallurgical efficiency and plant throughput by the application of appropriate mining and processing strategies, as well as supporting production planning and operational strategies to reduce the impact of highly variable ores. With flotation being the dominant concentrating process in the mineral value chain, the bench-scale flotation test is an important characterization tool – a relatively cheap, simple, and rapid way to obtain key information about the ore and its amenability to economic extraction of valuable minerals. This includes the evaluation of different ore types and the implications of mineralogical composition and texture for comminution and floatability, the effect of the grinding environment on the liberation of minerals, the electrochemical environment in the pulp (Bradshaw *et al.*, 2006), the screening of reagents to improve floatability (Ekmekçi *et al.*, 2003), and the role of hydrodynamics in the recovery of valuables and the entrainment of gangue (Amini *et al.*, 2016; Wang *et al.*, 2016). It is also a critical tool in auditing the performance of a flotation plant by hot floats, paving the way for concept and feasibility studies and providing essential data on kinetics for the purposes of scale-up, optimization, and simulation of flotation circuits.

Bench test best practice

While it appears to be a reasonably straightforward procedure, bench testing poses pitfalls that can result in unacceptable repeatability, misleading results, and hence costly mistakes when the findings are applied at plant level. As explained succinctly by Lotter, Whiteman, and Bradshaw (2014), a flotation test programme should produce 'clear, unambiguous results … that are significant, cogent, reproducible, and have a good probability of successful scale-up'. In support of these fundamental principles, Table I lists a collection of best practices to be considered in laboratory bench test campaigns.

Interpretation

In the interpretation and modelling of bench flotation results for scale-up to pilot and commercial applications, two factors are of notable relevance, *viz.* the froth recovery and the contribution of entrainment to total recovery. Both these factors involve considerable effort and time to establish experimentally and a pertinent question is thus to what extent this could, or should, form part of a geometallurgical study.

Table I

Key bench flotation best practices

Feed properties
Use samples, and not specimens – sampling and blending procedures are of crucial importance (Lotter, Whiteman, and Bradshaw, 2014) PSD to match that of target ore and thus liberation profile, not only with respect to % passing (Runge, Tabosa, and Jankovic, 2013) Rougher feed pulp normally at 30–35% solids by mass, but depends on specific ore
Types of cell
Denver D-12 – flexible, reliable, easy to operate. Only drawback is the central standpipe (impedes scraping) Transparent plexiglass construction to observe solids suspension, froth depth, and stability of interface Bottom-driven cell preferred for reproducibility and accuracy; difficult to clean out, stator to be removable
Chemical environment
Filtered or synthetic plant water (Corin *et al*., 2011) rather than tap water for making up slurry Measure pulp potential (Eh), pH to establish propensity of certain species to form (Buswell *et al*.., 2002)
Aeration and agitation
Compressed air and rotameter rather than self-induced air (which varies with impeller speed) Superficial gas velocities typically from 0.6 to 1 cm/s Agitation adequate to suspend all solids but not disrupt pulp-froth interface Cleaners run at lower impeller speeds than roughers Use tangential tip speed (m/s) rather than r/min as descriptor. Bench scale typically approx. 4 m/s, industry 6–7 m/s (Deglon, Egey-Mensah, and Franzidis, 2000)
Froth depth
Froth surface to be maximum level without concentrate overflowing the lip Froth depth to be recorded throughout as proxy for changes in froth stability
Scraping rate, depth
Industry applications range from 1 to 15 seconds, scraping rate affects froth recovery (Amelunxen *et al*.., 2014) Scrape to 1 cm below concentrate lip only, scraper vertical /inclined back for optimum froth collection
Duration, reproducibility
Time $t = 0$ taken as first scrape being one scrape interval (e.g., 15 seconds) into the float, rather than the moment air is turned on; reduce duration of first concentrate interval accordingly Float for sufficient time to capture slow-floating kinetics, thus to extend well past inflection point and at least five data-points (successive intervals doubling in duration) Three replicate tests where possible; check reproducibility on wet and dry masses before combining concentrates

Froth recovery

Froth recovery (*Rf*) is defined as the fraction of floated material that enters the froth attached to bubbles and is transported into the concentrate. The relevance of *Rf* is in deriving suitable scale-up parameters for converting bench batch data into plant prediction, based on the assumption that the pulp kinetics in the bench test represents that of the plant-scale equivalent. *Rf* is also used in research studies that seek to decouple the flotation rate constant into its key components, such as, for example, work in the AMIRA P9 programme (Amini, Bradshaw, and Xie, 2016).

A common assumption in bench tests is that the froth recovery is 100%, the main reasoning behind this being the notion that because the froth is comparatively shallow and being scraped, all floating material is being recovered. Amelunxen *et al.*, (2014), however, in a series of bench tests on a sulphide ore, showed conclusively that in a typical test, the figure is closer to 30 to 40% only. This finding can be substantiated by considering, for example, a laboratory flotation cell at a typical superficial gas velocity (*Jg*) of 1 cm/s and froth being scraped every 15 seconds to a depth of 1.5 cm. The froth therefore is replenished to its full height in approximately 1.5 seconds after the scrape and for the 13-odd seconds until the next scrape, floatable material is thus entering that top layer of the froth. Since the recovery of air, *Rg*, towards the end of a test approaches zero as bubbles burst at the froth surface and are not recovered into the concentrate, a portion of the attached particles will start dropping back in the froth. It follows that, unless they all re-attach to bubbles in the froth and remain in the top layer, froth recovery will be less than 100%. In the case of there being no such accumulation, *Rf* amounts to a mere 1.5/15, or 10%. For *Rf* to approach 100%, the scraping interval under these conditions should be less than 1.5 seconds, as also suggested by the data of Amelunxen *et al.*, (2014).

Another key aspect, but one that is rarely considered in assessing *Rf* at bench scale, is the systematic decay in the froth stability as the float progresses, due to the depletion of the pulp in floatable material. The bubbles therefore coalesce more readily, and the ability of the froth to retain floatable material drops accordingly. This results in an increased proportion of the floated material not reaching the top layer in the first instance, further reducing *Rf* and therefore the overall rate of flotation. Finally, a factor that should also be taken cognisance of in modelling and scale-up exercises is that froth recovery is also dependent on particle size, the finer fractions being recovered to the concentrate more readily than coarser particles (Rahman, Ata, and Jameson, 2012).

Entrainment

An estimation of the contribution of entrainment to the total recovery of valuable mineral and gangue is often required in studies on froth mechanisms where the extent of true flotation needs to be quantified, but this is also sometimes incorporated in tests aimed at plant auditing and scale-up. The dominant mechanism of entrainment is by the hydraulic transport of particles in the wake of bubbles and into the froth across the pulp-froth interface. Several factors affect entrainment, major ones being the size and density distributions of particles in the

pulp (Wang *et al.*, 2016), their concentration below the interface, the stability and depth of the froth, as well as the cell design and operation in terms of concentrate lip length and agitation.

Over the years, several angles have been explored at bench scale to better quantify entrainment, most of which involve the relationship between the recovery to the concentrate of water and that of particles. These vary from comparisons of recoveries through experimental design, the development of empirical relationships, or the use of hydrophilic, non-floatable gangue as tracer or proxy for entrainment (*e.g.*, Wang *et al.*, 2016). These tracer tests are normally done with pure minerals in the absence of floatable material – and therefore the absence of a stable froth – and the extent to which the froth stability affects the degree of entrainment is thus not readily determinable. In this regard, the spiking of an ore with hydrophilic, uniquely identifiable material and inferring the entrainment behaviour of the ore itself from the relative particle sizes and densities is recommended.

From a geometallurgical perspective, however, the above techniques are time-consuming and can be relatively costly, and do not lend themselves readily to producing adequate information when limited sample is available. In this regard, the use of a parameter Cfi that expresses the classification between solids in species i and water across the froth has found use (Johnson, 2005); for ultrafine particles, Cfi approaches unity, and zero for coarse particles. The mass flow rate $Ment,i$ of species i into the concentrate due to entrainment can thus be expressed as

$$Ment,i = Cfi \cdot \varphi i \cdot Mw \quad [1]$$

where φi is the solids/water mass ratio in the pulp just below the pulp-froth interface (since the pulp phase is well mixed in a bench cell, it can reasonably be assumed to refer to the entire pulp volume) and Mw is the mass flow rate of water into the concentrate. The product $Cfi^{*}\varphi i$ is commonly referred to as $ENTi$, or the degree of entrainment for species i. The value of Cfi is estimated from experimentally derived data for a given ore and corrected for density, or by plotting Cfi against flotation time and assuming that the predominant mechanism of recovery towards the end of a flotation test is entrainment. An important point to note in this approach is that entrainment is largely independent (or so it is assumed) of the surface properties of particles, and hence their grade. The value of Cfi is therefore to be expressed in terms of the mass ratios of solids and water rather than the grade ratios of a valuable species, as it refers to the entrainability of solids, and not floatability.

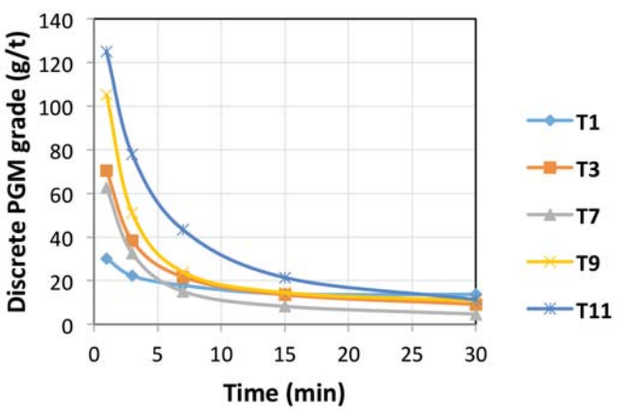

Figure 1—Changes in the discrete grade of the concentrate over the course of bench flotation tests on a UG2 PGM ore at 75% –75 µm

The assumption of entrainment being the predominant contribution to recovery towards the end of the test is, however, one that requires careful analysis. As shown for example in Figure 1 for a range of tests on an Upper Group 2 (UG2) PGM ore ground to 75% –75 µm, the discrete concentrate grade decreases consistently over the course of the float and flattens out with the final samples averaging between 5 and 15 g/t, the corresponding tailings grades varying from 0.6 to 0.9 g/t only. It is thus clear that even after 30 minutes of flotation, a fair quantity of slow-floating material was still being extracted into the concentrate, strongly challenging the validity of the above assumption.

The second point to be considered is the assumption that Cf is independent of flotation time, *i.e.*, that the classification occurring across the pulp-froth interface and in the froth towards the end of the float is representative of the rest of the test. This is debatable to the extent that it, for instance, does not account for the decay in the stability of the froth as the pulp is being depleted of particles of various sizes and densities at different rates during the test, resulting for instance in especially coarser particles being less likely to be entrained in an unstable froth towards the end of the test.

The above observations suggest a need for approaches to better account for the contribution of entrainment, and especially to reduce the additional effort and cost. It is the opinion of the author that this would best be pursued in academic studies focusing on a better understanding of the underlying mechanisms. There appears to be ample scope for simplifying laboratory procedures or developing more sophisticated proxies that can provide fast and reliable indicators of entrainment. In the next section of the paper, which deals with the interpretation and modelling of bench flotation kinetic data, the contribution of entrainment is thus not separately accounted for.

Modelling of kinetics

A variety of models have been developed over the years to analyse flotation kinetics, being derived from chemical reaction kinetics theory and assuming different orders of reaction, distributions of rate constants, and ultimate recovery (Alvarez-Silva *et al.*, 2016; Ramlall and Loveday, 2015; Bu *et al.*, 2017). Despite the substantial research on different ores and experimental conditions, currently there does not seem to be a 'one-model-fits-all' solution. Arising from this is the drawback that the use of a specific model for a data-set invariably locks the analysis into the model framework and does not provide a means for relating the analysis with those of other fitted data-sets. Also crucial to the debate is the number of model parameters and the accuracy that they provide, as well as their physical significance and implications for scale-up.

Bench flotation kinetic data is modelled mostly by using different versions of a first-order rate equation, a preferred approach to account for the fact that not all valuable material is recoverable, mainly due to a certain portion of valuable mineral being locked within (usually, coarser) gangue particles which cannot float, and which are also unlikely to be recovered by entrainment (Zhang and Subasinghe, 2016). The first-order flotation rate equation thus takes the form

$$Ri(t) = Rmax,i\,[1 - \exp(-Ki.t)] \quad [2]$$

where $Ri(t)$ is the recovery of species i after flotation time t, $Rmax,i$ is the maximum attainable recovery, and Ki the flotation rate constant (min^{-1}). $Rmax$ is a fitted value suggested by the

shape of the kinetics curve up to the end of the test and thus has little practical bearing, although introducing the important concept of less than 100% recovery. The overall rate constant *K* lumps together a host of factors, including the degree to which the valuable component is liberated and thus floatable, the hydrodynamics of the cell (the degree of agitation, aeration rate, bubble size, surface area flux, energy dissipation *etc.*), the effect of the electrochemical environment on floatability (Eh, reagent dosage, ionic strength), and all the parameters impacting on froth stability, residence time, and froth recovery. The AMIRA P9 programme decouples it into the following key drivers:

$$Ki = Pi.Sb.Rf.æ.EFV \quad [3]$$

which incorporates the key effects above, including floatability (*Pi*), bubble surface area flux (*Sb*), froth recovery (*Rfi*), and recently, the addition of turbulent kinetic energy (denoted by the term *æ.EVF*, the latter representing the 'efficient volume for flotation') (Amini, Bradshaw, and Xie, 2016). Typically, an overall *K* for each valuable component in the ore and gangue is established by a least-squares regression on experimental recovery data (the regression minimizing the sum of squared residuals), and only in detailed research studies are the feed and various products analysed in terms of discrete particle size fractions or floatability classes, due to this being a laborious, complex, and costly route with difficult-to-reconcile mass balances due to errors in sizing and assaying.

Due to the inherent limitations of the single-component model when applied to the overall flotation response, which is characterized by a distribution of rate constants, the use of one of two variants of the two-component Kelsall model has become the platform for a variety of research studies. These models account for a 'fast-floating' and a 'slow-floating' fraction of the valuable component(s) as well as for the gangue, the classic version being based on an assumed *Rmax* of 100% and in the modified version, *Rmax* <100% due to the mineralogical constraints discussed above. Equation [2] thus extends to the form

$$R(t) = Rmax\,[Qf * (1 - \exp(-Kf*t)) + (1 - Qf) * (1 - \exp(-Ks*t))] \quad [4]$$

where *Qf* is the fraction of fast-floating material, *Kf* is the rate constant of the fast-floating fraction, and *Ks* that of the slow-floating fraction. Later versions even discretize the floating component into three fractions, *viz.* 'fast', 'medium', and 'slow'. Interestingly, Hay and Rule (2003) make specific mention of the fact that the classic Kelsall (or Jowett) equation was chosen as basis for their kinetic modelling and simulation, seemingly specifically due to it not involving the concept of *Rmax*. While the reasoning for this is not clear (apart perhaps from the model having fewer variables), the concept of infinite flotation time is in our opinion not the issue at stake, but rather the fact that *Rmax* is an important metallurgical concept and indicator, especially regarding the fineness of grind and thus the liberation of the valuable mineral.

While both versions of the model are simple to use and the modified (four-parameter) version in particular provides accurate fits of experimental data, it remains somewhat of a 'number-crunching' exercise in which the 'fast-floating' rate constant is, for instance, often inflated strongly in model fitting to straighten the kinetics curve during the early stages of flotation. In construct it not only bears only a distant resemblance to reality, where a flotation feed presents not one or two, but a distribution of floatability classes due to the confluence of particle size and liberation classes, but can also turn the interpretation into a daunting task.

Novel approach

The above context prompted us to investigate an alternative approach to more reliably benchmark different ores, also as far as the principles and requirements for geometallurgical classification are concerned. One challenge was to negate the obstacles posed by individual models and rather present a metallurgically more representative view of the process kinetics. For example, instead of the over-simplification of a single component or two components only in the feed that float at the same respective rates for the duration of the experiment, we chose to reflect the changes in the rate of flotation as the cumulative result of a multitude of floatability components and also the mass pull. To simplify the practical implementation, the approach also combines the contributions of flotation and entrainment.

The approach is based on the principle that, for each successive concentrate interval *j*, the maximum obtainable recovery *Rmax,j* reduces according to what has been recovered cumulatively by the end of the previous interval. For interval j:

$$Rmax(j) = Rmax - R(j\text{-}1) \quad [5]$$

where *Rmax(j)* is the residual maximum recovery after interval *j*. Assuming first-order kinetics of the material remaining within each interval, the overall rate of recovery *K(j)* is thus:

$$K(j) = -\ln(1 - R'(j)/Rmax(j)) / (t(j) - t(j-1)) \quad [6]$$

where *R'(j)* is the discrete recovery in interval *j, i.e.*

$$R'(j) = R(j) - R(j\text{-}1) \quad [7]$$

Due to the continued depletion of the faster-floating material in the pulp over the course of the test, the kinetics should always display a consistent decay with time, similar to the mass pull. A significant body of research and operational evidence points to the fact that the rate of flotation is a function not only of the floatability distribution, but also the froth stability and hence the mass pull *MP(t)* at any point in the float, and a relationship between the rate of flotation and mass pull such as the one depicted in Figure 2 (Set 1) should therefore be evident. This relationship can be approximated by the following equation:

$$K(t) = KO*\exp(-b*t) + Kmp*MP(t) \quad [8]$$

where *KO* denotes the initial rate of flotation, *b* expresses the rate at which the kinetics are decreasing with the float, and *Kmp* is

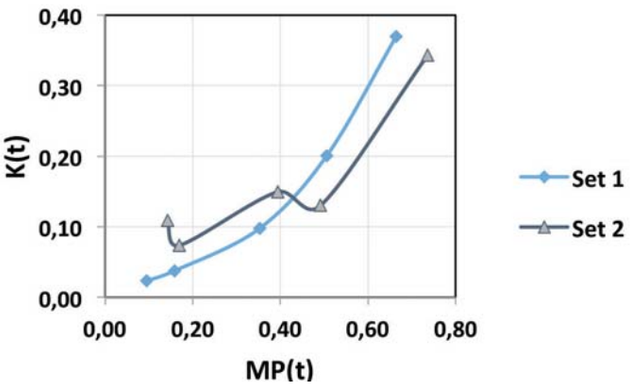

Figure 2 – Relationship between *K(t)* and *MP(t)* for two bench kinetic floats

a coefficient that relates the kinetics to the discrete rate of mass pull *MP(t)* (%/s) within each concentrate interval. The equation is applied to each interval successively to reflect the cumulative overall kinetic response.

An added potential benefit of this method is that it could also enable an initial analysis of the accuracy of bench flotation data, such as identifying deviations from the asymptotic *K(t) vs MP(t)* relationship caused, for instance, by inconsistent operating procedures or incorrect assays or mass recovery measurements. Such an example is shown in Figure 2 (Set 2), where the first-order rate of flotation increased in intervals 3 and 5 over that in intervals 2 and 4 respectively, for the particular *Rmax* (the time axis in this case running from right to left, interval 1 represented by the maximum *K(t)–MP(t)* coordinate). This could, for instance, be the result of a change in operating conditions such as a shallower froth or the operator scraping more deeply into the froth, resulting in faster apparent kinetics, or an over-assay of the concentrates. Further investigation is under way to understand these aspects in more detail; worth noting, however, is that while a kinetic model such as Equation [4] would still be able to fit the recovery kinetics reasonably well under these circumstances, it would not highlight the suspected anomaly in the recovery–mass pull data and as such, the resulting values of parameters may not be valid.

Results

The recovery–mass pull relationships of case studies on three PGM ores under different experimental conditions are shown in Figure 3. Case study 1 represents an altered UG2 ore from the Bushveld Complex with a 4E head grade of 3.1 g/t, yielding a lower overall recovery and slower initial kinetics but a consistent tail and characterized by a high mass pull to the concentrate. Case study 2 used a good quality and easily floatable UG2 ore (4E head grade of 4.0 g/t), characterized by a strong fast-floating component and consistent slow-floating behaviour. Case study 3 was conducted on a UG2 ore similar in head grade to case study 2, but instead of a mechanical Denver cell, the sample was floated in a pneumo-mechanical cell of the same 8 L volume. The float was characterized by significantly reduced mass pulls and improved PGM kinetics, and even after 30 minutes of flotation the PGM recovery-mass pull relationship was still strong.

The fits of the first-order model variants in Equations [2] and [4] and that of the new 'exponential decay, mass-pull-linked' method are shown in Figures 4 to 6. For maximum graphical resolution, only the inflection of the curve and the slow-floating kinetics are shown. Table II details the model parameters for the three first-order models, while Table III provides the parameters for the newly proposed method. In each case the experimental data-points each represent a single flotation test; further work is under way to investigate the model fits with replicate tests where the variance in data-sets also affects the fit.

As shown in Figure 4 (case study 1), the single-component, first-order model returned an *Rmax* of just over 70%, and clearly did not provide a good fit to the overall kinetics, returning an R^2 value of 0.9711 and a sum of squares (SSQ) of 34.1. (We have included the SSQ values in each case to provide a better resolution of the extent to which the various models were able to fit the experimental data). Typical of the application of this model, the kinetics are overestimated as the *Rmax* constitutes a ceiling to the recovery. Under these conditions, the classic (three-parameter) Kelsall model also did not cope well and, reflecting the experience on a database of other PGM ores, it tends to under-predict the kinetics up to around halfway in the float, subsequently compensating by overshooting the experimental recovery after 30 minutes. It does not offer a good description of the slow-floating fraction and it is to be expected that in cases where the kinetics are lower than in this case, the model fit would be worse. As expected, the modified (four-parameter) Kelsall model provided the best fit of the three with an R^2 of 0.9991 (SSQ 0.96) for the five experimental data-points, tracking the overall kinetics well throughout the duration of the experiment. (Note that the fit of this model is obscured on the graph by that of the proposed 'new' approach, the two being very similar.)

The results in Table II highlight the disconnect between the rate constants and ultimate recoveries in the various models. While the value of *Rmax* for the single-component model, at 70.8%, is clearly a significant underestimation and has no relevance for interpretation or modelling, the modified Kelsall returned a value of 74.3% which, judging from visual extrapolation of the experimental data and the 74.25% final experimental recovery, is conservative. The latter is due to a correction of the slight overshoot of the experimental recovery after 15 minutes, thereby flattening the predicted kinetics. The proposed mass-pull-related model, with four parameters, was able to match the fit of the modified Kelsall with an R^2 of 0.9991 and *Rmax* of 75.7%, which from visual observation appears to be more representative of the experimental data. It should be noted that the value of *Rmax* is adjusted according to Equations [5] to [7] to provide the optimum description of the experimental kinetic data as per Equation [8].

Case study 2 (Figure 5) shows that, as before, the first-order single-component model is not able to cope with the

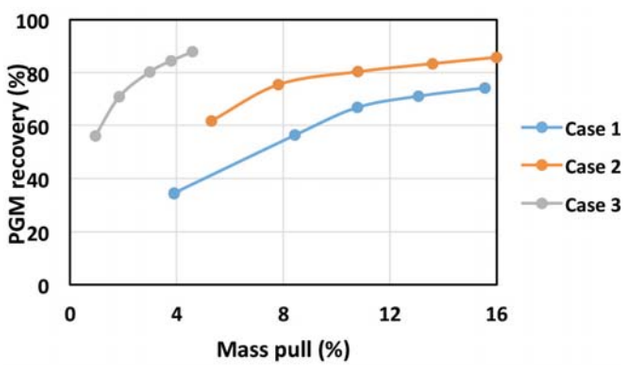

Figure 3—Recovery–mass pull relationships for the three case studies

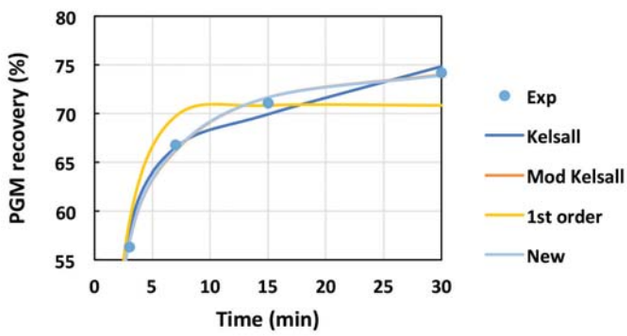

Figure 4—Model fits of overall PGM kinetics: case study 1

Table II

Comparison of kinetic parameters of first-order models from three PGM case studies

Case study	Model	k	*Rmax*	*Kf*	*Ks*	*Qf*	R^2	SSQ*
1	1 component	0.59	70.8	-	-	-	0.9711	34.1
	Kelsall	-	-	0.72	0.012	0.64	0.9950	8.6
	Mod. Kelsall	-	74.3	0.90	0.14	0.72	0.9991	0.96
2	1 component	1.35	81.8	-	-	-	0.8767	45.7
	Kelsall	-	-	1.61	0.019	0.76	0.9846	5.67
	Mod. Kelsall	-	85.9	1.84	0.13	0.83	0.9990	0.38
3	1 component	1.04	82.3	-	-	-	0.8397	108.7
	Kelsall	-	-	1.46	0.034	0.71	0.9762	15.76
	Mod. Kelsall	-	88.0	1.87	0.14	0.71	0.9992	0.49

*Sum of squares, five recovery data points

Table III

Model parameters of the proposed approach for the three PGM ore case studies

Parameter	Case 1	Case 2	Case 3
K0	0.145	1.296	1.545
b	0.047	0.728	1.146
Kmp	0.118	0.064	0.405
Rmax	75.7	99.6	96.5
R^2	0.9991	1.0000	1.0000
SSQ	0.951	0.008	0.024

overall kinetics, returning an R^2 of 0.8767 (SSQ 45.7) but, as expected from the nature of the ore, significantly enhanced *K* and *Rmax* values compared to those of case study 1. The classic Kelsall model was even less able to cope with the shape of the kinetics curve than before, again a significant underestimation of recovery at the middle of the test being compensated by an overshoot of the experimental recovery after 30 minutes of flotation. As before, the modified Kelsall was the best of the three conventional models, with an R^2 of 0.9990 (SSQ 0.38) and *Rmax* of 85.9% which, from the final experimental recovery of 85.8% and the relatively steep slope of the recovery curve, again seems to be underestimated. As seen from comparison of the regression values in Tables II and III, the new (four-parameter) model was able to fit the experimental data very well for this ore and outperformed the modified Kelsall, with an R^2 of 1.000 (SSQ 0.008). The optimum kinetic fit was achieved at an *Rmax* of 99.6%, which seems to be a significant overestimation which was related to erratic experimental results and is an aspect that needs further improvement in the model.

Case study 3 (Figure 6) again highlighted that the single-component model is not a feasible option for this ore. As observed earlier, the three-parameter Kelsall model displayed a consistent drawback in these UG2 case studies by overshooting the initial fast-floating kinetics to compensate for its inability to describe the slow-floating kinetics well. The interpretation of model parameters in this case therefore needs to be approached with caution. Consistent with the other two studies, the modified Kelsall model tracked the kinetics profile well (R^2 of 0.9992); a point of note, though, being the overestimation of the recovery after the fourth (second-last) interval and that of the last being fitted closely, leading to an *Rmax* of 88% which is again clearly conservative in view of the final experimental recovery of 87.9%. Fitting of the kinetic profile with the new model proved the most successful, outperforming the modified Kelsall by a substantial margin (R^2 of 1.000). As with case study 2, the *Rmax* of 96.5% at which the model fitted the experimental kinetics best suggests that further improvement in the model formulation should be pursued.

This also allows for initial observations as to the interpretation of the results of the 'exponential decay, mass-pull-linked' model. The parameter *K0* is the key determinant of the recovery-mass pull curve, an increasing value indicating improved recovery at a given mass pull and translating into an

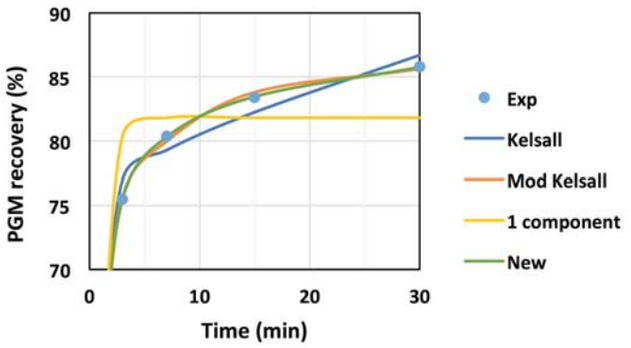

Figure 5—Model fits of overall PGM kinetics: case study 2

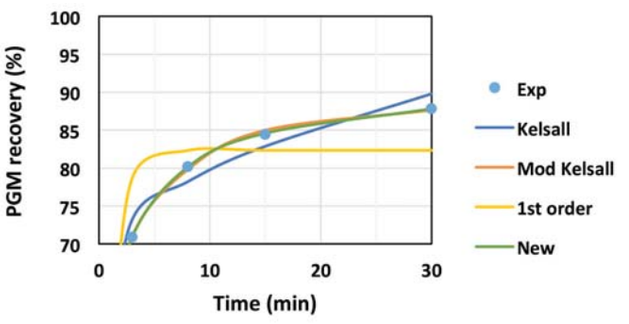

Figure 6—Model fits of overall PGM kinetics: case study 3

increased concentrate grade. Parameter *b* represents the rate at which the kinetics decay during the test and thus, in conjunction with *KO*, provides a measure of the extent of the fast-floating component of the ore. As evidenced from Table III, this was the highest for case study 3 where the conditions of high shear in the pneumo-mechanical cell resulted in very fast kinetics. The mass pull coefficient *Kmp* defines the relationship between the kinetics of the slow-floating fraction and that of mass pull towards the end of the float, and from the limited initial data appears to be sensitive to scenarios both of high recovery-low mass pull and low recovery-high mass pull. This can be explained by the steepness of both the recovery-mass pull curves. For case study 1 it was to be expected that the high mass pull, but low grade of the feed, would combine into a strong kinetic dependency on mass pull and probably a higher contribution by entrainment, while for case study 3, the steep recovery-mass pull relationship was clearly driving the high *Kmp*.

Conclusions

Bench flotation tests play a crucial role in the process geometallurgical value chain and are a relatively cheap, simple, and quick approach to obtain key information about an ore and its amenability to economic extraction of valuable minerals. Despite their apparent simplicity, a good understanding of potential pitfalls with respect to operation and interpretation of results is required. In this paper, some key practical considerations to ensure the integrity and reproducibility of data were reviewed. Subsequently, the validity of assumptions common to estimating entrainment and froth recovery at bench scale was addressed, suggesting that these can lead to errors in scale-up. The added effort and cost entailed in estimating the contribution of entrainment to overall recovery is deemed not worthwhile in a geometallurgical context, and scope exists for the development of better techniques to quantify these parameters.

A brief review was also made of first-order models for bench flotation kinetics, and a method has been proposed that accounts for the distribution of rate constants in an ore and also the fact these are driven by the froth stability, as proxied by the mass pull to the concentrate. An expression $K(t) = KO^{*}exp(-b^{*}t) + Kmp^{*}MP(t)$, where *KO* and *b* describe the floatability of the valuable mineral and *Kmp* incorporates the rate of mass pull at time *t* (*MP(t)*), was used. An added potential benefit of this method is that it enables analysis of the accuracy and quality of bench flotation data, such as deviations from an asymptotic *K(t) vs MP(t)* relationship caused by inconsistent operating procedures, and incorrect assays or concentrate mass measurements.

The application of the four-parameter kinetic model has been demonstrated for case studies on three PGM ores, achieving overall kinetics fits that matched, or outperformed, the three- and four-parameter first-order, two-component (Kelsall) kinetic models. The strongest relationship between the PGM recovery and mass pull was indicated for the case in which a UG2 ore was processed in a pneumo-mechanical cell and was characterized by fast PGM kinetics and low mass pull. The altered ore exhibited the slowest kinetics but was relatively strongly dependent on mass pull. The unaltered ore, on the other hand, showed stronger initial kinetics but coupled with a faster decay, and the smallest dependency on the mass pull.

Acknowledgements

The permission of Mintek management to publish the results, the support of the School of Chemical and Metallurgical Engineering at the University of the Witwatersrand, and that of the Department of Process Engineering at the University of Stellenbosch to generate metallurgical results, is gratefully acknowledged.

References

Alvarez-Silva, M., Vinnett, L., Langlois, R., and Waters, K.E. 2016. A comparison of the predictability of batch flotation kinetic models. *Minerals Engineering*, vol. 99. pp. 142–150.

Amelunxen, P., Sandoval, G., Barrigab, D., and Amelunxen, R. 2014. The implications of the froth recovery at the laboratory scale. *Minerals Engineering*, vol. 66-68. pp. 54–61.

Amini, E., Bradshaw, D.J., and Xie, W. 2016. Influence of flotation cell hydrodynamics on the flotation kinetics and scale up, Part 1: Hydrodynamic parameter measurements and ore property determination. *Minerals Engineering*, vol. 99. pp. 40–51.

Bradshaw, D.J., Buswell, A.M., Harris, P.J., and Ekmekçi, Z. 2006. Interactive effects of the type of milling media and $CuSO_4$ addition on the flotation performance of sulphide minerals from Merensky ore Part I: Pulp chemistry. *International Journal of Mineral Processing*, vol. 78. pp. 153–163.

Bu, X., Xie, G., Peng, Y., Ge, L., and Ni, C. 2017. Kinetics of flotation. Order of process, rate constant distribution and ultimate recovery. *Physicochemical Problems in Mineral Processing*, vol. 53, no. 1., pp. 342–365.

Buswell, A.M., Bradshaw, D.J., Harris, P.J., and Ekmekçi, Z. 2002. The use of electrochemical measurements in the flotation of a platinum group minerals (PGM) bearing ore. *Minerals Engineering*, vol. 15. pp. 395–404.

Corin, K.C., Reddy, A., Miyen, L., Wiese, J.G., and Harris, P.J. 2011. The effect of ionic strength of plant water on valuable mineral and gangue recovery in a platinum bearing ore from the Merensky reef. *Minerals Engineering*, vol. 24, no. 2. pp. 131–137.

Deglon, D.A., Egey-Mensah, D., and Franzidis, J.P. 2000. Review of hydrodynamics and gas dispersion in flotation cells on South African platinum concentrators. *Minerals Engineering*, vol. 13, no. 3. pp. 235–244.

Ekmekçi, Z., Bradshaw, D.J., Allison, S.A., and Harris, P.J. 2003. Effects of frother type and froth height on the flotation behaviour of chromite in UG2 ore. *Minerals Engineering*, vol. 16. pp. 941–949.

Hay, M.P. and Rule, C.M. 2003. Supasim: A flotation plant design and analysis methodology. *Minerals Engineering*, vol. 16, no. 11. pp. 1103–1109.

Johnson, N.W. 2005. A review of the entrainment mechanism and its modelling in industrial flotation processes. *Proceedings of the Centenary of Flotation Symposium*. Jameson, G.J. (ed.). Australasian Institute of Mining and Metallurgy, Melbourne. pp. 487–496.

Lotter, N.O., Whiteman, E., and Bradshaw, D.J. 2014. Modern practice of laboratory flotation testing for flowsheet development – A review. *Minerals Engineering*, vol. 66–68. pp. 2–12.

Rahman, R.M., Ata, S., and Jameson, G.J. 2012. The effect of flotation variables on the recovery of different particle size fractions in the froth and the pulp. *International Journal of Mineral Processing*, vol. 106-109. pp. 70-77.

Ramlall, N.V. and Loveday, B.K. 2015. A comparison of models for the recovery of minerals in a UG2 platinum ore by batch flotation. *Journal of the Southern African Institute of Mining and Metallurgy*, vol. 115. pp. 221–228.

Runge, K.C., Tabosa, E., and Jankovic, A. 2013. Particle size distribution effects that should be considered when performing flotation geometallurgical testing. *Geomet 2013: Proceedings of the Second AusIMM International Geometallurgy Conference*, Brisbane, 30 September – 2 October. Australasian Institute of Mining and Metallurgy, Melbourne. pp. 335–344.

Wang, L., Runge, K., Peng, Y., and Vos, C. 2016. An empirical model for the degree of entrainment in froth flotation based on particle size and density. *Minerals Engineering*, vol. 98. pp. 187–193.

Zhang, J. and Subasinghe, N. 2016. Development of a flotation model incorporating liberation characteristics. *Minerals Engineering*, vol. 98. pp. 1–8. ◆

SAIMM MEMBERSHIP OR UPGRADE

SAIMM
THE SOUTHERN AFRICAN INSTITUTE OF MINING AND METALLURGY
FOUNDED 1894

Website: http://www.saimm.co.za

Reasons to join the SAIMM

- Receive the SAIMM Journal which communicates a high standard of technical knowledge to our members
- Access to **OneMine.org** and publications from other international mining and metallurgical societies
- Participation in technical excursions and social events which creates further opportunities for interactive personal and professional association and fellowship
- To make a contribution to the Mining and Metallurgy industries
- The opportunity to network with a wide cross-section of professional people in the mining and metallurgy industry
- Access to the output from international industry-related organizations
- Active participation leads to higher peer recognition of achievements in the minerals industry
- Members of the Institute who are registered with the Engineering Council of SA (ECSA) qualify for a rebate on their ECSA fees
- Opportunity to contribute to the development of young talent through mentoring and participating in schools
- Engagement and involvement in SAIMM structures and networking opportunities allow for additional Continuing Professional Development (CPD) point collection
- Discounted membership prices when attending events hosted by the institute.

Fifth Floor, Minerals Council South Africa
5 Hollard Street, Johannesburg, 2001
P.O. Box 61127, Marshalltown, 2107, South Africa
Tel: 27-11- 834-1273/7 · Fax: 27-11- 838-5923 or 833-8156
E-mail: membership@saimm.co.za

FOLLOW US ON...

www.facebook.com/TheSAIMM/ https://twitter.com/SAIMM1

https://www.linkedin.com/company/saimm--
-the-southern-african-institute-of-mining-and-metallurgy

Time-dependent failure of open stopes at Target Mine

P.J. Le Roux[1], K.R. Brentley[1], and F.P. Janse van Rensburg[2]

Affiliation:
[1]Brentley, Lucas & Associates, South Africa
[2]Harmony Gold Mining Company Limited, South Africa

Correspondence to:
P.J. Le Roux

Email:
Jaco.LeRoux@Harmony.co.za

Dates:
Received: 22 Nov. 2017
Revised: 26 Mar. 2018
Accepted: 5 September 2018
Published:

How to cite:
Le Roux, P.J., Brentley, K.R., and Janse van Rensburg, F.P. Time-dependent failure of open stopes at Target Mine. The Journal of the Southern African Insitute of Mining and Metallurgy

DOI ID:
http://dx.doi.org/10.17159/2411-9717/17/477/2019

ORCiD ID:
https://orchid.org/0000-0003-3900-1839

Synopsis

There are numerous factors that affect open stope stability and often result in falls of ground. These falls of ground can be attributed to factors such as beam failure due to a larger than normal roof area (hydraulic radius too large), adverse ground conditions, seismicity, the stress-strain environment, absence of support, and poor drill-and-blast practices. The effect of time on the stability of open stopes is sometimes underestimated and is relatively unknown, especially on Target Mine. Actual data was collected from open stopes at Target and analysed to show the effect of time on open stope stability. The benefits of this analysis will include improved understanding of time-dependent failure, which can assist in reducing dilution and the risk of sterilization of future mining blocks.

Keywords
stope stability, open stope, time-dependent failure, dilution.

Introduction

Target Mine is situated adjacent to the town of Allanridge, some 20 km from Welkom in South Africa's Free State Province, and is the most northerly mine in the Welkom Goldfields area (Figure 1). The mine consists of a single surface shaft system with a sub-shaft (Target 1C shaft) and a decline. Ownership was attained by Harmony Gold Mining Company Limited in May 2004 (Harmony Gold Mining Company Limited, 2010).

Before discussing the selection of open stopes for the back-analyses, a brief explanation of open stoping as practiced at Target Mine will be given. The orebody is some 180 m in thickness and 270 m wide and comprises multiple reefs overlying one another. The 180 m thick reef package is termed the Eldorado Reefs, as shown in Figure 2. The Eldorado Reefs suboutcrop against the Dreyerskuil Reefs, as shown in Figure 3. The dip of the reef varies from as low as 10° in the west to 75° in the east.

Compared with most Australian and Canadian open stoping mining operations, Target Mine is unique. In most Australian and Canadian mining operations the hangingwall and footwall of the open stopes comprise waste rock, and the orebody dips relatively steeply. Due to the depth of Target Mine, some 2300 m to 2500 m below surface, a destress slot (Figure 4) is mined to create an artificial, shallow mining environment whereby the field stress is managed and kept at values of around 60 MPa. The destress slot comprises a narrow tabular stope with an average width of 1.5 m, and is mined on the Dreyerskuil Reefs.

At Target Mine the hangingwall, sidewalls, and footwall of the open stopes all comprise reef of different grades, except for the EA1, where the EB footwall is waste rock. If a stope, for example, is mined alongside an existing old stope, the western sidewall of this stope will consist of backfill. The general mining direction of open stopes is from the lowest position of the reef on the west, progressing up towards the east as shown in Figure 5.

Open stoping is the process by which massive stopes are blasted to mine selected reef packages within the orebody. These open stopes are large, varying from 10 m to 45 m in width (span), 10 m to 35 m in height, and 10 m to 100 m in length. To establish an open stope, a reef drive is developed on strike at the lowest point where the stope will be situated, as shown in Figures 5–7. This reef drive is developed to the mining limit of that specific open stope. At the end of the open stope, slot cubbies are developed cutting across the dip of the strata.

In one of the cubbies, a drop raise is developed holing into the top drive for ventilation. Once developed, the slot is drilled, as well as the blast rings for the open stope. When completed, the slot is blasted and cleaned utilizing remote loading LHD (load, haul, and dump) mechanized equipment.

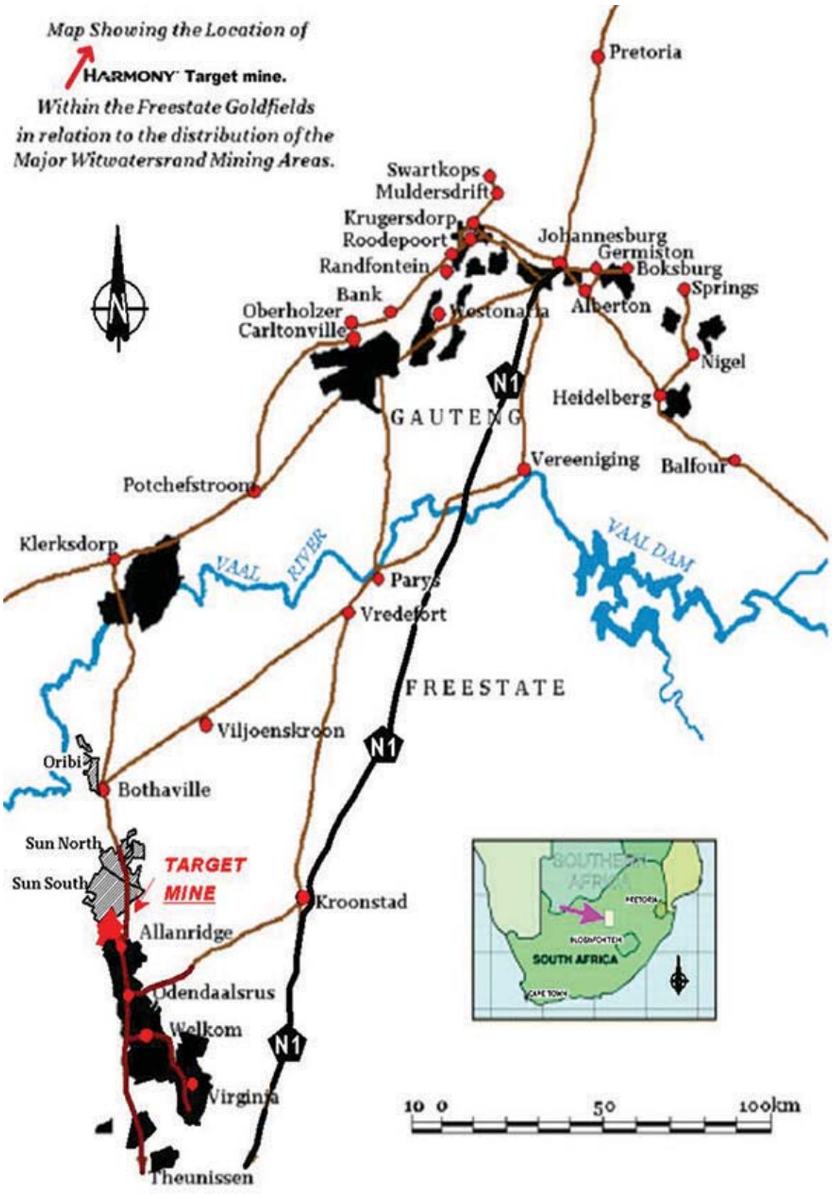

Figure 1—Location of Target Mine (Harrison, 2010

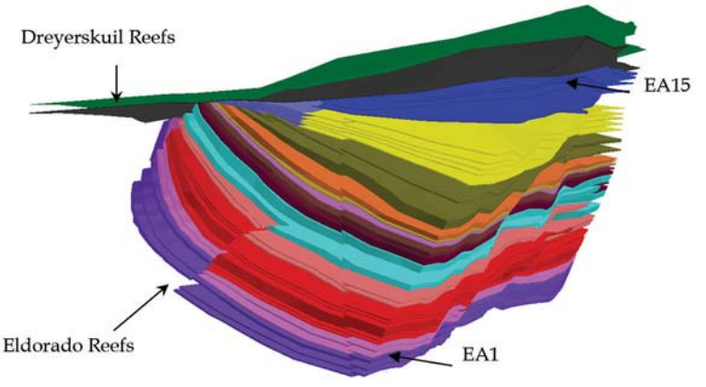

Figure 2—General isometric view looking north, showing the Eldorado Reefs suboutcropping against the Dreyerskuil Reefs (le Roux, 2015)

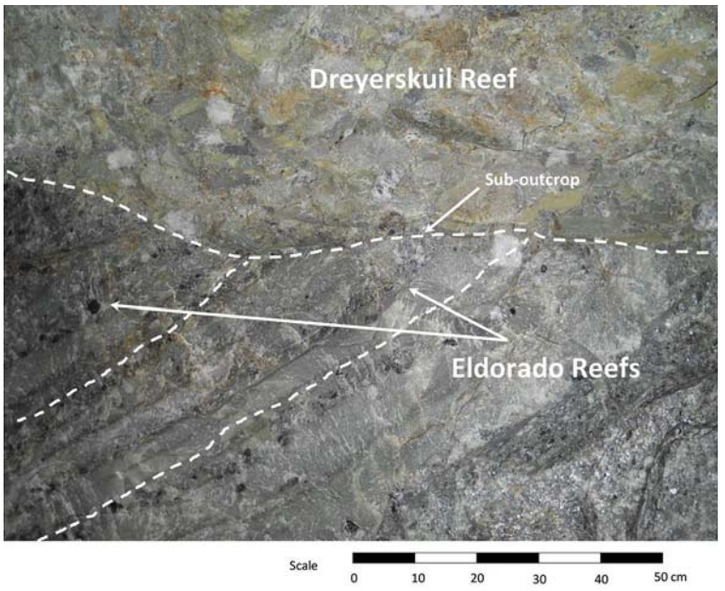

Figure 3—Photograph showing the Eldorado Reefs suboutcropping against the Dreyerskuil Reefs (le Roux, 2015)

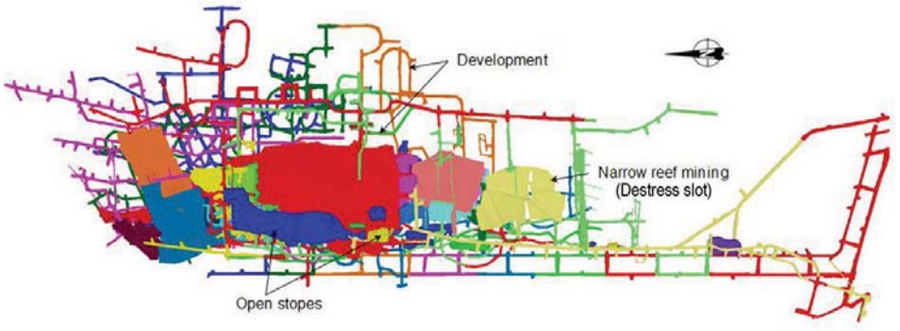

Figure 4—Plan view of Target mining block (le Roux, 2015)

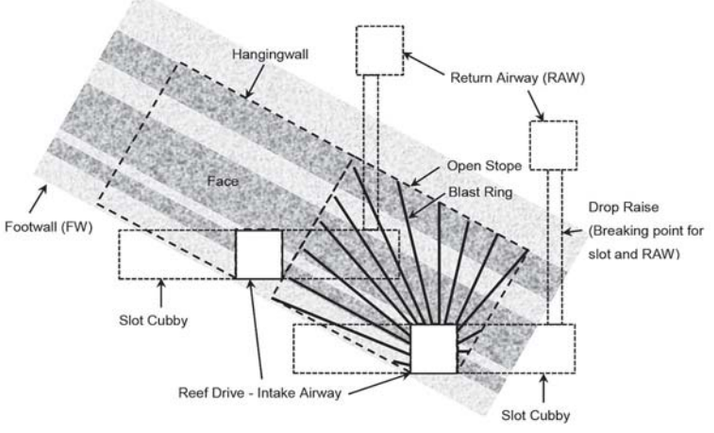

Figure 5—Cross-sectional view of a typical open stope design on Target Mine (le Roux, 2015)

The open stope is then created by blasting a maximum of four rings at a time, on retreat, and is cleaned utilizing remote-loading LHDs. No personnel are allowed to enter these open stopes at any time, as no support is installed.

Financial implication of dilution and falls of ground

Thirty-three open stopes were used for the back-analysis of fall-of-ground statistics. Dilution due to falls of ground in open stoping can have an impact on profitability. These falls of ground

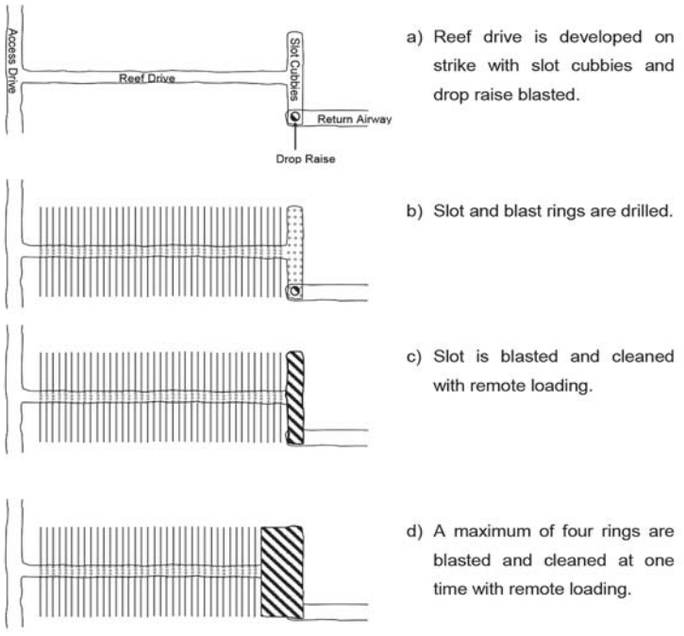

Figure 6—Plan view of a typical open stope design on Target Mine (le Roux, 2015)

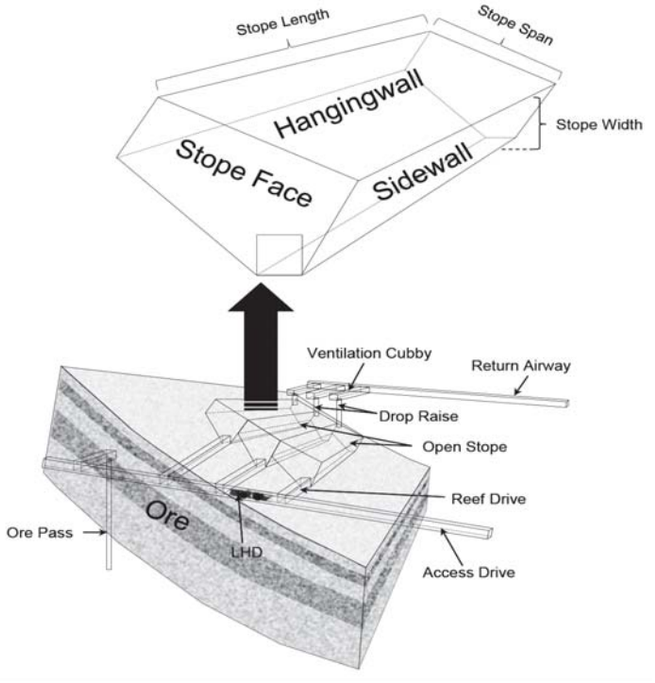

Figure 7—General isometric view of a typical open stope design on Target Mine (le Roux, 2015)

contribute significantly towards dilution as the rock from the falls is loaded with the blasted ore. This would be country rock in the case of typical open stopes, but at Target Mine the dilution may consist of unpay ore, backfill, waste rock, or a combination of these materials. One of the contributing factors to loss in profit is damage to and loss of mechanized equipment due to falls of ground, as shown in Figure 8.

Estimation of dilution using the DSSI

The extent of failure for the Target open stopes can be determined using the strain-based stability/design criterion, termed the dilution stress-strain index (DSSI) (le Roux, 2015). The relationship between mean stress σ_m and volumetric strain e_{vol} can be expressed as follows:

Figure 8—A TORO LH514 LHD in an open stope, damaged by a fall of ground (le Roux, 2015)

$$\sigma_m = q\varepsilon_{vol} \quad [1]$$

$$\varepsilon_{vol} = \frac{\sigma_m}{q} \quad [2]$$

where q is the slope of the linear trend lines. The DSSI is the relationship between mean stress and volumetric strain, expressed as follows:

$$DSSI = \frac{\sigma_m}{q\varepsilon_{vol}} \quad [3]$$

For a factor of safety of 1.0, the DSSI is equal to 1.0, thus no failure occurs. A DSSI greater than 1.0 will indicate failure conditions in tension. For a set value of mean stress, if the volumetric strain is less than the threshold, failure would occur due to relaxation. A DSSI of less than 1.0 will indicate failure conditions in compression. This method considers all three principal stresses and strains, which is appropriate for the three-dimensional environment of the open stopes at Target Mine (le Roux, 2015).

Applying the DSSI criterion at Target Mine enabled the planned dilution to be compared with the predicted dilution in an attempt to determine whether a particular open stope would be profitable to mine or not. In Figure 9 the actual percentage dilution is compared to predicted dilution, showing some good correlations. It is noted that in some of the case studies the actual dilution exceeded the predicted dilution. This can be attributed to excessive standing times during and subsequent to stoping, delays in placing backfill, adjacent mining activities (blasting), and seismicity. These falls of ground have the potential to sterilize the adjacent open stope.

Open stope failure and the effect of time

There are numerous factors that affect open stope stability and often result in falls of ground, such as beam failure due to a larger than normal roof span, adverse ground conditions, seismicity, the stress-strain environment, absence of support, and poor drill-and-blast practices. The effect of time on the stability of open stopes is sometimes underestimated and is relatively unknown, especially on Target Mine. Actual data collected from 33 open stopes at Target Mine was analysed to show the effect of time on open stope failure. To investigate and document the behaviour of open stopes and to evaluate alternative open stope design methods that could be beneficial, a comprehensive empirical database was established. This consisted of information such as rock mass properties, rock mass classification values, and cavity monitoring system (CMS) data. The following information from the 33 case study stopes at Target Mine was included in the database, as shown in Table I:

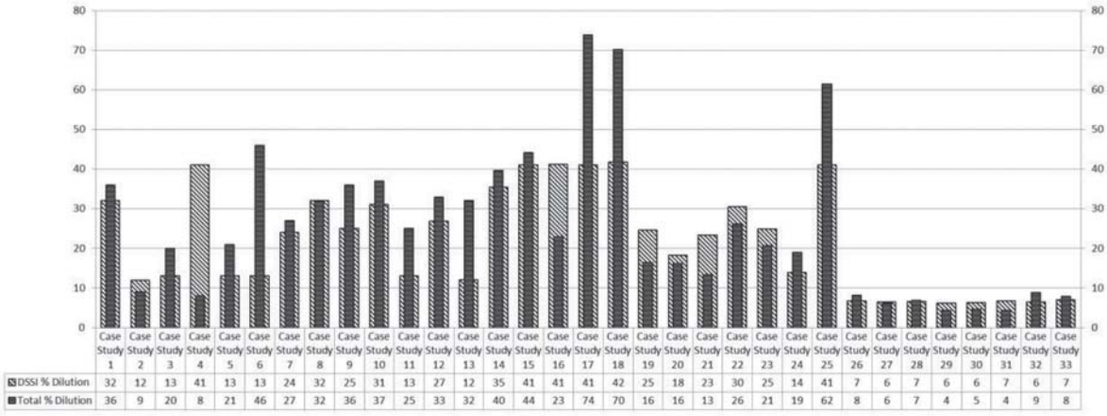

Figure 9 – Actual percentage dilution *versus* modelled percentage DSSI dilution

Table I

Case study data

Case study no.	Q	HR (m)	Hangingwall span (m)	Total actual % dilution	Predicted % dilution (DSSI)	Time (months) before FOG	Other contributing factors leading to FOG
1	0.03	12	47	36	32	0.5	Larger than normal span
2	0.47	6.9	19	9	12	1.0	None
3	0.12	6.9	17	20	13	3.0	Holed into up-dip open stope
4	0.14	7.5	19	8	41	1.0	Partially de-stressed
5	1.48	7.7	23	21	13	6.0	Holed into up-dip open stope
6	1.48	7.3	27	46	13	1.0	Not de-stressed
7	0.47	7.8	20	27	24	3.0	Blasting in close proximity
8	1.48	12	47	32	32	0.5	Larger than normal span
9	1.48	9.1	37	36	25	1.0	Not de-stressed
10	0.03	7.1	30	37	31	2.0	Partially de-stressed
11	0.03	6.9	20	25	13	1.0	Not de-stressed
12	0.03	6.8	18	33	27	3.0	Not de-stressed
13	0.03	9.1	31	32	12	1.0	Holed into NRM
14	0.03	8.1	20	40	35	3.0	Not de-stressed
15	9.23	16.9	45	44	41	1.0	Larger than normal span
16	0.92	13.0	34	23	41	72.0	Larger than normal span
17	16.08	18.7	45	74	41	1.0	Larger than normal span
18	1.85	14.7	36	70	42	1.0	Larger than normal span
19	0.47	5.5	9	16	25	6.0	Broken hangingwall beam (large brow)
20	0.92	11.4	25	16	18	2.0	Larger than normal span
21	0.47	7.0	18	13	23	3.0	Holed into NRM
22	2.74	11.5	30	26	30	1.0	Not de-stressed and larger than normal span
23	4.74	8.6	32	21	25	1.0	Not de-stressed
24	0.92	11.4	25	19	14	2.0	Larger than normal span
25	0.14	7.8	17	62	41	2.0	Holed into NRM
26	0.92	5.8	14	8	7	6.0	None
27	7.20	6.5	17	6	6	7.0	None
28	1.74	7.7	22	7	7	8.0	None
29	9.23	8.1	20	4	6	12.0	None
30	7.60	8.0	21	5	6	8.0	None
31	1.90	6.5	15	4	7	8.0	None
32	2.96	5.9	17	9	6	4.0	None
33	0.30	6.1	20	8	7	3.0	None

- Predicted stope dilution from DSSI
- Actual dilution from CMS survey data
- Stope geometry (beam span and hydraulic radius)
- Rock mass classification value, Q System (Barton, Lien, and Lunde, 1974)
- Time that open stope stood before failure (fall of ground)
- Possible contributing factor(s) to fall of ground in open stope.

To determine the Q-value, the Joint Water Reduction Factor (Jw), was taken as unity for all the open stopes on Target Mine. These stopes were either dry or had a minor inflow of water. The Stress Reduction Factor (SRF) was taken as between 0.5 and 2 for open stopes in high stress conditions and unity where medium stress or favourable stress conditions were found.

Major dilution is defined as dilution greater than 10% (local definition). Minor dilution is where the measured dilution is equal to or less than 10%, and underbreak is where the measured dilution is negative (<0%). At Target Mine, all open stopes are designed for a dilution of 5% and less, but this was rarely achieved. In 70% of the case study stopes, dilution was >10% and deemed as major failure; 30% had dilution <10% and were deemed as minor failure; open stopes with underbreak were excluded from this study.

The contributing factors to the falls of ground in open stopes (Table I) can be summarized as larger than normal span, holed into updip open stope, partially de-stressed, not de-stressed, blasting in close proximity, and holed into NRM (narrow reef mining).

Figure 10 is an adaption of the Q-value 'no support curve' after Houghton and Stacey (1980), used mainly to determine the stability of unsupported spans for long-term service excavations. While not really suitable for open stopes, plotting the Target Mine

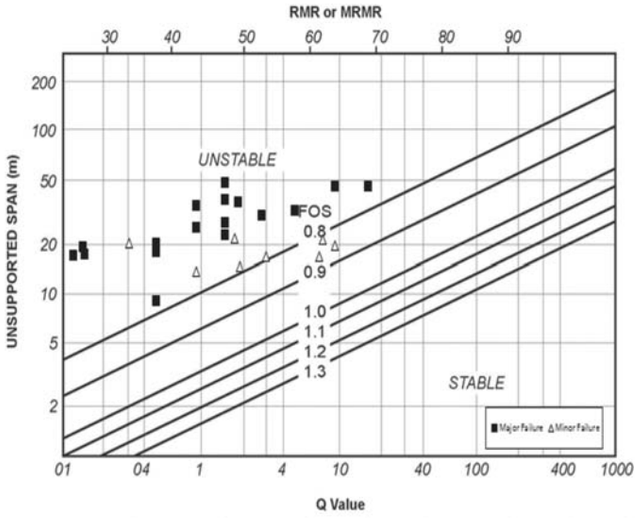

Figure 10—Plot of unsupported span (m) versus Q-value for Target Mine case studies with major and minor failure (after Houghton and Stacey, 1980)

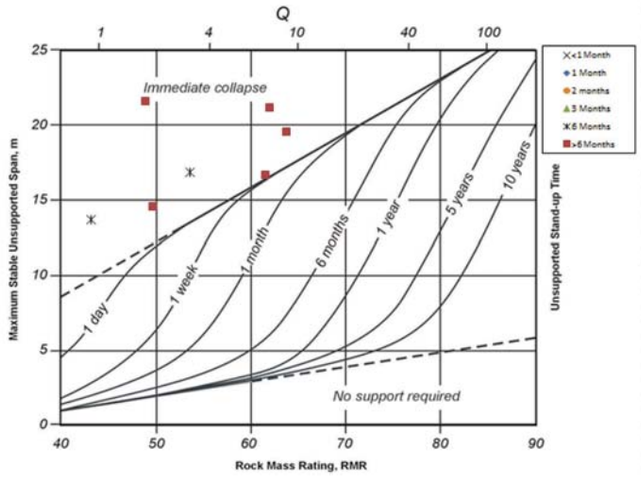

Figure 11—Unsupported span (m) versus Q-value (after Hutchinson and Diederichs, 1996)

results in this way indicates that eventually the beam will fail due to the multiple reefs overlying one another. The time to failure is still an unknown factor.

The graph in Figure 11 (after Hutchinson and Diederichs, 1996) allows one to estimate unsupported standup times for service excavations using unsupported spans, and the Q and RMR values. Figure 12 is an adaption of the Q-value 'no support curve' (after Hutchinson and Diederichs, 1996), used mainly to determine if entry into an open stope is permitted. Not all the case studies could plot on these graphs as some fall outside the ranges of the graphs, indicating that these stopes will collapse immediately (as shown in Figure 11), which was not the actual case. By modifying the Q-value *versus* unsupported span (m) chart in Figure 13 and plotting time (in months) for which open stopes remained stable before any major falls of ground occurred, the following became evident.

- Some open stopes had a standup time of less than 1 month, the shortest time to failure being 14 days.
- A number of open stopes remained stable for longer than 6 months, the longest being six years.
- Standup periods can be categorized and used in the design process.

As shown in Figure 13, one of the case study stopes (no. 16) should have failed within one month according to the data, but remained stable for six years. For case studies 1 and 8 the open stope spans were larger than the norm, resulting into a standup time of less than one month. For the case studies with a standup time of one month, the scatter in the data can be attributed to high stress conditions as a result of these stopes not being de-stressed, larger than the norm mining spans, and holing into narrow reef mining above the stope, as shown in Table I. The effect of larger than the normal mining spans, holing into updip open stopes, partial or no de-stressing, blasting in close proximity, creation of brows in open stopes, and holing into NRM should not be underestimated as contributing factors for these falls of ground at Target Mine. Mining only open stopes in de-stressed ground conditions, improved blasting practices, avoiding holing into narrow reef mining, and eliminating the creation of brows in the open stopes will all contribute to extending the standup time for these stopes.

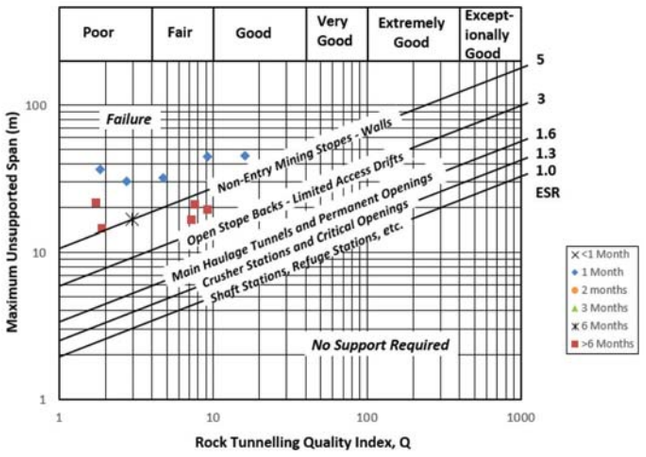

Figure 12—Unsupported span (m) *versus* Q-value (after Hutchinson and Diederichs, 1996)

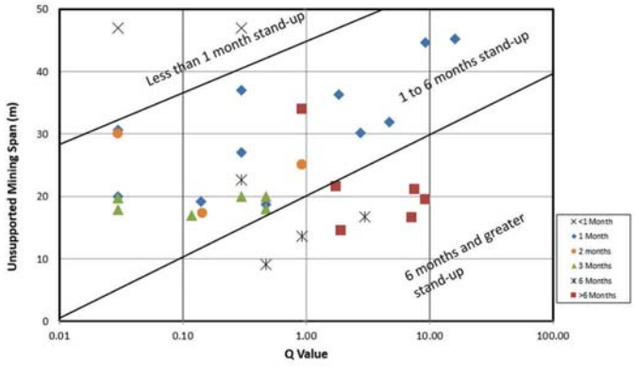

Figure 13—Modified standup time graph for unsupported span (m) *versus* Q-value for Target Mine open stope conditions

Conclusions

The objective of the study described in this paper was to develop a method that could assist in determining the standup time for open stopes at Target Mine. The DSSI method assists greatly in determining the potential dilution (depth of failure of hangingwall and sidewall in open stopes) for a given stope design. The stope design can then be modified should the required dilution factors not be achievable.

At Target, a number of open stopes can be extracted at a given time. This often requires the construction of backfill bulkheads and the placing of backfill to be carefully planned and sequenced. The standup times were determined for open stopes exposed to varying conditions, such as:

- Larger than normal mining spans
- Holing into updip open stopes
- Partially de-stressed or stressed stopes
- Blasting in close proximity to stopes
- Brow creation
- Holing into narrow de-stress slots.

All of the above are of vital importance to the proper planning and sequencing of open stopes. As more open stopes are mined at Target Mine, the empirical graph in Figure 13 will be updated. Although the graph in Figure 13 indicates standup times for various Q-values and unsupported mining spans, small falls of ground are not recorded and as such are not taken into consideration. The mine does, however, have a strict policy that no person is allowed to enter an open stope. Mucking of these open stopes is carried out by remote loading.

Acknowledgements

The authors would like to thank Harmony Gold Mining Company Limited for the privilege of presenting this research. The permission to include data and make use of equipment, as well as the assistance received from colleagues at Brentley, Lucas & Associates, Mining Consultants, is greatly appreciated.

References

Barton, N., Lien, R., and Lunde, J. 1974. Engineering classification of rock masses for the design of tunnel support. *Rock Mechanics*, vol. 6, no. 4. pp. 189–236.

Harmony Gold Mining Company Limited. 2010. Annual Report.

Harrison, A.G. 2010. Mineral Resource statement, Target Mine 2010.

Houghton, D.A. and Stacey, T.R. 1980. Application of probability techniques to underground situations. *Proceedings of the 7th Regional Conference for Africa on Soil Mechanics and Foundation Engineering*, Accra. Vol. 2. Balkema. pp. 879–883.

Hutchinson, D.J. and Diederichs, M.S. 1996. Cable bolting in underground mines, BiTech, Richmond, Canada. 401 pp.

Le Roux, P.J. 2015. Measurement and prediction of dilution in a gold mine operating with open stoping mining methods. PhD thesis, University of the Witwatersrand, Johannesburg.

Potvin, Y. 1988. Empirical open stope design in Canada. PhD thesis, University of British Columbia, Vancouver. ◆

Geotechnical data analysis to select a feasible method for development of a long axis, large diameter vertical ventilation shaft

E.J. Walls[1,2], W.C. Joughin[1], and H-D. Paetzold[3]

Affiliation:
[1]SRK Consulting (Pty) Ltd, South Africa
[2]JeWal Geotechnical (Pty) Ltd, South Africa
[3]Palabora Mining Company (Pty) Ltd, South Africa

Correspondence to:
E.J. Walls

Email:
jwalls@srk.co.za

Dates:
Received: 4 Sep. 2017
Revised: 24 Oct. 2018
Accepted: 14 Nov. 2018
Published: April 2019

How to cite:
Walls, E.J., Joughin, W.C., and Paetzold, H-D.
Geotechnical data analysis to select a feasible method for development of a long, large diameter vertical ventilation shaft.
The Southern African Insitute of Mining and Metallurgy

DOI ID:
http://dx.doi.org/10.17159/2411-9717/17/390/2019

ORCiD ID:
https://orcid.org/0000-0001-9212-1093

Synopsis

In selecting a suitable method to sink a vertical shaft for underground access, a number of constraints influence the ultimate decision of where and how to develop the shaft, not least among these being safety, development and construction time, and cost. Two additional considerations stand out: these being geotechnical conditions and technology, the latter taking into account existing underground access. Assuming a project for which an existing underground excavation is available, it is tempting to build a shaft sinking project from the outset based on the raiseboring method, which has the potential to be the safest, fastest, and least expensive method provided that geotechnical conditions permit.

And therein lies the rub: regardless of project time or cost constraints, when it comes to raiseboring a long (say, greater than 500 m), large diameter (greater than 4.5 m) shaft, the rock mass conditions ultimately dictate what method of shaft sinking will be feasible. Over the course of several studies for a particular project, several geotechnical analyses were carried out specifically for the purpose of developing a shaft by raiseboring. Risk analysis and experience showed that where the rock mass conditions indicated an unacceptably high risk potential, an alternative method needed to be considered, even if this meant increasing both the time and financial requirements.

In this paper we present an overview of geotechnical investigation practices for shaft sinking. Decision-making thresholds for raiseboring or other methods of shaft sinking are discussed, including probabilities of failure, empirical rock mass classification, basic wedge failure, and back-analysis of a failed case. The design of appropriate support, and analysis of relative safety benefits for various shaft sinking methods, falls outside the scope of this work, and will be presented in a separate paper.

Keywords
raiseboring, probability of failure, rock mass classification.

Introduction

The potential for rock mass failure during shaft development and construction affects whether a project is completed safely, on time and on budget. During the course of several studies to establish ventilation shafts for an underground expansion project, geotechnical analyses of rock mass stability and failure potential were carried out. The investigations were guided by the method of McCracken and Stacey (1989) together with insights from Peck and associates (Peck, 2000; Peck and Lee, 2007, 2008; Peck, Coombes, and Lee, 2011).

Considerations for method selection

Regardless of project constraints involving time, budget, and safety, an understanding of the geotechnical conditions together with technology limitations is critical for determining which method of shaft sinking will work. Where an existing underground excavation permits, raiseboring is attractive by way of being rapid and cost-effective, with limited exposure of workers within the shaft during excavation and therefore a relatively low safety risk compared with conventional, labour-intensive methods such as blind sinking, slipe and line, or other downward-orientated excavation methods, not to mention Alimak shafts, V-Mole, among others (Table I).

However, for a long (> 500 m), large diameter (> 4.5 m) raisebored shaft, the probability of encountering unfavourable (high-risk) rock conditions is greater than for a short shaft. This factor, in the authors' opinion, is currently inadequately addressed in shaft planning projects. Additionally, an increased diameter presents an increased surface area for wedges to form and stress-driven spalling to occur. The shaft walls must be able to stand up (be stable) for the period that it takes to complete the reaming. For example, a 1000 m or longer shaft that is advanced, say, 3 m to 5 m per day must be stable for up to six

Table I

Basic considerations in selecting an appropriate shaft sinking method

Constraint	"Top-down" (blind; slipe and line; secondary reaming, etc)	"Bottom-up" (raisebore)
Timing	Slow (can be preclusive but what if alternative methods' risk is too high?)	Rapid (appealing)
Cost (equipment, labour, support)	High (can be preclusive but what if alternative methods' risk is too high?)	Less than "top-down" (appealing)
Safety	Controlled (good) Higher exposure (bad)	Uncontrolled (bad) Limited exposure (good)
Support	Complete coverage (bad / good? – purpose driven); in-line (slow, bad); controlled (good)	Unsupported (good for unlined shafts; irrelevant for lined shaft; dependent on support installation methodology and sequence)
Geotechnical (stability / rock mass response)	Somewhat flexible i.t.o. - Feasibility (manageable conditions) - Siting (can be made to fit into layout)	Pivotally deterministic: inflexible and unforgiving: - Feasibility (unmanageable instability) - Siting (requires ideal conditions)

months to one year before staged support can be installed. Only once the shaft has been completed can support be installed, assuming that the shaft will be equipped with a headgear in order to do so (not typically needed for an unequipped ventilation shaft, as for this project).

Rock mass failure prior to completion of a raisebored shaft can have catastrophic consequence for the project. The project will incur increased costs, be delayed, the site may need to be abandoned entirely if it cannot be rehabilitated, and equipment may need to be sacrificed if not retrievable. Major wedge failure from the advancing face can occur, impacting the performance of the reamer. Alternately, uncontrolled unravelling of the sidewalls presents a risk to safety and equipment while attempting to retrieve the cutter head during cutter changes, as well as a risk to the long-term stability and functionality of the shaft.

Currently, technologies for raiseboring shafts longer than 500 m preclude the concurrent installation of support of any kind, be it shotcrete, tendons, mesh, or otherwise. This is due to the length of the shaft, which inhibits remote shotcrete efforts, the presence of an advancing face that makes conditions unsafe for personnel to access and install support, while if support is indeed installed, the reamer diameter must then be reduced in order to re-enter and complete the shaft.

It is therefore important to regard the potential risk of rock mass failure as a major deciding factor when choosing the best shaft-sinking method for a project. Geotechnical conditions must be favourable over an extended linear distance (> 1000 m in this case) and be within a tolerable threshold for failure risk.

Geotechnical risk analysis

An account of geotechnical risk analysis criteria was put forward by McCracken and Stacey (1989) followed by insights of Peck and associates (Peck; 2000; Peck and Lee, 2007, 2008; Peck, Coombes, and Lee, 2011). A summary of geotechnical risk considerations for the development of a large diameter (> 4.5 m), long (> 500 m), unlined and unsupported ventilation shaft is presented in Table II. Other risk parameters not included in the table are less influential. These include, among others:

- RQD/Jn: an indication of block failure potential in relation to shaft diameter where RQD represents rock quality designation and Jn represents the number of joint sets (Barton, 2002; Peck *et al*; McCracken and Stacey, 1989)
- Jr/Ja: an indication of shear failure potential, found to be somewhat inconclusive as an indicator for stability in relation to shaft diameter
- Work by Andersen (2015) includes a stability index (SSL) based on a combination of Jr and Ja (Barton, 2002); however, this work was not available at the time of the project and would be worthwhile to incorporate in shaft projects going forward.

It is worthwhile to note that the approaches of McCracken and Stacey (1989), and Peck, Coombes, and Lee e2011) are largely empirical and as such carry certain limitations (Figure 1. One such obvious limitation is the predominance of data from shafts with a diameter less than or equal to 4.5 m, and only a single case for 6.0 m, which failed. Although raisebored shafts greater than 4.5 m and up to 6.1 m diameter are known

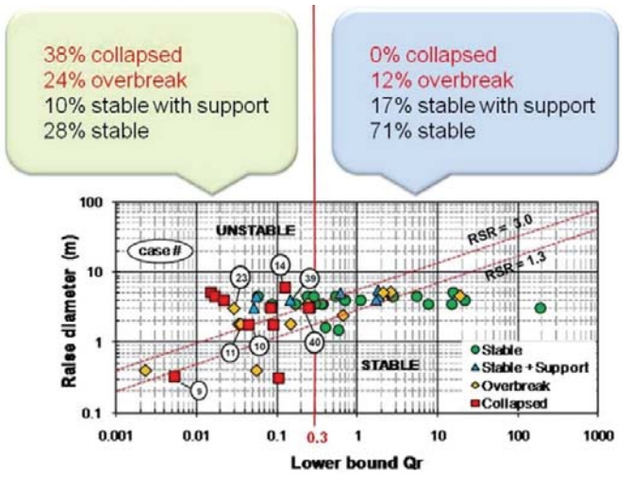

Figure 1—Failed *versus* unfailed raisebore shafts comprising the empirical database of Peck, Coombes, and Lee (2011)

Table II

Geotechnical risk thresholds for raiseboring a > 4.5 m diameter, > 500 m length ventilation shaft

Parameter	Range	Comment
Q_R	> 5.0	Must be situated in 'fair' (Class C) ground or better (Barton, 2002.)
Q_R	> 0.3	> 70% probability of instability where QR < 0.3, *i.e.* 'very poor' ground (Barton, 2002) (> 70% of case studies failed, suffered overbreak, or required support, regardless of shaft diameter) (Peck, Coombes, and Lee, 2011)
Risk interval length	< 3 m	Intervals with high-risk ground but confined to less than 3 m linear extent – failure likely to be constrained (Peck, Coombes, and Lee, 2011)
Standup time	> 6 months	Corresponds to RMR_{BIEN} > 50 ('fair' ground or better) (Bieniawski, 1973)
Risk tolerance	< 5%	Less than 5% probability of failure (PoF) tolerance (corresponds to ESR = 1.3; McCracken and Stacey, 1989)

to have been completed successfully, these are not contained in the empirical database. This precludes the establishment of a stability trend in relation to shaft diameter. Is the trend linear or nonlinear, for example? This is a question that is yet to be answered through research initiatives. An estimate of stability for large (> 4.5 m) diameter shafts can therefore be somewhat loosely (and potentially erroneously) based on empirical data from the literature and hence subject to preferentially biased decision-making. Nonetheless, as is evidenced in the outcomes of this project, minimum stability threshold indicators remain fairly reliable, such as the intolerably high probability of failure in conditions where Q < 0.3 over an interval length greater than 3 m.

The analysis of rock mass stability for a shaft sinking project is typically based on geotechnical core logging results from a single vertical borehole. A rock mass classification (RMC) value is obtained and related to excavation size to estimate probable stability or instability. Where orientated discontinuity data is available, the potential for wedge failure should be numerically analysed as presented in this paper. Similarly, the potential effects of local field stress conditions on shaft wall deformation (spalling or dog-earing) should be carried out, albeit empirically (Martin, Kaiser, and McCreath 1999) as a function of, and subject to, the quality of available local stress field data. This is the approach that was taken for the project. Only where the shaft is expected to undergo continuing disturbance during its serviceable lifespan, related to ongoing mining activities or unusual stress interactions, is further numerical analysis typically undertaken. In this case, numerical analysis of stress-driven deformation potential was undertaken independently and is not included in this paper.

A selection of representative examples from the suite of shaft analyses that were carried out for this project is presented in this paper.

Q_R and maximum stable unsupported span (MSUS)

The McCracken and Stacey (1989) method of estimating rock mass stability requires that a RMC value, QR, be calculated for a geotechnical interval, which interval is in the order of 3 m long along the length of core (Peck *et al.*, 1989) for a shaft investigation. Using this approach, the maximum stable unsupported span (MSUS) was estimated for face stability and wall stability in each interval according to the relationship:

$$MSUS = 2\ RSR\ Q_R^{0.4} \quad [1]$$

where RSR is a risk term (raisebore support ratio), in which *e.g.* RSR = 1.3 relates to a tolerance threshold of 5% probability of failure for a ventilation shaft. It is understood that such a shaft is typically not equipped but is expected to provide a life-of-mine service function and therefore must not suffer excessive or premature failure.

Results of MSUS for one of the shafts are presented in Figure 2 showing the comparison between wall and face stability, and highlighting potential diameters of interest ranging from 1.8 m (pilot shaft) through to 6.0 m. The tendency for increased instability of the face in comparison with that of the shaft walls is evident from the chart; this may be expected intuitively, given that the advancing face presents a horizontal free surface more susceptible to failure under the influence of gravity than the vertical shaft walls. More importantly, areas of poor stability are consistent for both the face and shaft walls.

It is clear from the plotted results that over a 70 m length of the shaft, from 1165 m to 1095 m above the bottom collar, a zone of distinctly unfavourable ground persists, such that a shaft of no more than 1.8 m diameter will be stable in the worst case, or up to 4.0 m in the slightly less severe segments.

Also of importance is that between the shaft bottom and top collars, the final reaming diameter will no doubt be reduced in relation to the initial diameter at the shaft bottom collar. This is because as cutters are changed and the reamer is lowered and raised again, it becomes more and more difficult for the reamer to re-enter the shaft and resume reaming unless the cutter diameter is reduced to accommodate changes in the rock mass conditions. This must be taken into account during the planning of the shaft diameter requirements for ventilation (or other purposes) in that the rock mass conditions must be suitable for a larger diameter at the base of the shaft than at the top. In Figure 2, for example, a 6 m diameter shaft commencing at 1050 m would probably need to be successively reduced in diameter by some 0.15 m at 950 m and again at 925 m to successfully negotiate each difficult zone. The reamer diameter cannot be enlarged at a later point after it has been reduced at any stage without reaming from the start of the constriction to restore the diameter.

Standup times

An estimate of the potential standup times for unsupported shaft walls was carried out according to Bieniawski's RMR_{BIEN} relationship with excavation span (modified by Lauffer, 1988) (Figure 3. During the geotechnical core logging, parameters had been logged according to the Laubscher RMR_{90} classification method owing to the particular software that was being used. These parameters therefore needed to be translated into suitably

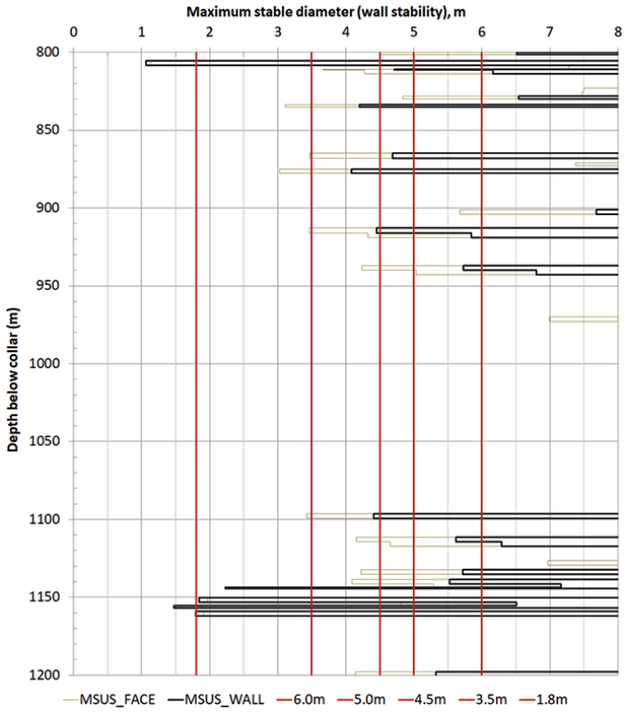

Figure 2—MSUS results for the length of core from 1200 m to 800 m depth below surface for MSUS_FACE and MSUS_WALL

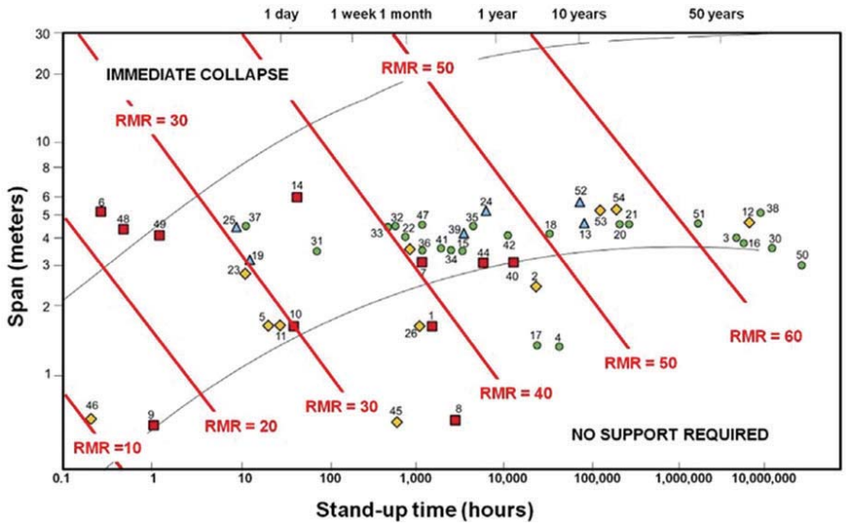

Figure 3—Standup time vs RMR and span (Bieniawski, 2007)

corresponding input values compatible with RMR_{BIEN}. This was achieved by a comparison of descriptors for the two methods and assigning values based on self-similar characteristics. This approach is not ideal and has the potential to result in an underestimation or overestimation of RMR_{BIEN} by up to ten. The relationship between standup time, RMR_{BIEN}, and excavation span is logarithmic, which means that a difference of $RMR_{BIEN} = 10$ can change the interpretation from a standup time of one week ($RMR_{BIEN} = 40$) to 1 year ($RMR_{BIEN} = 50$) for a 6 m diameter shaft.

It is for this reason, among others, that no one parameter should be read in isolation, but the interpretation requires a side-by-side 'reading' of composite results, presented for example in Figure 5.

The minimum required standup time for a raisebored shaft was estimated using the application of Bieniawski, Celada, and Galera (2007) for tunnel boring. For both the standup time and excavation time estimates it is important to remember that the empirical methods were developed for horizontal tunnels. Some selective 'engineering interpretation' is therefore necessary to apply adjustments for vertical orientation with respect to geotechnical conditions.

Estimates of raiseboring advance rates also affect the interpretation of required standup time. As this is an area that appears still to be relatively loosely documented, there is scope to investigate this further. For this project, an average advance rate of 10.5 m was estimated for the shaft (accounting for variable advance rates as a function of lithology type) using the TBM approach of Bieniawski, Celada, and Galera (2007). However, in line with findings from available literature (Anderson and Cox, 1991; Hickson, 1998) and personal communication with contractors, an advance rate in the order of 3.5 m per day was planned and achieved. The TBM estimation approach was found to be not well suited to estimating raisebore advance rates in this case. Nonetheless, the outcome was that for a 1200 m long shaft, and the shaft walls would need to be stable for at least six months or more, which requires 'good' ground (Peck, Coombes, and Lee, 2011) for the site.

One of the sites that were rejected for the planned shaft location contained a total of 15 discrete locations, each in excess of 3 m long, distributed along the length of the shaft axis from 1200 m to surface, for which $RMR_{BIEN} < 45$, *i.e.* less than one month standup time. This suggested that there was too high a risk associated with the site, and combined with the collective geotechnical indicators, presented a case for investigating an alternative location.

Stress-driven failure and SRF

The investigation into potential stress-driven failure or 'dog-earing' (spalling) through the selection of an appropriate stress reduction factor (SRF) was the subject of extended debate within the project. The SRF value is significant because it scales down the resulting RMC values by a factor that can range widely between a minimum of less than 2.5 and a maximum of more than 100, depending on the relationship between stress and rock strength. This has a major impact on the resulting rock mass class for the logging interval.

Based on somewhat limited local stress field information, the initial estimates of stress-driven failure potential led to overly conservative expectations of spalling potential. Initially, for the selection of an SRF value, the recommended approach of Peck, Coombes, and Lee (2011) was applied. The studies that comprise the empirical data of Peck, Coombes, and Lee (2011) are largely sourced from Australian locations, for which stress-driven effects are more telling than for this project located in South Africa. In contrast, observations of underground conditions on this project indicated that excessive stress-driven failure at depth (> 1000 m) was not to be expected. Similarly, results from the empirical estimate of dog-earing (spalling) using the approach of Martin, Kaiser, and McCreath (1999) also indicated greater potential for failure than observed on the operation. This created a conflict between 'theoretical' guidelines, field observations, and results from previous numerical analyses on the operation.

A serious outcome for the project was that the risk analysis based on stress effects appeared to be 'overly conservative' and created some uncertainty in interpreting the data. By applying the Australian approach too diligently in the initial investigation, it became apparent that the results were not in line with actual rock mass behaviour on the operation. As a result, it was necessary

to adjust the analysis going forward, but not before this had had a disastrous effect for the project when one of the shafts was excavated in unsuitable ground, which is discussed in a subsequent section.

Going forward, estimates of stress-driven rock mass response based on the approaches of Peck, Coombes, and Lee (2011) and Martin, Kaiser, and McCreath (1999) were rejected based on local observations of rock mass behaviour at the operation. Instead, an SRF value for each logging interval was selected in accordance with Barton's guidelines for local 'shear' or weakness zones (Barton, 2002). This approach was regarded as more appropriate in this environment, in which failure is largely governed by gravity-driven kinematic failure.

Wedge failure potential

To obtain a reliable estimate of the potential for wedge failure, it was necessary to extract joint set information from the geotechnical investigation holes. This was carried out through a combination of local in-pit field mapping, downhole geophysics (televiewer logs), and vertical core orientation. Vertical core orientation frequently presents a 'rotational' error challenge. Also, in a magnetite-influenced environment such as this one, televiewer orientation can be similarly problematic, being reliant on magnetic orientation. However, within a limited extent of intervals, say, 50–100 m, it is considerably less important in a circular shaft to obtain 'absolute' orientations than relative orientations, given that the dip angle can be determined reliably relative to the horizontal. While the absolute orientations were not confidently established, it was nonetheless possible to generate size, shape, and factor of safety (FoS) distributions for potential wedge failures over limited intervals using the relative dip direction orientations, spacings, and joint surface conditions of the respective joint sets.

From this data, the maximum wedge sizes (using Unwedge, a Rocscience application(Figure 5) and probability distribution of potential wedge failures (using the application JBlock, Figure 4) (Esterhuizen and Streuders, 1998) were generated. Based on these results, it was concluded that without support, blocks in the order of 5 m³ (15 t) could be expected to fail. Investigations were carried out to assess the PoF for wedges greater than 1 m³ with or without shotcrete and with or without tendons (Figure 4). It was determined that with, say, shotcrete alone, up to 16% of all the failed blocks would be larger than 1 m³, whereas with tendon support, this would be reduced to 0.5%. Given that blocks larger than 1 m³ have a mass in excess of 3 t, this was significant and led to the conclusion that raiseboring in certain locations would not be feasible without support, and in particular, tendon support.

Note that JBlock analysis has a shortcoming for circular shaft stability analysis, since it generates only 'flat', not circular, release surfaces and does not account for the limiting effect on wedge width as a function of the circular shaft surface. Results obtained with JBlock were therefore compared against the Unwedge analysis to establish an upper limit for potential block failure volume.

Probability of failure (risk analysis)

An understanding of the probability of failure (PoF) goes hand in hand with an integrated reading of the suite of empirical results, which may be presented in several ways. For example, in Figure 5, various data columns stacked side-by-side illustrate the variability of stability indicators down the length of the hole. Typically, these stability and excavability indicators include, among others, QR, MSUS, RQD/Jn (block size indicator), standup time, a stress factor (such as RCF), support requirements, and cutter life or boreability indices. Needless to say, the illustration can become somewhat crowded but it is helpful to obtain an overall impression of the shaft's PoF as a whole.

For this purpose, the McCracken and Stacey (1989) stability chart (Figure 1), as presented by Peck, Coombes, and Lee (2011), together with the relationship for MSUS (Equation [1]) was transformed to present an estimate of PoF for each logged interval along the length of the investigation hole (typically 3 m per interval, Equation [2] and Equation [3]). To translate the 'RSR' term to a PoF, the linear relationship (Equation [3]) was applied, based on RSR = 3.0 being equivalent to a 25% PoF and RSR = 1.3 equivalent to a 5% PoF. At this stage the PoF

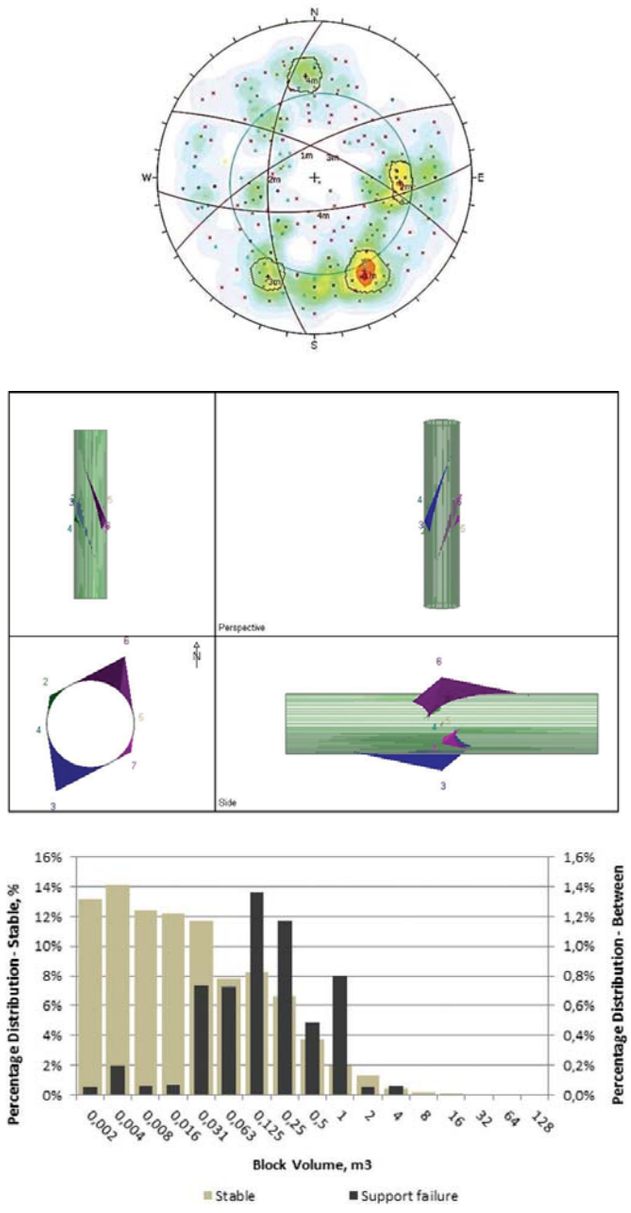

Figure 4—Wedge failure potential estimate with shotcrete (JBlock)

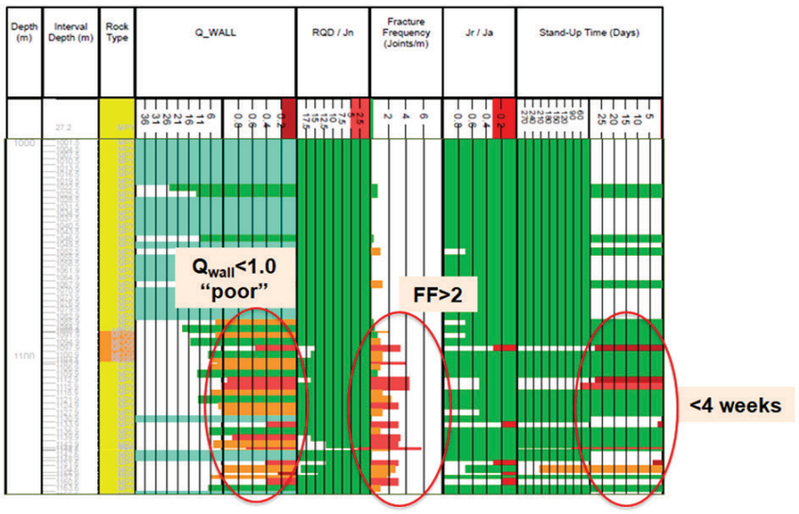

Figure 5—Example plot of composite results to aid interpretation of shaft wall stability

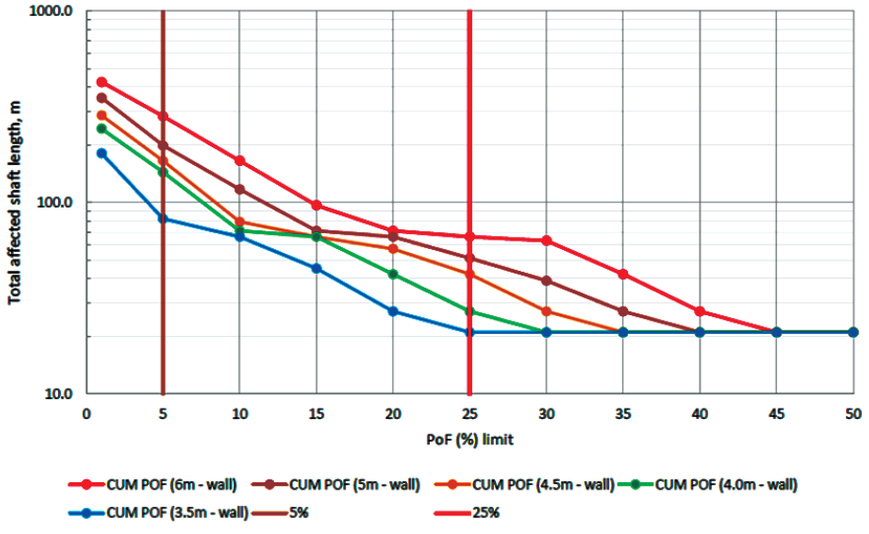

Figure 6—Total affected shaft length (m) with a PoF ≥ threshold (%)

thresholds (25% and 5%) are selected directly from McCracken and Stacey's recommendations (1989); however, to more fully appreciate the associated risk consequence, it would be helpful to associate these risk terms with time and cost factors going forward.

$$RSR = MSUS / (2\ Q_R^{0.4}) \quad [2]$$

$$PoF = 0.1176*RSR - 0.1029 \quad [3]$$

The total length of shaft (m) affected by a certain PoF threshold (say, length of shaft with PoF ≥ 5) for various shaft diameters, was generated (Figure 6). For example, at a particular site, for a 6 m diameter shaft, some 300 m was associated with a PoF ≥ 5%, whereas at the same site, a 3.5 m diameter shaft would have only 80 m with the same PoF ≥ 5%. For the same site, considering a threshold PoF ≥ 25% (unacceptably high risk), some 70 m of a 6 m diameter shaft would be susceptible to this high potential for failure, whereas this would be reduced to around 20 m if the diameter is reduced to 3.5 m. Over a total shaft length of 1200 m, a reduction from 70 m (cumulative total affected length of shaft) to 20 m of unstable ground is sufficiently significant to affect the feasibility of a project. In this manner, it was possible to directly compare the apparent risk of failure associated with shaft diameters to assist in the decision-making process for the project.

Failure analysis (back-analysis)

During the raiseboring of one of the large diameter (6.0 m) shafts for the project, severe failure was experienced which forced an abandonment of the site and revision of the project. An indication of the failure dimensions was obtained from visually recorded block sizes located on the muckpile at the base of the shaft (Figure 7 and Figure 8. Over a distance of some 100 m upwards

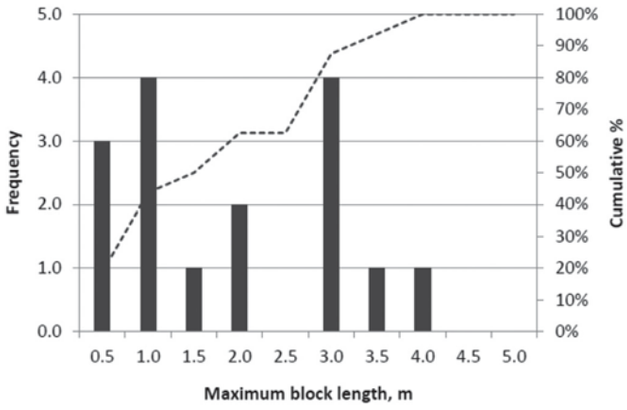

Figure 7—Block lengths (maximum side length) from failed wedges

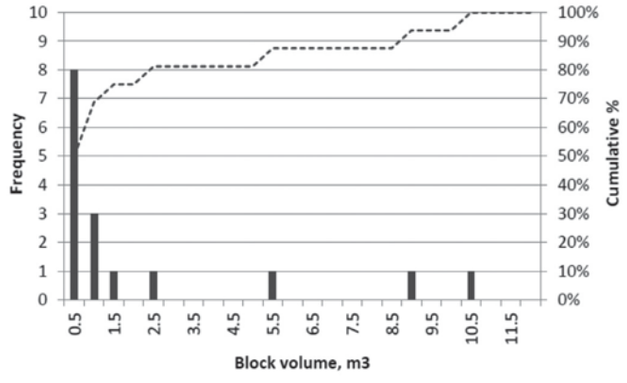

Figure 8—Block volumes (estimated from side lengths) from failed wedges

from the bottom collar, blocks as long as 4.0 m, with volumes in excess of 5 m³ were found to have fallen from the sidewalls of the shaft, with yet more blocks being wedged on top of the reamer.

Several factors were identified as having contributed to this outcome, of which unfavourable rock mass conditions and support deficiencies at the base of the shaft (bottom collar) were noteworthy. An interactive state of unravelling appears to have occurred, commencing at the shaft bottom collar and migrating progressively upwards. A remote camera inspection revealed a cavity estimated to be 20–30 m or more horizontally across. It was not possible to determine with confidence whether the effects of brow failure and subsequent shaft sidewall failure were directly linked. This was because rock mass conditions appeared to be susceptible to failure within the shaft independently of the brow condition. Nonetheless, it was firmly established that stability of the shaft bottom collar is essential to maintain stable conditions and mitigate against progressive wedge failure away from the base of the shaft.

The presence of near-vertical discontinuities also contributed to excessive failure within the shaft. Steep-dipping discontinuities result in shaft wall instability and present a distinct risk to unsupported vertical sidewalls. It is difficult to identify these features during the geotechnical investigation stage due to the combined constraints of small hole diameter and the vertical (sub-parallel) axis of the drill-hole, which precludes intersections with steep-dipping structures. A detailed discussion on the

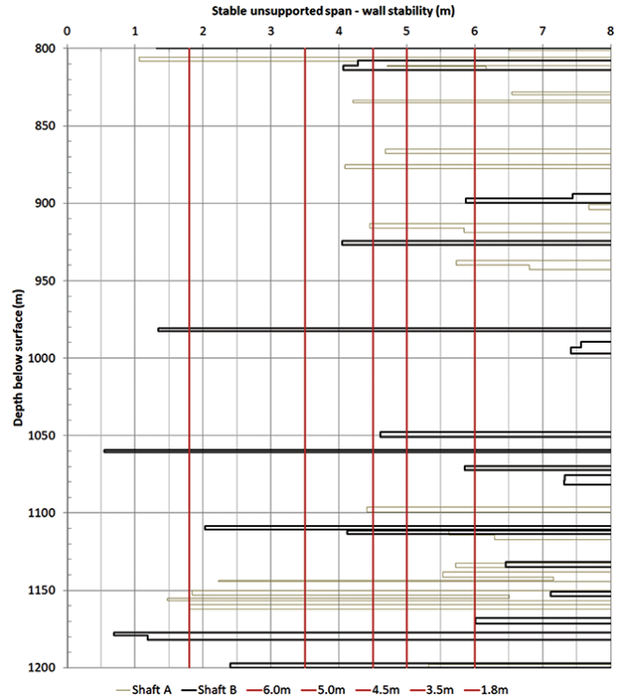

Figure 9—Comparative data for two shafts on the same operation

optimum distribution of geotechnical investigation holes and investigation practices falls outside the scope of this paper. However, for a large-scale, potentially high-risk project, information from several differently orientated investigation holes is vital to avoid overlooking risks for the sake of reducing upfront costs.

For comparison, Figure 9 shows results for MSUS from two separate large-diameter shafts within the same operation in similar rock types and in a similar area. Both sets of results (Shaft A and Shaft B) indicate problematic conditions for a large (> 4.5 m) diameter shaft. However, Shaft A was successful (albeit not without significant challenges) while Shaft B was unsuccessful (this case study, Figure 5). The overall appearance of results for Shaft A indicates intervals in which the shaft walls will be unstable for diameters greater than 4.5 m. However, these intervals are confined to substantially shorter extents and are constrained within more competent intervals, in contrast with the indicators for Shaft A. During execution, Shaft A did indeed suffer some setbacks such as large wedge failure, including, towards the final stages, shearing of the reamer, and the last 30 m was completed by drop-raising. However, the shaft walls as a whole did not suffer extensive failure and in spite of the challenges, the shaft was completed successfully and remains stable following the application of shotcrete. Risk mitigating measures for Shaft B, incorporating in-line remote shotcrete application had been considered but could not be put into effect due to project and technology constraints (> 500 m length shaft).

It is therefore perhaps easier to understand, in the context of 'successfully' completing Shaft A, as well as the difficult, yet successful, completion of an earlier shaft of similar dimensions (5.8 m diameter, 700 m length) within the same operation, that developing Shaft B by raiseboring may have seemed feasible. However, given the overall character of the data and outcome

of the shaft boring attempt, it was made clear that even though previous projects may have been completed successfully, each location needed to be regarded in its own right for feasibility investigationss.

Selection of a suitable shaft sinking methodology

The selection of a suitable excavation method for a project is governed by a number of considerations which can be summed up as either financial (budget and timing) or practical (safety, technology, accessibility, and rock mass conditions). It is always necessary to work within the financial constraints of a project, or there would be no way forward. However, the practical constraints must be similarly regarded in their own right. In a project such as this, where several shafts with similar dimensions (diameter and length) had been successfully completed (albeit not without problems) using raiseboring, it was understandably difficult to consider that the same method may not always work, particularly given the demand for low-cost, rapid completion of a critical shaft.

Unfortunately, conditions within an operation may be variable, as encountered here, with the result that an alternative method of shaft excavation has to be considered. This remains the subject of a current investigation, the results and outcome of which will be presented in a future paper.

Conclusions

The analysis approaches of McCracken and Stacey (1989) together with insights of Peck and associates (Peck 2000; Peck and Lee 2007, 2008; Peck, Coombes, and Lee 2011) were successfully applied to the risk analysis of several planned and completed shaft vertical shafts within a particular underground expansion project. These empirical approaches have certain limitations; nonetheless, when applied with reasonable insight, the method was found to be effective and reliable for the estimation of geotechnical risk associated with a shaft sinking project.

In selecting an appropriate method for developing a large-diameter (> 4.5 m), long (> 500 m) shaft, it is important to remember that technological constraints in conjunction with geotechnical conditions must be considered equally deterministic for a project as timing and financial considerations. The suggested risk tolerance threshold put forward by McCracken and Stacey, *i.e.* PoF ≤ 5% for an unlined, raisebored ventilation shaft, is still considered to be a reasonable criterion, beyond which alternative locations, risk indicators, or sinking methods must be considered.

It is helpful and worthwhile to supplement the empirical analysis of rock mass stability with analyses such as susceptibility to wedge (kinematic) failure and stress-driven deformation, and these analyses should be carried out for any shaft-sinking investigation. In order to achieve this, orientated structural data should be gathered not only from vertical investigation holes sited as close as practically possible to the planned shaft axis (accounting for limitations associated with the sinking method), but also from inclined investigation holes to detect sub-parallel (near-vertical) structures. It is furthermore vitally important to take into account observations of local conditions, together with literature and numerical studies, in decision-making. For this project, the rejection of stress-based estimations of failure in favour of the influence of 'shear structures' (SRF) was considered to be appropriate.

Going forward, it would be of great value to supplement the available empirical database with records of successful and unsuccessfully raisebored shafts in the order of ≥ 4.5 m diameter and ≥ 500 m in length as part of a research initiative. This would assist in improving the overall understanding of the probability of success in large raisebore shaft projects, as diameters upwards of 7.0 m are being pioneered.

Acknowledgements

The author would like to thank the client and contractor(s) (unnamed) for allowing the work to be published and for providing their invaluable insights into the outcomes of the analysis.

References

Andersen, N. 2015. Pre-sink shaft safety analysis using wireline geophysics. *Journal of the Southern African Institute of Mining and Metallurgy*, vol. 115. pp. 435–439,

Anderson, J.M. 1991. Optimisation of raisebore size. *AusIMM Proceedings*, no. 1. pp. 39–43.

Barton, N. 2002. Some new Q-value correlations to assist in site characterisation and tunnel design. *International Journal of Rock Mechanics & Mining Sciences*, vol 39. pp. 185–216.

Barton, N.L. 1974. Engineering classification of rock masses for the design of tunnel support. *Rock Mechanics*, vol. 6, no. 4. pp. 189–236.

Bieniawski, Z.T. 1973. Engineering classification of jointed rock masses. *Transactions of the South African Institution of Civil Engineers*, vol. 15. pp. 335–344.

Bieniawski, Z.T. 1989. Engineering Rock Mass Classifications, a Complete Manual for Engineers and Geologists in Mining, Civil, and Petroleum Engineering. Wiley, New York.

Bieniawski, Z.T., Celada, B., and Galera, J.M. 2007. Predicting TBM excavability. *Tunnels and Tunnelling International,* September. pp. 25–28

Esterhuizen, G.S. and Streuders, S.B. 1998. Rockfall hazard evaluation using probabilistic keyblock analysis. J*ournal of the South African Institute of Mining and Metallurgy*, vol. 98, no. 2. pp. 59–63.

Hickson, P.W. June 1988. Six metre raiseboring at Z C Mines. *Proceedings of the AusIMM North West Queensland Branch, Underground Operators' Conference*, June 1988. Australasian Institute of Mining and Metallurgy, Melbourne.

Laubscher, D.H. 1990. A geomechanics classification system for the rating of rock mass in mine design. *Journal of the South African Institute of Mining and Metallurgy*, vol. 90, no. 10. pp. 257–273.

Martin, C.D., Kaiser, P.K., and McCreath, D.R. 1999. Hoek-Brown parameters for predicting the depth of brittle failure around tunnels. *Canadian Geotechnical Journal*, vol 36. pp. 136–151.

McCracken, A. and Stacey, T.R. 1989. Geotechnical risk assessment for large-diameter raise-bored shafts. *Transactions of the Institution of Mining and Metallurgy, Section A: Mining Industry*, vol. 98. pp. A145–A150.

Peck, W.A. 2000. Determining the stress reduction factor in highly stressed jointed rock. *Australian Geomechanics*, vol. 35, no. 2. pp. 57–60.

Peck, W.A. and Lee, M.F. 2007. Application of the Q-system to Australian underground metal mines. *Proceedings of the International Workshop on Rock Mass Classification in Mining*, Vancouver. pp. 129–140. NIOSH, Cincinnatti, OH.

Peck, W.A. and Lee, M.F. 2008. Stability of raise bored shafts in Australian mines. *Proceedings of the 13th Australian Tunneling Conference*. Australasian Institute of Mining and Metallurgy, Melbourne. pp. 331–337.

Peck, W.A., Coombes, B., and Lee, M.F. 2011. Fine-tuning raise bore stability assessments and risk. *Proceedings of the 11th AusIMM Underground Operators' Conference*. Australasian Institute of Mining and Metallurgy, Melbourne. pp. 215–226.

Stacey, TR. and Harte, N.D. 1989. Deep level raise boring - Prediction of rock problems. *Proceedings of the ISRM Symposium: Rock at Great Depth*, Pau, France. Maury, V. and Fourmaintraux, D. (eds.). Balkema, Rotterdam. pp. 583–588. ◆

Laser surface deposition of niobium and titanium-niobium on Ti6A14V substrates for biomedical applications

S.L. Pityana[1,2], N. Baloyi[1], M. Tlotleng[2,3], and P. Popoola[1]

Affiliation:
[1]Tshwane University of Technology, Pretoria, South Africa
[2]CSIR, Pretoria, South Africa
[3]University of Johannesburg, South Africa

Correspondence to:
S. Pityana

Email:
SPityana@csir.co.za

Dates:
Received: 31 May 2016
Revised: 21 Feb. 2018
Accepted: 14 Nov. 2018
Published: April 2019

How to cite:
Pityana, S.L., Baloyi, N., Tlotleng, M., and Popoola, P. Laser surface deposition of niobium and titanium-niobium on Ti6A14V substrates for biomedical applications. The Southern African Insitute of Mining and Metallurgy.

DOI ID:
http://dx.doi.org/10.17159/2411-9717/16/211/2019

ORCiD ID:
https://orchid.org/0000-0002-9273-2043

Synopsis

The advantages of using Nb and Ti-Nb coatings for improving the hardness and corrosion resistance of Ti6Al4V were investigated. It has been reported that Ti6Al4V used in orthopaedic implants tends to release toxic Al and V ions into the surrounding tissue. Thin layers of Nb and Ti-Nb were deposited on Ti6Al4V substrates using a laser metal deposition technique. The deposited material was analysed using optical microscopy, scanning electron microscopy coupled with energy dispersive spectroscopy, and X-ray diffraction. The corrosion behaviour of the deposited layers was investigated using a Metrohm Autolab PG Stat101 compact potentiostat at 25°C in simulated body fluid. A Vickers hardness system was used to study the mechanical properties. Both Nb and Ti-Nb coatings exhibited good metallurgical bonding with the substrate. The microstructure and the XRD analyses for the Nb system showed that the α-Nb phase was most dominant, while the Ti-Nb system comprised a mixture of the α and β phases. The average hardness of the Ti6Al4V substrate was 350 $HV_{0.3}$, with a slight increase for the Nb coating (363 $HV_{0.3}$) and a much higher hardness from the Ti-Nb coating at 423 $HV_{0.3}$. The corrosion results show that the deposited Nb was more corrosion-resistant in the solution than either the Ti6Al4V substrate or the Ti-Nb coating.

Keywords
Corrosion, laser surface deposition, niobium (Nb), titanium (Ti), titanium-niobium (Ti-Nb), Ti6Al4V.

Introduction

Metals such as CoCrMo, 316L stainless steel, and NiTi alloy are used for manufacturing biomedical implants because of their distinct properties, including low Young's modulus and resistance to corrosion (Ryan, Pandit, and Apatsidis, 2006). These implants are required to remain in the body of the patient for many years. Due to a favourable combination of mechanical and corrosion properties, titanium (Ti) and its alloys have emerged as the material of choice for biomedical implants. Nevertheless, their use is not entirely without challenges. For example, in total hip replacement, surface degradation and release of metal debris from metal erosion caused by friction limit the service life of the implant (Oldani and Dominguez, 2012; Manivasagam, Dhinasekaran, and Rajamanickam, 2010). Ti6Al4V is generally regarded as the material of choice, but it has been found that over extended periods of time, the combination of surface corrosion and erosion releases toxic aluminium (Al) and vanadium (V) ions into the body (Khan, Williams, and Williams, 1996). This has led to the investigation of titanium alloys containing niobium (Nb), zirconium (Zr), tantalum (Ta), and molybdenum (Mo) as substitutes for the aluminium- and vanadium-containing Ti6Al4V (Okazaki *et al.*, 1997).

The objective of this work is not to alter the mechanical properties of Ti6Al4V, but rather to improve its surface properties by deposition of a biocompatible layer with improved wear resistance when subjected to friction. It is known that the titanium matrix can be stabilized as the α-Ti (hcp) or β-Ti (bcc) phase, depending on the element used; and it is acknowledged that alpha and beta alloys have different mechanical properties (Petrzhik, 2013). According to Rosenberg, Starosvetsky, and Gotman (2003), Zorn *et al.,* (2005), and Godly, Starosvetsky, and Gotman (2004), Nb alloys are noteworthy due to their remarkably low elastic modulus, excellent corrosion resistance, and the presence of a metastable β phase when dissolved in the Ti structure (Oldani and Dominguez, 2012; Kuphasuk *et al.*, 2001). As a result, the β-Nb phase has a higher hardness than Ti6Al4V. This β-Nb phase is also useful as it creates a passive layer when exposed to a corrosive environment such as body fluid (Kuphasuk *et al.*, 2001; Lee, Ju, and Chern Lin, 2002).

In this work, Nb and a mixture of Nb and Ti were investigated as surface coatings on a Ti6Al4V substrate. Thin layers of Nb and Ti-Nb were deposited on Ti6Al4V substrates using a laser deposition technique. The corrosion behaviour of the coatings was determined in a simulated body fluid (SBF) environment using a Metrohm Autolab PG Stat101 compact potentiostat at 25°C.

Table I

Powder specifications and process parameters for laser deposition

Type of alloy	PSD (µm)	Composition (wt% Nb)	Power (kW)	SS (mm.s^{-1})	BD* (mm)	PFR* (r.min^{-1})	Carrier gas flow (L.min^{-1})
Nb	210-10	100	0.5, 1.0, 1.2	9	4	3	5
Ti-Nb	350-10	87-13	1.0, 1.2, 1.5	9	4	3	5

* PSD: particle size distribution; SS: scanning speed; BD: beam diameter; PFR: power feed-rate

Experimental set-up

Laser deposition

A Rofin Sinar DY044, CW Nd:YAG laser system incorporating a three-way nozzle was used for the deposition. The laser head, mounted on a Kuka robot arm, was set at a standoff distance of 12 mm above the substrate. The laser beam spot and the scanning speed were kept constant at 4 mm and 9 mm.s^{-1}, respectively. Nb was deposited on Ti6Al4V using laser beam powers of 500, 1000, and 1200 W. Similarly, the laser beam power used for depositing Ti-Nb was 1000, 1200, and 1500 W. In order to prevent oxidation, the process was conducted in a rectangular container which was covered and purged with argon gas at 5 L.min^{-1}. The process parameters used in these experiments are summarized in Table I.

Material preparation and characterization

Single and multiple tracks of Nb and Ti+Nb were laser-deposited onto the surface of Ti6Al4V. The Nb powder had a mean particle size (d_{50}) of 100 µm. The Ti-Nb powder was obtained by mechanical mixing and pre-alloying of elemental Ti and Nb powders, using a Restch PM 400M ball mill. The particle size range of the pre-alloyed Ti-Nb powder was 10–50 µm. Ti6Al4V substrate specimens, with dimensions of 30 × 30 × 8 mm, were sandblasted and cleaned with acetone prior to the laser metal deposition process.

After deposition, the samples were sectioned in the transverse direction through the deposited layer for phase and microstructure analyses. The sectioned samples were mechanically polished and etched with either Keller's (Nb coatings) or Kroll's (Ti-Nb coatings) reagents. The microstructures of the Nb and Ti-Nb layers were examined by optical microscopy and scanning electron microscopy (SEM) using a JOEL instrument, and the chemical composition was analysed by SEM using energy dispersive X-ray spectroscopy (EDX). The microhardness of the layers was measured using a Matsuzawa Vickers hardness tester with a load of 300 g at intervals of 100 µm from the top of the cladding to the cladding-substrate interface.

Phase analyses of the clad layers were performed by X-ray diffraction (XRD) at 40 kV and 30 mA. X-ray crystallography was performed using a Ni-filtered Cu K radiation source. Their matching phases were identified with the characteristic peaks of those in the files of the Joint Committee on Powder Diffraction Standards (JCPDS) references (JCPDS, 1995).

Polarization and qualitative electrochemical impedance spectroscopy measurements on the coated surfaces were carried out in 50 ml of Hanks solution at room temperature (approx. 25°C) using a Metrohm Autolab PG Stat101 compact potentiostat, consisting of a three-electrode cell: a saturated calomel electrode (Hg/Hg_2Cl_2) in saturated KCl as the reference electrode and platinum as the counter-electrode. The samples were placed in a glass cell and a sample area of approximately 1.1 cm^2 was exposed to the electrolyte. The system was interfaced with a computer to determine the open circuit potential (OCP). The anodic and cathodic Tafel plots were recorded using NOVA software.

Results and discussion

Optical and scanning microscopy

The microstructures of typical single-layer Nb and Ti-Nb coatings produced by the laser deposition process on Ti6Al4V substrates are shown in the optical images in Figure 1. The images show that the deposited layers had bonded well with the substrate metal and formed coatings. The metallurgical interaction between the coatings and the substrate is more visible in the case of the Ti-Nb coating, which displays a pronounced dilution region as shown by the arrow in Figure 1b. The large, visible pores in the coatings are thought to be due to vaporization of the coating material. Of note is the good metallurgical bond between the cladding and the substrate.

Figure 2 shows optical micrographs of the cross-sections of the thin Nb layers deposited on the Ti6Al4V substrate at laser powers of 500 W, 1000 W, and 1200 W. The images indicate the presence of honeycomb structures at 500 W, a mixture of honeycomb and needle-like structures at 1000 W, and needle-like structures at 1200 W.

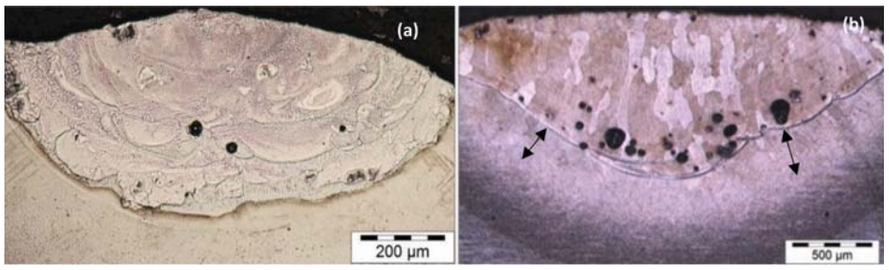

Figure 1—Typical single laser-deposited tracks of (a) Nb and (b) Ti-Nb coatings

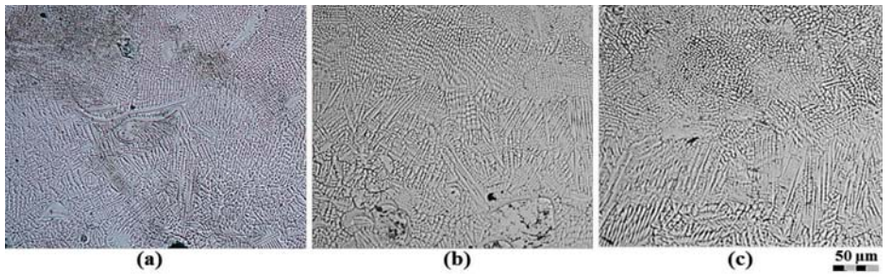

Figure 2—Cross-sections of Nb coatings deposited at (a) 500 W, (b) 1000 W, and (c) 1200 W

Table II

EDX analysis (wt%) of Nb coatings deposited at different laser powers

Element	500 W	1000 W	1200 W
C	4.77	5.26	3.84
O	2.31	1.83	1.71
Al	1.86	1.88	2.14
Ti	27.87	33.09	41.65
V	1.13	1.23	1.89
Nb	62.05	56.71	48.76

Table III

EDX analysis (wt%) of Ti-Nb coatings deposited at different laser powers

Element	1000 W	1200 W	1500 W
C	6.14	5.56	5.83
O	4.35	4.37	5.13
Al	3.34	3.91	3.09
Ti	75.23	77.74	74.28
V	1.98	1.81	1.41
Nb	8.95	6.59	10.26

Table II lists the compositions of the Nb coatings. The data indicates the effect of laser power on the dilution effect of Nb deposited coating in terms of Nb, Ti, Al, and V content. At 500 W laser power, the Nb content is 62%, decreasing markedly as the laser power increases. This decrease is attributed to increased dilution of Nb by the Ti matrix. The contents of Al and V remain within the range 1–2%, which is lower than that of Ti6Al4V (substrate).

Figure 3 shows optical micrographs of the cross-sections of the Ti-Nb layers deposited at different laser powers. Due to the effect of pre-alloying Nb and Ti, the microstructures obtained from this combination are fine and granular. The grain size varies with increasing laser power due to slow cooling.

Table III shows the EDX analyses of the Ti-Nb coatings deposited at different laser powers. The composition of the coating does not follow any trend with relation to change in laser power. The concentration of Al and V remained in the range 1.5–4%, whereas the Nb content varied from 6.5% to 10%.

X-ray diffraction

Figure 4 shows the XRD patterns of the Nb and Ti-Nb coatings deposited at various laser powers. There are no significant phase changes in either system when the laser power is increased. The pattern for Nb shows an orthorhombic (α') phase and a metastable β phase. The α' phase is attributed to the Ti6Al4V substrate; and the β phase is due to the Nb in the melt pool. The XRD results for the Ti-Nb system also show the occurrence of hexagonal (α' '-Ti) phase and the presence of β phase that seem to occur at the same angle for all the samples.

Microhardness

Microhardness profiles of the Nb and Ti-Nb deposits are shown in Figure 5. Figure 5a represents Nb deposition at various powers. All the curves indicate that hardness increases from the top of the layer to the heat-affected zone (HAZ) and then decreases again towards the substrate. Figure 5b depicts the profile for Ti-Nb deposition at various powers. All the curves indicate a steady decrease in hardness value from the top of the cladding to the HAZ and the substrate. The average hardnesses of the deposited materials relative to the substrate are plotted in Figure 6. The Nb deposit has an average hardness of 363 $HV_{0.3}$ on the points taken on the deposited layer and 350 $HV_{0.3}$ closer to the substrate. The average hardness of the Ti-Nb deposit was 423

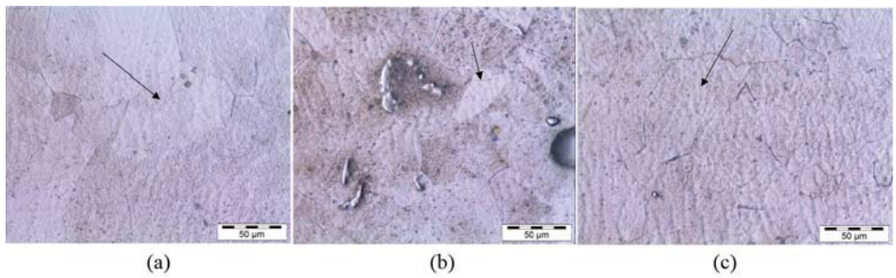

Figure 3—Cross-sections of Ti-Nb coatings deposited at (a) 1000 W, (b) 1200 W, and (c) 1500 W

$HV_{0.3}$, the hardness of the layers gradually decreasing to that of the substrate. This trend was apparent in all the layers. In this system (Ti-Nb), a hardness improvement was observed and the hardness of the deposit was approximately 70 $HV_{0.3}$ higher than that of the substrate.

Figure 6 represents the microhardnesses of the materials. Nb coatings show variable hardness behaviour, with an average hardness of 364 $HV_{0.3}$. Ti-Nb coatings display a steady decrease in hardness, with depth Figure 5b), with an average hardness value of 423 $HV_{0.3}$. This indicates that Ti had a positive effect on the coatings, due to the presence of harder phases.

The increase in hardness value for Nb coatings was approximately 5%, which is attributed to dilution of Nb by the substrate. The 8.4% increase in hardness for the Ti-Nb coatings is due to the presence of *α*-Ti, which results in a martensitic microstructure.

Corrosion behaviour

The potentiodynamic polariZation curves of all the Nb coatings in simulated body fluid (Hanks solution) electrolyte, under a standard working environment are plotted in Figure 7. The results presented were selected because of the nearest mean values of the current densities, and they indicate constant behaviour, especially during the first five minutes of immersion. The Tafel calculations have been deduced from the available data and are reported in Table IV.

The joint polarization curves in Figure 7 and the results in Table IV illustrate that the Nb coatings have better corrosion properties than the Ti-Nb coatings and the substrates. It is also observed that the corrosion potential (E_{corr}) of the Ti-Nb coating was slightly lower than that of the substrate (Table IV), while the Nb coating had the highest E_{corr}, 0.709 V higher that of Ti-Nb.

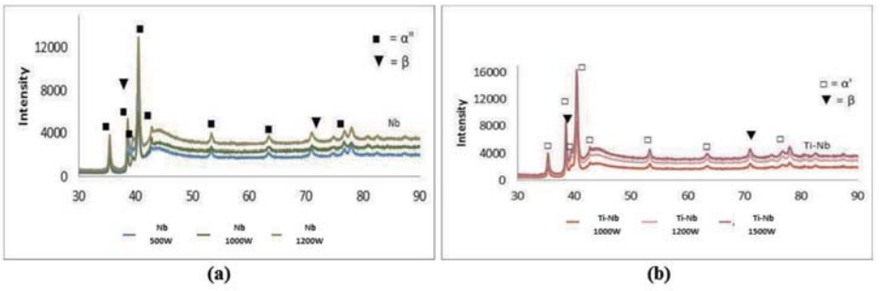

Figure 4—X-ray diffraction (XRD) patterns of laser-deposited (a) Nb and (b) Ti-Nb coatings

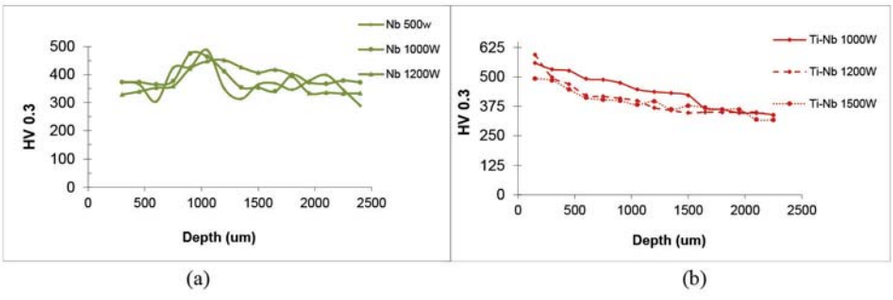

Figure 5—Hardness profiles measured from the edge of the coating. (a) Nb and (b) Ti-Nb

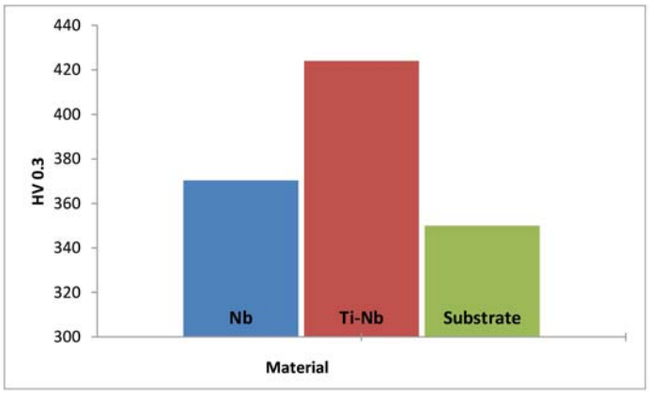

Figure 6—Average microhardness property plots for Nb and Ti-Nb coatings

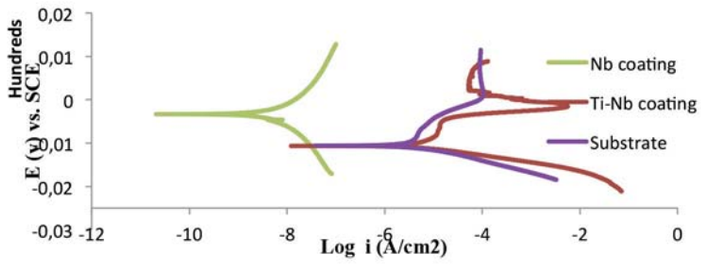

Figure 7—Potentiodynamic polarization curves of Ti-Nb and Nb deposited onto Ti6Al4V after immersion in a Hanks solution electrolyte at the standard condition

The Nb coating also exhibits the lowest corrosion current density while the Ti-Nb coating and the substrate displayed similar i_{corr} values in the same decade. This also indicates that the Nb coating is more corrosion-resistant.

According to Osorio *et al.,* (2011), the corrosion resistance of alloys depends on the microstructure and the presence of defects. This was also observed in this study. The coatings with microstructures formed in the presence of oxide layers showed passivation behaviour and consequently mitigate against further corrosion. This is seen in the microstructures of the Nb coatings; the highest resistance to corrosion was exhibited where less dilution and fewer pores were present. Furthermore, these coatings had the lowest hardness due to the low Ti content. All these factors are connected to the latent heat of materials. During heating, niobium reacted with oxygen to form an oxide layer that is resistant to corrosion. Furthermore, the refractory nature of Nb also contributes to its corrosion resistance. Similar to Nb, molten Ti (Ti-Nb) would easily react with oxygen and form a passive TiO_2 layer, which is also corrosion-resistant. This corrosion reaction of Ti-Nb seems to resemble that which occurs on Ti6Al4V surfaces when exposed to simulated body fluids, as explained by Mythili, *et al.,* (2007). The overall performance of Nb surpassed that of Ti-Nb and Ti6Al4V; irrespective of the passive layer and improved hardness due to the presence of TiO_2, the Nb coating performed better in Hanks solution.

Conclusions

Nb and Nb-Ti were successfully coated onto Ti-6Al-4V alloy substrates using laser deposition. The hardness and corrosion behaviour of the coatings were investigated, resulting in the following observations.

- Ti-Nb deposited on the Ti6Al4V substrate resulted in a fine microstructure consisting of α' and β phases that have a higher hardness than that of the substrate. This alloy displayed a similar corrosion resistance to the Ti6Al4V substrate.
- Nb deposited on the Ti6Al4V substrate resulted in a dendritic microstructure with an uneven hardness profile. The XRD pattern indicated the presence of the α' orthorhombic phase, which is significantly more resistant to corrosion than the substrate and Ti-Nb layers.
- The high latent heat of Nb influences the dilution, microstructure, and hardness of the coating.
- Based on corrosion results alone, Nb-cladded Ti6Al4V will be a better option than Ti-Nb as a coating to improve the surface properties of surgical implants.

Table IV

Corrosion behaviour of the laser-deposited materials

Sample	i_{corr} (A/cm²)	E_{corr} (V)	Corrosion rate (mm/a)
Substrate	4.37E-07	-1.06	1.79E-02
Ti-Nb	9.70E-07	-1.15	4.24E-03
Nb	1.30E-10	-0.33	2.16E-08

Acknowledgements

This paper is based upon work supported financially by the National Research Foundation. The National Laser Centre, CSIR, Pretoria is thanked for use of the laser facility. Appreciation goes to the project initiators, Tshwane University of Technology, and to everyone who assisted with the analyses and interpretation of the results.

References

Godley, R., Starosvetsky, D., and Gotman, I. 2004. Bonelike apatite formation on niobium metal treated in aqueous NaOH. *Journal of Materials Science: Materials in Medicine,* vol. 15, no. 10. pp. 1073–1077.

JCPDS. 1995. Powder Diffraction File. Joint Committee on Powder Diffraction Standards (JCPDS)-International Centre for Diffraction Data (ICDD); Swarthmore, PA, USA: 1995. Card no. 44–1294.

Khan, M.A., Williams, R.L., and Williams, D.F. 1996. In-vitro corrosion and wear of titanium alloys in the biological environment. *Biomaterials*, vol. 17, no. 22. pp. 2117–2126.

Kuphasuk, C., Oshida, Y., Andres, C.J., Hovijitra, S.T., Barco, M.T., and Brown, D.T. 2001. Electrochemical corrosion of titanium and titanium-based alloys. *Journal of Prosthetic Dentistry*, vol. 85, no. 2. pp. 195–202.

Lee, C.M., Ju, C.P., and Chern Lin, J.H. 2002. Structure–property relationship of cast Ti–Nb alloys. *Journal of Oral Rehabilitation*, vol. 29, no. 4. pp. 314–322.

Manivasagam, G., Dhinasekaran, D., and Rajamanickam, A. 2010. Biomedical implants: corrosion and its prevention – a review. *Recent Patents on Corrosion Science*, 2010, no. 2. pp. 40-54. https://pdfs.semanticscholar.org/84c0/a7dcb2a9f567e67ec847801410a6f097c2d2.pdf

Mythili, R., Shankar, A.R., Saroja, S., Raju, V.R., Vijayalakshmi, M., Dayal, R.K., and Balasubramaniam, R. 2007. Influence of microstructure on corrosion behavior of Ti–5% Ta–1.8% Nb alloy. *Journal of Materials Science*, vol. 42, no. 15. pp. 5924–5935.

Okazaki, Y., Kyo, K., Ito, Y., and Tateishi, T. 1997. Effects of Mo and Pd on corrosion resistance of V-free titanium alloys for medical implants. *Materials Transactions, JIM,* vol. 38, no. 4. pp. 344–352.

Oldani, C. and Dominguez, A. 2012. Titanium as a biomaterial for implants. *Recent Advances in Arthroplasty*. InTech. https://www.intechopen.com/books/recent-advances-in-arthroplasty/titanium-as-a-biomaterial-for-implants

Osorio, W.R., Mountinho, D.J., Peixoto. L.C., Ferreira, I.L., and Garcia, A. 2011. Macrosegregation and microstructure dendritic array affecting the electrochemical behavior of ternary Al-Cu-Si alloys. *Electrochimica Acta,* vol. 24. pp. 8412–8421.

Petrzhik, M. 2013. Dynamics of martensitic structure at TiNb-based quenched alloys under heating and loading. *Journal of Physics: Conference Series*, vol. 438, no. 1. p. 012020. IOP Publishing. http://iopscience.iop.org/article/10.1088/1742-6596/438/1/012020

Rosenberg, R., Starosvetsky, D., and Gotman, I. 2003. Surface modification of a low modulus Ti-Nb alloy for use in medical implants. *Journal of Materials Science Letters,* vol. 22, no. 1. pp. 29–32.

Ryan, G., Pandit, A., and Apatsidis, D.P. 2006. Fabrication methods of porous metals for use in orthopaedic applications. *Biomaterials*, vol. 27, no. 13. pp. 2651–2670.

Zorn, G., Gotman, I., Gutmanas, E.Y., Adadi, R., Salitra, G., and Sukenik, C.N. 2005. Surface modification of Ti45Nb alloy with an alkylphosphonic acid self-assembled monolayer. *Chemistry of Materials*, vol. 17, no. 16. pp. 4218–4226. ◆





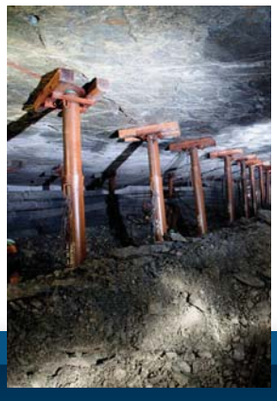



SAIMM
THE SOUTHERN AFRICAN INSTITUTE OF MINING AND METALLURGY

SA MINING SUPPLY CHAIN
CONFERENCE AND STRATEGY WORKSHOP

22-23 May 2019

Bateleur Conference Venue, Nasrec, Johannesburg

(parallel to Southern African Local Manufacturing Expo)

LOCAL SOUTHERN AFRICAN Manufacturing Expo
Industry ▸ Construction ▸ Mining ▸ Agriculture ▸ Power

Local is lekker
Creating capacity and capability for mining companies to buy local

This conference and workshop is aimed at creating awareness of new supply chain requirements as included in Mining Charter 3, and at creating capacity and capability in South Africa to be able to meet these requirements, whether this be for consumables, capital goods or services.

Attendees at this event will therefore get insight into the roles and objectives of the MMP, MEMSA and SAMPEC, and the assistance they can give.

22 May 2019 CONFERENCE TOPICS

- The SA Mining Supply Chain - strength, weaknesses, opportunities, threats
- Implications of Mining Charter 3 for the SA supply chain
- Successful supplier development - Case Studies
- Measuring and maximising local content
- Standards and codes - potential game changers

23 May 2019 WORKSHOP TOPICS:

- Strategies to build the local mining supply chain
- The potential role of an SA mining services cluster

WHO SHOULD ATTEND

- Mining company executives
- Procurement Managers
- Commercial managers
- South African original equipment manufacturers (OEMs)
- International OEMs with local manufacturing footprint
- Members of MEMSA, SAMPEC, VAMCOSA, and other supply chain clusters
- Consultants
- Advisers
- Government departments and officials
- Researchers
- Mining contractors and EPCMs
- Mining service companies

PREMIUM SPONSOR

MANDELA MINING PRECINCT
MINDS FOR MINES

PARTNERS

MEMSA
MINING EQUIPMENT MANUFACTURERS OF SOUTH AFRICA

SAMPEC
SOUTH AFRICAN MINERAL PROCESSING EQUIPMENT CLUSTER

FOR FURTHER INFORMATION CONTACT:
Yolanda Ndimande · Conference Co-ordinator · SAIMM
E-mail: yolanda@saimm.co.za · Tel: +27 11 834 1273/7 · Website: www.saimm.co.za

Limiting the influence of extreme grades in ordinary kriged estimates

A. Fourie[1], C. Morgan[2], and R.C.A. Minnitt[3]

Affiliation:
[1]Harmony Gold Mining Company Limited, Welkom, Free State, South Africa
[3]Harmony Gold Mining Company Limited, South Africa

Correspondence to:
A. Fourie

Email:
Dries.fourie@vodamail.co.za

Dates:
Received: 25 May 2018
Revised: 26 Sep. 2018
Accepted: 21 Aug. 2018
Published: April 2019

How to cite:
Fourie, A., Morgan, C., and Minnitt, R.
Limiting the influence of extreme grades in ordinary kriged estimates.
The Journal of the Southern African Insitute of Mining and Metallurgy

DOI ID:
http://dx.doi.org/10.17159/2411-9717/18/090/2019

ORCHiD ID:
https://orchid.org/0000-0001-9403-1008

Synopsis

The management of outlier grades in positively skewed gold distributions is a contentious issue. Incorporating outliers in standard ordinary kriging (OK) estimation procedures in a way that honours the data without smearing extreme grades into surrounding areas has been problematic. Cutting or capping of outliers to mitigate their influence in estimation techniques is common practice, while methods that manipulate the OK system of equations fail to honour the data. We propose a method of post-processing of kriging weights that provides realistic OK estimates and mitigates smearing without manipulating kriging equations or changing the original grades. The method requires that the data is not clustered, is approximately equally spaced, and is of the same support. Positively skewed data is ordered on attribute grade and nonlinearly transformed to a Gaussian histogram of categorical bins whose frequency is based on their likelihood of occurrence and location in the sample distributions. Factors that restrict kriging weights are calculated by dividing the percentage frequency of data in each bin by the percentage frequency of data in the bin with the highest frequency. Restriction factors applied to the kriging weights in the OK estimation restrict the range of influence in proportion to their probability of occurrence in the distribution. Smear reduction post-processing is easy to implement and addresses issues arising from negative kriging weights while considering the spatial location of samples, the sample grades, and their probability of occurrence. The method mitigates both smoothing and conditional bias .

Keywords
Outliers, reduced smearing post-processing, range of sample influence.

Introduction

Outliers are sample observations that deviate considerably from the standard or expected (Hawkins, 1980). These deviations can be high or low in grade depending on the distribution. The presence of outliers in a mine sampling campaign could provoke mixed reactions. Mining engineers might view high-grade outliers as a promise of achieving higher grades, while the geostatisticians view outliers as affecting the accuracy and precision of the overall estimate, among other issues. Having identified outliers, the geostatistician must decide how to account for their presence and treat them so that true underlying estimates are not distorted. Advanced knowledge of the deposit allows the geostatistician to identify and treat outliers acceptably, especially where samples are limited in number and the true grade distribution is uncertain. If ignored, or treated incorrectly, outliers are likely to lead to smearing of extreme grades into the surrounding estimates, thereby steering regions towards potential under- or over-estimation.

Methods of identifying outliers, the way they arise, and ways of dealing with them are considered. A description of current approaches to dealing with the smearing effects of outliers in kriging estimates is followed by a new method for mitigating over- and under-estimation of grade in areas immediately adjacent to outliers. Restriction factors are calculated and applied in a post-processing step to all kriged values, constraining smearing effects to an appropriate area around the outliers. The effectiveness of the method is demonstrated using face chip sample results taken along a raise in a deep-level gold mine in the Free State Province of South Africa.

Kriging, as with all minimum mean-square error spatial estimators, tends to smooth estimates due to its weighted averaging routine (Isaaks and Srivastava, 1988; Deutsch and Journel, 1998). Smoothing of kriged estimates can be detected and modelled using cross-validation, but the method also results in systematic errors and an inability to reproduce the semivariogram (Olea and Pawlowsky, 1996). Ordinary kriged estimates using data containing uncapped outliers are compared with the newly proposed method of post-processing ordinary kriging (OK) weights. The method applies a weight reduction factor based on the likelihood of outlier occurrence and the restrictions on their spatial continuity. Issues related to honouring

the data and negative kriging weights associated with an outlier are considered. This tool provides more reliable and realistic OK estimates in areas surrounding outliers.

Identifying and dealing with outliers

Outliers could be the result of sampling or assaying error, or could simply be due to the highly erratic nature of the grades in the orebody. Nevertheless, the user must decide whether to accept or reject unrepresentative or outlying observations in the data-set (Barnett and Lewis, 1979). Many orebodies display highly skewed distributions (Krige, 1999), with sample observations from the tail of the distribution often being considered as extreme grades or outliers. The presence of outliers in a small sample set introduces many problems, including excessive variability into measures such as mean and variance, and under- or over-estimation or smearing of extreme grades (Sinclair and Blackwell, 2004).

Outliers may be capped or removed from the data-set, or treated as a separate population (Sinclair and Blackwell, 2004), but assuming sampling and assaying are correct, the outlier must be considered a legitimate member of a continuous population distribution (Krige, 1999) and cannot be ignored. Ordinary kriging, a linear weighting estimation method, is known to smear outlier grades into surrounding areas (Pan, 1994), especially where sample numbers are limited. With limited data, outliers can disproportionately inflate the tail-end estimates of a distribution relative to the true grades. The proposed post-processing solution avoids the smearing of outlier grades into surrounding areas where sample coverage is limited once outliers in the sample data have been identified.

Sampling methods

Poor sampling methods introduce not only error or bias in sample assay results (Gy 1979, 1982; Pitard 1993), but may also result in outliers or extreme grades (Fourie and Minnitt, 2013). However, not all outliers are a result of poor sampling, but may be an integral part of the naturally occurring positively skewed distribution for gold. If the extreme value, defined here as an 'outlier', is part of a naturally occurring distribution, the grade is taken as true and must be honoured at that point. However, when performing an estimation, its influence on the surrounding areas should be restricted. For any estimation technique including kriging, the sample grades are the best unbiased estimators of grade at that point. So whatever estimation technique is used should honour the sample points unless it is known that there is sampling error associated with that value. If there is doubt about the validity of the outlier, it should be re-assayed or omitted. Sampling by diamond drill core generally results in better sample extraction, whereas chip sampling can introduce both errors and bias (Cawood, 2003; Freeze, Flitton. and Pillay, 2013; Magri and McKenna, 1986). The decision about how outliers should be treated, depends on whether they originate from natural causes, such as the occurrence of coarse gold nuggets (Dominy, 2010), or as a result of sampling errors. Erroneous outlying results that cannot be rectified should be removed.

Facies and geological domains

Sample data should be assigned to facies or domains, characterized by well-defined geological features or properties, before outliers are identified (Krige, 1999). Geostatistical problems related to outliers include inaccurate semivariogram modelling (Krige and Magri, 1982). Some practitioners have been known to ignore outliers during semivariogram modelling, but they reintroduce and include them during resource estimation (Sinclair and Blackwell, 2004). Exploratory data analysis should identify outlier grades as those that do not form part of the distribution. Extreme grades in a positively skewed distribution usually occur as discontinuous points at the very high-grade end of the tail.

Areas characterized by samples with distinctive spatial and grade attributes can be disaggregated into well-defined domains in which samples are treated differently from those in adjacent domains (Sinclair and Blackwell, 2004). Outliers are then classified as observations that deviate significantly from other members of the domain in which they occur (Barnet and Lewis, 1979).

Methods for identifying outliers

Once erroneous sample data has been corrected or removed, and remaining grades have been assigned to a specific geological domain, the outliers can be identified using graphical methods such as histograms, quantiles, probability plots, and semivariogram plots (Srivastava, 2001; Babakhani, 2014). Outliers can also be identified using a cross-validation plot. A popular industry method for identifying extreme values is to set a percentile threshold; any value exceeding this threshold is classed as an outlier (Parker, 1991).

Current methods of addressing smearing of outlier grades into kriging estimates

Once they have been identified, the options regarding the treatment of outliers include leaving them unchanged, removing or cutting them, or reducing their influence through capping (Sinclair and Blackwell, 2004). Sound judgement and good reasons should support whichever method is employed because hard-and-fast rules about treating outliers do not exist. Most practitioners quote a single value above or below which data-points are classed as outliers. Although capping is a common technique (Sinclair and Blackwell, 2004; Babakhani, 2014), it is possible to use capping or lower percentiles to mask underlying mining issues. Consultants making a first visit to a mining operation, should probably accept current mine practice for handling outliers and suggest necessary changes once the effects of outlier treatment have been observed. OK is a linear weighting estimation technique that attributes kriging weights to samples within the defined search radius, and depending on sampling density and the range of influence, one extreme value in a set of data can produce a bias in many surrounding estimates. Despite the well-meaning intention of capping to reduce the influence of outliers in kriged estimation results, high grades are still smeared into surrounding areas (Leuangthong and Nowak, 2015), particularly if the data is limited. The smearing of kriged grade into areas adjacent to outliers is the problem addressed in this paper.

Cressie and Hawkins (1980) proposed robust kriging as a means of reducing the effect of outliers in Ore Reserve estimation, a technique that was confirmed by Costa (2003). According to Cressie (1991) the method involves downweighting outliers using neighbouring grades, and recalculation of the original OK weights before final estimation. The actual data grades are edited through a winsorizing approach, which according to Dixon (1960) involves replacing extreme grades of

a data-set with a certain percentile value from each end to obtain a less skewed distribution. Winsorizing is acceptable if there is certainty that an extreme value is a legitimate member of the distribution, but for outliers belonging to a different distribution, trimming is more acceptable (Cross Validated, 2018).

Outlier restricted kriging, another method of mitigating the effects of outliers, was proposed by Arik (1992). This method edits the OK matrix by introducing the additional requirement that the weights of the outliers sums to the probability of their occurrence. In this approach, an additional Lagrange multiplier is used, and an additional row and column in the kriging matrix. Outlier restricted kriging adjusts the kriging weights through an additional requirement that the weights of the outliers sum to the probability of outlier occurrence. Other methods proposed by Deutsch, Boisvert, and Deutsch (2011) and Rivoirard *et al.*, (2013) include moving outliers to a higher dimension and a decomposition of the grade variables, respectively. The outlier resistance of simulation approach was proposed by Babakhani (2014) as a means to determine the cutting level for kriging and other estimation techniques. This approach was further developed by Chiquini and Deutsch (2017), who proposed the use of simulation to calibrate a cutting level for estimation.

Both robust kriging and outlier restricted kriging modify the OK system prior to estimation, and neither approach is an exact interpolator of the outlier value. The approach taken in this paper does not adjust the OK system of equations, but rather applies a post-processing approach after estimation that honours all the sample points.

New proposed method for addressing smearing of outlier grades into kriging estimates

The post-processing method proposed here for overcoming the smearing effect of outlier grades into surrounding kriging estimates is based on the much lower probability of occurrence and sparsity of outliers in positively skewed distributions. Smearing of grade occurs because kriging weights are only related to the spatial distribution of sample points relative to the point being estimated, taking no cognizance of the actual sample grades. Based on their low probability of occurrence, outliers should also have a smaller range of sample influence (ROSI), meaning that kriging weights associated with outliers should also be reduced.

The proposed method is a three-stage post-processing procedure that does not interfere with the OK matrix. Based on probability of occurrence, both high- and low-grade outliers can occur in a positively skewed distribution, although low-grade outliers are not usually recognized or eliminated. Firstly, these high- and low-grade outliers in the highly positively skewed distribution must be identified; secondly, restriction factors based on the probability of outlier occurrence are calculated; and thirdly, factors that reduce the weights for the grade contribution to estimates are applied, so that the influence of extreme grades is constrained to an acceptable fringe around the outlier. The size of this acceptable fringe is somewhat subjective, but is determined by the qualified and experienced practitioner. This post-processing procedure is demonstrated through a one-dimensional kriging example.

Successful application of the proposed technique requires firstly, that the data be approximately equally spaced since the method is not effective if outliers are clustered. If data is clustered, domaining should be considered so that the data in that domain provides a reliable indication of continuity of grade at the most common sampling distance. Secondly, the data should all be of the same support in order to mitigate the potentially erroneous mixing of distributions with different support.

Identifying low- and high-grade outliers

Rarely are outliers found adjacent to one another; they are typically very high or very low isolated grades with a low probability of occurrence and a low ROSI. This method uses the fact that gold grades in a positively skewed distribution can be transformed into a Gaussian distribution of categorical variables, as shown in Figure 1, based on their probability of occurrence. There is no hard-and-fast rule or template for undertaking this procedure. In this particular example seven bins were selected and a 0.8% probability of occurrence for extreme outliers was considered adequate. The choice of the number of bins and the probability of occurrence depends on the distribution of the data and should be supported by the final validation. This determines how much constraint one would like to place on the outlier influence. The sample frequency (above) and percentage frequency (below) are shown at the top of each bin in Figure 1. Implementation is subjective, as the application is potentially sensitive to the number of bins and the percentage used. However, it depends on the deposit type. The method is subjective, but it is no more subjective than selecting a capping threshold or selecting an appropriate estimation technique. Ultimately the results need to be validated by a knowledgeable practitioner. It is important, as far as possible, to verify that the method produces results that can be reconciled with production

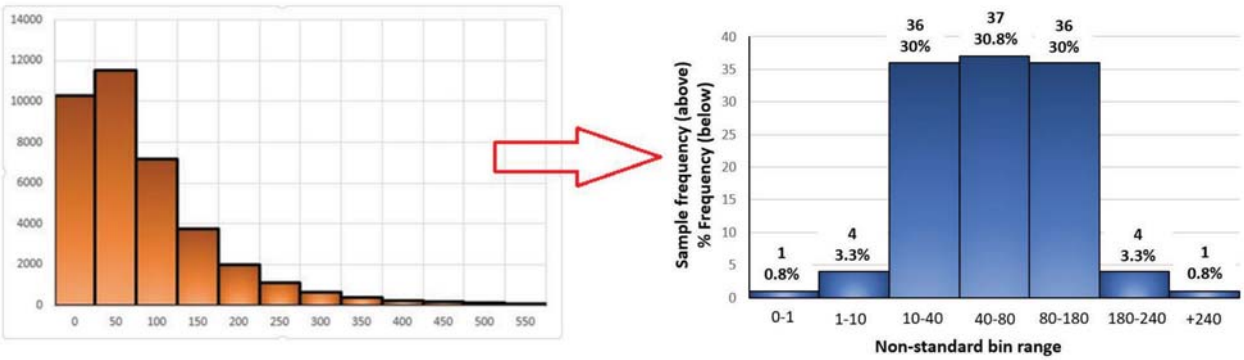

Figure 1—Positively skewed gold grades are transformed to a Gaussian distribution of seven categorical bins based on their probability of occurrence

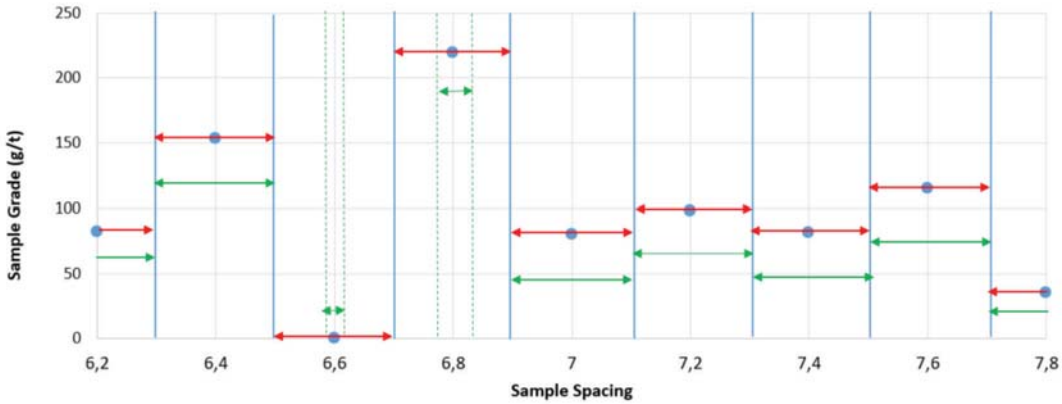

Figure 2—Range of sample influence is the red line between two adjacent sample points

data. The mining practitioner's experience, knowledge of the orebody, and visual confirmation of sample behaviour is important for the choice of the number of bins and the probability of occurrence of outliers.

Grades at the ends of the distribution are identified by ordering the data from lowest to highest, so the low- and high-end bins, comprising the lower and upper 4.1% of the overall distribution, each contain five data grades classed as outliers, based on their probability of occurrence. This is a nonlinear transformation of positively skewed data to a Gaussian distribution of categorical bins. In this case, data is assigned to one of seven equally spaced categories from bin 1 to bin 7, depending on each sample's probability of occurrence in the distribution. Low-grade outliers, which occur only 0.8% and 3.3% of the time in the distribution, are assigned to bins 1 and 2, respectively, whereas high-grade outliers that only occur 0.8% and 3.3% of the time are assigned to bins 6 and 7 (Figure 1). The four bins containing outliers in this particular example occur in the upper and lower tails of the distribution. The central 90.8% of data is assigned to bins 3, 4, and 5, having percentage frequencies in this example of 30%, 30.8%, and 30%, respectively (Figure 1). These percentages are illustrative for this example, but it is left to the practitioner to determine the optimal bin frequencies for a particular mineral deposit.

Range of sample influence (ROSI)

The ROSI is the influence range of the grade between two adjacent sample points and is defined as half the distance between the sample and its adjacent sample, as shown in Figure 2.

The ROSI for each sample in a standard kriging equation is shown as a red line in Figure 2. Samples with average grades, the green and red arrows, have the same range of sample influence. The range of sample influence for outliers, shown as short green lines, is reduced because their frequency of occurrence is low. Hence the very low outlier at 6.6 m and the very high outlier at 6.8 m (Figure 2), should have shorter ranges of influence than samples close to the average grade.

The ROSI for the one-dimensional, equally spaced samples at 20 cm intervals in Figure 3 is 20 cm, being 10 cm to the left and 10 cm to the right of each sample point. For the chip sampling shown in Figure 4 the ROSI is defined as a block centred on each sample extending 2.5 m north, east, south, and west of that sample, which is a 5 × 5 m block. The colours of the samples in Figures 3 and 4 correspond to their probability of occurrence in the distribution. High and low outlier data, shown in red, occur infrequently and occupy bins 1 and 7 at the extreme ends of the distribution in the lowest 1% and highest 1% of the data grades. The next most frequently occurring data, shown in green, occupies bins 2 and 6 with a frequency of occurrence of 4% for the lowest 4% and highest 4% of data grades, whose spatial continuity and probability of occurrence is less than that for the yellow samples. The most frequently occurring grades, shown in yellow, lie between 10 g/t and 180 g/t in the central 90% of the distribution and occupy bins 3, 4, and 5 in the range between the 5% and 95% (Figure 3). The continuity from one sample and the next is high, meaning that the ROSI of 10 cm on either side is valid and restriction factors are null to low. Based on their probability of occurrence and limited continuity, the ROSI for the green and red samples should be less than 10 cm.

In typical mining situations the spacing between samples on the mining face, in winzes, shafts, and on conveyor belts is likely to be very similar for each sample setting. Evenly spaced chip samples on a two-dimensional 5 × 5 m sample spacing over large areas is typical of the routine production or chip sampling that is conducted in Witwatersrand-type gold deposits in South Africa, shown in Figure 4. Shallow-dipping, narrow conglomeratic and carboniferous reefs contain pyrite and finely disseminated gold mineralization; no clustering of extreme grades is evident in Figure 4. The lowest 5% of grades are shown in blue and highest 5% in red. The remaining grades, between 5% and 95%, are shown in green.

The data is ordered from lowest to highest by attribute value and potential outliers are found in the upper and lower frequency bins holding 0.8% and 3.3% of the data, respectively. Based on their probability of occurrence, outliers have a shorter ROSI compared to other data in the set. For this reason, the OK weights assigned to extreme data should be restricted accordingly.

Figure 3—A line of 120 samples at 20 cm intervals showing frequently occurring grades in green, less frequently occurring grades in blue, and rare grades (outliers) in red; blue represents the lower 5% and red upper 95% spatially for 120 samples

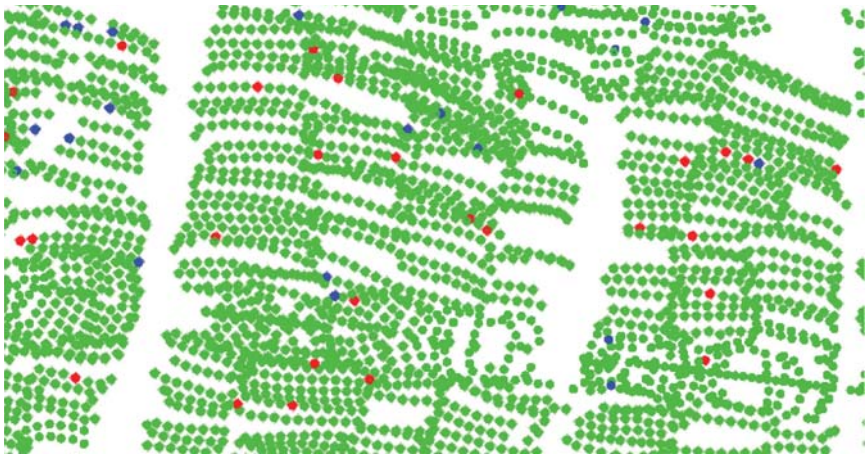

Figure 4—Coverage on a 5 m by 5 m grid of chip samples on advancing mining faces in a typical Wits-type gold deposit

Table I

Sample frequency, percentage frequency, and restriction factors for the 120 data categorized in seven bins

Category min. (>=)	Category max. (<=)	Sample frequency	Percentage frequency=(frequency/total samples)*100	Restriction factor (frequency/median)
0	1	1	0.8	0.027
1	10	4	3.3	0.108
10	40	36	30.0	0.973
40	80	37	30.8	1.000
80	180	36	30.0	0.973
180	240	5	4.2	0.135
240	270	1	0.8	0.027
	Total	120	100	

Calculation of restricted kriging weights

A kriging weight reduction factor is assigned to all sample grades lying within bins whose percentage frequency is less than the median frequency of bin 4, namely, 30.8% as shown in Table I. The weight restriction factors are calculated by measuring the frequency of occurrence of data in each of the categorical bins as a percentage of total frequency of bin 4. The frequency of data in bins 1 and 7 is 1 in 120 samples, so the percentage frequency is equal to 1/120, or 0.8%, and the weight restriction factor for each bin is therefore 0.8 % divided by 30.8%. or 0.027, as shown in Table I. Similarly, in bins 2 and 6 there are 4 and 5 samples respectively, with percentage frequencies of 3.3% and 4.2%, equating to weighting restriction factors of 0.108 and 0.135. The weight restriction factors for bins 3, 4, and 5 are likewise 0.973, 1.000, and 0.973, respectively (Table I).

Reduced smearing post-processing (RSPP)

Due to the variability of grades typically found in gold deposits and because OK is a linear arithmetic averaging technique, the output is likely to be smoothed and subject to conditional bias, but the occurrence of outliers will exacerbate the problem. The RSPP approach applies a weight reduction factor to the OK weights for each sample, such that the estimate at a given

Table II

Descriptive statistics for 120 sampled values at 0.2 m intervals

Statistic	Value
Mean grade (g/t)	70.10
Standard error (g/t)	4.87
Median (g/t)	57.56
Mode (g/t)	28.57
Standard deviation (g/t)	53.34
Sample variance $(g/t)^2$	2845.30
Kurtosis	1.94
Skewness	1.37
Range (g/t)	266.63
Minimum (g/t)	0.24
Maximum (g/t)	266.87
Sum (g/t)	8412.49
Count	120
Confidence level (95.0%	9.64

Table III

Comparative estimation results

Sample location (m)	Sample value used for kriging estimation	Actual sampled grade	OK uncapped estimate	OK capped estimate	ROK estimate	OK uncapped with RSPP estimate
0	90.2	90.2	90.2	90.2	91.51	90.2
0.2		114.26	101.86	103.12	116.9	122.72
0.4		146.63	113.42	114.38	125.16	129.13
0.6		83.72	125.86	126.52	134.37	136.52
0.8		141.87	133.96	134.49	141.14	143.16
1	175.01	175.01	175.01	175.01	176.32	175.01
1.2		7.38	133.39	133.12	131.66	128.27
1.4		74.92	126.74	126.17	121.78	116.78
1.6		126.37	111.7	111.26	108.24	104.21
1.8		26.15	88.7	88.3	85.67	80.47
2	69.31	69.31	69.31	69.31	70.62	69.31
2.2		14.48	80.11	79.87	78.74	75.08
2.4		19.4	58.44	58.21	57.34	52.62
2.6		11.73	51.22	50.86	48.59	41.71
2.8		10.52	35.51	35.85	40.47	36.83
3	9.68	9.68	9.68	9.68	10.99	9.68
3.2		13.44	54.33	52.04	30.61	10.54
3.4		14.16	60.96	58.81	38.89	20.39
3.6		14.52	61.55	59.81	43.92	29.12
3.8		12.92	65.66	63.56	44.1	28.49
4	48.92	48.92	48.92	48.92	50.23	48.92
4.2		80.08	-1.11	3.01	45.15	65.9
4.4		121.4	17.02	20.25	53.53	70.61
4.6		104.02	26.42	28.59	51.45	62.39
4.8		45.42	34.56	35.95	50.96	57.52
5	28.57	28.57	28.57	28.57	29.88	28.57
5.2		28.53	31.97	31.49	28.08	24.02
5.4		3.86	39.79	38.92	31.64	24.86
5.6		33.75	40.92	40.44	37.06	32.75
5.8		49.63	40.68	40.46	39.58	36.47
6	85.46	85.46	85.46	85.46	86.77	85.46
6.2		82.27	93.24	92.38	85.22	78.48
6.4		153.35	92.73	92.4	90.39	86.44
6.6		0.24	97	96.35	91.28	85.31
6.8		219.2	92.1	92.12	93.62	91.69
7	79.84	79.84	79.84	79.84	81.15	79.84
7.2		97.85	89.43	89.55	91.98	92.82
7.4		81.39	94.84	94.8	95.73	96.1
7.6		114.77	97.79	97.96	100.89	103.03
7.8		35.14	125.3	123.38	105.66	96.43
8	83.31	83.31	83.31	83.31	84.62	83.31
8.2		58.73	116.74	113.49	82.6	61.4
8.4		98.85	139.64	134.68	86.79	55.97
8.6		93.87	162.31	155.4	88.24	46.03
8.8		52.36	180.88	172.88	94.91	46.37
9	231.03	231.03	231.03	219	101.08	231.03
9.2		106.37	163.87	158.24	103.73	70.53
9.4		61.43	153.42	148.88	105.24	77.81

Table III

Comparative estimation results

Sample location (m)	Sample value used for kriging estimation	Actual sampled grade	OK uncapped estimate	OK capped estimate	ROK estimate	OK uncapped with RSPP estimate
9.6		70.4	135.58	133.02	108.87	92.7
9.8		83.35	120.15	119.35	112.76	106.75
10	113.8	113.8	113.8	113.8	115.11	113.8
Average grade	92.28	73.02	90.27	89.28	80.81	77.13
Statistics on estimates for 10 m portion						
Median		74.92	90.2	90.2	86.77	77.81
Standard deviation		54.16	48.76	46.92	35.20	42.85
Sample variance		2934	2378	2202	1239	1836
Kurtosis		0.77	0.15	-0.10	-0.29	2.20
Skewness		0.86	0.43	0.35	0.15	1.02
Range		231	232	216	165	221
Minimum		0.24	-1.11	3.01	10.99	9.68
Maximum		231	231	219	176	231
Sum		3724	4604	4553	4121	3934

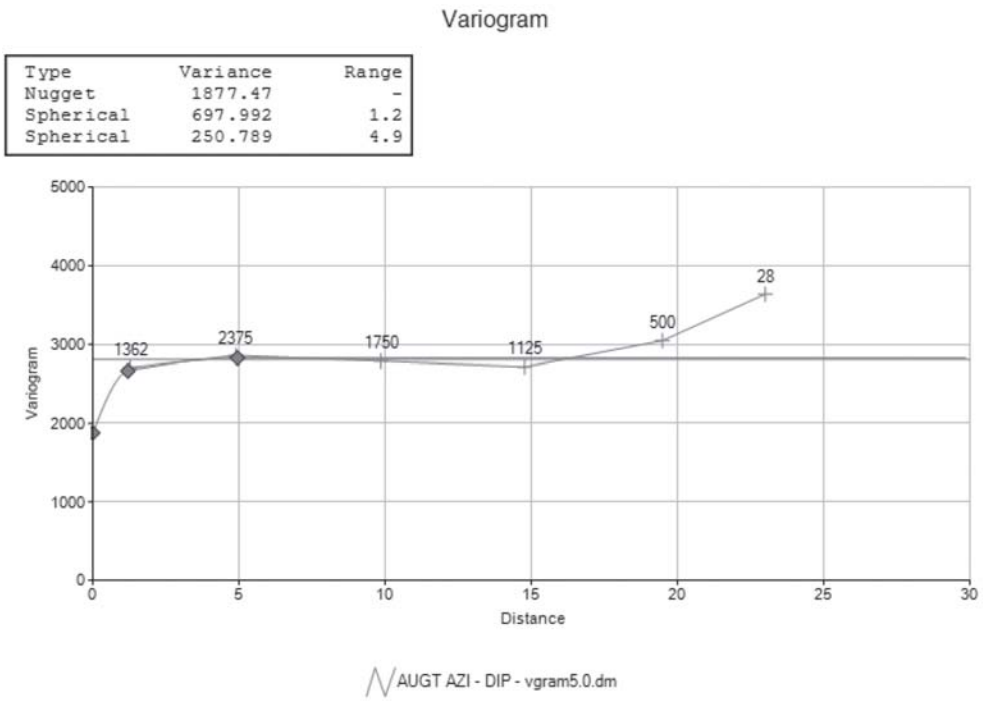

Figure 5—Variogram modelled for 120 samples at 5 m lag

sample point is honoured. The OK weight of each sample is recalculated based on the categorical bin in which it occurs. Using the percentage frequency and restriction factors provided in Table I, consider a basic example for a point informed and estimated by five nearby samples. The grades 3, 65, 83, 48, and 266 g/t have OK weights of 0.18, 0.25, 0.09, 0.31, and 0.17 respectively, so that the linear weighted sum of the grades is 84.4 g/t. The reduced smearing post-processing (RSPP) approach using the restriction factors listed in Table I returns a grade of 39.7 g/t using exactly the same sample data. Descriptive statistics for this data are shown in Table II.

Whereas OK weights must sum to 100% for each estimate, weights calculated by the RSPP method do not. The RSPP approach considers both the spatial positioning of a sample relative to the block being estimated and the value of samples used to make the estimate. A restriction factor is applied to all

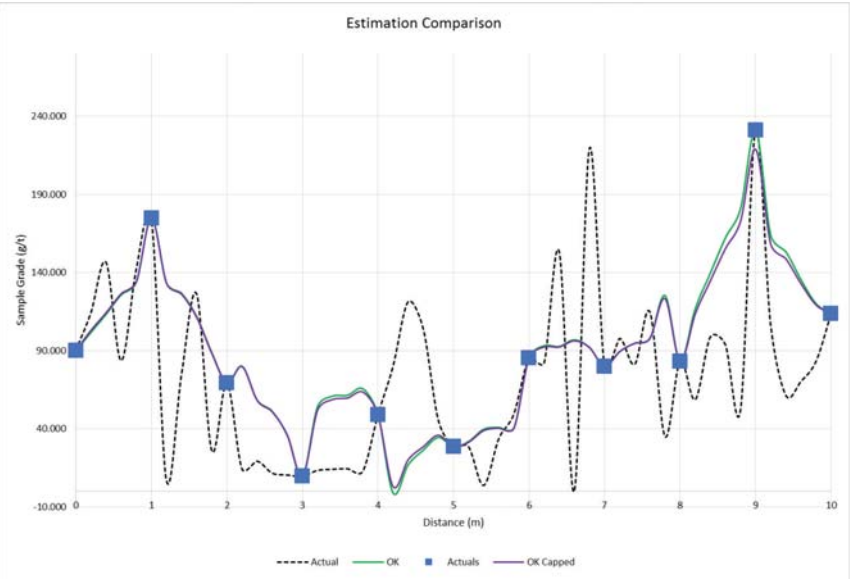

Figure 6—OK estimate of uncapped (green curve), capped (purple curve), and actual sample grades (dotted curve)

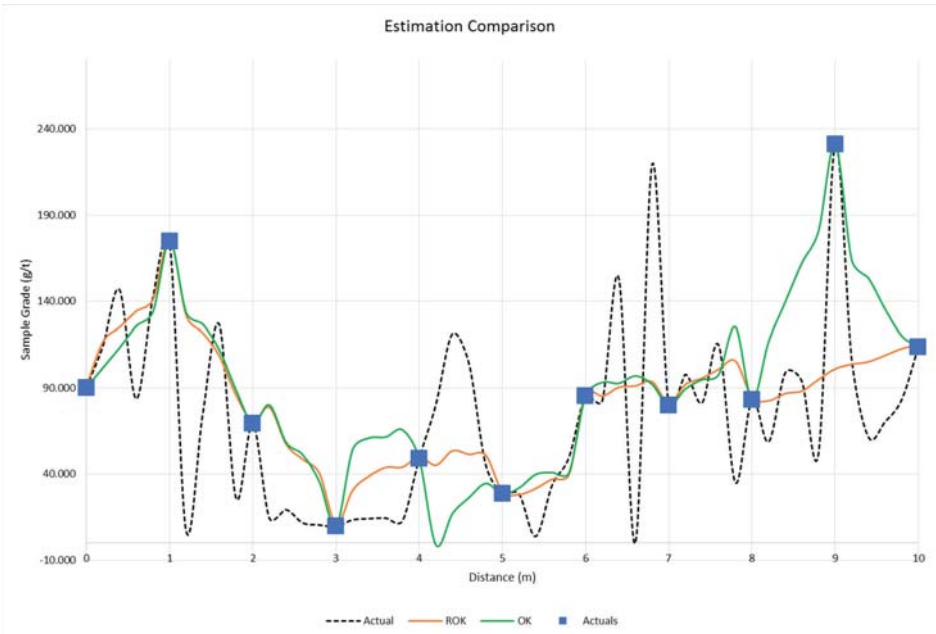

Figure 7—Comparison between block estimates produced using OK *versus* ROK

weights except those arising from samples occurring inside the median bin, namely bin 4 (Table I).

Implementation of reduced smear post-processing

The following examples illustrate the effectiveness of RSPP in mitigating an over-estimation of ordinary kriged grade around a high-grade outlier along a one-dimensional environment. It is assumed that the sampling was done correctly and that no sampling errors are included in the assay grades. This example is based on actual face-chip sampling results from a deep-level gold mine in the Free State Province of South Africa. The data forms part of an investigation into the effect of chip sampling of carboniferous reef types (Fourie and Minnitt, 2013), where the samples were extracted at 0.2 m intervals to model the variability of grades over very short intervals.

A variogram (Figure. 5) was compiled from the sample data, and OK was used to estimate grades selected at 1 m intervals (starting at zero metres). Four different estimation regimes were considered: OK with uncapped data, OK with data capped to the 98th percentile, restrictive ordinary kriging (ROK), and finally OK of uncapped data with the RSPP technique proposed. The sample data and OK estimates obtained are listed in Table III.

Limiting the influence of extreme grades in ordinary kriged estimates

Of the four methods applied, the RSPP technique provides a mean grade of 77.13 g/t Au, which is closer to the actual sampled grade of 73.02 g/t Au than any of the other methods. The estimates obtained from the four different methods are plotted in Figure 8.

OK estimate of uncapped and capped versus actual sample grade

The visual representation of estimates obtained using OK without capping is shown as the green curve in Figure 6, and indicates a poor match between the variability of sample data and variability of block grade estimates.

This well-known smoothing characteristic of kriged estimates means that OK cannot reproduce the local variability in the original sample data in the estimated block grades. Instead there is smoothing of the estimated block grades such that Var Z^* = Var Z_0 – SK_{VAR} (Chiles and Delfiner, 2012). The erroneous spread of the estimated grade (smearing) between positions 8 and 10 is due to the single high-grade sample at position 9. This single outlier results in an over-estimation of the gold content in regions

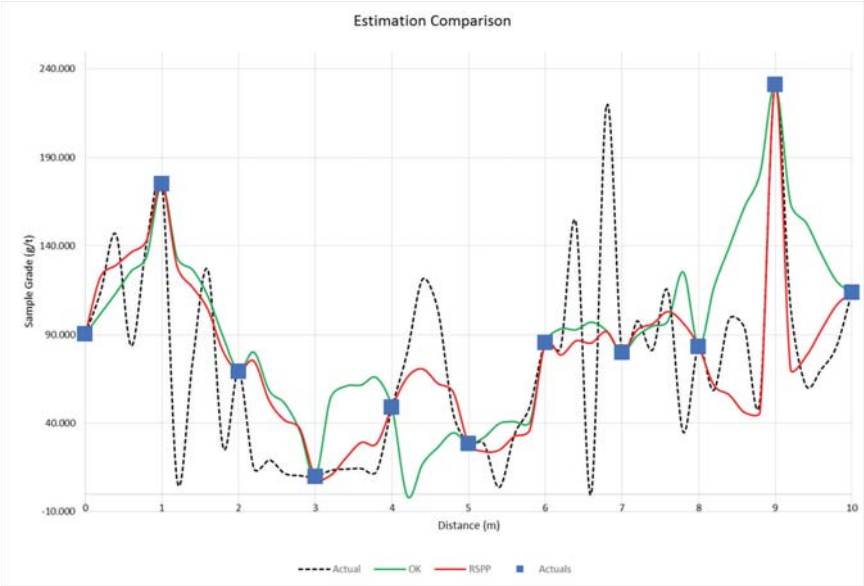

Figure 8—Comparison between uncapped OK estimates and estimates using the reduced smear post-processing

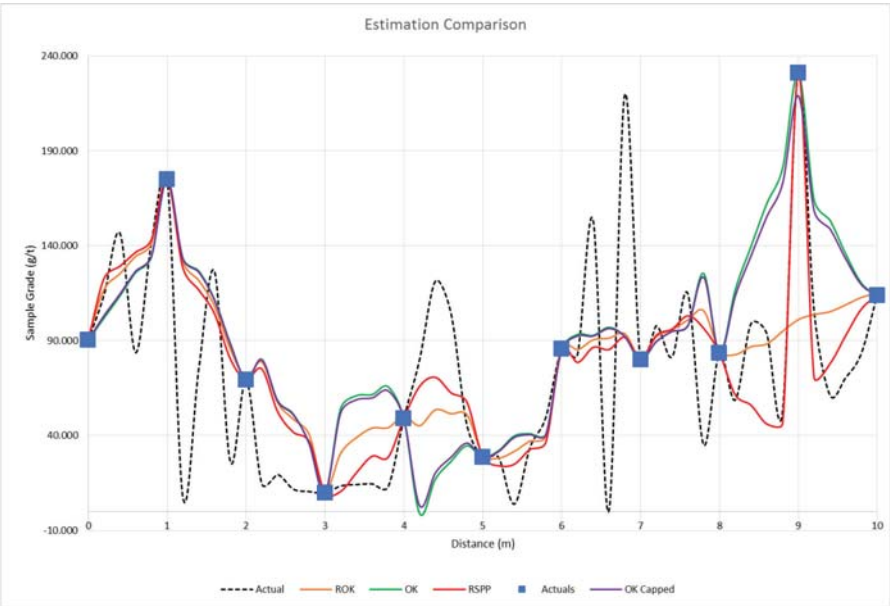

Figure 9—Combination chart of the different estimation methods and their correlation with actual grade distribution

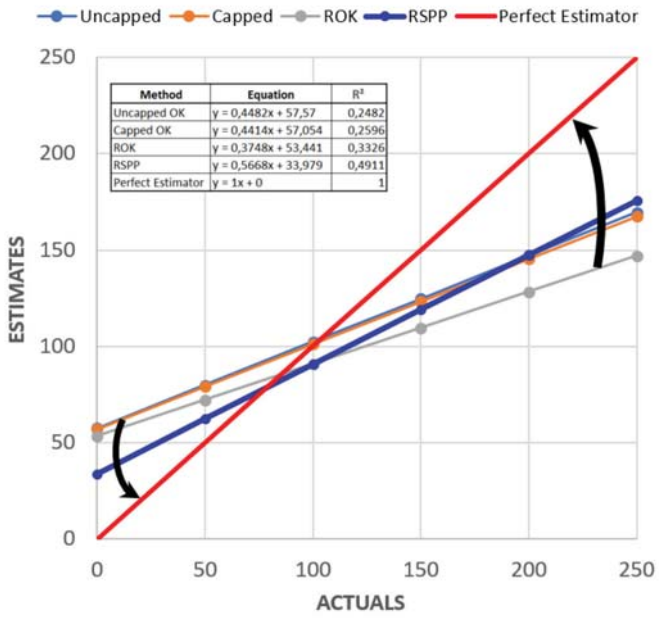

Figure 10—Comparison of trend lines through data points derived by the four different kriging techniques described here against the 45-degree line; arrows show the direction of movement for lines indicating an improved kriging result

adjacent to sample 9 between points 8 and 10. In addition to the problems associated with the outlier at sample location 9, negative kriging weights in the region to the right of sample 4 will result in poor estimation between sample points 3 and 5 (Figure 6). Because this is a simple linear one-dimensional point estimate example, a well-defined qualitative kriging neighbour analysis was not relevant to the illustration and therefore negative weights appear. Nevertheless, the RSPP method reduces the negative weights accordingly.

The OK estimates using sample data capped to the 98th percentile and uncapped sample data are compared in Figure 6. Capping the data, one of the most common techniques for mitigating the effects of high-grade outliers, smears the estimates between sample positions 8 and 10. Neither does it resolve problems associated with the negative OK weight occurring between samples 3 and 5. Thus, capping alone does not alleviate the smoothing or the estimation effect of the negative kriging weights.

OK estimate of uncapped data versus restrictive OK (ROK)

The difference in OK and ROK block estimates, especially in regard to the influence of outliers between samples 3 and 5 and at sample location 9, as shown in Figure 7, is noteworthy. ROK mitigates the over-estimation of block grades between samples 8 and 10, and returns a quite different estimate to OK in the region affected by negative kriging weights, between samples 3 and 5.

The average ROK estimate of 80.81 g/t Au is significantly less than the 90.27 g/t Au OK estimate using uncapped data. The actual average grade of 73.02 g/t Au is the true *in-situ* grade (based on the 0.2 m sampling distance) and is lower than both kriging estimates at 1 m sample intervals. However, ROK does not honour the sample value at point 9, and furthermore requires a restructuring of the kriging system of equations (Arik, 1992).

Uncapped OK estimate versus RSPP of the same estimate

Results obtained from the RSPP method applied to the OK estimates of uncapped data are shown in red in Figure 8. Again, the high-grade smearing between locations 8 and 10 is mitigated, while still honouring the data at location 9 and not requiring any changes to the OK system of equations. The estimates between sample locations 3 and 5 are also improved, as the negative OK weights assigned to the outlying value is reduced by the post-processing reduction factor.

Estimates produced by all four kriging techniques are compared in Figure 9, showing the superior results of the RSPP in terms of smearing and dealing with negative kriging weight associated with an outlier. The benefit of RSPP over the ROK is that no adjustments need to be made to the OK system of equations. This implies that RSPP can be applied to any commercial package offering OK without any additional editing of source code. The RSPP estimates have an average grade of 77.13 g/t Au, which is much nearer to the true grade 73.02 g/t and is significantly lower than the OK estimate of 90.27 g/t Au.

Conclusions

The capping of high-grade sample grades prior to kriging estimation in an attempt to mitigate the smearing of higher grades into lower grade areas is inefficient in this worked example, and does not achieve much by way of improvement in the estimates. Restricted OK (ROK) fails to honour the sample data and requires manipulation of the OK system of equations.

The method proposed here involves an adjustment of the OK weights that identifies outliers and calculates a weight reduction factor based on the likelihood of occurrence. This significantly removes smearing while still honouring the data and addresses issues arising from negative kriging weights associated with an

outlier. It is easy to implement with most software, because it is merely a post-process and does not require additional computing time to changes the OK system of equations. The smear reduction post-processing method complements the OK weight calculation process by considering the spatial location of samples relative to one another and the point being estimated, as well as the actual sample grades and their probability of occurrence.

The RSPP method will not remove the conditional bias, but it will definitely mitigate this age-old problem in geostatistical estimation techniques, as illustrated in Figure 10.

Figure 10 shows a comparison of the outcomes of the different kriging methods using trend lines for the different data-sets and the 45-degree line representing perfect correlation between actual and estimated grades. This plot indicates that the thick blue line, representing the RSPP method, is rotated considerably more towards the 45-degree line than any of the other trend lines. Another important aspect is that the R^2 value for the correlation coefficient of the RSPP method is about twice that for the uncapped and capped OK methods, and significantly better than for the ROK technique. This indicates that the RSPP estimates are considerably less smoothed than the kriging outputs from the other techniques and hence RSPP goes a long way towards balancing the tensions between smoothing and conditional bias.

References

Arik, A. 1992. Outlier restricted kriging: a new kriging algorithm for handling of outlier high grade data in ore reserve estimation. *Proceedings of the 23rd International Symposium on the Application of Computers and Operations Research in the Minerals Industry.* Kim, Y.C. (ed.). Society of Mining Engineers, Littleton, CO. pp. 181–187

Barnett, V. and Lewis, T. 1979. Outliers in statistical data. *Physics Today*, vol. 32, no. 9, September 1979. p. 73.

Babakhani, M. 2014. Geostatistical modeling in presence of extreme values. MSc thesis, Department of Civil and Environmental Engineering, University of Alberta, Edmonton, Canada. 85 pp.

Cawood, F.T. 2003. Underground face sampling on narrow gold reefs. Sampling practice and its impact on the Mine Call Factor on Witwatersrand gold mines: Lessons learned. *Journal of the Institute of Mine Surveyors of South Africa*, vol. XXXI, no. 7. pp. 202–216.

Chilès, J.P. and Delfiner, P. 2012. Geostatistics: Modeling Spatial Uncertainty. Wiley, New York

Chiquini, A.P. and Deutsch, C.V. 2017. A simulation approach to determine the cutting level. *Geostatistics Lessons*. Deutsch, J.L. (ed.). http://www.geostatisticslessons.com/lessons/simulationcutting

Costa, J.F. 2003. Reducing the impact of outliers in ore reserves estimation. *Mathematical Geology*, vol. 35, no. 3, April 2003. pp. 323–345.

Cressie, N.A.C. 1991. Statistics for Spatial Data. Wiley, New York. 920 pp.

Cressie, N.A.C. and Hawkins, D.M. 1980. Robust estimation of the variograms. *Mathematical Geology*, vol. 12, no. 2. pp. 115–125.

Cross Validated. 2018. What are the relative merits of Winsorizing vs. Trimming data? https://stats.stackexchange.com/questions/90443/what-are-the-relative-merits-of-winsorizing-vs-trimming-data [accessed 20 January 2018].

Deutsch, J., Boisvert, J., and Deutsch, C. 2011. New dimension to account for sample error and volume support in resource estimation. *Transactions of the Society for Mining, Metallurgy, and Exploration*, vol. 330. pp. 598–605.

Deutsch, C.V. and Journel, A.G. 1998. GSLIB: Geostatistical Software Library and User's Guide. 2nd edn. *Applied Geostatistics Series*. Oxford University Press, New York. 369 pp.

Dixon, W.J. 1960. Simplified estimation from censored normal samples. *Annals of Mathematical Statistics*, vol. 31. pp. 385–391

Dominy, S. 2010. Sampling high-nugget effect gold deposits workshop. Snowden Mining Industry Consultants Limited, Ballarat, Australia. September 2010

Fourie, D. and Minnitt, R.C.A. 2013. The simulated chip-sample model as a method for quantifying error and bias in sampling thin carboniferous reef type, South Africa. *Proceedings of Sampling and Analysis: Best-practice in African Mining* 2013, Misty Hills, Muldersdrift. Southern African Institute of Mining and Metallurgy, Johannesburg.

Freeze, B., Flitton, T., and Pillay, A. 2013. Quality control and assurance of underground chip sampling at Kopanang Mine, South Africa. *Proceedings of Sampling and Analysis: Best-practice in African Mining 2013*, Misty Hills, Muldersdrift. Southern African Institute of Mining and Metallurgy, Johannesburg.

Gy, P.M. 1979. Sampling of Particulate Materials, Theory and Practice. *Developments in Geomathematics* 4. Elsevier Scientific Publishing.

Gy, P.M. 1982. Sampling of Particulate Materials Theory and Practice. 2nd revised edn. Elsevier, Amsterdam. 431 pp.

Hawkins, D.M. 1980. Identification of Outliers. Chapman and Hall, London and New York. 188 pp.

Hawkins, D.M. and Cressie, N.A.C. 1984. Robust kriging – A proposal. *Journal of the International Association for Mathematical Geosciences*, vol. 16, no. 1. pp 3-18.

Isaaks, E.H. and Srivastava, R.M. 1988. Spatial continuity measures for probabilistic and deterministic geostatistics. *Mathematical Geology*, vol. 20, no. 4. pp. 313–341.

Krige, D.G. 1999. Essential basic concepts in mining geostatistics and their links with geology and classicwal statistics. *South African Journal of Geology*, vol. 102, no. 2. pp. 147–151.

Krige, D.G. and Magri, E.J. 1982. Studies on the effects of outliers and data transformation on variogram estimates for a base metal and a gold ore body. *Mathematical Geology*, vol. 14, no. 6. pp. 557-564.

Leuangthong, O. and Nowak, M. 2015. Dealing with high-grade data in resource estimation. *Journal of the Southern African Institute of Mining and Metallurgy*, vol. 115. pp. 27-36.

Magri, E.J. and McKenna, P. 1986. A geostatistical study of diamond-saw sampling versus chip sampling. *Journal of the South African Institute of Mining and Metallurgy*. vol. 86, no. 8. pp. 36–37.

Olea, R.A. and Pawlowsky, V. 1996. Compensating for estimation smoothing in kriging. *Mathematical Geology*, vol. 28, no. 4. pp 407–417.

Pan, G. 1994. Restricted Kriging: A link between sample value and sample configuration. *Mathematical Geology*, vol. 26, no. I. pp. 135–155.

Parker, H.M. 1991. Statistical treatment of outlier data in epithermal gold deposit reserve estimation. *Mathematical Geology*, vol. 23, no. 2. pp. 175–199.

Pitard, F.F. 1993. Pierre Gy's Sampling Theory and Sampling Practice. 2nd edn, July 1993. CRC Press, Boca Raton, FL.

Rivoirard, J., Demange, C., Freulon, X., and Lécureuil, A, 2013. A top-cut model for deposits with heavy-tailed grade distribution. *Mathematical Geosciences*, vol. 45, no. 8. pp. 967–982.

Sinclair, A.J. and Blackwell, G.H. 2004. Applied Mineral Inventory Estimation. Cambridge University Press, UK.

Srivastava, R.M. 2001. Outliers - A guide for data analysts and interpreters on how to evaluate unexpected high values. *Contaminated Sites Statistical Applications Guidance Document no*. 12-8. Province of British Columbia, Canada. 4 pp. https://www2.gov.bc.ca/assets/gov/environment/air-land-water/site-remediation/docs/guidance-documents/gd08.pdf ◆

SAIMM
THE SOUTHERN AFRICAN INSTITUTE OF MINING AND METALLURGY

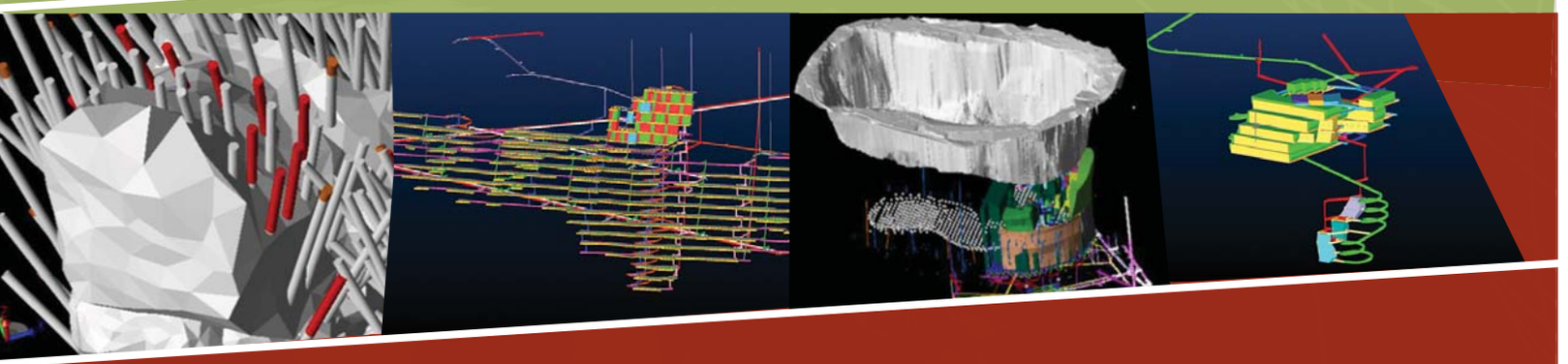

Mine Planner's Colloquium 2019

Skills for the future – yours and your mine's

22–23 May 2019

Glenhove Conference Centre, Melrose Estate, Johannesburg

BACKGROUND

Previous SAIMM Mine Planning forums have clearly highlighted deficiencies in mine planning skills. The 2012, 2014, and 2017 colloquia all illustrated developing skill-sets with a variety of mine planning tools in a context of multiple mining methods. Newer tools and newer skills for the future of mining will feature in 2019.

OBJECTIVES

Using a backdrop of a generic description of the multidisciplinary mine planning process, the forum provides a platform for the mine planning fraternity to share mining business-relevant experiences amongst peers. While different mining environments have their specific information requirements, all require the integration of inputs from different technical experts, each with their own toolsets.

The forum's presentations will highlight contributions from a series of technical experts on current best practice, and will be augmented by displays of state-of-the-art mine planning tools in order to create a learning experience for increased planning competencies.

WHO SHOULD ATTEND

- Mine planners and practitioners
- Mine designers
- Technical support staff
- Cost and financial modellers
- Chief planners
- Mineral resource managers
- Mine managers responsible for planning
- Consultants
- Independent mine planning consultants

FOR FURTHER INFORMATION CONTACT:
Camielah Jardine • Head of Conferencing • SAIMM
Tel: +27 11 834-1273/7 • Fax: +27 11 833-8156
E-mail:camielah@saimm.co.za •Website: http://www.saimm.co.za

Compaction tests on coking coals. Part 1: Laboratory-scale compaction with a 4-ton hydraulic press

G. Coetzer

Affiliation:
Previously from Exxaro Resources

Correspondence to:
G. Coetzer

Email:
atomium@iafrica.com

Dates:
Received: 22 Feb. 2017
Revised: 26 July 2018
Accepted: 8 Nov. 2018
Published: April 2019

How to cite:
Coetzer, G.
Compaction tests on coking coals. Part 1: Laboratory-scale compaction with a 4-ton hydraulic press
The Journal of the Southern African Insitute of Mining and Metallurgy

DOI ID:
http://dx.doi.org/10.17159/2411-9717/17/070/2019

Synopsis

Prior to operating a non-recovery coke pilot plant, it was critical to ascertain coal cake stability during the loading of a 1 m³ coal cake into the oven. Various compaction parameters were verified and established on a small laboratory-scale compaction machine to obtain a coal cake of acceptable stability. These parameters include cake density, cake surface moisture, transverse strength (force applied perpendicular to the original compacted coal cake layers), and applied force to the coal cake. This work determined the behavioural characteristics of the coal while being compacted either with a full-sized or a $^1/_3$-sized compaction plate in a 9 kg capacity mould. Two different coals were evaluated, namely Waterberg semi-soft coking coal (sscc) and Oaky North hard coking coal.

The target wet cake density of 1 100 kg/m³ (79% of 1 400 kg/m³ relative density) was achieved for Waterberg sscc, with a particle size d_{50} varying between 0.6 mm and 1 mm, utilizing the $^1/_3$-sized compaction plate in the laboratory-scale set-up, with 11.6% surface moisture and 92.2 t/m² commercial equivalent applied force. For Oaky North hard coking coal, a wet cake density of 1 189 kg/m³ (85% of 1 400 kg/m³ relative density) was achieved at a surface moisture content of 12.3% and at a lower applied force than that for Waterberg sscc, *i.e.* 78.5 t/m².

Coal cakes of acceptable strength, and therefore sufficient stability for further processing, were obtained for all materials evaluated during this study.

Further studies should be conducted to determine the effect of zeta potential during the compaction of coals.

Keywords
coking coal, compaction test, coal coke stability, wet coke density, laboratory scale.

Introduction

Exxaro Resources has successfully installed and commissioned a world-class stamp-charging horizontal 1 t electrically-heated pilot-scale coke oven at its Metallurgy Services facility. Prior to operating the coke non-recovery pilot plant, it is essential to ascertain coal cake stability during the loading of a 1 m³ coal cake into the oven. The design of Exxaro's pilot plant is such that the coal cake is pushed inside the oven by means of a pusher plate, rather than through a 'spoon' feed mechanism, such as is found in industrial horizontal coke ovens. The pusher plate loading mechanism dictates that the coal cake should possess high stability and inherent strength during loading into the oven, owing to frictional forces exerted by the oven floor. In order to obtain a coal cake of acceptable stability, various compaction parameters needed to be verified and established on a small laboratory-scale compaction machine.

This work determined the behavioural characteristics of the coal while being compacted under pressure. Focus was placed on parameters such as cake density, cake moisture, transverse strength (force applied perpendicular to the original compacted coal cake layers), and applied force to the coal cake. These parameters are crucial for the successful operation of a non-recovery coke oven.

Literature survey

Coking of coal blends utilizing high-volatile coals, with poor coking ability, to produce a high-quality coke for blast furnace application is possible by compacting the coal blend prior to the carbonization process (Kuyumcu and Sander, 2014). Coking of a single-component coking coal, such as Waterberg semi-soft coking coal (sscc), should therefore also benefit through the utilization of compaction. The coke produced from 100% Waterberg sscc is destined for the ferro-alloy industry and for blast furnace processes.

Compaction tests on coking coals. Part I: Laboratory-scale compaction with a 4-ton hydraulic press

During coal compaction, an increase in oven bulk density leads to an increase in coke strength after reaction (CSR) and to homogeneity throughout the coke oven chamber. This phenomenon is attributed to enhanced coal particle adhesion and improved plasticity during the plastic phase. This, in turn, results in the growth of carbon forms and improves the degree of carbon crystallization; thus also the coke strength (Nyathi *et al.*, 2013). Coke strength development is dependent on (i) the extent of coal particle adhesion, and (ii) the presence of unfilled gaps between particles (porosity) (Nishioka and Yoshida, 1983).

The benefits of an increase in coal cake bulk density include:

- A less porous coke product, which is beneficial for mechanical strength (Nishioka and Yoshida, 1983). The decrease in total porosity is indicative of limited swelling, restraining pore enlargement and this, presumably, is attributable to the compact nature of the coal bed under high oven bulk density (Nyathi *et al.*, 2013)
- Closer proximity of coal particles during softening, which results in the development of a stronger bond between the coke cells (Kumar *et al.*, 2008)
- The induction of homogeneity throughout the coal cake (Kuyumcu, Rosenkranz, and Abel, 2010)
- An increase in the proportion of less-reactive carbon forms, and an improved degree of crystallization (Nyathi *et al.*, 2013)
- Decreased porosity causing an increase in the water saturation index, *i.e.* filling of the total pore volume (Rejdak and Wasielewski, 2015)
- Improvement in the coke strength owing to increased coal particle contact and increased coke density (Rejdak and Wasielewski, 2015).

The bulk density and mechanical strength of compressed coal cake are controlled by varying the compressing energy, compacting time (when stamping with cyclic impacts of the stampers), coal type, coal surface moisture, coal granulometric properties (particle size distribution, particle shape, and particle density), and coal surface properties, as well as by using bulk density modifiers, such as oil (Nyathi *et al.*, 2013; Kuyumcu and Sander, 2014; Burat. Kuyumcu, and Sander, 2015; Rejdak and Wasielewski, 2015).

Coal cake density is influenced by the surface (wettability) and mechanical (grindability and hardness of coal structure) properties. According to Rejdak and Wasielewski (2015), the wettability of coals depends on various factors, such as the degree of coalification, the mineral content, and the maceral composition. The mineral components in coals are hydrophilic, and pure coal repels water, which in this case works against the cohesion of the blend. Hence, the lower the mineral content, the lower the bulk density of the coal cake, and this decreases the oven throughput (Dash *et al.*, 2005). Less coalified coals contain more oxygen and hydrophilic functional groups than more coalified coals do. The higher wettability of the surface of coal grains is associated with higher works of adhesion (reversible work to separate the interfaces of two coal grains), which can adversely affect the rearranging of coal particles and can prevent the creation of a dense coal cake. The coal surface moisture acts as a binder, and the water added to the coal has a direct impact on coal cake strength. The strength increases during compaction with an increasing pore saturation index to a maximum value of 80% (Abel, Rosenkranz, and Kuyumcu, 2009).

In the case of different mechanical properties (Abel, Rosenkranz, and Kuyumcu, 2009; Rejdak and Wasielewski, 2015), higher coal cake density can be obtained through the spalling of coal particles. For coking coals, the grindability, which reflects coal structure hardness, decreases with an increase in the content of volatile matter. During the compaction process, a plastic-elastic deformation occurs. Locally, the mechanical strength of the particles may be exceeded; thus, some parts of the coal grains can be crushed (degree of fineness) to fill interparticle voids, hence increasing the number of particle contacts (liquid bridges), and the number of pores (capillaries). The particle strength is also dependent on the coal particle size (Abel, Rosenkranz, and Kuyumcu, 2009). The smaller a particle, the greater its rigidity. This is due to the smaller probability of imperfections in the grain lattice. Therefore, densification of the coal cake cannot be considered without taking into account the granulometric properties of the coal.

The rearrangement of the particles during compaction is enhanced by the surface moisture, which reduces the internal friction (Kuyumcu and Sander, 2014). The water acts as a lubricant that increases the sliding movement between the coal particles so that they can rearrange more easily and achieve a higher packing density (Kuyumcu and Sander, 2014; Rejdak and Wasielewski, 2015). This, in turn, enhances the tendency of the particles to converge with an increase in compaction energy, as a result of which air voids decrease; thus, cake density increases (Kuyumcu, Sander, and Burat, 2012). This is due to the presence of capillary forces (liquid bridges and capillary pressure) between coal particles. With further strain, an elastic-plastic deformation of the particles begins to occur, resulting in particle breakage and the filling of small pores with the fragments (Madias and de Córdova, 2013). While the pore volume decreases, the pore saturation by water rises, causing a damping effect. For low-rank coals, with lower grindability, this phenomenon might be limited. Excessive particle breakage during compaction can adversely affect the bulk density of a coal cake. The pressed cake can be classed as a so-called wet agglomerate, which is characterized by the adhesive forces resulting from liquid bridges within the capillary pore system (Kuyumcu and Sander, 2014).

The presence of water is detrimental with respect to both the thermal (a higher energy demand to evaporate water) and ecological (a greater volume of wastewater) balance of the carbonization process (Kuyumcu, Rosenkranz, and Abel, 2010; Rejdak and Wasielewski, 2015). High volumes of interstitial water absorb the impact of the compactor/pressing plate and also prevent particle breakage that contributes to a dense packing of the coal cake. For a water content higher than 14%, the compression energy is mostly used to expel the water from the coal cake (Kuyumcu Rosenkranz, and Abel, 2010). In addition, water can adversely affect the ceramic lining of the coke ovens. Therefore, determining the optimum water content with respect to coal cake stability is vital (Kuyumcu, Abel, and Rosenkranz, 2011).

Industrial stamp charge technology employs a combined stamping-charging-pushing machine, which increases the bulk density of the feed coal to a compact density of 80% of the

true coal density, *i.e.* a compact density of around 1 100 kg/m^3, depending on the true density of the coal, before charging the oven (Abel, Rosenkranz, and Kuyumcu, 2009; Kuyumcu, Rosenkranz, and Abel, 2010; Kuyumcu and Sander, 2014). The stamping process increases the mechanical strength of the coal cake and makes trouble-free charging possible. In the case of mechanical failure, the coal cake usually does not collapse completely as one would expect from flowing bulk solids. Most commonly, portions in the range of 12% to 16% break from the cake when the mechanical strength is exceeded locally. This can be due to one or a combination of the following, when dynamic forces act on the cake (Abel, Rosenkranz, and Kuyumcu, 2009; Madias and de Córdova, 2013; Kuyumcu and Sander, 2014):

- Cake weight (*i.e.* critical cake height)
- A local reduction of shear strength along a plane that is sloped according to a decreased angle of internal friction (cake failure by shear fracture with the fracture along a sliding plane)
- Bending or compressive stress when the tensile strength of the compact is too low (cake failure by cleavage fracture where the fracture plane is vertical to the tensile load)
- Poor water distribution or wetting.

A criterion for the sufficient mechanical strength of the coal cake, therefore, has to relate that strength to the loading conditions, considering the weakening of the cake and the dynamic stress, through the introduction of appropriate safety margins (Abel, Rosenkranz, and Kuyumcu, 2009).

The specific aim of this study was to obtain a coal cake of acceptable stability with a compacted wet cake density of 1 100 kg/m^3 or higher, with surface moisture content as low as possible, as proposed by Kuyumcu and Sander (2014), by utilizing either a full-sized or $^1/_3$-sized compaction plate on a laboratory scale. Two different coals were evaluated, namely Waterberg sscc and a hard coking coal (Oaky North).

Table I

Properties of various coals evaluated

Property	Waterberg sscc 1	Waterberg sscc 2	Waterberg sscc 3	Oaky North
Inherent moisture (%)	2.5	3.2	2.0	0.6
Mineral content (dry) (%)	9.7	11.5	10.7	9.7
Volatiles (dry) (%)	36.5	37.0	37.6	24.1
Fixed carbon (calc.) (%) (dry)	51.3	51.5	51.7	66.2
Gross calorific value (MJ/kg)	29.68	28.73	29.40	32.45
Vitrinite (%)	91.5	87.5	87.7	81.6
Rank ($RoV_{max,}$ %)	0.69	0.70	0.70	1.20

Experimental

Sample preparation

Bulk Waterberg sscc samples (10 t) were bagged in plastic-lined bulk bags to preserve moisture in the samples. These samples were then homogenized and transferred to plastic drums fitted with rubber seals to prevent drying and minimize oxidation and the effects of ageing. Oaky North hard coking coal (10 t) was obtained from AMSA (Vanderbijlpark) from the commercial stockpile. This was homogenized and stored in a similar manner as described for the Waterberg sscc coal.

The Waterberg sscc and Oaky North materials were crushed by a hammer mill to the specific particle size distributions (PSDs) depicted in Figure 1.

A 200 kg bulk Waterberg sscc sample containing 12% surface moisture was prepared and gradually dried on a plastic sheet in the laboratory to a surface moisture level of 6%. Samples were collected over the drying period at targeted surface moisture

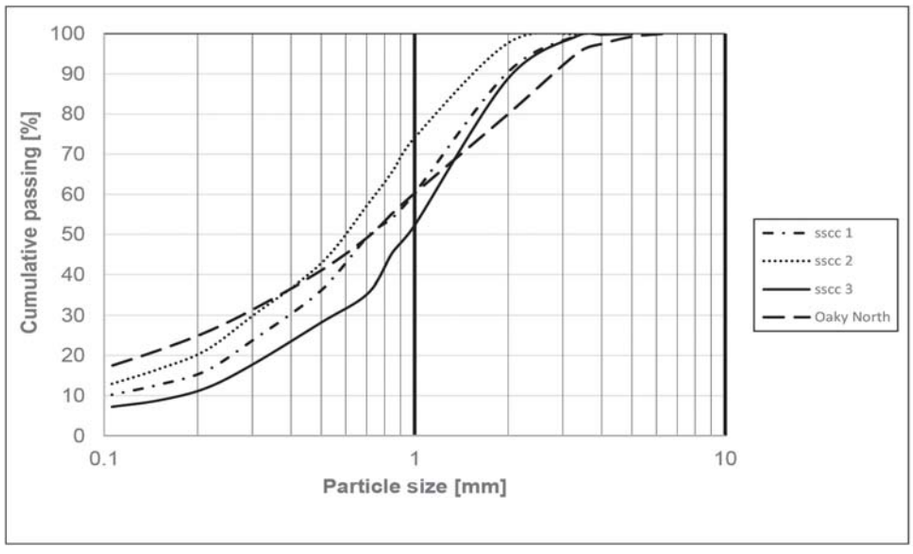

Figure 1—PSDs for the material types

levels between these levels. The coal was mixed intermittently by coning and quartering to obtain a representative sample, and also to control the moisture distribution. The surface moisture content was determined simultaneously using two Ohaus moisture analysers fitted with a programmable heating sequence, over a period of 20 minutes to a temperature of 105°C. The average moisture levels were determined. A similar preparation method was adopted for the Oaky North sample.

Sample properties

Table I summarizes properties of the coal materials evaluated.

Coal compaction

Two different types of compaction plates were evaluated, namely a full-sized plate covering the cross-sectional area of the coal cake and a 1/3-sized plate. The following procedure was used during the compaction of the coal cake.

- Coal was transferred into a mould (dimensions 200 mm × 200 mm × 330 mm) fitted with removable sides.

Figure 2—Compaction machine with mould

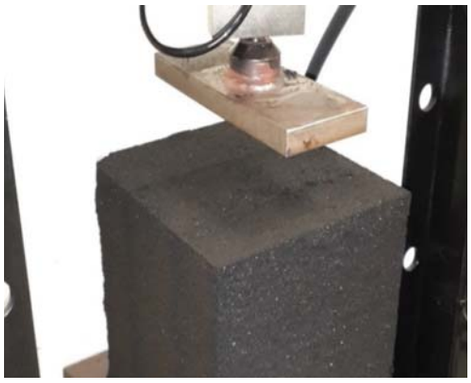

Figure 3—Compacted coal cake after removal of mould sides

- Coal layers (three in total, 9 kg in total) were compacted individually, and the thickness of each layer changed owing to compaction. Each layer was compacted from side to side during overlapping compaction with the 1/3-sized plate in order to expel as much air as possible from each layer.
- Once the coal cake was fully compacted, three of the four sides of the mould were removed (Figure 3). The mould was then tilted through 90° for the transverse strength test.

Transverse strength test

Transverse strength tests were performed with the 1/3-sized compaction plate aligned perpendicular to the angle at which the cake was compacted. This was to simulate the pushing forces exerted on a compacted coal cake during loading into a 1 t pilot plant coking oven. The transverse strength was calculated from the maximum transverse force applied, before final breakage of the coal cake, in relation to the cross-sectional area of the cake.

Results and discussion

Particle size distribution

The PSDs for each of the coals are depicted in Figure 1. The d_{50} of the Waterberg sscc materials varied between 0.6 mm and 1 mm, whereas the crushing fineness was more than 99% < 3.25 mm. The particle sizes of the coals utilized in this study were similar to those suggested for compaction or stamping by various workers in the field, namely 85% to 99% < 3.25 mm (Dash *et al.*, 2005; Kumar *et al.*, 2008, Tiwari *et al.*, 2012; Madias and de Córdova, 2013; Rejdak and Wasielewski, 2015). In the case of the Oaky North sample, the d_{50} was 0.7 mm with a crushing fineness of 95% < 3.25 mm.

Results from full-sized plate

Sample Waterberg sscc 1 was utilized for the full-sized plate compaction tests (see Table I and Figure 1 for PSD). It follows from Figure 4 that the general trend was a linear increase in wet cake density with increasing surface moisture using the full-sized compaction plate. This trend can be expected for a range of increasing moisture until the cake density begins to decrease. However, no attempt was made to determine this inflection point.

It should be noted that the scatter seen in Figure 4 is relatively high, for applied forces both at 64 t/m² (commercial equivalent applied force) and 77.5 t/m², whereas the relationships are linear (R^2 = 0.73 for 64 t/m² and 0.90 for 77.5 t/m² applied force). The variations are characteristic of applying a full-sized compaction plate since air and excess water were not expelled completely from the cake during compaction, resulting in an inconsistent compaction. Figure 4 also indicates that higher wet densities were obtained with an increase of applied force. The maximum cake bulk density recorded was 977 kg/m³ at a surface moisture content of 10.3% and 77.5 t/m² applied force. Therefore, the required wet cake density of 1 100 kg/m³ was not achieved with the full-sized plate at the conditions considered.

The calculated average porosity[1] (dry basis) in these two

[1]Porosity was calculated from the relationship

$$[1 - \frac{cake\ bulk\ density\ (dry\ based)}{relative\ density}]*100$$

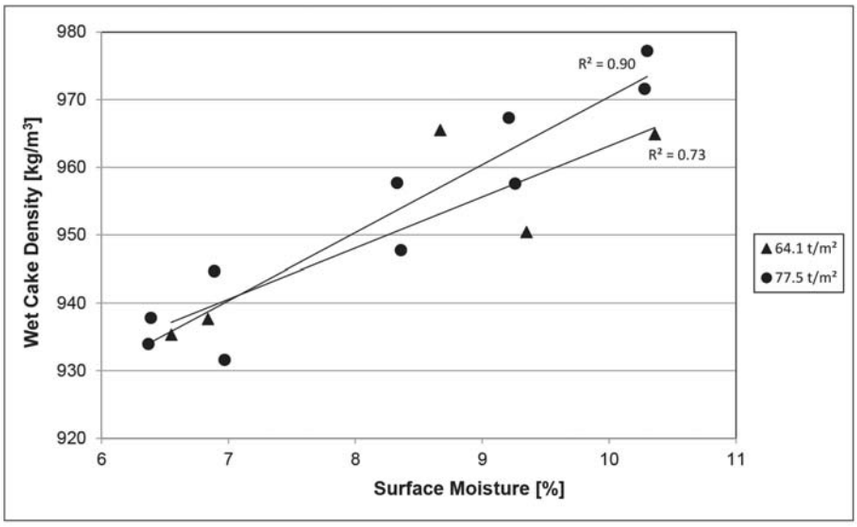

Figure 4—Wet cake density of Waterberg sscc as a function of surface moisture for a full-sized compaction plate

different tests was 39.8%, compared to a starting porosity of 53%. The latter was based on a dry bulk density (630 kg/m^3) determined for a surface moisture content of 9% for crushed Waterberg sscc. These figures correspond to those mentioned by Sand. Rosenkranz, and Kuyumcu (2012), *i.e.* starting porosity is about 50%, decreasing to as low as 20% after compaction. This indicates the potential for further improving the bulk densities during laboratory-scale compaction.

The transverse strengths obtained for Waterberg sscc 1 as a function of surface moisture at various applied forces are shown in Figure 5. Slightly lower average transverse strengths were recorded for the lower applied force (64.1 t/m^2), *i.e.* 10.6 ± 0.5 kN/m^2, compared to 11.7 ± 0.6 kN/m^2 at 77.5 t/m^2 applied force. The variations noted for the 77.5 t/m^2 applied force are within acceptable statistical limits and are reported, in general, in a straight line. A somewhat negative behaviour in terms of transverse strength was noted at higher levels of surface moisture, above 10%. This might be ascribed either to (i) entrapped air in the coal cake that interfered with bonding between particles and water, or (ii) the moisture level that was too high resulting in the sliding of the particles over each other owing to a lowering of van der Waals bonding. Maximum transverse strengths were recorded at the lower preferred surface moisture levels of around 6.5%, *i.e.* 12.2 kN/m^2 at 77.5 t/m^2 applied force. These results show that the moisture content can be lowered, although no attempt was made to investigate this further since the transverse strengths were too low. The transverse strengths obtained in this study resemble the typical shear strength figures obtained by Rejdak and Wasielewski (2015) for various coals, namely between 8

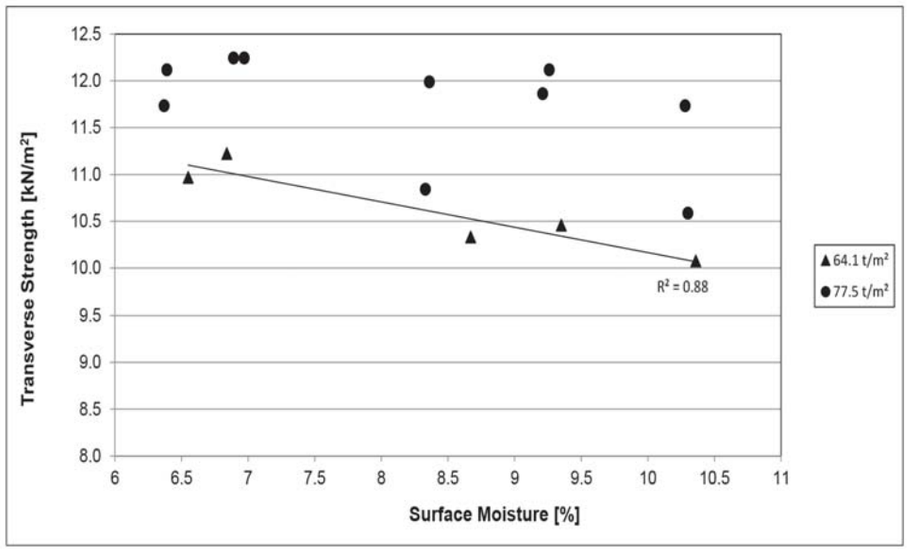

Figure 5—Transverse strength of Waterberg sscc as a function of surface moisture for a full-sized compaction plate

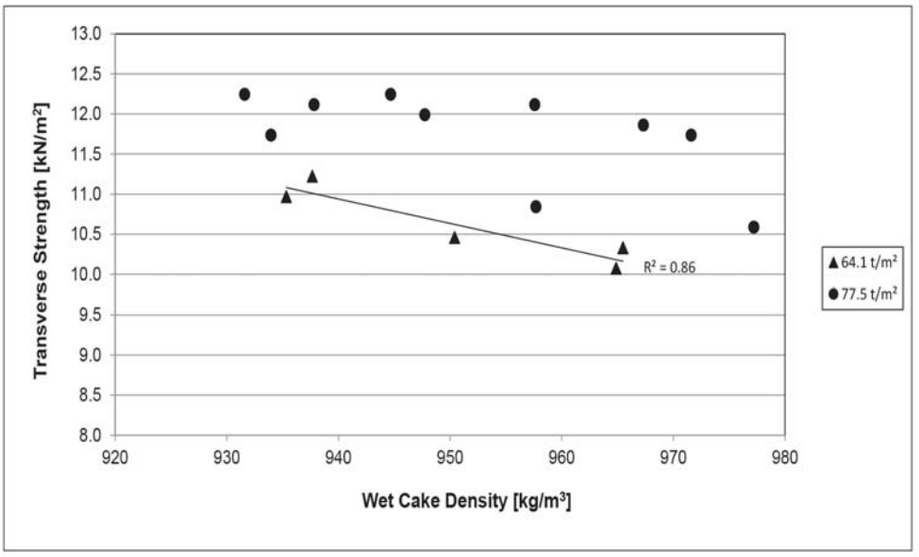

Figure 6—Transverse strength of Waterberg sscc as a function of wet cake density for the full-sized plate tests

kN/m² and 18 kN/m².

When depicting transverse strength as a function of wet cake density (Figure 6), a similar trend was observed as that shown in Figure 5, as expected, since the cake density increased with moisture content. The transverse strength was adversely affected by increasing moisture. According to Abel, Rosenkranz, and Kuyumcu (2009), with increasing cake density the transverse strength should increase. Therefore, the negative trend indicates that excessive moisture played a significant role.

In terms of the observed maximum transverse strength levels (12.0 kN/m² to 12.5 kN/m²) and surface moisture (6.4% to 10.3%) in Figures 5 and 6, the maximum wet cake density obtained was between 930 kg/m³ and 958 kg/m³ for the full-sized plate compaction method for the compaction conditions that were considered.

Results from 1/3-sized plate

Waterberg sscc 1, 2, and 3 and Oaky North materials were utilized during compaction tests with a 1/3-sized compaction plate, *i.e.* covering one-third of the cross-sectional area of the cake. The properties of Waterberg sscc 1, 2, and 3 are very similar and the coals are comparable in behaviour (see Table I). The effect of the 1/3-sized plate was evaluated in an attempt to reach the target densities as well as to expel more trapped air and water from the coal cake during compaction.

Figure 7 depicts the wet cake densities obtained as a function of surface moisture when a 1/3-sized compaction plate was utilized. The wet cake densities increased linearly with increased surface moisture content, showing high R^2 values, *i.e.* between 0.88 and 1.00. Figure 7 also shows that the wet cake density

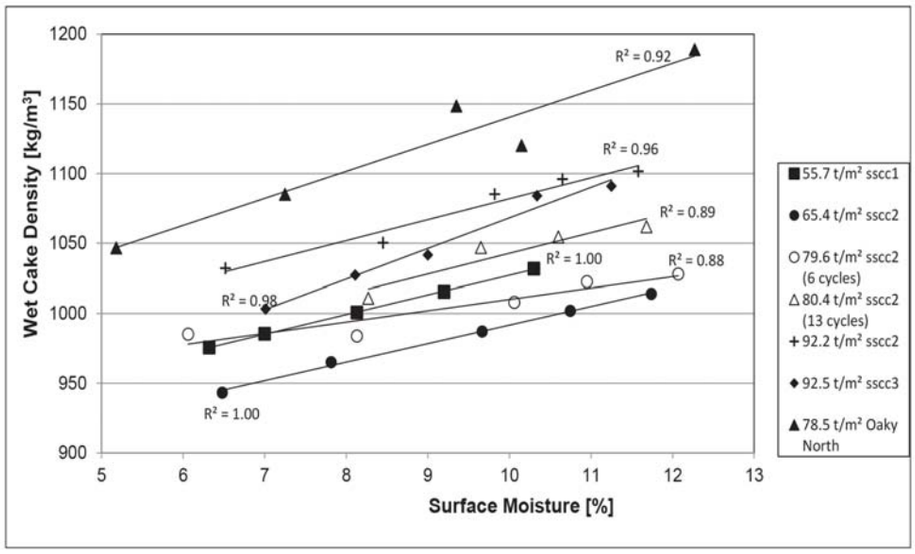

Figure 7—Wet cake density as a function of surface moisture for the 1/3-sized plate tests for various applied forces and samples

increased, in general, for Waterberg sscc with an increase in applied force. A maximum coal cake density of 1 102 kg/m^3 was obtained at 92.2 t/m^2 applied force and 11.58% surface moisture content. In the case of Oaky North, a similar trend was observed as for Waterberg sscc, although a lower applied force, *i.e.* 78.5 t/m^2, was required to achieve a similar wet cake density of 1 189 kg/m^3 with a surface moisture content of 12.27%. Thus, a hard coking coal seems to compact more easily than a semi-soft coking coal.

The applied force of 92.2 t/m^2 for Waterberg sscc 2 is about 30–40 t/m^2 higher than would be expected in a commercial application to obtain a 1 100 kg/m^3 wet compaction density. In the case of Oaky North, the applied force was closer to that of a commercial application, *i.e.* 78.5 t/m^2 vs 60 t/m^2. These higher applied force values obtained in the laboratory are probably due to friction forces from the mould sides during compaction on such a small scale.

When comparing the scatter of results in Figure 4 and Figure 7, a significant improvement was noted for Waterberg sscc wet cake densities as a function of surface moisture, *i.e.* a 12.8% increase from 977 kg/m^3 to 1 100 kg/m^3 for the 1/3-sized compaction plate. This improvement is probably due to the increased consistency obtained during compaction when more air and water were expelled from the coal cake during the utilization of the 1/3-sized plate.

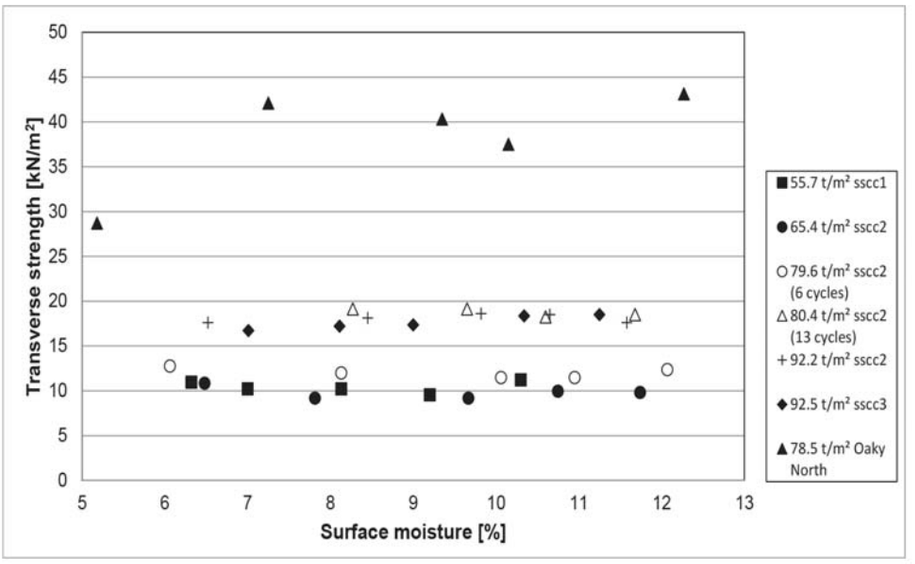

Figure 8—Transverse strength as a function of surface moisture for 1/3-sized plate compaction for various applied forces

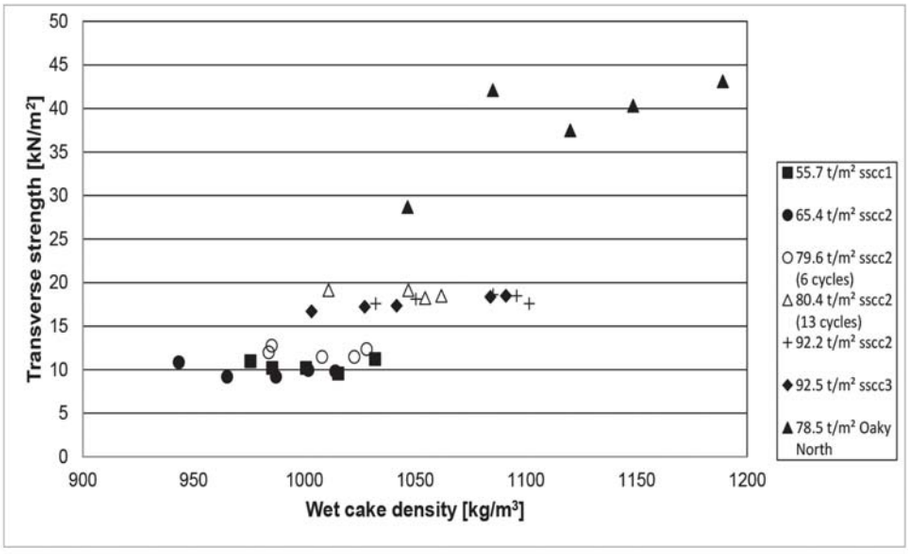

Figure 9—Transverse strength as a function of wet cake density for 1/3-sized plate compaction at various applied forces

The surface moisture content did not have any appreciable effect on the transverse strength, as shown in Figure 8. The applied force had the most significant impact on the transverse strength of Waterberg sscc materials, where the transverse strength increased to 19 kN/m^2 with 80–92 t/m^2 applied force. This equates to an increase of 52.8% compared to the results obtained with the full-sized plate, indicating the benefit of using a $^1/_3$-sized compaction plate. These transverse strengths are close to the shear strengths reported by Rejdak and Wasielewski (2015). In the case of Oaky North coal, the transverse strength increased significantly to 46.7 kN/m^2. This is ascribed to the different properties of the Oaky North hard coking coal, such as higher rank and lower vitrinite content (see Table I), compared to Waterberg sscc, which increased the transverse strength of this coal owing to its lower wettability properties (Rejdak and Wasielewski, 2015).

The increase in transverse strength obtained at an applied force of 80.4 t/m^2 for Waterberg sscc is ascribed to an increased number of iterations (13 compaction cycles) per layer of compaction during the preparation of the coal cake, compared to 79.6 t/m^2 applied force (six compaction cycles). In the former case, a coal layer was compacted 13 times with the $^1/_3$--sized compaction plate in overlapping sections compared to six times for the 79.6 t/m^2 test. This greater compaction intensity might have caused (i) a higher volume of air and water to be expelled from the coal cake, as well as (ii) particle breakage that created new surfaces for bonding between particles containing moisture. No attempt was made to determine the PSD differences between compacted coal cakes in each of these two tests in order to expound upon this result.

When transverse strength was plotted as a function of wet cake density (Figure 9), a similar trend was observed to that shown in Figure 8, as expected, since the cake density increased with surface moisture. The transverse strength of Waterberg sscc materials was only slightly influenced by the wet cake density, in contrast to the results obtained with the full-sized compaction plate. Although the transverse strengths for Oaky North are significantly higher than those for the Waterberg sscc materials, these are, in general, not affected by wet cake density.

The calculated porosities in the tests performed with the $^1/_3$-sized compaction plate as a function of applied force are depicted in Figure 10. A higher applied force resulted in lower porosity, with the porosity decreasing linearly (R^2 = 0.65) for all the Waterberg sscc materials evaluated. The lowest porosity obtained for Waterberg sscc with a $^1/_3$-sized compaction plate, *i.e.* 32%, was a 20% improvement compared to a full-sized plate. This again indicates that an opportunity still exists to improve the bulk densities during compaction. In the case of Oaky North, the lowest porosity obtained was 26%. In this case, it was assumed that the relative density of Oaky North is similar to that of Waterberg sscc based on coal processing parameters, namely 1 400 kg/m^3.

The normal stress that a compacted coal cake is exposed to owing to its own weight is a function of its height, compaction density, and gravity (Kuyumcu, Abel, and Rosenkranz, 2011). Therefore, for a typical Waterberg sscc coal cake prepared in this study with a height of 0.206 m and 1 102 kg/m^3 compaction density, the normal stress owing to its weight is 2.2 kN/m^2. The transverse strength obtained for this specific coal cake was 17.6 kN/m^2 – eight times the normal strength. This strength should be sufficient to withstand handling while the cake is being pushed into a 1 t pilot plant coke oven without breaking or collapsing owing to its own weight. It must be noted that, in this case, the compacted coal cake is rammed into the pilot plant oven by a pusher arm and not by a feeder sole plate as is the case for commercial applications. In the case of the Oaky North coal,

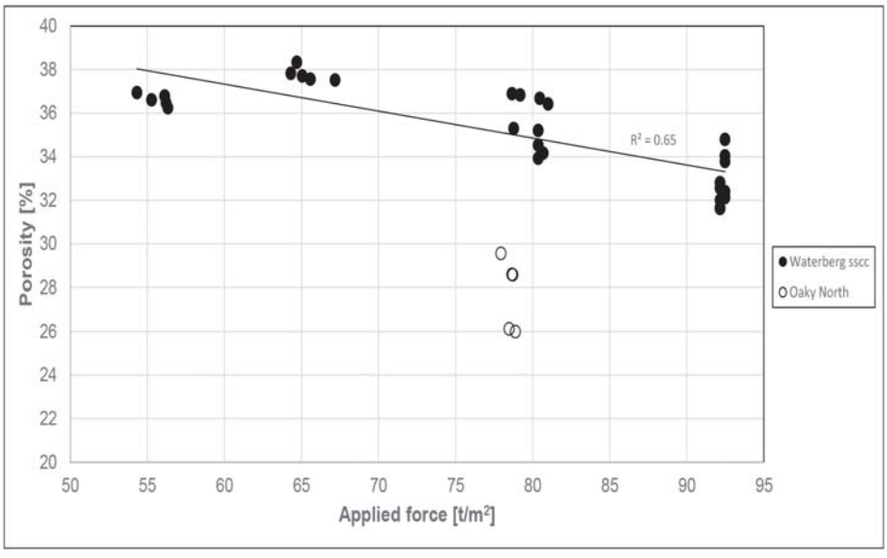

Figure 10—Coal cake porosity as a function of applied force for ⅓-sized plate compaction

the transverse strength exceeded the normal stress by about 20 times for a 1 189 kg/m^3 wet density coal cake, indicating once again a sufficient strength. Therefore, strong coal cakes of sufficient stability can be expected during 1 t coke pilot plant oven operations.

Conclusions

- The results confirm the importance of a suitable coal cake compaction method, *i.e.* a $^1/_3$-sized compaction plate rather than a full-sized plate, to remove entrapped air and water from compacted coal layers.
- The target wet cake density of 1 100 kg/m^3 (79% of material density) was achieved for Waterberg sscc using the $^1/_3$-sized compaction plate in the laboratory-scale set-up with 11.6% surface moisture and 92.2 t/m^2 (commercially equivalent) applied force. For Oaky North hard coking coal, a wet cake density of 1 189 kg/m^3 (85% of material density) was obtained at a surface moisture content of 12.27% and a lower applied force, *i.e.* 78.5 t/m^2.
- Wet cake density increased linearly with increased surface moisture and applied force for the investigated surface moisture range of 6–12.3% for both sizes of compaction plate evaluated, as well as for all materials investigated.
- Higher wet cake densities and transverse strengths were achieved with an increase of applied force.
- Coal cake transverse strength was only very slightly affected by an increase in surface moisture content during the $^1/_3$-sized compaction plate tests.
- Coal cake transverse strengths obtained in this study are related to typical coal cake shear strengths obtained by other workers in this field.
- Acceptable coal cake strengths, and therefore stability, were obtained for all materials evaluated during this study.
- The minimum porosities obtained at the compaction conditions considered during this study were 32% and 27.8% for Waterberg sscc and Oaky North, respectively, indicating that further improvements in terms of increasing wet cake densities and decreasing moisture contents should be possible at suitable coal cake strengths.
- It is recommended that a study be conducted to evaluate the impact of the manipulation of the zeta potential of the coal surfaces prior to compaction in order to decrease repulsive forces between the coal surfaces, and thus to enhance coal cake strengths and compaction densities.

Acknowledgements

The author would like to thank Exxaro Resources for permission to publish this work.

References

Abel, F., Rosenkranz, J., and Kuyumcu, H. Z. 2009. Stamped coal cakes in cokemaking technology. Part 1 – A parameter study on stampability. *Ironmaking and Steelmaking,* vol. 36, no. 5. pp. 321–326.

Burat, F., Kuyumcu, H.Z., and Sander, S. 2015. Effect of particle-size distribution and degree of saturation on coal-compacting processes within a coke-making operation. *International Journal of Coal Preparation and Utilization,* vol. 35, no. 4. pp. 216–231.

Dash, P.S., Krishnan, S.H., Sharma, R., Banerjee, P.K., and Haldar, S.K. 2005. Laboratory scale investigation to improve the productivity of stamp charge coke oven through optimisation of bulk density of coal cake. *ISIJ International,* vol. 45, no. 11. pp. 1577–1586.

Kumar, P.P., Barman, S., Ranjan, M., Ghosh, S., and Raju, V.V.S. 2008. Maximisation of non-coking coals in coke production from non-recovery coke ovens. *Ironmaking and Steelmaking*, vol. 35, no. 1. pp. 33–37.

Kuyumcu, H.Z., Abel, F., and Rosenkranz, J. 2011. Analyses of the coal densification behaviour and the coal cake stability within the stamped charge coke making operation. *Proceedings of the Conference in Minerals Engineering 2011*, Luleå, Sweden, 8-9 February 2011. Alatalo, J. (ed.). Luleå Tekniska Universitet. pp. 123-137. https://www.scribd.com/document/55547012/Analyses-of-the-Coal-Densification-Behaviour-and-the-Coal-Cake-Stability-Within-the-Stamped-Charge-Coke-Making-Operation [accessed 3 March 2014].

Kuyumcu, H.Z., Rosenkranz, J., and Abel, F. 2010. Densification behaviour of coking coals within stamp charge operation. *Proceedings of the International Coal Preparation Congress*. Honaker, R.Q. (ed.). Society for Mining, Metallurgy and Exploration, Littleton, CO. pp. 947–956.

Kuyumcu, H.Z. and Sander, S. 2014. Stamped and pressed coal cakes for carbonisation in by-product and heat-recovery coke ovens. *Fuel*, vol. 121. pp. 48–56.

Kuyumcu, H.Z., Sander, S., and Burat, F. 2012. Investigation on the coal compacting processes in the cokemaking industry. *Proceedings of the XIII International Mineral Processing Symposium*, Bodrum, Turkey, 10-12 October 2012. Department of Mining Engineering, Eskisehir Osmangazi University. 9 pp.

Madias, J. and de Córdova, M. 2013. A review on stamped charging of coal. *Proceedings of the Association for Iron and Steel Technology*, Pittsburgh, PA, 6-9 May 2013. Vol 1. pp. 253–262.

Nishioka, K. and Yoshida, S. 1983. Strength estimation of coke as porous material. *ISIJ International*, vol. 23, no. 5, pp. 387–392.

Nyathi, M.S., Kruse, R., Mastalerz, M., and Bish, D.L. 2013. Impact of oven bulk density and coking rate on stamp-charged metallurgical coke structural properties. *Energy Fuels*, vol. 27. pp. 7876–7884.

Rejdak, M. and Wasielewski, R. 2015. Mechanical compaction of coking coals for carbonization in stamp-charging coke oven batteries. *Physicochemical Problems of Mineral Processing*, vol. 51, no. 1. pp. 151–61.

Sand, A., Rosenkranz, J., and Kuyumcu, H.Z. 2012. DEM modelling and simulation of coal compaction by stamping. http://www.edemsimulation.com/papers/dem-modelling-and-simulation-of-coal-compaction-by-stamping/ [accessed 5 February 2015].

Tiwari, H.P., Saxena, C.K., Banerjee, P.K., Haldar, S.K., Sharma, R., and Sanjoy, P. 2012. Study on heating of coal during carbonization in non-recovery oven. *International Journal of Metallurgical Engineering*, vol. 1, no. 6. pp. 135–142.

Wikipedia. 2014. Strength of materials. http://en.wikipedia.org/wiki/Strength_of_materials [accessed 12 September 2014]. ◆

SMART MINING
SMART ENVIRONMENT
SMART SOCIETY

Implementing change now, for the mine of the future




4-5 July 2019

Accolades Boutique Venue, Midrand

BACKGROUND

Society in general, and the economy in particular, is evolving at breakneck speed. Old jobs are being lost and new ones are constantly being created. It is likely that mines developed in the next ten years will have a very different staff complement to those currently in production. It is also clear that we are at tipping points for climate systems and for biodiversity: the challenges facing the extractive sector in the coming decades are likely to be much greater than anything in the past century. What does this mean for environmental management? How should we be planning mines to reduce environmental footprints? What skills do we need to do this? Which energy sources will be available and will they have an impact on production? Can we close mines in a way that ensures that viable post-mining economies can be established? This conference bridges the gap between practitioners and decision-makers and managers in both the public and private sectors. The intention is to transfer knowledge and to debate the big issues facing regulators, mining companies, labour, and communities in a way that identifies solutions. The conference will consist of a number of invited keynote speakers who will focus on strategic issues, with the possibility of a workshop included.

WHO SHOULD ATTEND

The conference should be of interest to anyone working in or with the mining sector, including government and civil society organizations. It would be of particular relevance to advisors, consultants, practitioners, researchers, organized labour, government officials, and specialists working in the following areas:

- Environmental Management
- Sustainability
- Stakeholder Engagement
- Local and Regional Development Planning
- Mining Legislation.

SAIMM
THE SOUTHERN AFRICAN INSTITUTE OF MINING AND METALLURGY

FOR FURTHER INFORMATION CONTACT:
Yolanda Ndimande, Conference Co-ordinator, SAIMM
P O Box 61127, Marshalltown 2107 · Tel: +27 (0) 11 834-1273/7
E-mail: yolanda@saimm.co.za · Website: http://www.saimm.co.za

Compaction tests on coking coals. Part 2: Pilot-plant-scale compaction with a 60-ton hydraulic press

G. Coetzer

Affiliation:
Previously from Exxaro Resources

Correspondence to:
G. Coetzer

Email:
atomium@iafrica.com

Dates:
Received: 22 Feb. 2017
Revised: 26 July 2018
Accepted: 8 Nov. 2018
Published: April 2019

How to cite:
Coetzer, G.
Compaction tests on coking coals. Part 2: Pilot-plant-scale compaction with a 60-ton hydraulic press. The Journal of the Southern African Insitute of Mining and Metallurgy

DOI ID:
http://dx.doi.org/10.17159/2411-9717/17/071/2019

Synopsis

Prior to operating a non-recovery coke pilot plant oven, it was essential to ascertain coal cake stability during the loading of a 1 m^3 (1 m × 1 m × 1 m) coal cake into the cold pilot-plant oven by a pusher mechanism. Previously established laboratory-scale compaction parameters, to obtain coal cakes with sufficient stability, were employed during the loading tests of the coal cakes. Two different coals were evaluated, namely Waterberg semi-soft coking coal (sscc) and Oaky North hard coking coal.

It was demonstrated that lower applied compaction forces (14%) can be utilized during 1 m^3 compaction, in comparison to laboratory-scale tests, to obtain similar wet cake densities, owing to differences in the effect of frictional forces. Wet cake densities for Waterberg sscc improved slightly (3%) to 1.13 t/m^3 when utilizing 79 t/m^2 applied force for a 1 m^3 coal cake, in comparison to laboratory-scale tests. Similar results were obtained for Oaky North hard coking coal, with a 6% density increase to 1.27 t/m^3 at a similar applied force. Porosities decreased by 13% and 32% for Waterberg sscc and Oaky North coal, respectively, when 1 m^3 compaction was compared to laboratory-scale tests. An opportunity exists to further decrease the porosities of Waterberg sscc during compaction, whereas acceptable compaction parameters were achieved for Oaky North hard coking coal. Most major vertical cracks and the partial collapse of coal cakes were mitigated, and high-stability coal cakes were obtained that could be successfully loaded into the pilot-plant coke oven by a pusher mechanism.

Factors contributing to the instability of the coal cake during loading into the oven, such as vertical cracks, are (i) the cubic geometry (1 m^3) of the coal cake, (ii) friction exerted by the oven floor, and (iii) mechanical problems, such as a misalignment between the pusher machine feeder plate and the oven floor.

Keywords
coking coal, compaction test, coal cake stability, wet coke density, pilot scale.

Introduction

Operation of the stamp-charging horizontal 1 t electrically heated coke pilot-plant oven at Exxaro Resources requires coal cake stability during the loading of a 1 m^3 compacted coal cake into the oven. In this case, a pusher plate is utilized to push the coal cake into the oven over the oven floor. This is in contrast to a 'spoon' or bottom plate feeding mechanism as found in industrial horizontal coke ovens. The pusher plate loading mechanism dictates that the coal cake should possess high stability and inherent strength owing to frictional forces exerted by the oven floor. In order to obtain a coal cake of acceptable stability for the 1 t coke oven, various compaction parameters need to be verified and established.

Coetzer (2019) reported on the parameter settings required during laboratory-scale investigations of different coking coals. These findings are preconditions for obtaining high-stability coal cakes for loading into the 1 t pilot plant coke oven to ensure successful cokemaking. Needle-shaped coke, such as that formed by Waterberg semi-soft coking coal (sscc), can pose a risk to operations if the coal cake collapses inside the oven during loading, since the needles of the resultant coke product may wedge into the oven walls, preventing the pushing of the coke. Severe collapsing of the coal cake during loading may also prevent the closing of the oven door. Furthermore, it can affect the repeatability of coking time and coke yield. Therefore, it is essential to obtain a high-stability coal cake for the successful operation of the oven. Cold coal cake stability should also transfer to thermal stability in the coke oven; this is a prerequisite to allow the uninterrupted pushing of coke after the coking process. Figures 1 to 3 illustrate various examples of thermal stability in the produced coke.

This work determined the behavioural characteristics of the coal when compacted by a 60 t hydraulic press, similar to those utilized commercially (Xiaobing, 2013), and loaded into a pilot-plant coke oven. The

Figure 1—Coke collapsed inside the oven owing to the loading of an unstable coal cake

Figure 2—High-stability coke cake inside the coke oven

Figure 3—Successful pushing of coke into the quenching chute

focus was on parameters such as cake density, cake moisture, applied force to the coal cake, and coal cake stability. These parameters are crucial for the successful operation of a non-recovery coke oven.

Apart from these parameters, other mechanical challenges were addressed to enhance coal cake stability during its loading into the oven, such as:

- Alignment of the compaction box with the oven floor during the pushing of the coal cake
- Smoothing and levelling of the coke oven floor with diamond cup discs
- Strengthening of the compaction box floor and sides
- Repositioning of the compaction box fitment on top of the pusher machine, to align the box in respect of the oven floor
- Repositioning of pusher machine rails with respect to the oven floor, to ensure centring of the coal cake inside the oven.

Literature survey

The stability of a compacted coal cake is a crucial requirement before loading it into a heat recovery coke oven. Various coal cake parameters need to be optimized during the compaction process. The parameters of importance, according to Abel, Rosenkranz, and Kuyumcu, (2009), Kuyumcu and Sander (2014), Burat, Kuyumcu, and Sander, (2015), and Rejdak and Wasielewski (2015) include:

- Wet coal cake bulk density
- Surface moisture level
- Surface properties of the coal (wettability)
- Applied force
- Mechanical strength of the compacted coal cake
- Granulometric properties of coal particles (particle size distribution (PSD), particle shape, particle density, and grindability).

Water is unfavourable with respect both to the thermal (a higher energy demand to evaporate water) and to the ecological (a greater volume of wastewater) balance of a carbonization process (Kuyumcu, Rosenkranz, and Abel, 2010; Rejdak and Wasielewski, 2015). High volumes of interstitial water absorb the impact of the compactor/pressing plate and prevent the particle breakage that contributes to a dense packing of the coal cake. For water contents higher than 14%, the compression energy is mostly used to expel the water (Kuyumcu, Rosenkranz, and Abel, 2010). In addition, water can affect the ceramic lining of the coke ovens negatively. Therefore, it is necessary to determine the optimum water content with respect to cake stability (Kuyumcu, Abel, and Rosenkranz, 2011).

Industrial stamp charge technology encompasses the use of a combined stamping-charging-pushing machine. Various authors in this field (Abel, Rosenkranz, and Kuyumcu, 2009; Kuyumcu, Rosenkranz, and Abel, 2010; Kuyumcu and Sander, 2014) have indicated that during this process the bulk density of the feed coal is increased to a compact density of 80% of the true coal density, *i.e.* a compact density of about 1 100 kg/m^3, depending on the true density of the coal, before charging to the oven. The stamping process increases the mechanical strength of the coal cake and makes charging straightforward from the stamping-charging-pushing machine into the oven. The coal cake usually does not collapse entirely in the case of mechanical failure as one would expect from flowing bulk solids. Most commonly, portions in the range of 12% to 16% break from the cake when the mechanical strength is exceeded locally. Coetzer (2019) summarized the causes for this phenomenon identified by

various authors (Abel, Rosenkranz, and Kuyumcu, 2009; Madias and de Córdova, 2013; Kuyumcu and Sander, 2014) when dynamic forces act on the cake:

- Cake weight (*i.e.* critical cake height)
- A local reduction of shear strength along a plane that is sloped according to a decreased angle of internal friction (cake failure by shear fracture with the fracture along a sliding plane)
- Bending or compressive stress when the tensile strength of the compact is too low (cake failure by cleavage fracture where the fracture plane is vertical to the tensile load)
- Poor water distribution or wetting.

Abel, Rosenkranz, and Kuyumcu (2009) indicated that a criterion for the sufficient mechanical strength of the coal cake relates that strength to the loading conditions, considering the weakening of the cake and the dynamic stress, through the introduction of appropriate safety margins.

Coetzer (2019) previously showed, during laboratory test work, that for both Waterberg sscc and Oaky North hard coking coal, the transverse strength of the coal cake was relatively independent of the wet cake density. Since no compressive or transverse strength tests were performed during this study on 1 m^3 coal cakes owing to some limitations of the pilot plant set-up at the time, the aim was to obtain coal cakes of a suitably wet cake density and stability.

The specific aim of this study was to obtain a 1 m^3 coal cake with high stability and a compacted wet cake density of 1 100 kg/m^3 or higher, with a surface moisture content as low as possible, and applied force as proposed by Kuyumcu and Sander (2014), by utilizing a 60 t press. Two different coals were evaluated, namely Waterberg sscc and an Oaky North hard coking coal.

Experimental

Materials

The preparation of Waterberg sscc and Oaky North hard coking coal samples is described by Coetzer (2019). The material properties of these coals utilized during the 1 m^3 coal stability tests are summarized in Table I.

Compaction

A 60 t hydraulic press with a compaction platform was utilized to produce 1 m^3 (1 m × 1 m × 1 m) coal cakes (Figure 4). A compaction box fitted onto the platform was manoeuvred hydraulically into position prior to filling and compaction. A hopper was filled with a predetermined volume of coal (usually one layer) and this prepared coal (crushed and moisture level adjusted) was transported by a forklift from the preparation area to the hydraulic press. The sliding gate of the hopper was opened while the coal was suspended above the compaction box. An operator ensured that the hopper was emptied completely. The hopper was removed and transported back to the preparation area. This was followed by the compaction of the coal layers with a $^1/_3$-sized plate (see Figure 5), instead of a full-sized plate, according to a preselected compaction philosophy. Laboratory tests have shown that higher compaction wet cake bulk densities and transverse strengths are obtainable with a $^1/_3$-sized compaction plate than with a full-sized plate (Coetzer, 2019). Various layers of compaction (six in total) were utilized to ensure uniform compaction density and mechanical stability of the compacted coal cake to obtain a final coal cake height of 1 m. Each layer was compacted in an overlaying manner of 5× in sections of 5, *i.e.* 1,2,3,4,5, followed by 5,4,3,2,1, *etc.*; thus 25 presses per layer. This was to ensure that as much entrapped air and water as possible was expelled, leading to a more homogeneous compact. The total mass of coal charged was 1 125 kg in each case. Care was taken to ensure that each compacted layer was levelled inside the compaction box prior to introducing the next layer. The supplier of the press calibrated the compaction pressure applied to the coal cake, based on the hydraulic pressure.

Table I

Properties of various coals evaluated

Property	Waterberg sscc	Oaky North
Inherent moisture (%)	2.0	0.6
Mineral content (dry) (%)	10.7	9.7
Volatiles (dry) (%)	37.6	24.1
Fixed carbon (calc.) (%) (dry)	51.7	66.2
Gross calorific value (MJ/kg)	29.40	32.45
Vitrinite (%)	87.7	81.6
Rank (RoVmax, %)	0.70	1.20

Figure 4—60 t hydraulic press with platform

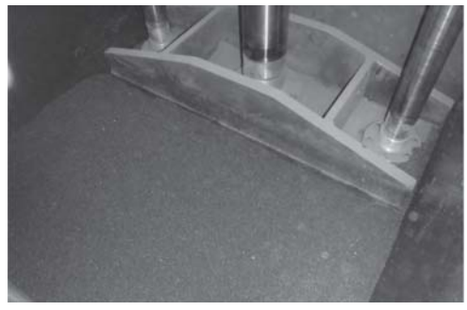

Figure 5—Hydraulic press in action inside compaction box

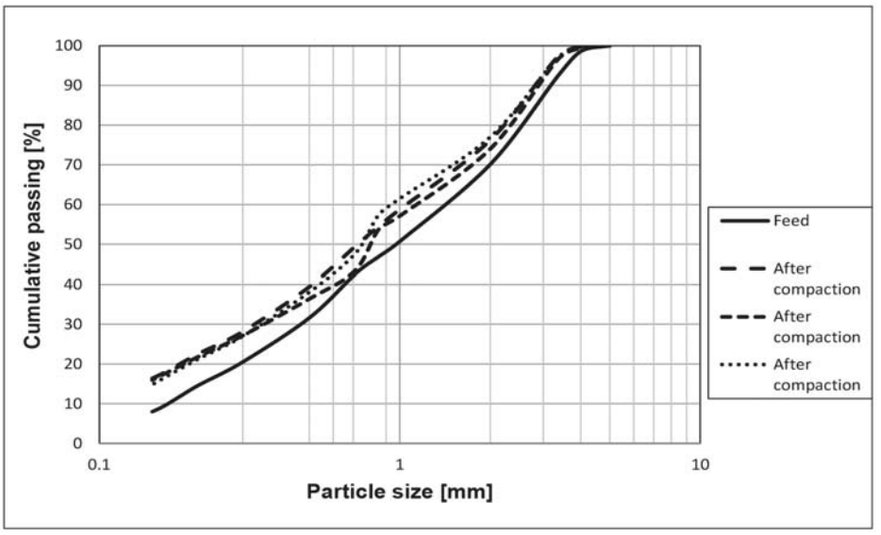

Figure 6—Particle breakage of Waterberg sscc during compaction with a 60 t hydraulic press

Results

Particle breakage

PSD tests were performed on the Waterberg sscc before and after compaction and de-agglomeration during stability tests at 65 t/m^2 applied force. Figure 6 shows the change towards slightly finer material, *i.e.* an average increase in fineness of 4% to 6%. The largest increase was reported for the –1 mm fraction, *i.e.* 6% to 11%. These results correspond with those reported by Kuyumcu, Rosenkranz, and Abel (2010). This is a positive finding, since further particle breakage assists in filling the interstitial voids with smaller particles during the compaction operation. In addition, excess surface moisture will be adsorbed on the newly created surfaces of smaller particles and will reduce internal friction (Kuyumcu and Sander, 2014). This, in turn, facilitates an increase in binding strength, *i.e.* cohesion forces between particles; thus, in overall cake compaction density and stability.

Wet cake density

Figure 7 shows the relationship between wet coal cake density and surface moisture for various coals and applied forces. In the case of Waterberg sscc, increased applied forces from 62 t/m^2 to 79 t/m^2, by means of changing the hydraulic pressure of the press, at surface moisture levels between 9.1% and 11.2%, slightly enhanced the wet cake density from 1.05 t/m^3 to 1.14 t/m^3 (an 8% increase), although the results were somewhat scattered at each applied force. The coefficient of variation for the wet cake density results obtained at 79 t/m^2 applied force, for example, was 0.66% (1.12 ± 0.007 t/m^2), which was well within experimental error range. The scattering of the results was mainly due to ongoing mechanical changes that were made to the compaction box. For example, it was found that the relatively low wet bulk density of 1.09 t/m^3 at an applied force of 79 t/m^2 was due to the flexing of the bottom floor of the compaction box. This was addressed, and higher cake densities were obtained.

During laboratory tests on Waterberg sscc (Coetzer, 2019), the maximum obtainable wet cake density was 1.10 t/m^3 at a commercially equivalent 92 t/m^2 applied force, at 12.6% surface moisture. A maximum wet density of 1.13 t/m^3 was obtained at a significantly lower applied force (14% lower), *i.e.* 79 t/m^2, at a lower surface moisture level (11%) for a 1 m^3 coal cake. This indicates that a marginal (3%) increase in wet cake density is possible with the 1 m^3 compaction bin in comparison to the laboratory scale. This difference was most likely due to frictional forces caused by the mould's sides in the laboratory-scale test. In order to improve the wet cake density further, other factors such as zeta potentials and the impact of mine process water during compaction need to be evaluated.

In the case of Oaky North coal, similar trends were noted as those obtained for Waterberg sscc. In this case, the wet cake density increased by 6% from 1.19 t/m^3 to 1.27 t/m^3 at similar applied forces (79 t/m^2) compared to the laboratory tests.

Cake porosity

Figure 8 shows coal cake porosities[1] obtained during laboratory and 1 m^3 compaction tests. In the case of Waterberg sscc, the porosities decreased by 25% during 1 t compaction tests when compared to laboratory tests, *i.e.* from 39.8% to about 30% at 65 t/m^2 applied force. A 13% decrease in porosity was achieved for these scenarios at 79 t/m^2 applied force. These positive results, *i.e.* lower porosities, indicate that frictional force effects of the compaction bin were exceeded in the 1 m^3 compaction bin compared to the 9 kg laboratory mould. The results also indicate that an opportunity still exists to improve on the bulk densities

[1]Porosity was calculated from the relationship:

$$\left[1 - \frac{cake\ bulk\ density\ (dry\ based)}{relative\ density}\right] * 100$$

The latter relative density referred to 1.4 as being utilized during the preparation of sscc at Waterberg mine.

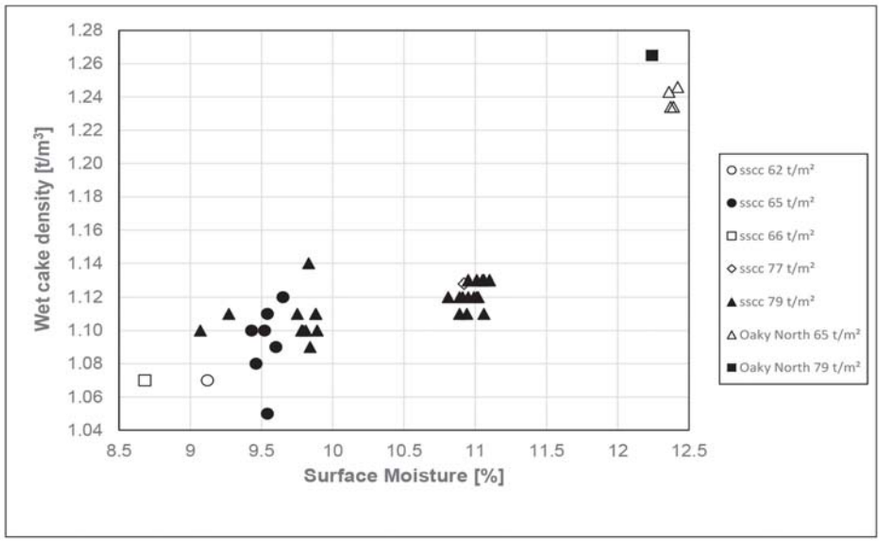

Figure 7—Wet coal cake density as a function of surface moisture for various coals and applied forces

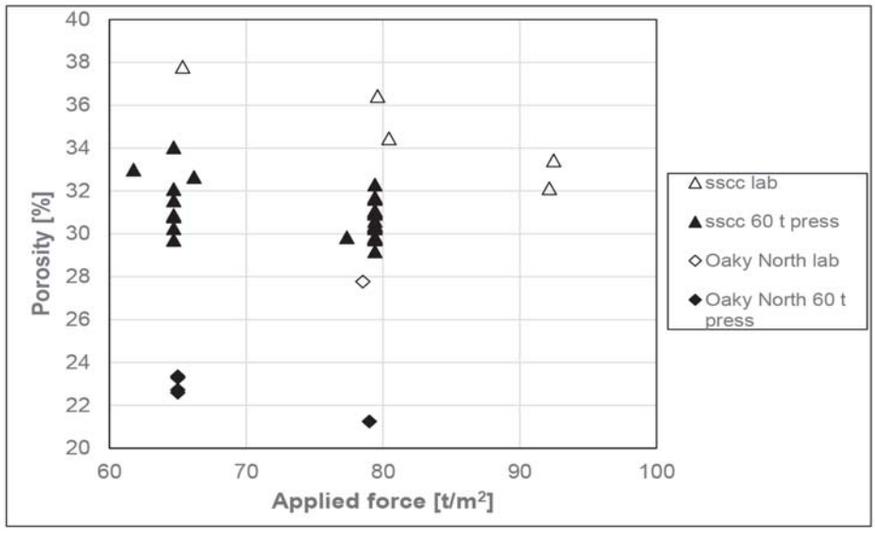

Figure 8—Coal cake porosity as a function of applied force

during compaction, since the lower porosity limit is in the region of 20% (Sand, Rosenkranz, and Kuyumcu, 2012).

In the case of Oaky North, the porosities dropped significantly (32%) from 28% to 21% at 79 t/m^2 applied force, indicating that maximum compaction conditions had most likely been reached for this coal, based on the low final porosity obtained, as indicated by Sand, Rosenkranz, and Kuyumcu (2012). In this case, it was assumed that the relative density of Oaky North is 1.4, similar to that of Waterberg sscc, based on coal processing parameters.

Cake stability

The stability of 1 m^3 compacted coal cakes, *i.e.* the ability to maintain the original configuration after compaction in the compaction bin, was evaluated during the pushing or loading of the cakes into the cold pilot-plant coke oven. Coal cake stability challenges of the compacted coal cakes that were overcome during loading into the 1 t coke pilot plant oven are as follows:

- Coal cake collapse or partial collapse
- Flaking of the coal cake sides
- Coal sticking to the side plates of the compaction box
- Cracking of the coal cake
- Residual coal left behind in the compaction bin after loading the coal cake into the oven

➤ The pusher plate of the pusher machine should fit flush with the coal cake before pushing it into oven; otherwise the sudden force on the coal cake might disturb the staility.

Some of these mechanical instabilities encountered when loading the coal cake into the coke oven are shown in Figure 9. This figure clearly indicates disintegration or collapse of the sides

Figure 9—Collapsing of coal cake inside the pilot plant oven

Figure 10—Large crack on top of the coal cake

Figure 11—High-stability Waterberg sscc coal cake

Figure 12—High stability Oaky North coal cake

of the coal cake when loaded into the cold oven, as well as the following flaws: (i) flaking of the front of the cake, (ii) shavings on the oven floor, and (iii) a large vertical crack (see Figure 10) that spread through the cake. Partial collapsing of the coal cake and severe flaking of the surfaces can interfere with the coking process. The formation of fingers or needles against the oven walls, especially in the case of Waterberg sscc, will interfere with the pushing of the coke product (see Figure 1), resulting in inferior coke, since the benefit of dense compaction of the coal is lost in these sections.

Figures 11 and 12 show high-stability coal cakes that were successfully loaded into the cold pilot-plant oven with only minor flaws, such as flaking and small hairline cracks. The latter are not visible in these pictures.

It was noted during compaction of Oaky North coal that some water seepage had occurred at the bottom of the mould. This implies that the total moisture content of the Oaky North feed material was slightly too high. The additional water had absorbed some of the applied compaction force, which was not transferred to the coal particles during compaction. Rather, it was used to expel the water from the coal cake. Therefore, surface moisture can be further decreased. A surface moisture content of 12.4% was utilized during the coking tests in order to compare the results of the various testing campaigns. It must also be borne in mind that excess water can adversely affect the ceramic lining of the coke oven (Rejdak and Wasielewski, 2015).

Mechanical changes made to the pusher plate, compaction box, and oven floor resulted in some improvement in the overall stability of the coal cakes. However, it was difficult to eliminate the spreading of a large crack in each case. These large cracks do not cause problems during coke formation, as long as the cake does not collapse against the walls of the oven. However, high-stability coal cakes were indeed obtained for both Waterberg sscc and Oaky North coal, as indicated in Figures 11 and 12.

All cracks commenced the moment the coal cakes were pushed into the cold oven on the refractory floor. In order to investigate this further, a metal flooring plate was inserted onto the oven floor to evaluate the effects of stability of the oven floor and the friction exerted on the pushed coal cake. The results showed a significant improvement in stability, although hairline cracks occurred. Therefore, it seems that a possible cause

contributing to the instability of the coal cake was the friction of the refractory oven floor. The dimensions of the coal cake (1 m × 1 m × 1 m), with its centre of gravity situated in the middle of the cake, also contributed. The height should have been lower in order to increase stability. It was noted that the pusher plate bulged towards the coal cake. This factor might have contributed to an uneven pushing of the cake into the oven, causing some disruption of the compacted layers. This was noticeable in the cracks that spread through the thickness of the cake for most coal cakes. During the loading of a coal cake into a hot oven at 900°C, prior to cokemaking, the friction on the oven floor should be lower than during cold loading owing to the effect of temperature on frictional forces. The introduction of sawdust to the hot oven prior to the loading of the coal cake also assisted in the loading.

In summary, the cubic geometry of the coal cake (1 m^3), as well as friction on the oven floor, fundamentally contributed to the instability of the coal cake during loading into the cold oven, since the cracking of the cake could only be eliminated when extremely high compaction wet densities were employed, *i.e.* > 1.1 t/m^3. Such high densities will most likely not be utilized on a commercial scale owing to the costs involved in obtaining these densities. A previous preliminary test performed by the author with a coal cake 730 mm in height, instead of 1 000 mm, eliminated crack formation, indicating the importance of cake geometry for mechanical stability. In hindsight, the aspect ratio of the coke pilot plant oven should rather be 1.5:1:1 (length, width, height) in order to overcome geometric stresses within the compacted coal cake.

Conclusions

- No significant enhancement in wet cake density was observed for Waterberg sscc when the surface moisture increased from 9.1% to 11.2% at similarly applied forces.
- Wet cake densities for Waterberg sscc improved slightly (by 3%) from 1.10 t/m^3 to 1.13 t/m^3 when compacting a 1 m^3 cake utilizing a 60 t press, in comparison to laboratory-scale tests. Similar results were obtained for Oaky North coal. with a 6% increase in wet cake density to 1.27 t/m^3 at similarly applied forces, *i.e.* 79 t/m^2.
- Lower applied forces (14%) can be utilized during 1 m^3 compaction when compared to laboratory-scale tests to obtain similar wet cake densities, owing to frictional force effects.
- Porosities decreased by 13% and 32% for Waterberg sscc and Oaky North coal, respectively, when 1 m^3 compaction was compared with laboratory scale tests at 79 t/m^2 applied force. An opportunity still exists to lower the porosities for Waterberg sscc from 30% to about 20% during compaction, whereas maximum compaction conditions had probably been reached for Oaky North coal at 21% porosity.
- The instability of compacted coal cakes during loading into the cold pilot-plant oven was also related to mechanical loading problems, such as a misalignment between the pusher machine feeder plate and the oven floor.
- Most major vertical cracks and the partial collapse of coal cakes were mitigated, and high-stability coal cakes were successfully loaded into the cold pilot-plant coke oven with a pusher mechanism.
- The cubic geometry of the coal cake (1 m^3), as well as the friction exerted by the oven floor, fundamentally contributed to the instability of the coal cake during loading into the oven, since the cracking of the cake during loading can only be eliminated when extremely high compaction densities are employed, *i.e.* > 1.1 t/m^3. Such high densities will most likely not be utilized on a commercial scale owing to the costs involved in obtaining these densities. Changes to the aspect ratio of the coal cake should enhance the stability of the loaded cake.

Acknowledgements

The author would like to thank Exxaro Resources for permission to publish this work.

References

Abel, F., Rosenkranz, J., and Kuyumcu, H.Z. 2009. Stamped coal cakes in cokemaking technology. Part 1 – A parameter study on stampability. *Ironmaking and Steelmaking*, vol. 36, no. 5. pp. 321–326.

Burat, F., Kuyumcu, H.Z., and Sander, S. 2015. Effect of particle-size distribution and degree of saturation on coal-compacting processes within a coke-making operation. *International Journal of Coal Preparation and Utilization*, vol. 35, no. 4. pp. 216–231.

Coetzer, G. 2019. Coal Compaction tests on coking coals. Part 1: Laboratory-scale compaction with a 4-ton hydraulic press. *Journal of the South African Institute of Mining and Metallurgy*, vol. 119, no. 4. pp. 403–412.

Kuyumcu, H.Z., Abel, F., and Rosenkranz, J. 2011. Analyses of the coal densification behaviour and the coal cake stability within the stamped charge coke making operation. *Proceedings of the Conference in Minerals Engineering 2011*, Luleå, Sweden, 8-9 February 2011. Alatalo, J. (ed.). Luleå Tekniska Universitet. pp. 123-137. https://www.scribd.com/document/55547012/Analyses-of-the-Coal-Densification-Behaviour-and-the-Coal-Cake-Stability-Within-the-Stamped-Charge-Coke-Making-Operation [accessed 3 March 2014].

Kuyumcu, H.Z., Rosenkranz, J., and Abel, F. 2010. Densification behaviour of coking coals within stamp charge operation. *Proceedings of the International Coal Preparation Congress*. Honaker, R.Q. (ed.). Society for Mining, Metallurgy and Exploration, Littleton, CO. pp. 947–956.

Kuyumcu, H.Z., and Sander, S. 2014. Stamped and pressed coal cakes for carbonisation in by-product and heat-recovery coke ovens. *Fuel*, vol. 121. pp. 48–56.

Madias, J., and de Córdova, M. 2013. A review on stamped charging of coal. *Proceedings of the Association for Iron and Steel Technology,* Pittsburgh, PA, 6-9 May 2013. Vol 1. pp. 253–262.

Rejdak, M., and Wasielewski, R. 2015. Mechanical compaction of coking coals for carbonization in stamp-charging coke oven batteries. *Physicochemical Problems of Mineral Processing*, vol. 51, no. 1. pp. 151–61.

Sand, A., Rosenkranz, J., and Kuyumcu, H.Z. 2012. DEM modelling and simulation of coal compaction by stamping. http://www.edemsimulation.com/papers/dem-modelling-and-simulation-of-coal-compaction-by-stamping/ [accessed 5 February 2015]

Xiaobing, Z. 2013. Metallurgical Engineering & Project Corporation (MEPC) (China). Personal communication. ◆

31 July – 1 August 2019

The Canvas Riversands, Fourways
Johannesburg, South Africa

ENTREPRENEURSHIP IN THE MINERALS INDUSTRY CONFERENCE 2019

BRINGING IDEAS TO LIFE

BACKGROUND

The adoption of the Mining Charter 3 and refined policies in South Africa presents a new dawn for SMEs and entrepreneurs in the Minerals and Metals sector. While large business is changing their operating models to remain competitive, there is a firm belief that small-scale and emerging business will unlock future employment opportunities and drive economic activity both locally and globally.

WHO SHOULD ATTEND

This event will appeal to young professionals, SMEs, junior miners and entrepreneurs in the minerals sectors, mining industry leaders, original equipment manufacturers (OEMs) both local and international, researchers, government departments and funding agencies

OBJECTIVES

This conference seeks to provide a platform for stakeholders to broaden their view of the industry and identify and leverage on available opportunities.

The various conference sessions are aimed at highlighting how mining companies and OEMs are currently adapting and applying their supplier development strategies and how SMEs, emerging business and entrepreneurs can leverage from these initiatives. The objectives of the conference will be achieved through the following four Forums:

- Supplier Development
- Finance
- Innovation
- Turning ideas into business opportunities

FOR FURTHER INFORMATION CONTACT:
Camielah Jardine · Head of Conferencing · SAIMM
E-mail: camielah@saimm.co.za
Tel: +27 11 834 1273/7 · Website: www.saimm.co.za

YOUNG PROFESSIONALS COUNCIL

THE SOUTHERN AFRICAN INSTITUTE OF MINING AND METALLURGY

NATIONAL & INTERNATIONAL ACTIVITIES

2019

8–10 May 2019 — 22nd International Conference on Paste, Thickened and Filtered Tailings
The Westin, Cape Town, South Africa
Email: paste2019@patersoncooke.com
Website: www.paste2019.co.za

18–25 May 2019 — ALTA 2019 Nickel-Cobalt-Copper
Uranium-REE, Gold-PM, In Situ Recovery, Lithium Processing Conference & Exhibition, Perth, Australia
Contact: Allison Taylor
Tel: +61 411 692 442, E-mail: allisontaylor@altamet.com.au
Website: https://www.altamet.com.au/conferences/alta-2019/

21–22 May 2019 — Hydrometallurgy Colloquium 2019
'Impurity removal in hydrometallurgy'
Glenhove Conference Centre, Melrose Estate, Johannesburg
Contact: Yolanda Ndimande
Tel: +27 11 834-1273/7, Fax: +27 11 838-5923/833-8156
E-mail: yolanda@saimm.co.za, Website: http://www.saimm.co.za

22–23 May 2019 — SA Mining Supply Chain Conference and Strategy Workshop
Bateleur Conference Venue, Nasrec, Johannesburg
Contact: Yolanda Ndimande
Tel: +27 11 834-1273/7, Fax: +27 11 838-5923/833-8156
E-mail: yolanda@saimm.co.za, Website: http://www.saimm.co.za

22–23 May 2019 — Mine Planner's Colloquium 2019
'Skills for the future – yours and your mine's'
Glenhove Conference Centre, Melrose Estate, Johannesburg
Contact: Camielah Jardine
Tel: +27 11 834-1273/7, Fax: +27 11 838-5923/833-8156
E-mail: camielah@saimm.co.za, Website: http://www.saimm.co.za

27–29 May 2019 — The 9th International Conference on Sustainable Development in the Minerals Industry
Park Royal Darling Harbour, Sydney , Australia
Contact: Georgios Barakos
Tel: +49(0)3731 39 3602, Fax: +49(0)3731 39 2087
E-mail: Georgios.Barakos@mabb.tu-freiberg.de
Website: http://sdimi.ausimm.com/

5–6 June 2019 — New Technology Conference and Trade Show
'Embracing the Fourth Industrial Revolution in the Minerals Industry'
The Canvas Riversands, Fourways, Johannesburg, South Africa
Contact: Yolanda Ndimande
Tel: +27 11 834-1273/7, Fax: +27 11 838-5923/833-8156
E-mail: yolanda@saimm.co.za, Website: http://www.saimm.co.za

24–27 June 2019 — Ninth International Conference on Deep and High Stress Mining 2019
Misty Hills Country Hotel & Conference Centre, Muldersdrift, Johannesburg
Contact: Camielah Jardine
Tel: +27 11 834-1273/7, Fax: +27 11 838-5923/833-8156
E-mail: camielah@saimm.co.za, Website: http://www.saimm.co.za

4–5 July 2019 — Smart Mining, Smart Environment, Smart Society
'Implementing change now, for the mine of the future'
Accolades Boutique Venue, Midrand
Contact: Yolanda Ndimande
Tel: +27 11 834-1273/7, Fax: +27 11 838-5923/833-8156
E-mail: yolanda@saimm.co.za, Website: http://www.saimm.co.za

10–11 July 2019 — Revitalising exploration activity in southern Africa
Misty Hills Country Hotel & Conference Centre, Muldersdrift, Johannesburg
Contact: Camielah Jardine
Tel: +27 11 834-1273/7, Fax: +27 11 838-5923/833-8156
E-mail: camielah@saimm.co.za, Website: http://www.saimm.co.za

31 July–1 August 2019 — Entrepreneurship in the Minerals Industry Conference 2019
'Bringing ideas to life'
The Canvas Riversands, Fourways, Johannesburg, South Africa
Contact: Camielah Jardine
Tel: +27 11 834-1273/7, Fax: +27 11 838-5923/833-8156
E-mail: camielah@saimm.co.za, Website: http://www.saimm.co.za

5–7 August 2019 — The Southern African Institute of Mining and Metallurgy in collaboration with the Zululand Branch is organising The Eleventh International Heavy Minerals Conference
'Renewed focus on Process and Optimization'
The Vineyard, Cape Town, South Africa
Contact: Yolanda Ndimande
Tel: +27 11 834-1273/7, Fax: +27 11 838-5923/833-8156
E-mail: yolanda@saimm.co.za, Website: http://www.saimm.co.za

18–21 August 2019 — Copper 2019
Vancouver Convention Centre, Canada
Contact: Brigitte Farah
Tel: +1 514-939-2710 (ext. 1329), E-mail: metsoc@cim.org
Website: http://com.metsoc.org

19–22 Augusts 2019 — Southern African Coal Processing Society 2019 Conference and Networking Opportunity
Graceland Hotel Casino and Country Club, Secunda
Contact: Johan de Korte
Tel: 079 872-6403
E-mail: dekorte.johan@gmail.com
Website: http://www.sacoalprep.co.za

28–30 August 2019 — IFAC MMM 2019 Symposium
Stellenbosch Institute for Advanced Studies Conference Centre, Stellenbosch, Cape Town, South Africa
Email: info@ifacmmm2019.org
Website: https://www.ifacmmm2019.org

4–5 September 2019 — Surface Mining Masterclass 2019
Birchwood Hotel & OR Tambo Conference Centre, Johannesburg
Contact: Camielah Jardine
Tel: +27 11 834-1273/7, Fax: +27 11 838-5923/833-8156
E-mail: camielah@saimm.co.za, Website: http://www.saimm.co.za

16–17 October 2019 — Tailing Storage Conference 2019
'Investing in a Sustainable Future'
Birchwood Hotel & OR Tambo Conference Centre, Johannesburg
Contact: Camielah Jardine
Tel: +27 11 834-1273/7, Fax: +27 11 838-5923/833-8156
E-mail: camielah@saimm.co.za, Website: http://www.saimm.co.za

31 October–1 November 2019 — International Mine Health and SafetyConference 2019
Misty Hills Country Hotel & Conference Centre, Muldersdrift, Johannesburg
Contact: Camielah Jardine
Tel: +27 11 834-1273/7, Fax: +27 11 838-5923/833-8156
E-mail: camielah@saimm.co.za, Website: http://www.saimm.co.za

13–15 November 2019 — XIX International Coal Preparation Congress & Expo 2019
New Delhi, India
Contact: Coal Preparation Society of India
Tel/Fax: +91-11-26136416, 4166 1820
E-mail: cpsidelhi. india@gmail.com, president@cpsi.org. inrksachdev01@gmail.com, hi.sapru@monnetgroup.com

2020

25–29 May 2020 — The 11th International Conference on Molten Slags, Fluxes and Salts
The Westin Chosun Seoul Hotel, Seoul, Korea
Tel: +82-2-565-3571, Email: secretary@molten2020.org
http://www.molten2020.org

Company affiliates

The following organizations have been admitted to the Institute as Company Affiliates

3M South Africa (Pty) Limited
AECOM SA (Pty) Ltd
AEL Mining Services Limited
Air Liquide (PTY) Ltd
Alexander Proudfoot Africa (Pty) Ltd
AMEC Foster Wheeler
AMIRA International Africa (Pty) Ltd
ANDRITZ Delkor(Pty) Ltd
Anglo Operations Proprietary Limited
Anglogold Ashanti Ltd
Arcus Gibb (Pty) Ltd
ASPASA
Atlas Copco Holdings South Africa (Pty) Limited
Aurecon South Africa (Pty) Ltd
Aveng Engineering
Aveng Mining Shafts and Underground
Axis House Pty Ltd
Bafokeng Rasimone Platinum Mine
Barloworld Equipment -Mining
BASF Holdings SA (Pty) Ltd
BCL Limited
Becker Mining (Pty) Ltd
BedRock Mining Support Pty Ltd
BHP Billiton Energy Coal SA Ltd
Blue Cube Systems (Pty) Ltd
Bluhm Burton Engineering Pty Ltd
Bouygues Travaux Public
CDM Group
CGG Services SA
Coalmin Process Technologies CC
Concor Opencast Mining
Concor Technicrete
Council for Geoscience Library
CRONIMET Mining Processing SA Pty Ltd
CSIR Natural Resources and the Environment (NRE)
Data Mine SA
Digby Wells and Associates
DRA Mineral Projects (Pty) Ltd
DTP Mining - Bouygues Construction
Duraset
Elbroc Mining Products (Pty) Ltd
eThekwini Municipality
Expectra 2004 (Pty) Ltd
Exxaro Coal (Pty) Ltd
Exxaro Resources Limited
Filtaquip (Pty) Ltd
FLSmidth Minerals (Pty) Ltd
Fluor Daniel SA (Pty) Ltd
Franki Africa (Pty) Ltd-JHB
Fraser Alexander (Pty) Ltd
G H H Mining Machines (Pty) Ltd
Geobrugg Southern Africa (Pty) Ltd
Glencore
Hall Core Drilling (Pty) Ltd
Hatch (Pty) Ltd
Herrenknecht AG
HPE Hydro Power Equipment (Pty) Ltd
Immersive Technologies
IMS Engineering (Pty) Ltd
Ingwenya Mineral Processing
Ivanhoe Mines SA
Joy Global Inc.(Africa)
Kudumane Manganese Resources
Leco Africa (Pty) Limited
Longyear South Africa (Pty) Ltd
Lonmin Plc
Lull Storm Trading (Pty) Ltd
Maccaferri SA (Pty) Ltd
Magnetech (Pty) Ltd
MAGOTTEAUX (PTY) LTD
Maptek (Pty) Ltd
MBE Minerals SA Pty Ltd
MCC Contracts (Pty) Ltd
MD Mineral Technologies SA (Pty) Ltd
MDM Technical Africa (Pty) Ltd
Metalock Engineering RSA (Pty)Ltd
Metorex Limited
Metso Minerals (South Africa) Pty Ltd
Minerals Council of South Africa
Minerals Operations Executive (Pty) Ltd
MineRP Holding (Pty) Ltd
Mintek
MIP Process Technologies (Pty) Limited
Modular Mining Systems Africa (Pty) Ltd
MSA Group (Pty) Ltd
Multotec (Pty) Ltd
Murray and Roberts Cementation
Nalco Africa (Pty) Ltd
Namakwa Sands(Pty) Ltd
Ncamiso Trading (Pty) Ltd
New Concept Mining (Pty) Limited
Northam Platinum Ltd - Zondereinde
OPTRON (Pty) Ltd
PANalytical (Pty) Ltd
Paterson & Cooke Consulting Engineers (Pty) Ltd
Perkinelmer
Polysius A Division Of Thyssenkrupp Industrial Sol
Precious Metals Refiners
Rand Refinery Limited
Redpath Mining (South Africa) (Pty) Ltd
Rocbolt Technologies
Rosond (Pty) Ltd
Royal Bafokeng Platinum
Roytec Global (Pty) Ltd
RungePincockMinarco Limited
Rustenburg Platinum Mines Limited
Salene Mining (Pty) Ltd
Sandvik Mining and Construction Delmas (Pty) Ltd
Sandvik Mining and Construction RSA(Pty) Ltd
SANIRE
Schauenburg (Pty) Ltd
Sebilo Resources (Pty) Ltd
SENET (Pty) Ltd
Senmin International (Pty) Ltd
Smec South Africa
Sound Mining Solution (Pty) Ltd
SRK Consulting SA (Pty) Ltd
Time Mining and Processing (Pty) Ltd
Timrite Pty Ltd
Tomra (Pty) Ltd
Ukwazi Mining Solutions (Pty) Ltd
Umgeni Water
Webber Wentzel
Weir Minerals Africa
Worley Parsons RSA (Pty) Ltd

DEEP MINING 2019 CONFERENCE

NINTH INTERNATIONAL CONFERENCE ON DEEP AND HIGH STRESS MINING 2019

24–25 JUNE 2019 - CONFERENCE

26 JUNE 2019 - SARES 2019

27 JUNE 2019 - TECHNICAL VISIT

MISTY HILLS CONFERENCE CENTRE, MULDERSDRIFT, JOHANNESBURG, SOUTH AFRICA

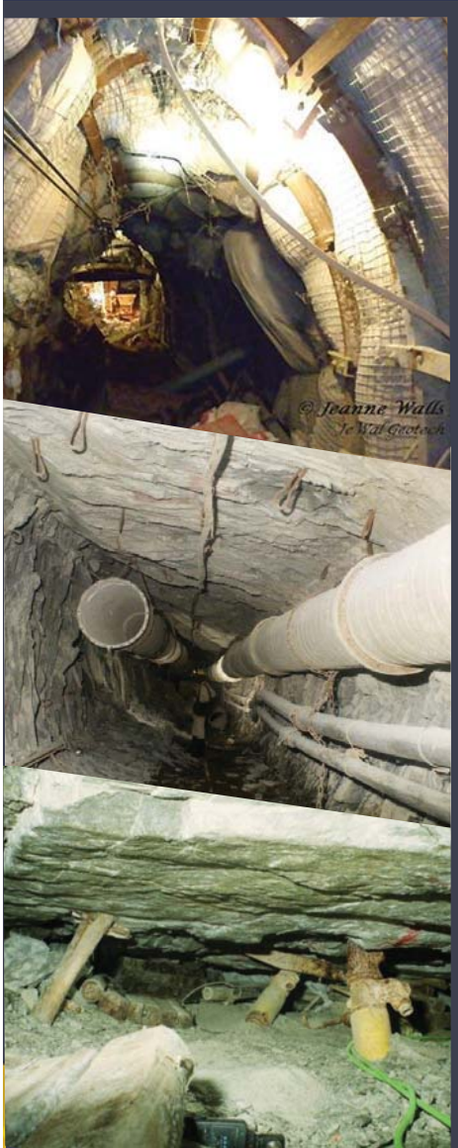

BACKGROUND

The Ninth International Conference on Deep and High Stress Mining (Deep Mining 2019) will be held at the Misty Hills Conference Centre, Muldersdrift, Johannesburg on 24 and 25 June 2019. Conferences in this series have previously been hosted in Australia, South Africa, Canada, and Chile. Around the world, mines are getting deeper and the challenges of stress damage, squeezing ground, and rockbursts are ever-present and increasing. Mining methods and support systems have evolved slowly to improve the management of excavation damage and safety of personnel, but damage still occurs and personnel are injured. Techniques for modelling and monitoring have been adapted and enhanced to help us understand rock mass behaviour under high stress. Many efficacious dynamic support products have been developed, but our understanding of the demand and capacity of support systems remains uncertain.

OBJECTIVE

To create an international forum for discussing the challenges associated with deep and high stress mining and to present advances in technology.

WHO SHOULD ATTEND

- Rock engineering practitioners
- Mining engineers
- Researchers
- Academics
- Geotechnical engineers
- Hydraulic fracturing engineers
- High stress mining engineers
- Waste repository engineers
- Rock engineers
- Petroleum engineers
- Tunnelling engineers

Sponsors

FLUOR

GEOBRUGG BRUGG Safety is our nature

ITASCA

MINOVA

New Concept Mining
Support for the World's Deepest Mines

OHMS

REUTECH MINING

ROCBOLT TECHNOLOGIES

srk

For further information contact:

Camielah Jardine, Head of Conferencing, SAIMM, Tel: +27 11 834-1273/7, Fax: +27 11 833-8156 or +27 11 838-5923
E-mail: camielah@saimm.co.za, Website: http://www.saimm.co.za

SAIMM
THE SOUTHERN AFRICAN INSTITUTE OF MINING AND METALLURGY

SANIRE
SOUTH AFRICAN NATIONAL INSTITUTE OF ROCK ENGINEERING

ACG AUSTRALIAN CENTRE FOR GEOMECHANICS
CSIRO | The University of Western Australia | Joint Venture

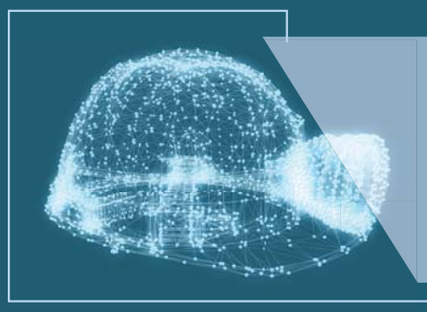

THE MINERALS INDUSTRY OF THE FUTURE

NEW TECHNOLOGY
CONFERENCE AND TRADE SHOW

Embracing the Fourth Industrial Revolution in the Minerals Industry

Driving competitiveness through people, processes and technology in a modernised environment

5–6 JUNE 2019 | THE CANVAS RIVERSANDS | FOURWAYS | SOUTH AFRICA

BACKGROUND

The SAIMM ran a very successful conference in 2017, which was called 'New Technology and Innovation in Mining'. Now, two years on, it is time to update ourselves on the latest developments, both in the digital world as well as the physical world of the minerals industry.

Our industry, steeped in great tradition and innovation, now finds itself facing new challenges, and many operations have already embraced these challenges and introduced people-centric technologies that are truly at the cutting edge of innovation.

Besides showcasing many exciting innovations and case studies, the conference will be supplemented with a trade show where many of these technologies will be featured.

OBJECTIVES

To showcase, explain and demonstrate the potential for operational improvement through innovative but practical technological solutions aimed at improvements in quality, output and productivity.

It is also aimed at achieving a common vision of 'the art of the possible' as well as exploring new paradigms for mining and metallurgy in the future.

WHO SHOULD ATTEND

- Mine managers
- Operational managers
- Mine engineers
- Mine planners
- Geologists
- Mining technical staff
- Technical information specialists
- Consultants
- Contractors
- Students
- Academics
- Researchers
- Metallurgical Managers
- Metallurgists
- Process design engineers

TOPICS

- Data mining
- Artificial intelligence
- New equipment
- Automation
- Remote operation
- Information management
- Communications technology
- New efficient equipment
- Renewable energy/energy efficiency

FOR EXHIBITION AND SPONSORSHIP OPPORTUNITIES CONTACT THE CONFERENCE CO-ORDINATORW

SAIMM
THE SOUTHERN AFRICAN INSTITUTE OF MINING AND METALLURGY

Contact: Yolanda Ndimande • Conference Co-ordinator • Tel: +27 11 834-1273/7
Fax: +27 11 833-8156 or+27 11 838-5923 • E-mail: yolanda@saimm.co.za
Website: http://www.saimm.co.za